Rotation Capacity of Self-Compacting Steel Fiber Reinforced Concrete

Rotation Capacity
of Self-Compacting
Steel Fiber Reinforced Concrete

Proefschrift

ter verkrijging van de graad van doctor
aan de Technische Universiteit Delft,
op gezag van de Rector Magnificus prof. dr.ir. J.T. Fokkema,
voorzitter van het College voor Promoties,
in het openbaar te verdedigen

op dinsdag 14 november 2006 om 10.00 uur

door

Petra SCHUMACHER

Diplom-Ingenieurin
(Darmstadt University of Technology, Duitsland)
geboren te Darmstadt, Duitsland.

Dit proefschrift is goedgekeurd door de promotor:

Prof.dr.ir. J.C. Walraven

Samenstelling promotiecommissie:

Rector Magnificus,	Technische Universiteit Delft, voorzitter.
Prof.dr.ir. J.C. Walraven,	Technische Universiteit Delft, promotor.
Univ.-Prof. Dr.-Ing. H. Falkner,	Technische Universität Braunschweig, Duitsland.
Prof.dr.ir. D.A. Hordijk,	Technische Universiteit Eindhoven.
Prof.dr.ir. J.G. Rots,	Technische Universiteit Delft.
Dr.-Ing. B. Schnütgen,	Ruhr-Universität Bochum, Duitsland.
Ir. J.A. den Uijl,	Technische Universiteit Delft.
Prof.dr.ir. L. Vandewalle,	Katholieke Universiteit Leuven, België.
Prof.dipl.ing. J.N.J.A. Vamberský,	Technische Universiteit Delft, reservelid.

ISBN-10: 90-9021297-3
ISBN-13: 978-90-9021297-5

Keywords:
Rotation capacity, SFRC, self-compacting steel fiber reinforced concrete

Printed in the Netherlands

Summary

Rotation Capacity of Self-Compacting Steel Fiber Reinforced Concrete

The use of nonlinear calculation models including the theory of plasticity can lead to cost savings in the amount of concrete and steel. When using this approach it has to be guaranteed that the deformation capacity provided by the structure exceeds the demand. The addition of fibers to concrete increases its deformation ability in compression and in tension. This may suggest that it improves the rotation capacity of plastic hinges in reinforced concrete (RC) members as well. This research project aims at providing knowledge about the influence of the addition of fibers on the rotation capacity of plastic hinges in self-compacting concrete (SCC). Rotation capacity is defined as the rotation at maximum load minus the rotation at the onset of steel yielding. The research objective was approached by investigating the effect of the addition of fibers to plain self-compacting concrete with regard to the behavior in compression, tension and bond. The results of these investigations were used to assess the effect of steel fibers on the rotation capacity of concrete members.

Chapter 2 presents a summary and evaluation of the available knowledge about the rotation capacity of reinforced concrete members and about the influence of steel fibers on the rotation capacity of structural members in general and tunnel segments in particular.

In chapter 3, the Compressive Damage Zone (CDZ) model is extended to self-compacting steel fiber reinforced concrete (SCSFRC). To this end, an extensive experimental program was performed on SCC and SCSFRC prisms. The test variables were the amount of fibers, the fiber aspect ratio, the fiber length, the concrete compressive strength and the eccentricity of the load. The experiments showed that the compressive strength was not influenced by the amount of steel wire fibers used in this investigation. The toughness of the concrete in compression was increased by the addition of the fibers. The CDZ model was extended to take this effect into account as a function of the amount of steel fibers, fiber geometry and eccentricity of the load.

In chapter 4, models from the literature for describing the tensile behavior of steel fiber reinforced (SFRC) concrete are presented and evaluated. Special attention is paid to the fact that due to a varying fiber orientation the tensile properties are direction dependent. In this study, the tensile properties in the direction along the member axis and an average of the tensile properties perpendicular to it were considered separately in modeling. The tensile properties along the member axis represented the tensile behavior in the cracks, whereas the average of the tensile properties perpendicular to it represented the tensile behavior necessary to evaluate the confinement capacity of the concrete surrounding a reinforcing bar. The tensile stress-crack width relation of Kützing (2000) was modified and used in the further investigations.

The bond behavior of ribbed bars in concrete is described in chapter 5. Pull-out tests were performed on ribbed steel bars (d_s = 10 mm) in a normal strength SCC without fibers and with 60 kg/m^3 hooked-end steel fibers (l_f = 30 mm, l_f/d_f = 80) varying the concrete cover (c = 15 to 95 mm). A non-linear finite element analysis showed that the confining capacity is increased even if no fibers are present in the concrete cover region.

Contrary to plain concrete, the contribution of the concrete to the load transfer in the cracks cannot be neglected in modeling SFRC. After modifying some input parameters and including the contribution of the fibers to the load transfer in the crack, the analytical bond model of Den Uijl & Bigaj (1996) has been used to describe the bond behavior of SCSFRC with satisfactory agreement of experimental and simulation results. Due to crack bridging of

the fibers, the tensile strength is reached after a shorter transfer length in steel fiber reinforced concrete (SFRC) compared to plain concrete. Therefore, the crack spacing and the crack widths in the SLS are smaller for SFRC than for reinforced concrete (RC) and the SFRC member is stiffer than a similar RC member. In a reinforced tensile member without fibers, the deformations localize in various cracks. However, in a reinforced tensile member with fibers, the deformations may localize in only one crack due to the fact that the softening of the SFRC may dominate the hardening of the reinforcing steel so that localization is more likely to occur. In this respect, the scatter in the properties of the SFRC also plays a role. As the first crack forms at the weakest cross-section, the steel in the neighboring cracks is less likely to reach the yielding stage, which would result in large crack widths. To investigate the phenomenon of localization of the deformations in one large crack, a parameter study was carried out. The tensile member hardening ratio was found to be proportional to the steel hardening ratio and inversely proportional to the fiber content.

The findings from the chapters 3 to 5 were then used as input for the rotation model presented in chapter 6. The experimental program included four tests on beams (h = 300 mm, b = 150 mm, l_0 = 3000 mm) loaded at mid-span up to steel or concrete failure. The beams were reinforced with two ribbed bars (d_s = 10 mm). The test variables were fiber content and normal compressive force. In the experiments, the addition of steel fibers in combination with the applied amount of reinforcing bars led to an increase in maximum moment of approximately 10% and to cracking but no spalling in the compressive zone. The specimens tested with fibers had a smaller rotation capacity than those tested without fibers. As explained in chapter 5, this decrease in deformation capacity, which was observed in the experiments and in the simulations, is explained with localization of the deformations in one large crack in case of the SCSFRC specimens compared to several large cracks in case of the SCC specimens. This was an important result. The reduction in total deformation can be dangerous when it leads to brittle failure, and therefore it has to be kept in mind in elastic design with redistribution of forces or plastic design of concrete structures.

In some cases it may be desired to capture the complete behavior including the descending branch of the moment-rotation curve. In those cases, the rotation at the ultimate load step minus the rotation at the beginning of steel yielding is of interest. Both in the beam tests and the simulations, this difference was smaller for the SCSFRC compared to the SCC in case of steel failure due to the localization of deformations in one crack, but it was slightly larger in case of concrete crushing due to the increased concrete ductility.

Chapter 7 presents the results of a parameter study. The findings of the parameter study correspond well with the trends observed in chapter 6. Chapter 8 gives the conclusions of this research with general recommendations and an indication for practical applications of the developed theory.

Petra Schumacher, Delft University of Technology

Samenvatting

Rotatiecapaciteit van zelfverdichtend staalvezelbeton

Het gebruik van niet-lineaire modellen inclusief de plasticiteitstheorie kan kostenbesparingen opleveren door een reductie in de benodigde hoeveelheid beton of staal. Indien deze modellen gebruikt worden moet gegarandeerd worden dat de vervormingscapaciteit die door de constructie geleverd kan worden groter is dan degene die voor herverdeling nodig is. Het toevoegen van vezels aan beton vergroot de taaiheid van dit materiaal onder druk en onder trek. Dit zou er op kunnen duiden dat het ook de rotatiecapaciteit van plastische scharnieren in gewapend betonnen constructiedelen verbetert. Dit onderzoeksproject heeft als doel om kennis te vergaren over de invloed van het toevoegen van vezels op de rotatiecapaciteit van plastische scharnieren in zelfverdichtend beton. De rotatiecapaciteit is gedefinieerd als de rotatie bij maximale last verminderd met de rotatie bij het begin van vloeien van het staal. Het doel van dit onderzoek werd stapsgewijze benaderd door de invloed van het toevoegen van vezels aan zelfverdichtend beton op het gedrag bij druk, trek en aanhechting te onderzoeken. De resultaten van deze onderzoeken werden gebruikt om het effect van staalvezels op de rotatiecapaciteit van betonnen constructiedelen te berekenen.

Hoofdstuk 2 levert een samenvatting en evaluatie van beschikbare kennis op het gebied van rotatiecapaciteit in gewapend betonnen constructiedelen en van de invloed van staalvezels op de rotatiecapaciteit van constructiedelen in het algemeen en voor tunnelsegmenten in het bijzonder.

In hoofdstuk 3 wordt het Compressive Damage Zone (CDZ) model uitgebreid naar zelfverdichtend staalvezelbeton. Daarvoor werd een uitgebreide testserie gedaan op ongewapende en staalvezelversterkte zelfverdichtende betonnen prisma's. De testvariablen waren de vezelhoeveelheid, de vezelslankheid, de vezellengte, de betondruksterkte en de excentriciteit van de last. De betondruksterkte was onafhankelijk van de hoeveelheid staalvezels die in dit onderzoek gebruikt werden. De taaiheid van beton onder druk werd groter door de toevoeging van vezels. Deze vergroting is in het gemodificeerde model geïntroduceerd als een functie van de vezelhoeveelheid, de vezelgeometrie en de excentriciteit van de last.

In hoofdstuk 4 worden modellen uit de literatuur die het gedrag van staalvezelbeton onder trek beschrijven, gepresenteerd en geëvalueerd. Bijzondere aandacht wordt besteed aan het feit dat de trekeigenschappen richtingsafhankelijk zijn vanwege een variërende vezeloriëntatie. In dit proefschrift worden daarom de trekeigenschappen van staalvezelbeton langs de as van een constructiedeel en de gemiddelde trekeigenschappen haaks daarop apart in rekening gebracht. De trekeigenschappen in langsrichting staan voor het trekgedrag in de scheuren, terwijl het gemiddelde van de trekeigenschappen haaks er op het trekgedrag voor het berekenen van de omsnoeringswerking van beton rond om een wapeningsstaaf beschrijft. Het model van Kützing (2000) werd gemodificeerd en gebruikt in de verdere studieonderdelen.

Het aanhechtgedrag van geribde wapeningsstaven in beton wordt in hoofdstuk 5 beschreven. Uittrekproeven werden gedaan op staven (d_s = 10 mm) in een zelfverdichtende normale sterkte beton zonder vezels en met 60 kg/m^3 staalvezels met eindhaken (l_f = 30 mm, l_f/d_f = 80) en variërende betondekking (c = 15 tot 95 mm). Een niet-lineaire eindige elementen analyse toonde aan dat de omsnoeringswerking door toevoeging van staalvezels vergroot wordt, ook al zijn er geen vezels aanwezig in de dekking.

Anders dan bij gewapend beton kan de bijdrage van het beton aan de krachtoverdracht in de scheuren bij het modelleren van staalvezelbeton niet verwaarloosd worden. Na modificatie

van sommige input parameters en toevoegen van de bijdrage van de vezels aan de krachtsoverdracht in een scheur werd het analytische aanhechtmodel van Den Uijl & Bigaj (1996) gebruikt om het aanhechtgedrag van zelfverdichtend staalvezelbeton met tevredenstellende overeenstemming van experimenten en simulaties te beschrijven. Door de scheuroverbruggende werking van de vezels wordt de treksterkte in staalvezelbeton over een kortere inleidingslengte opgebouwd dan in vezelvrij beton. Daarom zijn de scheurafstanden en de scheurwijdtes in staalvezelbeton kleiner vergeleken met vezelvrij beton en een staalvezelbetonstaaf gedraagt zich stijver dan een een vezelvrije. In een gewapend betonnen constructiedeel zonder vezels lokaliseren de vervormingen in verscheidene scheuren. In gewapende constructiedelen met staalvezels kan het echter gebeuren dat de vervormingen in een enkele scheur lokaliseren omdat het ontstevigende gedrag van het staalvezelbeton het verstevigende gedrag van het gewapend beton kan domineren en er op die manier makkelijker lokalisatie kan optreden. De spreiding van de materiaaleigenschappen van het staalvezelbeton draagt hier ook aan bij. Omdat de eerste scheur in de zwakste doorsnede ontstaat, is het minder waarschijnlijk dat het staal in de naburige scheuren de vloeispanning bereikt, hetgeen weer tot grotere scheurwijdtes zou leiden. Om het fenomeen van lokalisatie van de vervormingen in een grote scheur te onderzoeken, werd een parameterstudie uitgevoerd. De verstevigingsverhouding van een trekstaaf was daarin evenredig aan de verstevigingsverhouding van het wapeningsstaal en omgekeerd evenredig aan de hoeveelheid staalvezels.

De uitkomsten van hoofdstuk 3 tot 5 werden vervolgens gebruikt als input voor het model voor rotatiecapaciteit dat in hoofdstuk 6 gepresenteerd wordt. Het experimentele programma bestond uit vier proeven op balken (h = 300 mm, b = 150 mm, l_0 = 3000 mm), die in het midden tot bezwijken van het staal of het beton belast werden. De balken waren gewapend met twee wapeningsstaven (d_s = 10 mm). De testvariabelen waren vezelgehalte en normaaldrukkracht. In de experimenten leidde het toevoegen van staalvezels in combinatie met de toegepaste hoeveelheid wapeningsstaven tot een vergroting van het maximale moment met circa 10% en tot scheuren maar niet afspatten in de betondrukzone. De proefstukken met vezels hadden een kleinere rotatiecapaciteit dan degenen zonder vezels. Zoals in hoofdstuk 5 uitgelegd, wordt deze afname in vervormingsvermogen, die zowel in de experimenten als ook in de berekeningen terug te vinden was, verklaard met de lokalisatie van de vervormingen in één grote scheur in het geval van zelfverdichtend staalvezelbeton in plaats van verscheidene grote scheuren zoals bij de zelfverdichtend betonnen proefstukken. Dit was een belangrijk resultaat. De afname in totale vervorming kan gevaarlijk zijn indien het leidt tot bros bezwijken en moet daarom in gedachten gehouden worden in een elastisch ontwerp met herverdeling van krachten of in het plastisch ontwerpen van betonconstructies.

In sommige gevallen kan het wenselijk zijn om het complete gedrag inclusief de dalende tak van een moment-rotatiecurve in beschouwing te nemen. In die gevallen is de rotatie net voor bezwijken minus de rotatie bij begin van staalvloeien van belang. In de balkproeven en in de berekeningen was dit verschil kleiner voor de vezelbeton proefstukken dan voor de vezelvrije vanwege de lokalisatie van de vervormingen in één scheur in het geval van staalbezwijken, maar iets groter in het geval van betonbezwijken vanwege de vergrote taaiheid van beton onder druk.

Hoofdstuk 7 geeft de resultaten van een parameterstudie weer. De uitkomsten komen overeen met de trends die al in hoofdstuk 6 beschreven werden. Hoofdstuk 8 geeft de conclusies van dit onderzoek met algemene aanbevelingen en een indicatie voor praktische toepassingen van de ontwikkelde theorie.

Petra Schumacher, Technische Universiteit Delft

Acknowledgements

The research project reported in this thesis has been performed at the Stevin II Laboratory of the Concrete Structures Group, Faculty of Civil Engineering and Geosciences, Delft University of Technology, the Netherlands.

Doing research and writing a thesis is the result of the efforts of not only one person, but many. Some contribute directly to the thesis by providing guidance, constructive comments, technical support or finances. Others do not contribute to the thesis directly, but provide friendship, encouragement and support. I would like to thank all of them for their contribution to this work.

First of all, I would like to express my sincere gratitude to Prof. dr.ir. Joost Walraven for having given me the opportunity to work on this research project, for the fruitful discussions about the topic, for his guidance and for creating an excellent working environment with good facilities, nice colleagues and numerous opportunities to attend conferences and take courses. I am particularly grateful that I was given the opportunity to participate in the RILEM TC 162-TDF task group, which has greatly stimulated my research interests.

I am also deeply indebted to my supervisors Ir. Joop den Uijl from Delft University of Technology and Dr.ir. Agnieszka Bigaj-van Vliet from TNO Built Environment and Geosciences for their suggestions, advice, encouragement and for sharing their profound knowledge in concrete and research skills. I am very thankful to Ir. Joop den Uijl for his valuable frequent advice in dealing with technical matters as well as the frustrations that technical problems sometimes cause.

I would like to express my gratitude to the thesis defense committee, Prof. dr.ir. Lucie Vandewalle, Univ.-Prof. Dr.-Ing. Horst Falkner, Prof. dr.ir. Dick Hordijk, Prof. dr.ir. Jan Rots, Dr.-Ing. Bernd Schnütgen and Prof. dipl.ing. Jan Vamberský for their interest in my research and the time and effort they put into reading this thesis.

I would like to thank the technical staff of the Stevin Laboratory, Arjen van Rhijn, Ger Nagtegaal, Albert Bosman, Fred Schilperoort, Ron Mulder, Ton Blom, Erik Horeweg, René van der Baars, for the good cooperation and technical support. I would like to thank Theo Steijn and Henk Spiewakowski for the drawings.

This research project was funded by Delft Cluster (project number 01.06.03). It was part of a program on the application of new materials in shield driven tunnel linings. The financial support of Delft Cluster is gratefully acknowledged as well as the donation of the steel fibers by the Belgian company Bekaert. Furthermore, the financial support of the Research School for Structural Engineering for courses and trainings is gratefully acknowledged.

I would also like to thank my colleagues and steel fiber friends M.Sc. Åse Døssland, Dr.-Ing. Erol Erdem, Dr.ir. Steffen Grünewald, Dipl.-Ing. Eleni Lappa, M.Sc. Alberto Meda, Dr.ir. Tarig Medani, Dr.-Ing. Juliane Möller, M.Sc. Roy Shionaga and Dr.-Ing. Manfred Teutsch for reading preliminary chapters of this thesis. I would like to thank all of my colleagues - former and present - for the good work environment and the fruitful discussions we had during my time at Delft University of Technology. I am also very thankful to all the nice people I met at conferences and who discussed earlier publications and presentations with me and provided me with information on their own projects as well as a nice and friendly environment.

I would like to express my sincere gratitude to my parents and to my brother for their support during all these years. I also would like to express my deep gratitude to all my friends at home in Germany, in Delft and all over the world for their support, encouragement and prayers. Finally, and above all, my gratitude towards God, who is faithful beyond human comprehension, cannot be expressed by words.

The thesis presents the results of this research project and is intended to be a contribution to the knowledge about concrete. It is my hope that it will be read and reviewed critically and that any comments and suggestions regarding its content will be directed to me.

Petra Schumacher

Table of Contents

1 Introduction

1.1 General Introduction

This thesis deals with the question on how steel fibers influence the rotation capacity of concrete tunnel linings reinforced with steel fibers or combinations of steel fibers and conventional reinforcement.

Tunnel Design and Construction Methods

A large part of the world's population lives in urban areas. These areas are densely populated and therefore, there is an increasing need to use the available space multidimensionally. Transportation is one particular aspect that can be placed underground without causing problems with regard to the health or the comfort of the users. Tunnel structures are therefore frequently found in urban areas.

Tunnels can be designed and constructed in different ways. The choice of the construction method mainly depends on the soil properties and the requirements with regard to acceptable disturbances of the activities above ground. Fig. 1.1 gives an overview of tunnel construction methods that are used in modern tunneling.

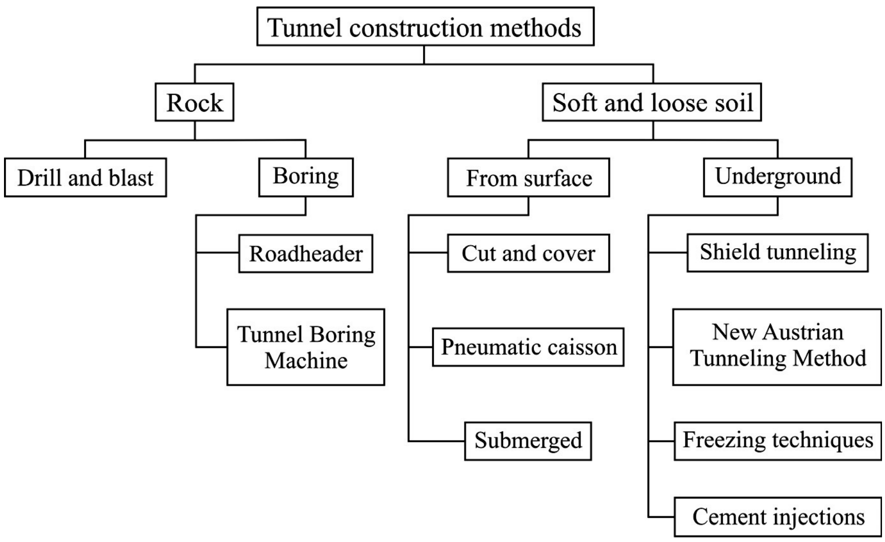

Fig. 1.1: Tunnel construction methods [Glerum, 1992]

In the Netherlands, the soil is soft (e.g. clay or peat) and the groundwater table is high. In the past, most tunnels built in the Netherlands were designed and constructed as submerged or cut and cover tunnels. In recent years, however, approximately half of the tunnels constructed in the Netherlands is built with the shield tunneling technique using a tunnel boring machine

(TBM). This method has the advantage that the activities at the surface are not significantly disturbed during the building process and that the local infrastructure is not affected.

Tunnels built with a TBM usually have a circular cross-section. Sometimes multi-face shields are used and two or three circular cross-sections are combined to provide space, e.g. for stations etc.

Most tunnel linings built with a TBM are made of segments. In some cases, a monolithic lining is made. In case of a segmental lining, a number of segments and one keystone form a ring. The joint between two rings is called the lateral joint and the joint between two segments in one ring is called the longitudinal joint, see Fig. 1.2.

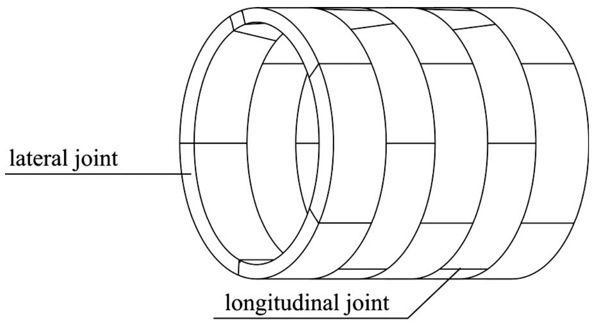

Fig. 1.2: Lateral and longitudinal joints of a segmental tunnel lining

Elastic and Plastic Design

Up to now, tunnels have usually been designed on the basis of an assumed linear elastic behavior. The deformations are limited in order to satisfy the Serviceability Limit State (SLS) criteria. It is commonly assumed that more advanced calculation methods for the structural resistance are not considered useful in tunneling because the soil properties have a large scatter and therefore, the acting forces are not known exactly [Herzog, 1999]. This leads to large safety margins. Herzog (1999) even reported a margin of a factor 12 between failure load and design load for the investigated tunnels.

According to some standards, e.g. Eurocode 2 (1992), the design of concrete structures in the Ultimate Limit State (ULS) is possible using nonlinear approaches including the theory of plasticity. If an engineer decides to use these approaches it has to be guaranteed that the deformation capacity provided by the structure is higher than a certain limit value. Before the ultimate load of the structure is reached, redistribution of forces takes place and plastic hinges are formed, which make this redistribution possible. The design is only safe if the assumed plastic hinges can deform as desired and no premature failure occurs. There are various models to calculate the available rotation capacity of beams and slabs [CEB, 1998]. The designer has to make sure that sufficient plastic rotation without loss of load bearing capacity is possible in the structure.

If these plastic or non-linear design approaches could be used in tunnels, considerable cost savings could be achieved. These cost savings relate to:

- savings in the tunnel lining thickness
- savings in the amount of reinforcement
- savings in the volume of soil excavation
- in case of tunnel segments: savings in transportation costs.

In this respect it is illustrative to quote the analysis of the failure of a ring in a tunnel by Blom (2002). He showed an example of a tunnel that fails due to “snap through”, see Fig. 1.3. The increase of the ovaliszation load from the first plastic hinge to final failure (3 plastic hinges in a circular cross-section) was a factor 3, see Fig. 1.4. In order to mobilize the complete hinge mechanism and thereby designing more economically, a certain minimum rotation capacity must be available in the structure after the first hinge has been formed.

It is noted that the interaction between the rings can be the reason why a hinge forms in the segment rather than in the longitudinal joint, e.g. when a hinge continues from a longitudinal joint through a tunnel segment to the next longitudinal joint, see Fig. 1.5.

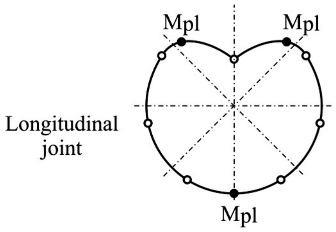

Fig. 1.3: Deformed shape of a tunnel ring at snap through [Blom, 2002]

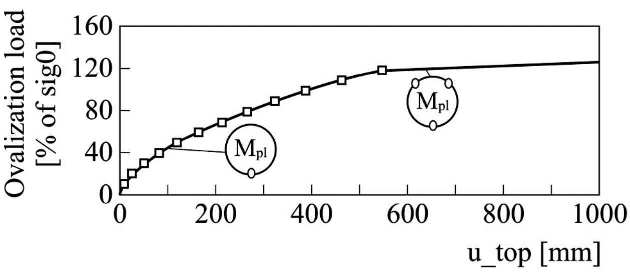

Fig. 1.4: Ovalization load as a function of the top deformation of the tunnel ring in the snap through failure case [Blom, 2002]

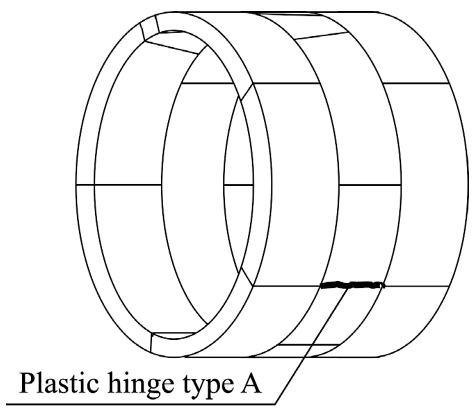

Fig. 1.5: Hinge type A in 3-D

The larger and the more reliable the rotation capacity of a hinge is, the more favorable the structural behavior will be. In this respect it is noted that, in recent times, a number of new, high performance materials have been developed. Especially large progress has been achieved in the field of fiber reinforced concretes. The addition of fibers to concrete increases its post-cracking strength. This might mean that it improves the rotation capacity of plastic hinges in concrete structures as well. This opens interesting possibilities for the design of tunnel linings, for the reasons given previously. However, then it should be investigated if, and to what extent, the addition of fibers improves the rotation capacity of plastic hinges in concrete.

ULS and SLS

Failure of a tunnel lining, driving up of the tunnel and snap through are considered ULS phenomena, whereas cracking, large deformations and leakage are considered SLS phenomena [COB/CUR, 2000].

The optimum deformation behavior of a tunnel has to fulfill a number of requirements, which are to a certain extent contradictory:

- In the SLS, joint rotations and crack widths should be limited in order to keep the tunnel watertight, and to ensure durability.
- In the ULS, a ductile structural behavior and a large rotation capacity of the plastic hinges are desired in order to prevent brittle failure and to allow for stress redistributions.

The structure needs to fulfill the criteria of both requirements at prescribed reliability levels. In the SLS, the crack widths and the rotations are limited in order to satisfy the requirements of water tightness and durability. With regard to the rotation capacity (ULS) it is noted that the required plastic rotation capacity usually taken into account for beams and slabs is not necessarily valid for tunnels because of different boundary conditions [Hemmy & Falkner, 2004]. In tunneling, the required rotations have not yet been defined for general cases [Hemmy, 2003]. Especially, the available rotation capacity is not fully predictable for SFRC or a combination of steel fibers and conventional bar reinforcement.

Location and Number of Plastic Hinges in a Tunnel Ring

In a continuous tunnel lining, a plastic hinge can form at any place as soon as the reinforcement starts to yield. In prefabricated tunnel segments, a plastic hinge can either form in the segment (hinge type A in Fig. 1.6) or at a longitudinal joint (hinge type B in Fig. 1.6), depending on the loading conditions. The hinge in a continuous tunnel lining and in a segment can be modeled in the same way (hinge type A).

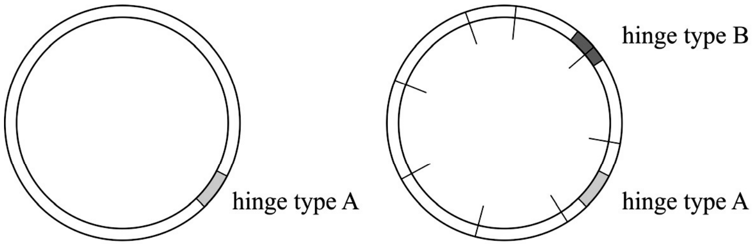

Fig. 1.6: Type and location of hinges in continuous (left) and segmental (right) tunnel lining

A typical joint, in which hinge type B occurs, can be seen in Fig. 1.7. The height of the contact area is smaller than the segment thickness in order to avoid spalling of the edges. The forces are transmitted by direct contact and friction. Rotation capacity is also required in this type of hinge.

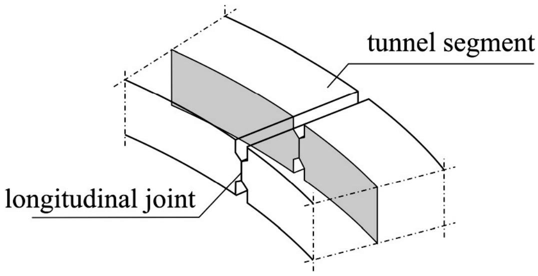

Fig. 1.7: Longitudinal joint [De Waal, 2000]

1.2 Application of Steel Fibers in Tunnel Linings

In most segmental tunnel linings, the segments are made of conventionally reinforced concrete, usually containing 70-120 kg steel per m^3 concrete [IFT, 2004]. The reinforcement is placed symmetrically at the outer and inner side of the lining. The two layers are held together by stirrups, which are widely spaced and therefore do not provide additional confinement of the compressive zone. A typical reinforcement cage can be seen in Fig. 1.8.

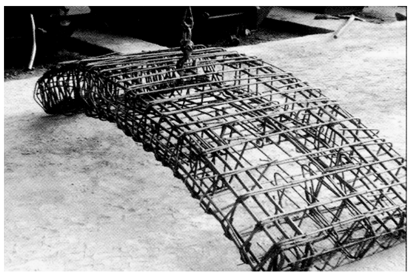

Fig. 1.8: Typical reinforcement cage for a conventionally reinforced tunnel segment [Bekaert, 2000]

The production and the storage of these reinforcement cages are time consuming and therefore cost-intensive. Furthermore, the concrete cover is rather thick in tunnel linings due to the required durability (corrosion protection, fire resistance). Therefore, the cover is vulnerable to spalling of concrete along the unreinforced edges. Possible damage patterns can be seen in Fig. 1.9.

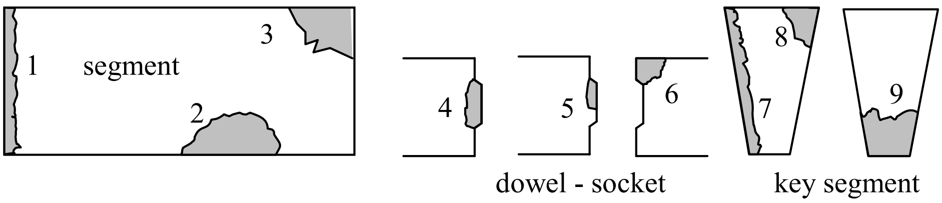

Fig. 1.9: Observed damage patterns (spalling) in tunnel segments [Blom, 2002]

A combination of fiber reinforcement and traditional reinforcement can allow a reduction of the amount of traditional reinforcement or the thickness of the tunnel lining. Steel fiber reinforced concrete (SFRC) has been used in tunnels since the late 1970's [Maidl, 1995] and design recommendations are available [Teutsch, 2006]. Tunnels have been made of extruded steel fiber reinforced concrete, fiber reinforced shotcrete or SFRC tunnel segments. The application of steel fibers in tunnel linings has proven to have several advantages. Some of these advantages include [Hemmy, 2002; Falkner & Teutsch, 2006]:

- cost savings not having to manufacture and store the reinforcement cages
- strengthening of the edges and therefore reduced spalling
- multiaxial loads can be carried due to the three-dimensional reinforcement
- better absorption of impact loads during placing and transport of tunnel segments
- crack width control
- larger deformation capacity in compression
- in case of absence of reinforcing bars larger deformation capacity in tension
- reduced spalling in case of corrosion of the reinforcement.

The central question of this thesis is, however, how steel fibers influence the rotation capacity of concrete members.

Another promising development is the use of self-compacting concrete (SCC) and self-compacting steel fiber reinforced concrete (SCSFRC). Well used, SCC offers many advantages:

- it levels out and deairates without further compaction
- shorter construction time
- less energy is consumed and machines for compaction are not necessary
- the quality of the concrete, which is usually sensitive to the quality of compaction, can be assumed as good

- the formwork can be filled completely
- a sound concrete surface
- densely reinforced structures can be cast
- the concrete is homogeneous
- less wear of the formwork
- improved working conditions due to noise and dust reduction, which results in less frequent work-related illnesses.

Taking into account these recent developments in concrete technology, it was decided in the scope of this thesis, to investigate the further application of SFRC and SCC to tunnel structures and to analyze the advantages of using self-compacting steel fiber reinforced concrete (SCSFRC).

With regard to rotation capacity it is important to know how the workability and thus the fiber distribution and orientation, the tensile properties of the hardened concrete and thereby the rotation capacity is influenced by the use of SCC.

1.3 Research Objective

The current state of knowledge does not allow to answer the following question:

- **What is the rotation capacity of concrete tunnel linings reinforced with steel fibers or combinations of steel fibers and conventional reinforcement in SCC?**

In order to answer this question, SFRC members subjected to combinations of a normal compressive force and a bending moment have to be analyzed.

This research aims at providing more knowledge about the factors influencing the rotation capacity of plastic hinges in SFRC and about the contribution of steel fibers to the rotation capacity of members with combined steel fiber and bar reinforcement.

Extensive research on SFRC was carried out in the scope of two previous PhD theses [De Waal, 2000; Kooiman, 2000]. Both theses covered several aspects of SFRC, but did not regard the influence of steel fibers on the rotation capacity.

The rotation capacity of plastic hinges in reinforced concrete structures without fibers was investigated by Bigaj (1999). One of her conclusions was that the effects of concrete grade and brittleness on the rotation capacity of plastic hinges need to be further investigated.

Besides, most of the past research on rotation capacity was performed on beams or slabs without a normal force. In tunneling, however, the main loading is a large normal force in combination with small bending moments.

It is the objective of the present thesis to combine the knowledge from previous investigations with new experimental findings and to model the rotation capacity of structural members made of SFRC.

1.4 Research Strategy

In this project, the rotation behavior of self-compacting concrete with and without steel fibers was investigated experimentally and theoretically. The main research objective was approached by solving the following questions:
How does the addition of fibers change the behavior of plain concrete with regard to
- compression?
- tension?
- bond?

The answers to these questions will be used to answer the final question:
- How do steel fibers influence the rotation capacity?

Answering these questions is a necessary precondition for developing a model to calculate the rotation capacity. A rational physical model for rotation capacity accounts for the behavior of concrete with and without steel fibers in compression and tension, the behavior of reinforcing bars and for the bond of the reinforcing bars to concrete.

In this thesis, attention is paid to the available rotation capacity of a single plastic hinge of type A (see Fig. 1.6 in a cross-section made of SFRC and a combination of SFRC and conventional reinforcement). Plastic hinge type B has been modeled by Janßen (1983) for conventional concrete. This thesis provides information that can be used for the analysis of local failure in a hinge, the formation of a hinge mechanism in the ULS and for the analysis of the deformations that may result in leakage in the SLS. All experiments were performed monotonously at low speeds up to failure to capture the behavior in short-term loading.

1.5 Outline of the Thesis

This thesis is divided into eight chapters. The introduction in chapter 1 defines the problem and indicates how a solution is approached.

Chapter 2 presents a summary of the present knowledge about the rotation capacity of reinforced concrete members and about the influence of steel fibers on the rotation capacity of structural members in general and tunnel segments in particular.

In chapter 3, the compressive behavior is described. Based on experiments performed on plain and steel fiber reinforced self-compacting concrete prisms, the Compressive Damage Zone (CDZ) model developed by Markeset (1993) for plain concrete is extended to steel fiber reinforced self-compacting concrete.

In chapter 4, models from the literature for describing the tensile behavior of steel fiber reinforced concrete are presented.

Based on the own experimental findings and approaches found in the literature, a model for the bond behavior of deformed bars in a concrete matrix with steel fibers is proposed in chapter 5.

The findings from the chapters 3 to 5 are used as input for the rotation model presented in chapter 6. This model is verified with experimental results. Chapter 7 presents the results of a parameter study.

Chapter 8 gives the conclusions of this research with general recommendations and an indication for practical applications of the developed theory.

Fig. 1.10 gives an overview over the structure of this thesis.

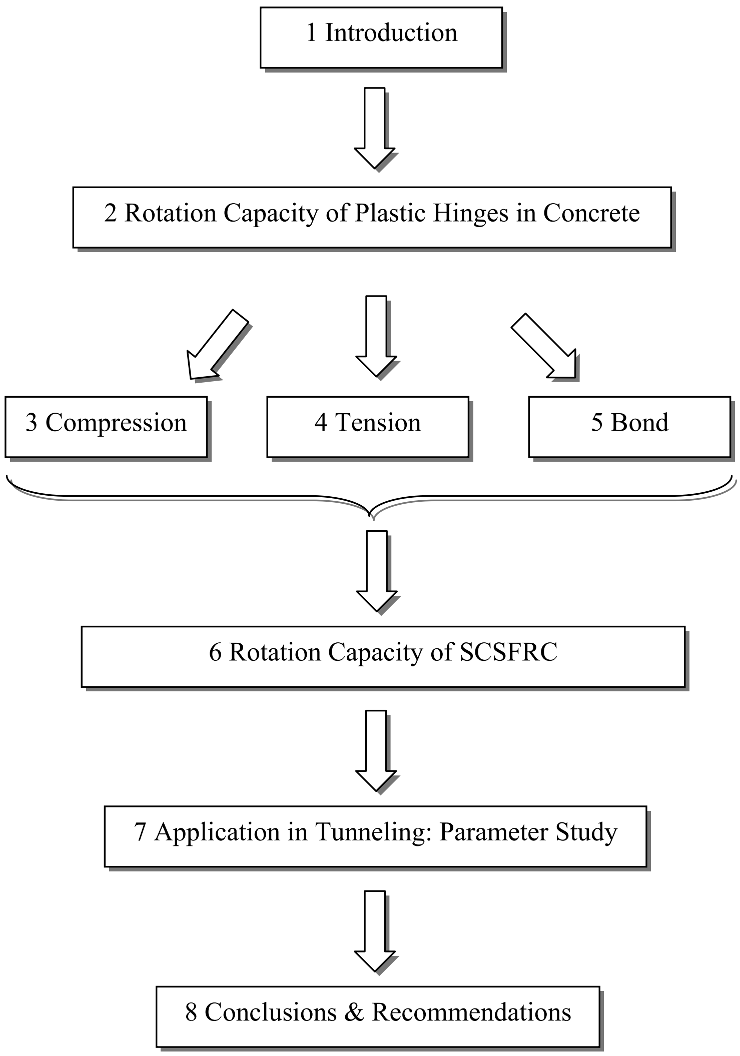

Fig. 1.10: Structure of the thesis

2 Rotation Capacity of Plastic Hinges

In statically indeterminate structures, a certain degree of redistribution of forces is allowed. This redistribution is desired because of several benefits, such as reduction of reinforcement in bending moment zones, a reduction of the amount of reinforcement in densely reinforced areas leading to an improved concrete quality in these areas and savings in reinforcing steel [CEB, 1998]. In order to allow the redistribution of forces, the available rotation capacity of a structure must be large enough to avoid brittle failure before the hinge mechanism has formed. The rotation capacity of reinforced concrete beams and slabs has been investigated since the 1960's, e.g. by Bachmann (1967, 1970), Baker (1956), Dilger (1966) and Eifler (1969, 1983). In the 1980's, the works of Langer (1987) and Graubner (1989) helped to clarify the influence of different parameters on rotational deformations. In the Comité Euro-International du Béton (CEB) Task Group 2.2 "Ductility Requirements for Structural Concrete – Reinforcement", many findings about the ductility of concrete structures were further explained. For more information on these findings, see CEB (1998).

The rotation capacity of plastic hinges is influenced by various factors. These factors are summarized in section 2.2. Some aspects of the influence of steel fibers on the rotation capacity are addressed in section 2.3. Existing models for calculating the available rotation capacity of plastic hinges in reinforced concrete are described and evaluated in section 2.4.

2.1 Rotation: Definition and Derivation from Experiments

2.1.1 Definitions of Rotation for Members with Bending Reinforement

The definition of rotation capacity depends on the general approach to analyze the deformations in statically indeterminate structures [CEB, 1998]. The rotation capacity is not unambiguously defined in literature, as shown in Fig. 2.1. In general, the total rotation Θ_{tot} is subdivided into elastic rotation Θ_{el} and plastic rotation Θ_{pl}. The rotation capacity is defined as the plastic rotation $\Theta_{pl} = \Theta_{tot} - \Theta_{el}$.

In this thesis, the approach according to CEB (1998) is followed. According to this approach, the rotations in a statically determinate beam with bending reinforcement, e.g. one that was cut out from a statically indeterminate structure at the points of zero moment, are defined as follows:

total rotation Θ_{tot}	the curvature at maximum load integrated over the total length of the beam
elastic rotation Θ_{el}	the curvature at the onset of yielding of the reinforcement integrated over the total length of the beam
plastic rotation Θ_{pl}	the difference between the total rotation of the hinge at the level of maximum moment and the elastic rotation: $\Theta_{pl} = \Theta_{tot} - \Theta_{el}$

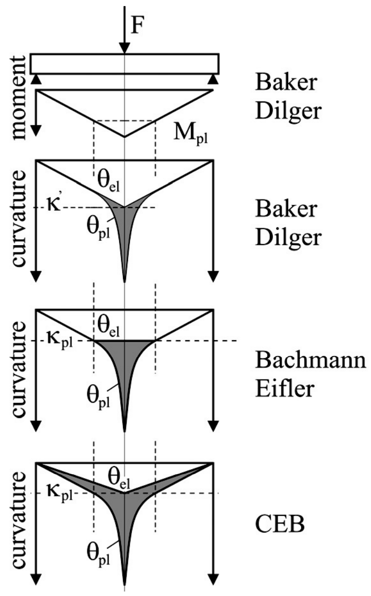

Fig. 2.1: Possible definitions of elastic, plastic and total rotation [CEB, 1998]

It is noted that the deformations may pass the peak load as long as the failure mechanism has not been formed. A limitation of the rotation capacity to the maximum is therefore on the safe side.

It is worth noticing that, in a study on high strength concrete (HSC), Pecce (1998) concluded that the commonly applied definition of rotation capacity (up to maximum load level) may need to be reconsidered in case of reinforced HSC members [CEB, 1998]. Pecce (1998) suggested a definition of plastic rotation taking into account the descending branch up to a decrease in load of approximately 5%.

A change of the definition of the rotation capacity by adopting e.g. the point of a significant drop of the load as the criterion for the ultimate rotation results in a significant increase of the considered plastic hinge deformation and thus an increase of the estimated value of the rotation capacity [CEB, 1998]. This is illustrated in Fig. 2.2.

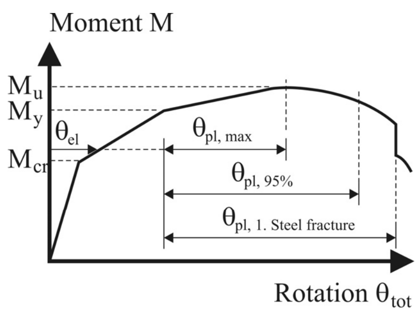

Fig. 2.2: Different portions of the rotation in the moment-rotation diagram [Bühler & Eibl, 1991]

2.1.2 Definitions of Rotation for Members without Bending Reinforcement

For members without bending reinforcement, the definitions of reinforced concrete discussed above are not applicable. In this case it is proposed to define the rotations as follows [Baker, 1956], see Fig. 2.3:

total rotation Θ_{tot}	the curvature at maximum load integrated over the total length of the beam
elastic rotation Θ_{el}	the curvature at the point at which the moment curvature relationships deviates significantly from the initial elastic branch integrated over the total length of the beam, see Fig. 2.3.
plastic rotation Θ_{pl}	the difference between the total rotation of the hinge at the level of maximum moment and the elastic rotation: $\Theta_{pl} = \Theta_{tot} - \Theta_{el}$

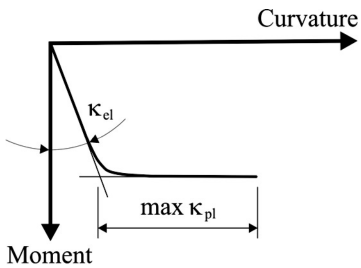

Fig. 2.3: Definition of elastic and plastic curvature [Baker, 1956]

2.1.3 Measuring and Calculating the Rotation

In order to experimentally assess the rotation of a member the following measurements shall be done on the specimen:

- strains on top and bottom
- deflection in the middle of the specimen
- crack widths
- rotation angle of the ends.

If the strains at the top (ε_c) and at the bottom (ε_t), see Fig. 2.4, are taken as the basis for calculating the rotation, the curvature can be calculated as:

$$\kappa = \frac{|\varepsilon_t - \varepsilon_c|}{h} = \frac{1}{R} \tag{2.1}$$

The rotation can then be calculated from the integration of the curvature along the member length as:

$$\Theta = \int \kappa(x) \cdot dx \tag{2.2}$$

The formula for deriving the rotation from the deflection measurements depends on the statical system. For a three-point bending test, the rotation can be calculated from the mid-span deflection as approximately:

$$\Theta = \frac{4 \cdot u_v}{L} \tag{2.3}$$

A lower boundary of the rotation can be calculated from the crack widths w_i divided by the crack lengths a_i as:

$$\Theta = \sum_i \frac{w_i}{a_i} \tag{2.4}$$

Finally, for a statically determinate beam, the rotation of a specimen can be calculated from the rotations at the ends as:

$$\Theta = \Theta_A + \Theta_B \tag{2.5}$$

The parameters used above are illustrated in Fig. 2.4.
where:

F	force
L	member length
N	normal force
R	radius
a_i	crack length
h	height of the member
s_{cr}	crack distance
u_v	vertical deflection at midspan
w_i	crack width
Θ	rotation
Θ_A	rotation at support A
Θ_B	rotation at support B
ε_c	strain in the compressive zone
ε_t	strain in the tensile zone
κ	curvature

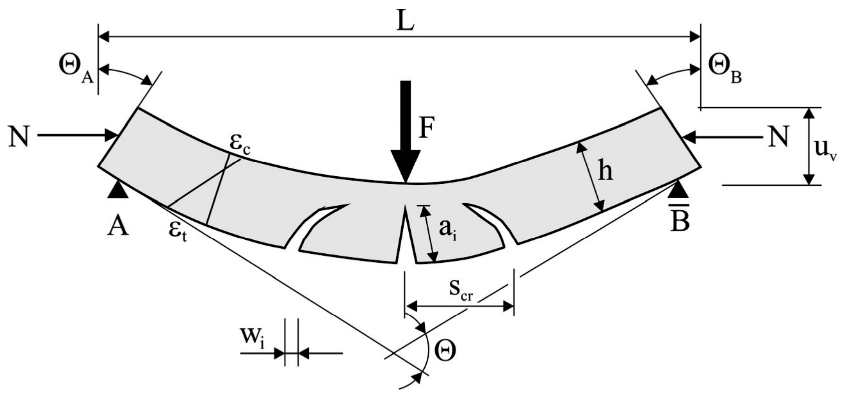

Fig. 2.4: Curvature and rotations

2.2 Influencing Factors on the Rotation Capacity

The available rotation capacity of plastic hinges in reinforced concrete is influenced by numerous factors. An overview for linear members in bending can be found in literature [Langer, 1987; Li, 1997; CEB, 1998; Bigaj, 1999; Akkermann, 2000; Hemmy, 2003]. The influencing factors can be subdivided into the categories material properties, geometric parameters and static system and load dependent parameters. Table 2.1 summarizes the influencing factors on the rotation capacity.

Due to the large number of influencing factors and their interaction, the evaluation of the rotation capacity is a complex issue. The scatter of experimentally derived values for the rotation capacity is large. Experimental results are rather difficult to compare and evaluate. Therefore, other researchers, e.g. Langer (1987) and Bigaj (1999), performed extensive parameter studies in which the effect of single influencing factors could be determined and then verified against experimental results.

Summaries of the effect of the variation of different influencing factors on the rotation capacity of reinforced concrete members can be found in Langer (1987), Graubner (1989), Li (1997), CEB (1998), Bigaj (1999), and König et al. (1999).

The main focus in this thesis is on the practical application in tunneling with its typical combinations of moment and normal force, structural dimensions and reinforcement layouts. Therefore it is interesting to review the study of Hemmy (2003) in particular. Hemmy (2003) summarized the effect of different influencing parameters on the rotation capacity for the conditions relevant in tunnel linings. Tunnel linings usually have a relatively low reinforcement ratio. The inner and outer part of the lining are usually symmetrically reinforced because compressive and tensile zone can change depending on the loading conditions. The low reinforcement ratio and the compressive reinforcement are beneficial for the rotation capacity. Furthermore, the load is usually not introduced in a single point but is rather distributed, which is also beneficial for the rotation capacity. Large normal forces in tunnel linings decrease the rotation capacity in cases where concrete crushing prevails.

Table 2.1: Influencing parameters on the rotation capacity of structural concrete members

Parameter	Influence on rotation capacity Θ_{pl}
1. Material	
Concrete:	
Compressive strength	Θ_{pl} increases with increasing compressive strength in case of concrete failure.
Ultimate strain	Θ_{pl} increases with increasing ultimate strain in case of concrete failure.
	Θ_{pl} is not significantly influenced in case of steel failure.
Tensile strength	Θ_{pl} increases with increasing tensile strength in case of concrete failure.
Reinforcing steel:	
Strength	Θ_{pl} slightly increases with increasing steel strength.
Hardening ratio	Θ_{pl} increases with increasing hardening ratio in case of concrete failure.
Ultimate strain	Θ_{pl} increases with increasing ultimate strain in case of steel failure.
Length of yield plateau	Θ_{pl} increases with increasing yield plateau in case of steel failure.
	Θ_{pl} decreases with increasing yield plateau in case of concrete failure.
Interface/Bond:	
Bond strength	Θ_{pl} decreases with improved bond strength.
Tension stiffening	Θ_{pl} decreases with increasing tension stiffening.
2. Geometry	
Height	Θ_{pl} decreases with increasing height.
Slenderness ratio L/h	Θ_{pl} increases with increasing slenderness.
Size at constant slenderness	Θ_{pl} increases with decreasing size.
Tensile reinforcement ratio	Θ_{pl} increases with increasing reinforcement ratio in case of steel failure.
	Θ_{pl} decreases with increasing reinforcement ratio in case of concrete failure.
Compressive reinforcement ratio	Θ_{pl} increases with increasing reinforcement ratio.
Transverse reinforcement ratio	Θ_{pl} increases with increasing reinforcement ratio.
3. Static System and Loading	
Shear slenderness	Θ_{pl} increases with increasing shear slenderness if bending failure prevails.
Normal compressive force	Θ_{pl} decreases with increasing normal compressive force.
Shear forces	Θ_{pl} decreases with increasing shear force if bending failure prevails.
Width of the loading platen	Θ_{pl} increases with increasing width of the loading platen.
One or two single loads	Θ_{pl} is increased for two loads.
Load duration	Θ_{pl} decreases with increasing load duration.

2.3 Influence of Steel Fibers on the Rotation Capacity

As the rotation capacity of plastic hinges is influenced by a number of factors, the effect of steel fibers on the rotation capacity cannot be explained in a straightforward manner. The effect of steel fibers on these influencing factors can have counteracting consequences for the rotation capacity, i.e. some influencing factors are altered by the addition of steel fibers to result in an increased rotation capacity whereas others are altered to result in a decreased rotation capacity. It is therefore preferred to first analyze the effect of steel fibers on the above mentioned influencing parameters on rotation capacity. In the following sections, the effect of steel fibers on the factors influencing the rotation capacity is summarized.

2.3.1 Influence of Steel Fibers on the Compressive Properties of Concrete

The effect of steel fibers on the concrete compressive strength is much debated in literature. Most researchers found no significant effect of the fibers on the compressive strength, e.g. Kooiman (2000), Erdem (2002). However, some researchers found an increase of the concrete compressive strength due to fiber addition, e.g. Winterberg (1998). The effect of fibers on the compressive strength can be traced down to two counteracting actions [Grübl et al., 2001]: a lager amount of pores, which decreases the compressive strength, and the fiber bridging effect accross the micro cracks, which increases the compressive strength. Depending on the magnitude of both effects, the concrete compressive strength may change. The effect of steel fibers on the compressive strength therefore depends on the concrete mixture, the kind and amount of steel fibers and the manufacturing process. It is unclear whether the addition of steel fibers influences the rotation capacity of plastic hinges as a result of changes in the concrete compressive strength.

It is generally agreed that steel fibers enhance the ductility of concrete in compression, e.g. Grübl et al. (2001). Steel fibers as well as stirrup reinforcement increase the confining capacity of concrete. This is reflected in the stress-strain relationship of concrete with a more ductile post-peak behavior. For steel fibers, the orientation of the fibers needs to be perpendicular to the compressive loading in order to be effective. It is therefore expected that the addition of steel fibers increases the rotation capacity of plastic hinges in case of concrete failure as a result of the increase of concrete ductility in compression.

The effect of steel fibers on the strength and ductility of concrete in compression will be investigated in chapter 3.

2.3.2 Influence of Steel Fibers on the Tensile Properties of Concrete

As in compression, the tensile strength of concrete can be increased or decreased due to the addition of fibers, depending on the concrete mixture, the kind and amount of steel fibers and the manufacturing method. It is generally agreed that the addition of fibers leads to an increase in post-peak ductility. The magnitude of this increase will be discussed in chapter 4.

It is unclear whether the addition of steel fibers influences the rotation capacity of plastic hinges as a result of changes in the concrete tensile strength and post-peak behavior.

2.3.3 Influence of Steel Fibers on the Tension Stiffening Effect

Bigaj-van Vliet (2001) summarized the effect of steel fibers on the tension stiffening effect found in literature. The tension stiffening effect strongly depends on the tensile post-peak behavior of the concrete matrix. At increasing fiber content the fracture energy of the concrete increases [Schumacher et al., 2002b] and, consequently, the tension stiffening effect increases [Noghabai, 1998]. Mitchell et al. (1996) also found a significant increase in tension stiffening when fibers were added. They reported that after yielding of the reinforcing bar only the specimens containing fibers showed tension stiffening.

It is noted that an increasing tension stiffening effect decreases the rotation capacity. The effect of steel fibers on bond behavior will be described in more detail in chapter 5. There, attention will be paid to the consequences of this decrease on the structural safety.

2.3.4 Influence of Steel Fibers on the Shear Behavior

Depending on the magnitude of the shear force in the critical region of the member, Bachmann (1967) distinguished between two significantly different types of plastic hinges in reinforced concrete members: flexural hinges or shear crack hinges, see Fig. 2.5.

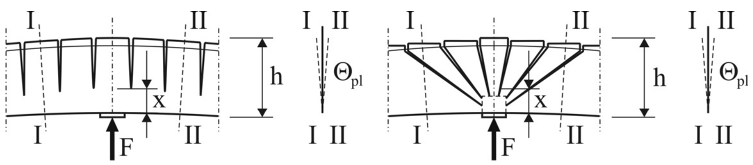

Fig. 2.5: Flexural crack hinge and shear crack hinge [Bachmann, 1967]

The flexural hinge occurs in a zone in which the bending moment is predominant. The shear crack hinge occurs in a zone in which a considerable shear force is present in addition to the bending moment. If the member has sufficient shear capacity to avoid shear failure shear crack hinges have a much larger rotation capacity than flexural crack hinges [CEB, 1998]. The influence of the shear stress on the rotation can be seen in Fig. 2.6.

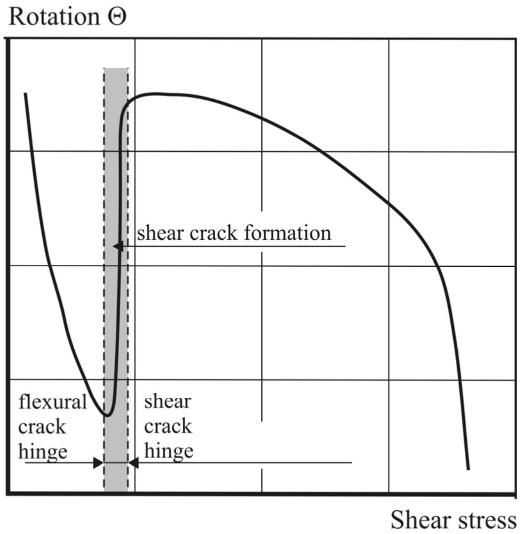

Fig. 2.6: The influence of the shear stress on the rotation [Bachmann, 1967]

At small shear stresses, only flexural cracks are present. It is noted that the figure is only qualitative and that the rotation at very low shear stresses is expected to be smaller in a quantitative illustration. If the shear stress in the beam reaches the shear crack stress, the extensions of the flexural cracks will be bent and become shear cracks (indicated by the dotted area in the figure) with an inclination in the direction of the load application. While the shear cracks are formed, the rotation in the beam increases from the value for beams without shear cracks to that for beams with shear cracks. From then on, the rotation capacity decreases with increasing shear stress.

The effect of inclined cracking should be included in a model for the rotation capacity. It is noted that shear failure can be excluded for a slenderness $L/h > 9$, which is normally the case in tunneling [Hemmy, 2003].

Steel fibers can be used to resist shear cracks. Steel fibers may also influence the inclination of the cracks. It is unclear whether the addition of steel fibers affects the rotation capacity of plastic hinges as a result of changes in the shear crack width and crack inclination.

2.3.5 Summary of the Influence of Steel Fibers on the Rotation Capacity

The influence of steel fibers on the rotation capacity is summarized in Table 2.2.

Table 2.2: Summary of the influence of steel fibers on the influencing factors on the rotation capacity of plastic hinges in reinforced concrete

Parameter	Influence of steel fibers on parameter
Compressive strength	Unclear
Ductility in compression	Increase
Tensile strength	Unclear
Ductility in tension	Increase
Bond	Unclear
Shear	Unclear

For structures solely reinforced with steel fibers, the addition of steel fibers to the plain concrete increases the rotation capacity because it increases the ductility of the concrete in compression as well as in tension. This also holds true for hinges with shear cracks.

However, for a combination of conventional and fiber reinforcement it is not clear whether the addition of steel fibers increases or decreases the overall rotation capacity due to the altered bond and shear behavior. To explain and quantify this phenomenon, the influence of steel fibers on the compressive, tensile and bond behavior is investigated in chapters 3 to 5 and a model for the rotation capacity is presented in chapter 6.

2.4 Existing Calculation Models for Reinforced Concrete

As the available rotation capacity of plastic hinges in reinforced concrete is influenced by numerous factors, which interact, numerical models are an important tool in predicting the rotation capacity and in studying the effect of the various influences independently and systematically [CEB, 1998].

A summary of existing models to determine the available rotation capacity of plastic hinges in reinforced concrete beams or slabs can be found in the CEB Bulletin No. 242 [CEB, 1998]. The summary includes the models of Langer (1987, 1997) and Li (1997), Cosenza et al. (1991 and 1992), Pommerening (1996), Sigrist (1995), and Bigaj (1999). The models comply with the definition of the rotations as mentioned at the beginning of this chapter. In a Round Robin analysis, the models were compared with the current MC90 provisions about the available rotation capacity of plastic hinges and similar results from all models were obtained [Bigaj-van Vliet & Mayer, 1998].

In the scope of this thesis (chapter 6), a similar approach to that of Langer (1987, 1997) and Li (1997) and of Bigaj (1999) is chosen. Therefore, only these models are summarized here.

2.4.1 The Models of Langer (1987) and Li (1997)

The model of Langer (1987, 1997) describes the available rotation capacity of plastic hinges in statically indeterminate structures. Structural modeling is done by isolating the part of the member between two points of zero moment, which is then analyzed as a statically determinate beam. Realistic stress-strain relationships of the compressive zone and the reinforcing steel are used to calculate the moment-curvature relationship. Bond is included by means of bond stress-slip relationships that vary with the distance to the crack. The influence of steel yielding is not taken into account explicitly.

In the calculations it is assumed that plane sections remain plane. The "naked" M-κ relationship is determined for the present reinforcement. Then, the crack spacing is calculated. The steel strains along the crack elements are determined, taking into account a bond model. The curvature is calculated from the steel strains and the effective height. The concrete deformations are neglected. The rotation is the integration of the curvature along the beam.

Li (1997) used the model of Langer (1987) and extended it for prestressed concrete.

2.4.2 The Model of Bigaj (1999)

Bigaj analyzed the behavior of flexural crack hinges. She focused on the size dependence of the rotation capacity of plastic hinges and considered the strain localization on compression as well as discrete cracking in tension in the hinge region. Realistic stress-strain relationships of the compressive zone, the reinforcing steel and bond behavior including the range of steel yielding are used as input. For the concrete tensile behavior, the Fictitious Crack Model (FCM) of Hillerborg (1976) is used. Concrete under compression is modeled with Markeset's Compressive Damage Zone Model (CDZ Model) [Markeset, 1993]. For bond, the bond model of Den Uijl & Bigaj (1996) is used.

The statically determined members are divided into crack elements after the crack spacing has been determined on the basis of the geometry and the material characteristics including bond.

The rotations of the crack elements are derived from the calculated stress in the reinforcement and in the upper fiber of the compression zone and integrated over the element length, which corresponds to the crack distance s_{cr}. The summation of the rotations of the elements leads to the total rotation in the hinge.

A major difference in the models of Langer and Li and Bigaj is that Bigaj includes strain localization in concrete and accounts for the effect of steel yielding on the bond behavior.

2.5 Concluding Remarks

In this chapter, the rotations are defined and their determination from experiments is explained. The main influencing factors on the available rotation capacity in reinforced concrete members are summarized. As the rotation capacity is influenced by a number of factors, the effect of steel fibers on the rotation capacity cannot be explained in a straightforward manner. It is therefore chosen to investigate the effect of steel fibers on the parameters influencing the rotation capacity. In general, the influence of fibers on the rotation capacity depends on the amount of conventional reinforcement and on the eccentricity of the load. If concrete failure is expected in case of high normal forces or when a large amount of conventional reinforcement is present, the influence of the steel fibers is to be sought in the increase of concrete ductility in the compressive zone. If steel failure is expected the steel fibers mainly influence the rotation capacity by influencing the tension stiffening behavior. For high reinforcement ratios, the effect of the steel fibers in case of steel failure is negligible, for low reinforcement ratios, the fibers do influence the behavior. In case of SFRC without any bar reinforcement, the fibers can significantly increase the rotation capacity [Ortu, 2000]. The effect of steel fibers on the most important influencing factors are investigated with regard to:

- compression in chapter 3
- tension in chapter 4
- bond in chapter 5.

The model for calculating the rotation capacity of SCSFRC members in chapter 6 is based on the model of Bigaj (1999) for calculating the rotation capacity of reinforced concrete members.

3 Compressive Behavior

3.1 Introduction

Research at Delft University of Technology on steel fiber reinforced concrete specimens [Kooiman, 2000] showed that the post-peak behavior in compression does not significantly influence the load bearing capacity in bending. It does, however, affect the deformation capacity of the cross-section. It is therefore important to correctly capture the post-peak behavior of concrete in compression in order to realistically predict the rotation capacity.

Section 3.2 summarizes the main mechanisms of softening of concrete loaded in compression and presents the Compressive Damage Zone (CDZ) model as proposed by Markeset (1993) and reviews the existing extensions.

Section 3.3 describes the experiments performed on concrete prisms in order to extend the CDZ model for self-compacting steel fiber reinforced concrete (SCSFRC). The parameters of the experimental investigation were:

- aspect ratio and amount of steel fibers
- eccentricity of the loading
- concrete strength.

Section 3.4 presents a proposal for an extension of the CDZ model for SCSFRC. The extended CDZ model will be implemented for the model for the calculation of the rotation capacity as shown in chapter 6.

3.2 Behavior of Concrete in Compression

Failure of concrete in compression is related to failure of concrete in tension. When concrete is loaded in uniaxial compression, tensile stresses act perpendicular to the direction of the compressive load, see Fig. 3.1.

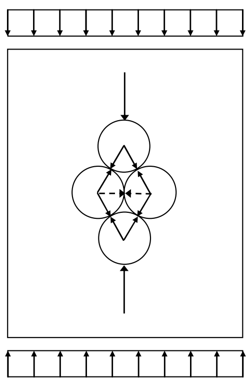

Fig. 3.1: Load bearing mechanism of concrete in compression

If concrete was completely homogeneous the stress field would be uniform. Due to the heterogeneity of the concrete on the micro level (crystal structure) and meso level (particle level [Van Mier, 1997]), a uniform stress field on a macro level results in a highly non-uniform distribution of internal stresses on the lower levels [Vonk, 1992]. Even if no load has been applied before, the concrete shows micro cracks at the interface between aggregate and cement paste due to internal shrinkage, see Fig. 3.2.

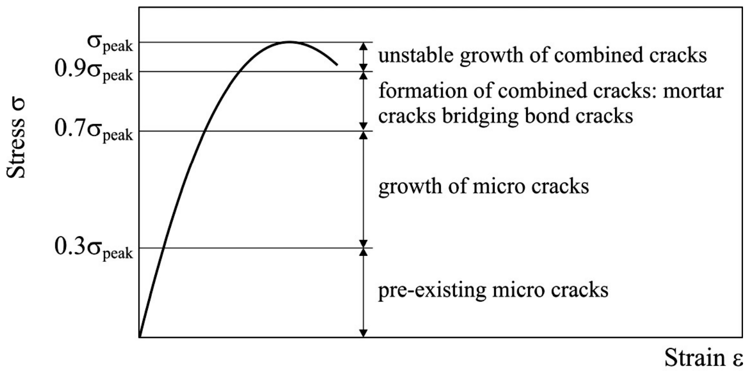

Fig. 3.2: Crack formation at different stress levels in normal strength concrete [Hsu et al., 1963]

Above approximately 30% of the maximum stress, more bond cracks are formed and the existing cracks start to grow at the interface between aggregate and paste. At further increase of the load, the cracks run through the mortar. The mortar cracks bridge the shortest distance between the bond cracks, see Fig. 3.3.

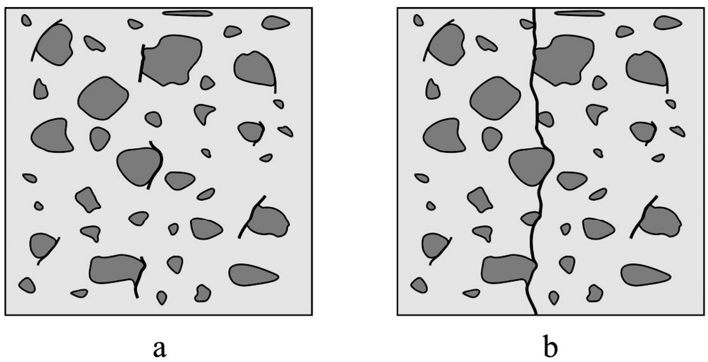

Fig. 3.3: Crack development in concrete [Winterberg, 1997]:
a) Development of micro cracks,b) Development of macro cracks

As the load further increases, more cracks coalesce and the crack growth becomes unstable. The crack pattern divides the concrete in several pieces, which can shear off [Van Mier, 1984]. In case of slender test specimens, a single shear crack occurs. The longitudinal cracks and the shear band in the localized failure zone can be seen in Fig. 3.4. More information on the softening of concrete loaded in compression and the failure mechanisms can be found in the work of Vonk (1992).

Fig. 3.4: Picture of a SCSFRC specimen after testing

Similar to failure of concrete in tension, failure of concrete in compression is a localized phenomenon [Van Mier, 1984]. This means that all deformations concentrate in the failure zone while the part of the specimen outside the failure zone unloads. The deformation in the failure zone is assumed to be identical regardless of the specimen length [Van Mier, 1984]. When represented in terms of strains, the longer specimens have a steeper unloading branch than the shorter ones with the same cross-section. This is because an identical displacement is divided by a larger specimen length, see Fig. 3.5 and Fig. 3.6 for tests with steel loading platens. In order to capture this localization, continuum models, such as the model of Pölling (2000), introduce a fictitious equivalent length in which the deformations are localized. This length is not a physical parameter, but has to be adapted to the specific case under consideration. A fracture mechanics approach can provide a sound physical explanation and is therefore preferred.

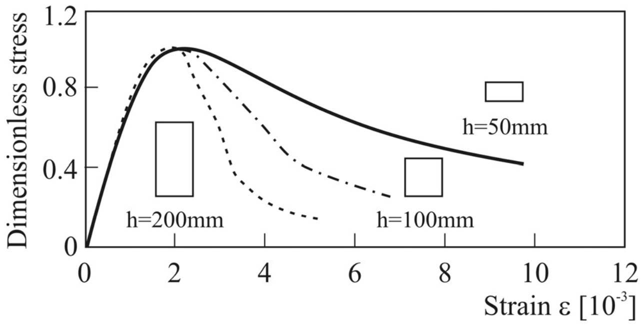

Fig. 3.5: Stress-strain curves for medium strength concrete in uniaxial compression: effect of slenderness ratio h/d (d = 100 mm for all tests) [Van Mier, 1984]

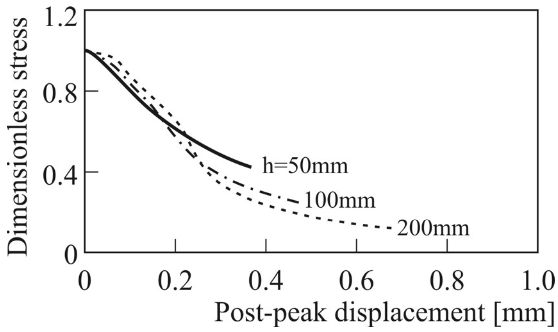

Fig. 3.6: Dimensionless stress-post peak deformation diagrams for prisms with different height [Van Mier, 1984]

3.2.1 The Compressive Damage Zone (CDZ) Model after Markeset

Gro Markeset (1993) proposed the fracture mechanics based CDZ model for describing the failure of concrete in compression. The CDZ model is a constitutive macro mechanical model that allows to calculate the stress-strain relationship of concrete in compression. It takes into account the localization of the compressive failure in a damage zone of limited length. It was calibrated with experiments on high strength concrete (HSC) and lightweight aggregate concrete (LWAC). The CDZ model takes into account the occurrence of longitudinal splitting cracks as well as the shear band and can be applied to centrically and eccentrically loaded concrete.

Basic Assumptions of the CDZ Model

Delibes Liniers (1987) observed a significant tensile strength loss in Brazilian splitting tests after the specimens had been subjected to compressive forces. The compressive stresses were varied between 50% and 95% of the ultimate stress. The plane of the tensile fracture was in the direction of the previous compressive loading.

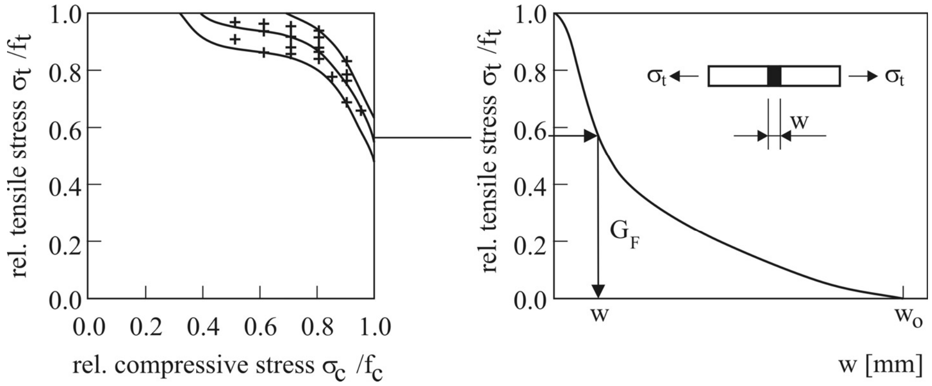

Fig. 3.7: Reduction of the tensile splitting strength normal to the direction of compressive preloading [Delibes Liniers, 1987], explained by means of the tensile softening behavior of the concrete [Markeset, 1993]

From Fig. 3.7 it can be seen that after a compressive load close to the maximum load had been applied, only approximately 50% of the original tensile splitting strength was measured. This observation led Markeset (1993) to the conclusion that not all of the fracture energy is dissipated in micro cracks or longitudinal cracks when the maximum compressive stress is reached. She linked the observations of Delibes Liniers (1987) with a softening relationship for concrete in tension and concluded that at the maximum compressive load only approximately 25% of the total fracture energy is dissipated in the longitudinal cracks and approximately 75% is still available to further widening of the cracks.

The CDZ model combines two approaches for modeling the softening of concrete: a continuum model, which assumes failure within a band of finite length [Bažant, 1989], and a fracture mechanics model for the damage zone [Hillerborg, 1988], which takes localized deformation into account.

Definitions and Calculation of the CDZ Model Parameters

The total length of the specimen is denoted as L^l, whereas the length of the damage zone, in which the compressive failure localizes, is denoted as L^d (Fig. 3.9). The damage zone can be seen in a tested specimen in Fig. 3.8. The damage zone length depends on the cross-sectional dimensions of the specimen and the eccentricity of the load. Markeset (1993) found L^d to be approximately 2.5 times the smallest lateral dimension for uniaxial compression tests.

Fig. 3.8: *Failure pattern of a specimen*

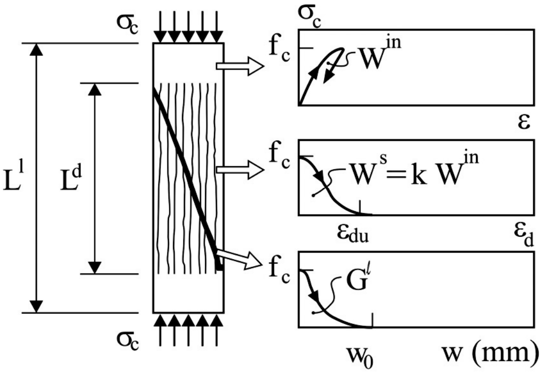

Fig. 3.9: Illustration of the CDZ model on a specimen loaded in uniaxial compression [Markeset, 1993]

The tensile fracture energy G_F is an important parameter in the model. The complete opening of a longitudinal crack was assumed to absorb the same amount of energy as the opening of a pure tensile crack [Markeset, 1995].

The different elements of the CDZ model (Fig. 3.9) are described hereafter. Firstly, the ascending branch of the stress-strain relationship of concrete in compression is described. Secondly, the descending branch is described for unloading outside the damage zone, longitudinal cracking and a shear band.

Ascending Branch

The deformations in the ascending branch are assumed to be uniformly distributed over the specimen height. The behavior in the ascending branch is described by conventional relationships, such as given in the CEB-FIP Model Code 1990 or Eurocode 2. Markeset (1993) used an equation suggested by Popovics (1973) for normal density concrete and a multilinear relationship for lightweight aggregate concrete.

Unloading Outside the Damage Zone

It is assumed that after the peak load, the failure zone localizes and outside the damage zone, the concrete unloads. This unloading is modeled as shown in Fig. 3.9 at the top of the figure, following the descending branch with the slope of the E-modulus. Fig. 3.10 shows the elastic and inelastic strain ε^{el} and ε^{in} and the elastic and inelastic energy W^{el} and W^{in} of the stress-strain curve.

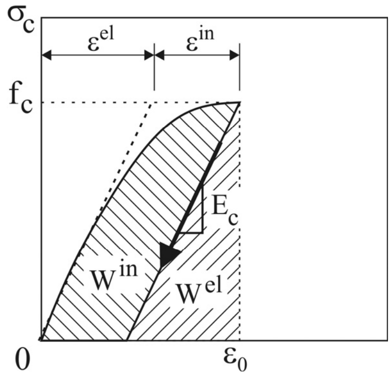

Fig. 3.10: Definition of W^{in}, W^{el}, ε^{in} and ε^{el} [Markeset, 1993]

It is noted that according to the CDZ model, the unloading is assumed to follow a descending branch, which has an inclination corresponding with the E-modulus (see Fig. 3.10). This is not completely correct because the stiffness decreases as the stress-strain relationship is followed [Pölling, 2000; Erdem, 2002].

The elastic strain ε^{el} is calculated as:

$$\varepsilon^{el} = f_c / E_c \tag{3.1}$$

where:

E_c	E-modulus
f_c	concrete compressive strength

The elastic energy per unit volume W^{el} is calculated as:

$$W^{el} = \frac{f_c^2}{2 E_c} \tag{3.2}$$

The energy per unit volume dissipated due to inelastic deformations up to the maximum load is denoted as inelastic energy per unit volume, W^{in}, see Fig. 3.10. This is the energy absorbed in developing micro cracks before the concrete strength f_c has been reached. It corresponds to the fracture energy consumed at maximum strength (Fig. 3.7), which was assumed to be much lower than the total fracture energy. The inelastic energy per unit volume, W^{in}, is defined as:

$$W^{in} = W^{uptopeakload} - W^{el} \tag{3.3}$$

The CDZ model parameter α_{fd} is the filling degree. It is calculated by:

$$\alpha_{fd} = \frac{W^{in}}{f_c\,\varepsilon^{in}} \tag{3.4}$$

with:

$$\varepsilon^{in} = \varepsilon_0 - \varepsilon^{el} \tag{3.5}$$

where:

ε_0 compressive strain at peak stress

The parameter α_{fd} was proposed to be 0.80 [Markeset, 1993].

Longitudinal Cracking

Inside the damage zone, the energy is dissipated in longitudinal cracks and in a shear band. The energy per unit volume dissipated in the longitudinal cracks is denoted by W^s as shown in Fig. 3.9 and Fig. 3.11. This contribution to the descending branch is represented by the relationship between the stress and the average additional strain ε_d, which is caused by the opening of the longitudinal cracks.

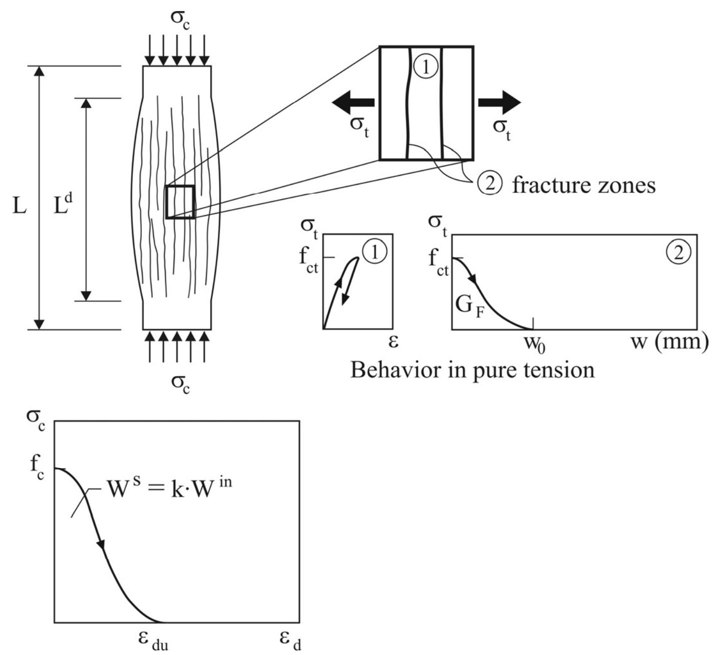

Fig. 3.11: Localization of failure in the longitudinal cracks [Markeset, 1993]

W^s is assumed to be proportional to the inelastic energy per unit volume W^{in} and can be calculated with:

$$W^s = k\,W^{in} \tag{3.6}$$

where:

k proportionality factor, ratio between energy consumed due to opening of the longitudinal cracks in the post-peak region to that consumed in the pre-peak region

The proportionality factor k was proposed to be approximately 3.0 for normal weight concrete by Markeset (1993) and 1.0 for lightweight aggregate concrete.

The total energy per unit volume absorbed in the longitudinal cracks W^d is assumed to be proportional to the tensile fracture energy G_F. It can be calculated with:

$$W^d = W^{in} + W^s = (1+k)\,W^{in} = \frac{G_F}{r} \tag{3.7}$$

where:

G_F fracture energy of concrete in tension [N/mm]

r material property related to the average distance between successive longitudinal cracks [mm]

The value of r was proposed to be approximately 1.25 mm for a maximum aggregate size of 16 mm. With the model parameters of Markeset, the inelastic energy per unit volume can be calculated as:

$$W^{in} = \frac{G_F}{r\,(1+k)} \tag{3.8}$$

and the energy per unit volume dissipated in the longitudinal cracks can be calculated as:

$$W^s = \frac{k\,G_F}{r\,(1+k)} \tag{3.9}$$

For calculations, Markeset approximated this contribution to the descending branch of the stress-strain relationship of concrete in compression by a straight line.

Shear Band

The third part of the energy is dissipated in a shear band. This branch is represented by a stress-deformation curve related to the deformations in the shear band. The deformation w is defined as the vertical component of the sliding deformation along the inclined shear band in the damage zone, with w_c being the deformation at failure, see Fig. 3.12.

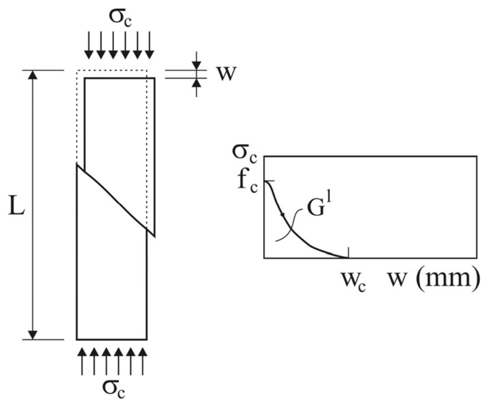

Fig. 3.12: Sliding failure in a localized shear band [Markeset, 1993]

The energy per unit area perpendicular to the σ_c consumed in the shear band is denoted by G^l, see Fig. 3.9. It can be calculated with:

$$G^l = \beta_{sf}\, f_c\, w_c \tag{3.10}$$

where:

w_c	localized deformation [mm]
β_{sf}	shape factor; 0.5 if a straight line is assumed [-]
f_c	maximum compressive stress in the test [N/mm^2]

The parameter w_c was found to be between 0.4 and 0.7 mm for normal density concrete (Markeset, 1993). The product of β_{sf} and w_c was proposed to be 0.36 for normal strength concrete and 0.217 for high strength concrete (Markeset, 1993). For calculations, this branch of the stress-deformation curve is approximated by a straight line.

Average Stress-Strain Response

The total compressive fracture energy dissipated per unit volume in the compressive zone of a concrete member W^c is the summation of the inelastic energy, the energy absorbed in the longitudinal cracks and the energy dissipated in the shear band. It can be calculated with:

$$W^c = W^{in} + W^s \frac{L^d}{L} + G^l \frac{1}{L} = \frac{G_F}{r(1+k)} \cdot (1 + k \cdot \frac{L^d}{L}) + \beta_{sf}\, f_c \frac{w_c}{L} \tag{3.11}$$

For further calculation in the model for the rotation capacity in chapter 6, a stress-strain relationship is used.

The relationships for the longitudinal cracking and the shear band described above were formulated for the damage zone. In order to obtain an average stress-strain response, these relationships have to be related to the specimen length L. The complete stress-strain relationship is composed as described in Fig. 3.13.

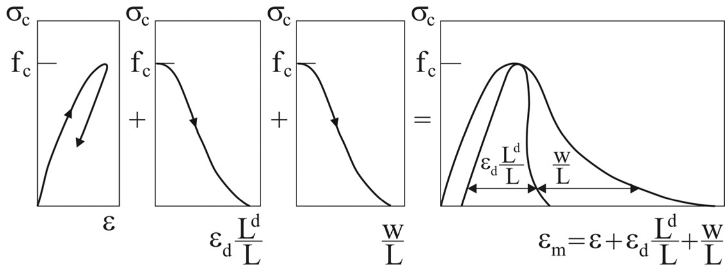

Fig. 3.13: Composition of the complete stress-strain curve [Markeset, 1993]

According to Fig. 3.13, the average strain ε_m can be calculated with:

$$\varepsilon_m = \varepsilon + \varepsilon_d \frac{L^d}{L} + \frac{w}{L} \qquad \text{for } L > L^d \qquad (3.12a)$$

and

$$\varepsilon_m = \varepsilon + \varepsilon_d + \frac{w}{L} \qquad \text{for } L \leq L^d \qquad (3.12b)$$

with:

$$\varepsilon_d = 2\alpha_{fd}\, k\, \varepsilon^{in} \qquad (3.13)$$

Markeset combined the parameters of the CDZ model in one parameter, γ, which is calculated by:

$$\gamma = \frac{1}{\alpha_{fd}\, r\,(1+k)} = \varepsilon^{in} \cdot \frac{f_c}{G_F} \qquad [\mathrm{mm}^{-1}] \qquad (3.14)$$

Markeset found the parameter γ to be 0.25 mm^{-1} for normal weight concrete and 0.50 for lightweight aggregate concrete.

The parameters of the CDZ model proposed by Markeset are summarized in Table 3.1.

Table 3.1: CDZ model parameters proposed by Markeset (1993)

Concrete	α_{fd} [-]	k [-]	r [mm]	γ [mm^{-1}]
Normal density	0.8	3.0	1.25	0.25
Lightweight aggregate	0.8	1.0	1.25	0.50

In modeling members in which a strain gradient is present, e.g. beams, the difference in deformation between the different parts of the member and the resulting differences in strength and ductility have to be taken into account. The length of the damage zone is likely to be proportional to the depth of the damage zone d^l.

$$L^d = k^l\, d^l \tag{3.15}$$

The factor k^l is 2.5 for pure compression and 5 for pure bending. The damage zone depth d^l is zero up to the peak load. In the descending branch it can be calculated as:

$$d^l = \frac{\varepsilon_{cm} - \varepsilon_0}{\varepsilon_{cm}} \cdot x \tag{3.16}$$

where:

ε_{cm}	compressive strain in the most stressed fiber
ε_0	compressive strain at peak stress
x	depth of the compressive zone

3.2.2 Existing Extensions of the CDZ Model

Markeset's model (1993) was successfully implemented in modeling conventional concrete (e.g. Bigaj, 1999; Han, 1996). The behavior of the ascending branch was described by different relationships, e.g. the parabolic relationship proposed in CEB-FIP Model Code 1990 [Han, 1996] or Eurocode 2 [Kützing, 2000; Meyer, 1998; Römer, 1998]. Bigaj (1999) used a bilinear relationship. Some researchers found slightly different values for the proportionality factor *k*: Grimm (1997) proposed a factor of 2.33 and Meyer (1998) proposed 2.6.

As the CDZ model is only valid for unconfined concrete, in the past years some researchers extended the model for additional confinement of the compressive zone with stirrup reinforcement. These extensions can be found in the literature [Grimm, 1997; Meyer, 1998; Sint, 2002]. Confinement can also be caused by the load introduction, e.g. a loading platen. In general, this additional confinement can be modeled by adding an extra strain $\Delta\varepsilon$, see Fig. 3.14.

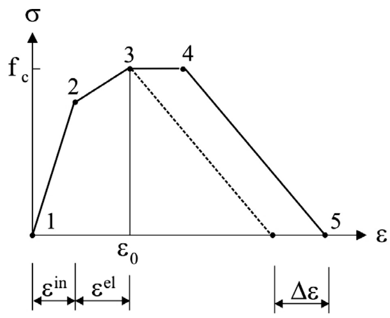

Fig. 3.14: Additional strain representing additional confinement

Kützing (2000) and Römer (1998) investigated the compressive behavior of normal and high strength concrete with steel fibers, polypropylene fibers or a combination of both. They determined the parameters for the CDZ model and used them in the calculation of columns with additional stirrup reinforcement.

In order to calculate the parameters of the CDZ model, Kützing [2000] performed deformation controlled compressive tests on concrete cylinders. The contribution of the fibers was solely assigned to the opening of the longitudinal cracks and it was not split into a fiber contribution in the energy absorption of the longitudinal cracks and a fiber contribution in the energy absorbed in the shear band. For fiber reinforced concrete, the value of k was influenced by the fiber type. The polypropylene fibers contributed to the development of micro cracks before the peak stress was reached and increased the inelastic energy absorption W^{in}. This resulted in a decrease of the parameter k. In contrast, the steel fibers increased the fracture energy G_F, which was absorbed during the formation of the longitudinal cracks after the peak compressive stress had been reached. This resulted in an increase in W^s and in an increase of the parameter k.

The evaluation of the tests of Kützing (2000) and Römer (1998) led to the following proposal concerning the parameter k for normal and medium strength concrete with a fiber cocktail of polypropylene (PP) and steel fibers (SF):

with 0.1 vol.-% PP fibers: $$k = 6 + 100\,\eta_{Vol\,SF} \tag{3.17}$$

with 0.2 vol.-% PP fibers: $$k = 5 + 100\,\eta_{Vol\,SF} \tag{3.18}$$

where:

$\eta_{Vol\,SF}$ steel fiber content [vol.-%]

For HSC, no model parameters could be derived by Römer (1998) from the test results due to the instable post peak behavior in case of mixtures containing applicable fiber contents. Evaluating the same test results, Kützing (2000) proposed the parameter α_{fd} to be 0.90.

3.3 Experiments on Centrically and Eccentrically Loaded SCSFRC Prisms

Eccentric prisms tests with a strain of zero at the less compressed side of the prism can be used to simulate the compressive zone in the part of a beam where no shear force is present, see Fig. 3.15. This idea can already be found in experiments of Rüsch et al. (1966). In a comparative study of beam and prism tests they mentioned that prism tests have the advantage that they are much easier to perform and that they lead to lower scatter of the test results.

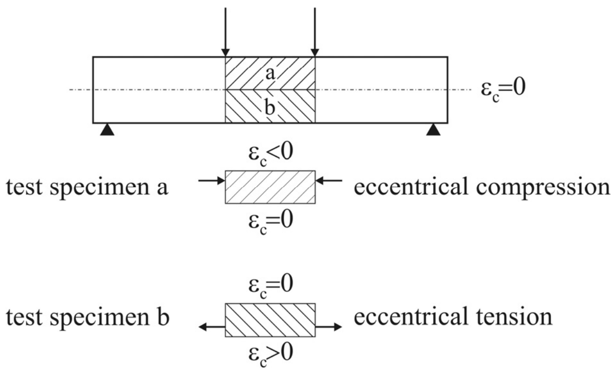

Fig. 3.15: Model for determining the concrete behavior in bending by examining eccentrically loaded prisms [Dietrich, 1992]

The experiments described in the following were performed as a part of this research in order to determine the effect of the amount of fibers, the fiber length, the aspect ratio (i.e. fiber length/diameter = l_f / d_f), the compressive strength, and the eccentricity of the load on the behavior of SCSFRC prisms and on the CDZ model parameters. The tests are reported and described in detail in Schumacher et al. (2003a). Here, a short summary is given.

3.3.1 Experimental Program

Deformation-controlled compressive tests were performed on concrete prisms as described in the following sections. The E-modulus, the compressive and the tensile splitting strength were determined in standard tests at an age of 28 days, see appendix C. Table 3.2 gives an overview of the experimental program. The concrete strengths were chosen to be a normal strength concrete (B45) and a high strength concrete (B105). Steel wire fibers with hooked ends were used.

The identification of the specimens and the fiber material characteristics are explained in appendix A. The mixture names consist of the desired concrete compressive strength, the fiber geometry (aspect ratio l_f / d_f [-] / fiber length l_f [mm]) and the amount of steel fibers in kg/m^3. The names of the test specimens consist of the mixture name, the eccentricity of the loading in mm and the number of the individual test of the parameter combination.

The choice of eccentricities was similar to the test set-up of Markeset (1993) and resulted in theoretical stress distributions as shown in Fig. 3.16. The number of test specimens per experiment was chosen to be three.

Table 3.2: Experimental program (e = eccentricity, h = width of the specimen)

Mixture	Fiber	Steel fibers [kg/m^3]	Number of tests performed		
			$e = 0$	$e = h/18$	$e = h/6$
B45.0.0	-	0	3	3	6
B45.45/30.60	45/30	60	3	3	3
B45.45/30.120	45/30	120	3	3	3
B45.80/30.60	80/30	60	3	3	3
B45.80/60.60	80/60	60	3	3	3
B105.0.0	-	0	1	0	3
B105.80/30.60	80/30	60	1	3	3
B105.80/60.60	80/60	60	0	3	3

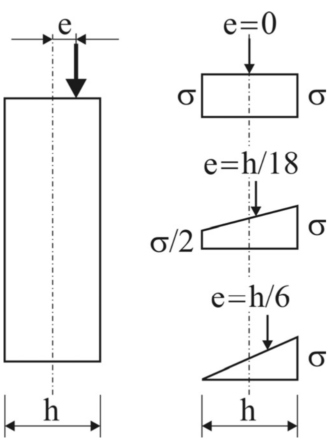

Fig. 3.16: Idealized stress distribution for the three loading cases [Markeset, 1993]

3.3.2 Specimens and Materials

Size of the Test Specimens

The test specimens for the prism tests were cast horizontally in steel moulds in order to obtain surfaces directly ready for testing. The specimens were 150×150 mm in cross-section and 600 mm in length. The width of the specimens had an accuracy of ±1 mm. The cubes to measure the compressive strength and splitting tensile strength had a size of 150 mm. The specimens to measure the E-modulus had a size of 100×100×400 mm.

Concrete Mixtures

The concrete mixtures were designed by Grünewald & Walraven (2002a) for the strength classes B45 and B105 (i.e. characteristic 28-day cube compressive strengths of 45 and 105 N/mm^2, respectively; 150 mm cubes). Table 3.3 gives details of the concrete reference mixtures. The composition of the mixtures was corrected for the moisture content of the aggregates. The amount of water given in Table 3.3 consists of the free water, the water contained in the aggregates exceeding the amount necessary to saturate them, the water in the superplasticizers and the water in the micro silica slurry. The amount of superplasticizers is given in parentheses because it is already contained in the amount of water.

For the mix design, the air content was assumed to be 2 vol.-% and 3 vol.-% for the B45 and B105, respectively. The actual air contents were 3.4 vol.-% and 2.7 vol.-%, respectively. The mixture compositions of the reference mixes given in Table 3.3 are adjusted according to the measured air content.

The B45 as well as the B105 were composed to be self-compacting. Both mixtures were self-compacting at a steel fiber content of 60 kg/m^3 fibers with an aspect ratio of 80.

Table 3.3: Composition of reference mixes [kg/m^3]

Ingredient	B45	B105
CEM III/B 42.5 LH HS	367	
CEM I 52.5 R		439
Fly ash	217	132
Slurry micro silica		32 (solid content)
Free water	173	167
Sand (0.125-4 mm)	1045	1051
Coarse aggregate (4-16 mm) - round	487	
Coarse aggregate (4-16 mm) - crushed		490
Superplasticizer Cugla LR	(2.17)	(10.89)
Superplasticizer Cugla HR	(1.09)	(7.26)

Steel Fiber Properties

The steel fibers used in the experiments were made of steel wire and had hooked ends. Table 3.4 shows the fiber properties.

Table 3.4: Steel fiber properties

Fiber	l_f/d_f [-]	l_f [mm]	package	min. tensile strength [N/mm^2]
45/30	45	30	loose	1000
80/30	80	30	collated	2000
80/60	80	60	collated	2000

Production of the Test Specimens

Mixing and Properties of the Fresh Concrete

Two times 110 liters were prepared because the concrete mixer had a limited capacity of 120 liter. The components were weighted separately and all ingredients were mixed according to the procedure shown in Fig. 3.17.

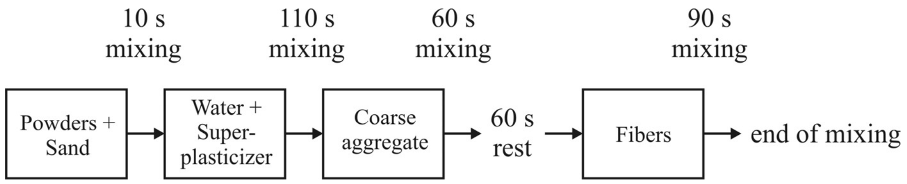

Fig. 3.17: Mixing procedure for SCSFRC [Grünewald, 2004]

Fine aggregate, cement and fly ash were put in the forced pan mixer and mixed for 10 seconds. Then, water, superplasticizers, and (in case of the B105) silica slurry were added. The batch was mixed for another 110 seconds. Then, the coarse aggregates were added and everything was mixed for another 60 seconds. After that, the mixture was left to rest for 60 seconds. Finally, the fibers were added through a steel mesh and all components were mixed for another 90 seconds.

After mixing the concrete, the slump flow and the t_{50} time were measured. The slump flow was between 560 mm and 620 mm for the mixtures with fibers and 700 mm for the mixtures without fibers. The diameters measured and the t_{50} time are given in appendix B. The temperature of the concrete after mixing was 25°C ± 2°C.

Transportation, Casting and Curing

The concrete was put into buckets with hand shovels, carried to the moulds, mixed with a rod and then placed in the moulds with hand shovels according to the procedure recommended by Vandewalle et al. (2000). The test specimens were finished and covered with a plastic sheet to avoid moisture loss at the surface.

As the concrete was self-compacting, no further compaction was necessary. As no vibration was used, the fibers did not orientate in a preferred direction due to vibration as usually happens when external vibration is used (fiber orientation perpendicular to the direction of vibration [Kooiman, 2000]). However, due to the flow of the concrete, a preferred orientation can occur in test specimens made of self-compacting concrete.

Grünewald & Walraven (2002b) investigated the fiber orientation in a saw cut perpendicular to the axial direction of standard test specimens for the three-point bending test. The fibers tended to orient in the axial direction, which is beneficial in the bending test. However, the same mixtures, moulds and filling method were used for the prisms for the compressive tests. In the compressive tests, the tensile stresses act perpendicular to the main direction of the loading and of the fibers. Therefore, the fibers contribute less to the ductility.

Consequently, this is a conservative approach to determine the ductility of the test specimens in compression.

The temperature in the laboratory was approximately 20°C. The test specimens were demoulded one day after casting and placed in a fog room at approximately 95% relative humidity (RH) and 20°C until testing.

Standard Test Results

The compressive and the tensile splitting strength were determined on 150 mm cubes in a standard test according to the Dutch Standards NEN 5968 and 5969, respectively. The loading direction was perpendicular to the casting direction in order to have smooth loading surfaces. The E-modulus was determined on concrete prisms (100×100×400 mm). The E-modulus was measured load-controlled at a speed of 1.0 kN/s. It was calculated as the secant modulus between the origin and 30% of the maximum load of the test specimen. The mean results and the standard deviations of the standard tests are given in Table 3.5. A complete overview of the data for all test specimens is given in the appendix C. It is noted that the standard deviation derived from three tests is not suitable for deriving characteristic values. It is given, however, to indicate the scatter.

Table 3.5: S*tandard test results: mean and (standard deviation)*

Mixture	Age at testing [days]	Cube compressive strength [N/mm^2]	Tensile splitting strength [N/mm^2]	E-modulus [kN/mm^2]
B45.0.0	28	54.3 (1.4)	4.72 (0.22)	37.0 (1.3)
B45.45/30.60	28	55.7 (3.2)	5.84 (0.78)	37.4 (1.4)
B45.45/30.120	28	56.4 (2.7)	6.81 (0.08)	38.9 (1.2)
B45.80/30.60	28	56.1 (4.7)	6.54 (0.27)	38.1 (0.5)
B45.80/60.60	28	60.7 (2.0)	6.70 (0.33)	38.1 (0.1)
B105.0.0	35	115.2 (4.7)	5.65 (0.28)	44.1 (0.2)
B105.80/30.60	28	116.7 (1.4)	11.69 (0.39)	43.0 (0.3)
B105.80/60.60	28	116.7 (1.9)	12.37 (0.71)	43.2 (0.4)

3.3.3 Test Set-Up for Compressive Tests

The testing machine with a test specimen can be seen in Fig. 3.18. The support conditions follow from Fig. 3.19. The capacity of the hydraulic jack was 5 MN. The maximum load expected on the prisms was approximately 2.6 MN (B105 with a mean strength of 115 N/mm^2 × 150 mm × 150 mm = 2.59 MN).

Fig. 3.18: Testing machine with specimen

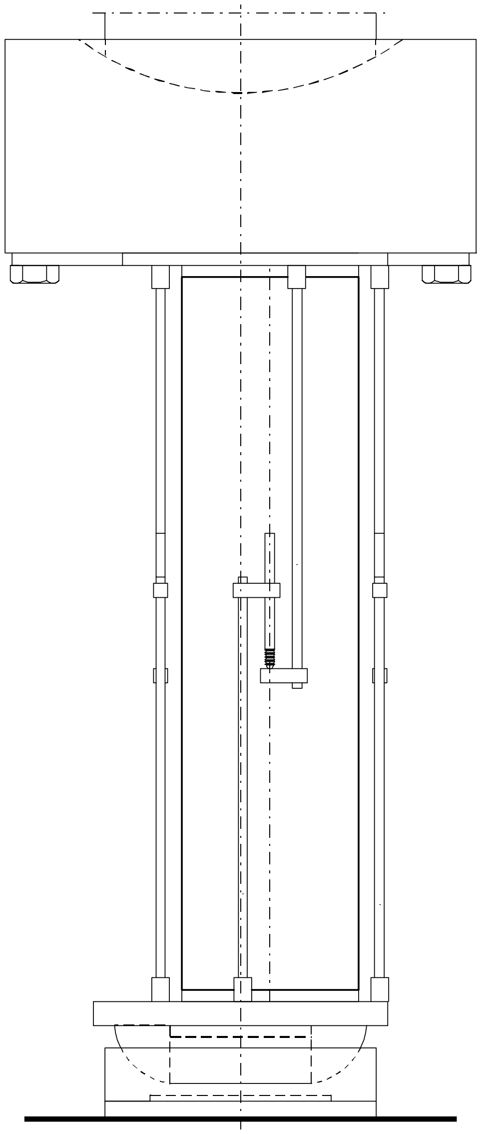

Fig. 3.19: Principles of test set-up

At each load step, the deformations were measured with LVDTs (Linear Variable Displacement Transducers). Fig. 3.20 gives an overview over all the LVDTs and their position on the test specimen.

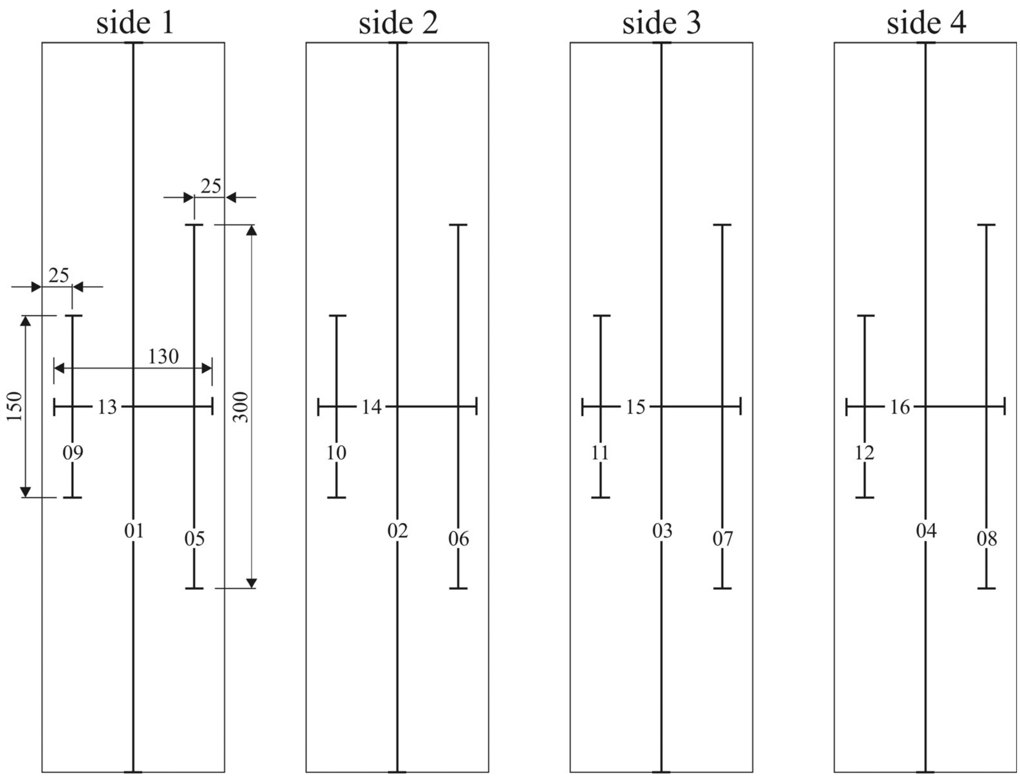

Fig. 3.20: LVDTs and their position on the test specimen

The deformation between the loading platens was measured with LVDT01 to LVDT04. The position of the LVDTs was chosen to prevent them from falling off the specimen. The LVDTs measured deformations in a 20 mm range over a measuring length of 600 mm. A closed-loop test set-up was used in the experiments. The concrete prisms were tested deformation-controlled at a speed of 10^{-5} s^{-1} (i.e. 0.01 mm/(m·s)). The signal with the highest strain rate out of LVDT 01 to 04 was used as control signal. This control system made it possible to run most tests in a stable manner.

Various LVDTs were placed to measure the localization of the deformations:

- LVDTs 01 to 04 measuring length 600 mm, range 20 mm, resolution 0.244%
- LVDTs 05 to 08 measuring length 300 mm, range 5 mm, resolution 0.061%
- LVDTs 09 to 12 measuring length 150 mm, range 5 mm, resolution 0.061%
- LVDTs 13 to 16 measuring length 130 mm, range 2 mm, resolution 0.024%.

The numbering of the sides of the test specimens and the direction of the eccentricity can be seen in Fig. 3.21. The casting surface was always called side 2. This was done in order to have a similar concrete quality in the compressive as well as in the tensile zone (sides 1 and 3 were the sides in the original batches; side 2 was the casting surface; side 4 was the bottom).

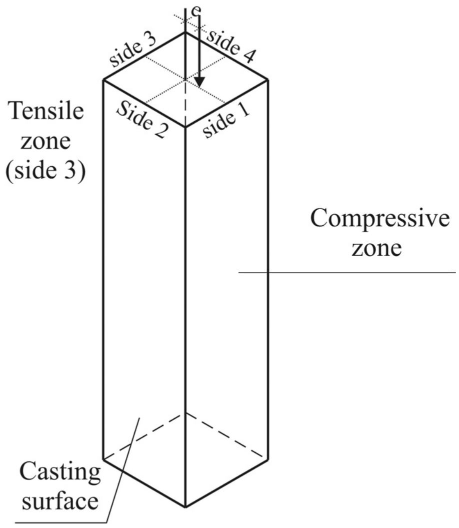

Fig. 3.21: Test specimen: numbering of the sides and eccentricity of the load

Steel loading platens were used, knowing that the boundary restraint may locally be increased due to confinement at the ends. However, with the chosen L/d ratio of the specimen of 600/150 = 4, the effects of the boundary conditions are likely to be only present at the ends of the specimens, but not in the 300 mm long part in the middle.

The prism tests were performed at a concrete age of 28 ±1 days. The standard tests were performed at a concrete age of 28 days.

3.3.4 Observed Failure Patterns

Kooiman (2000) assumed that due to the fiber addition, the shear capacity would be increased to such a degree that a shear band would not form. In the study of Kützing (2000), the cylinders that were reinforced with either steel fibers or polypropylene fibers failed with a shear band, whereas the cylinders that were reinforced with a fiber cocktail made of polypropylene as well as steel fibers failed without the presence of a shear band. In the present study, most specimens failed with a shear band [Schumacher et al., 2003a]. In fact, all of the centric specimens except for one failed with a pronounced shear band. The fibers did prevent large pieces of concrete from spalling off when the specimens failed. As an example, a plain concrete test specimen and a fiber reinforced one are given in Fig. 3.22 and Fig. 3.23.

As the shear band was observed in nearly all centric specimens and in most of the eccentric specimens it was concluded that the failure pattern was conform to that described by the CDZ model and that the CDZ model is therefore applicable for SCSFRC.

Some specimens, especially the high strength concrete prisms, failed explosively.

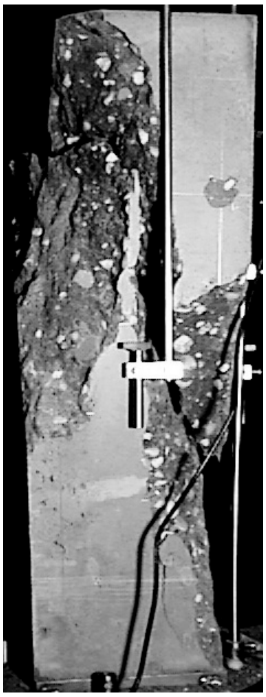

Fig. 3.22: Plain concrete under centric loading (B45.0.0.e00.2 Side 4)

Fig. 3.23: SCSFRC under centric loading (B45.80/30.60.e00.2 Side 4)

3.3.5 Processing the Data

The test data were evaluated and served as a basis to derive the model parameters of the CDZ model. More detailed information, the single test results and pictures of the specimens after testing are given in Schumacher et al. (2003a). The CDZ model parameters were determined from the test results based on the measurements over the whole specimen length. For the centric tests, the average curves from the measurements of the four sides of the specimens were used. For the eccentric tests, the most compressed side (side 1) was used.

There were only few tests in which the deformations were measured up to 10 ‰. Some of the test data could be realistically extrapolated (those with a gray background in Table 3.6 to Table 3.8). This extrapolation is illustrated in Fig. 3.24. It is noted that in this approach, the energy was not totally dissipated and that a certain amount of load bearing capacity remained in the specimen. However, the corresponding deformations would not be acceptable in building practice and therefore a cut at this point is reasonable.

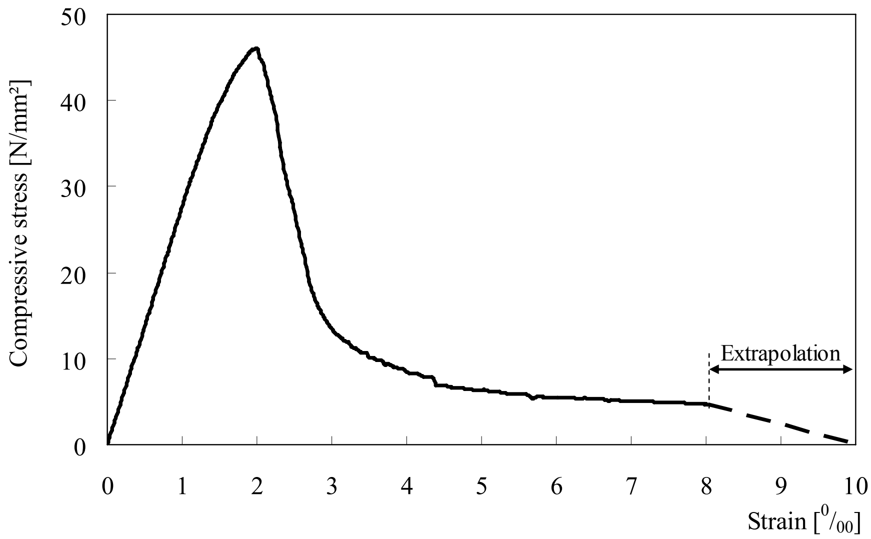

Fig. 3.24: Illustration of the extrapolation of the test data

3.4 Extension of the CDZ Model

3.4.1 Determination of the CDZ Model Parameters

The measured stress-strain relationships were used as input for determining the CDZ model parameters. To that end, the data reported in Schumacher et al. (2003a) were normalized to strain steps of 0.01 ‰ and the corresponding stresses on the most compressed side of the specimen were interpolated for the different measuring lengths. The stresses were calculated from the forces according to the following formula:

$$\sigma = \frac{F}{h^2} \cdot (1 + 6 \cdot \frac{e}{h}) \tag{3.19}$$

and more specifically:

$$\sigma = \frac{F}{h^2} \quad \text{for the centric tests} \tag{3.19a}$$

$$\sigma = \frac{F}{h^2} \cdot \frac{4}{3} \quad \text{for the tests with eccentricity h/18} \tag{3.19b}$$

$$\sigma = \frac{F}{h^2} \cdot 2 \quad \text{for the tests with eccentricity h/6} \tag{3.19c}$$

The maximum stress and the corresponding strain were selected. It is noted that the maximum stress of the eccentric tests calculated with this method does not correspond to what is usually denoted by f_c because the equations 3.19 are basically only valid for linear elastic behavior. Markeset (1993) had already found an increase of 10-30% in f_c at the mostly stressed side when a strain gradient was applied. The maximum stress that follows from the calculations with formula (3.19) will be denoted f_c^* in the remainder of this chapter in order to avoid confusion with the notation f_c, which is usually associated with the centric concrete compressive strength. The elastic and inelastic strains and energies shown in Fig. 3.10 were calculated as described in the following. The compressive strain at peak stress ε_0 is determined from the data with the help of look-up functions.

The elastic strain ε^{el} was determined by equation (3.1) with the modulus of elasticity calculated from the trendline equation between 20% and 40% of the maximum load as described in Schumacher et al. (2003a). With Hooke's law, $\sigma = E\,\varepsilon$, the modulus of elasticity was determined as:

$$E_c = \frac{\sigma}{\varepsilon} \tag{3.20}$$

with the stress σ calculated with equation (3.19) and the strain ε calculated by dividing the measured deformation by the measuring length.

The inelastic strain ε^{in} was determined by equation (3.5) and the elastic energy per unit volume W^{el} was calculated with equations (3.1) and (3.2). The total energy up to the peak load under the stress-strain curve was numerically integrated and the inelastic energy per unit volume W^{in} was calculated as the difference of the total energy up to the peak load minus the elastic energy per unit volume W^{el}. The factor α_{fd} was calculated with equation (3.4). The fracture energy of the plain concrete was calculated with a formula proposed by Remmel (1994) for concrete with a maximum aggregate size of 16 mm:

$$G_F = 65 \cdot \ln(1 + \frac{f_c^*}{10}) \tag{3.21}$$

The factor γ was then calculated with equations (3.11) and (3.14) as:

$$\gamma = \frac{\varepsilon^{in}}{\varepsilon^{el}} \cdot \frac{f_c^{*2}}{G_F\,E_c} \tag{3.22}$$

The damage zone length L^d was measured and the specimen length L was given. The total energy W^c up to a strain of 10‰ was obtained by numerical integration.

Although not all test specimens exhibited a pronounced shear band, the calculations were performed assuming a shear band. The frictional restraint in the shear band, $\beta_{sf} w_c$, was chosen according to the proposal of Markeset to be 0.217 mm for high strength concrete and 0.36 mm for normal strength concrete. The energy per unit area G^l consumed in the shear band over the specimen length L was calculated with equation (3.10), which was reformulated according to the following equation in order to obtain the stress-average strain curve:

$$G^l \cdot \frac{1}{L} = \beta_{sf} w_c \frac{f_c^*}{L} \tag{3.23}$$

With this approach, the energy per unit area G^l dissipated in the shear band was calculated as if it were independent of the steel fibers. Hence, the contribution of the steel fibers was solely assigned to the opening of the longitudinal cracks. This approach is mechanically not fully justified because the fibers increase the energy dissipated in the longitudinal cracks as well as the energy dissipated in the shear band. Nevertheless, this approach leads to a correct overall description of the concrete compressive failure.

The energy per unit volume consumed in the opening of the longitudinal cracks after peak load was calculated with equation (3.11), which was reformulated:

$$W^s \cdot \frac{L^d}{L} = W^c - W^{in} - G^l \cdot \frac{1}{L} \tag{3.24}$$

The proportionality factor k was calculated from equation (3.6), which was reformulated:

$$k = \frac{W^s \cdot \frac{L^d}{L}}{W^{in}} \cdot \frac{L}{L^d} = \frac{W^s}{W^{in}} \tag{3.25}$$

The material property r, which is related to the average distance between successive longitudinal cracks, is calculated with equation (3.14), which was reformulated:

$$r = \frac{1}{\alpha_{fd}\, \gamma\, (1+k)} \tag{3.26}$$

3.4.2 CDZ Model Parameters for SCSFRC Prism Tests

This chapter presents the CDZ model parameters found for the experimental data described above and in Schumacher et al. (2003a). Table 3.6 to Table 3.8 present the results of the tests performed up to a strain of 10‰ or those that were extrapolated (those with a gray background in the tables). The energies are given in appendix E.

Table 3.6: CDZ model parameters for the centric tests

Test	f_c^*	E_c	ε_0	ε^{el}	ε^{in}	$\varepsilon^{in} / \varepsilon^{el}$	α_{fd}	γ	k	r
	N/mm^2	N/mm^2	$^0/_{00}$	$^0/_{00}$	$^0/_{00}$	[-]	[-]	mm^{-1}	[-]	mm
B45.0.0.e00.1	50.80	31053	1.86	1.58	0.28	0.17	0.92	0.12	3.68	1.95
B45.45/30.60.e00.1	47.62	29493	1.96	1.61	0.35	0.21	0.89	0.14	8.91	0.78
B45.45/30.60.e00.2	47.42	30437	1.99	1.56	0.43	0.28	0.89	0.18	3.51	1.38
B45.45/30.60.e00.3	47.73	30589	1.92	1.56	0.36	0.23	0.89	0.15	5.87	1.09
B45.45/30.120.e00.1	46.08	27480	2.00	1.68	0.32	0.19	0.93	0.13	6.69	1.05
B45.45/30.120.e00.2	49.95	25111	2.07	1.71	0.36	0.21	0.93	0.14	8.56	0.79
B45.45/30.120.e00.3	48.71	24637	2.20	1.98	0.22	0.11	1.01	0.09	13.92	0.70
B45.80/30.60.e00.3	52.93	32285	2.04	1.64	0.40	0.24	0.90	0.18	5.55	0.95
B45.80/60.60.e00.1	47.03	23850	2.23	1.97	0.26	0.13	0.91	0.11	14.75	0.65
B45.80/60.60.e00.2	50.89	29992	2.03	1.70	0.33	0.20	0.93	0.14	9.17	0.73
B45.80/60.60.e00.3	48.29	25616	2.11	1.88	0.23	0.12	0.92	0.09	14.05	0.76

Table 3.7: CDZ model parameters for the tests with an eccentricity of h/18

Test	f_c^*	E_c	ε_0	ε^{el}	ε^{in}	$\varepsilon^{in} / \varepsilon^{el}$	α_{fd}	γ	k	r
	N/mm^2	N/mm^2	$^0/_{00}$	$^0/_{00}$	$^0/_{00}$	[-]	[-]	mm^{-1}	[-]	mm
B45.45/30.60.e08.1	61.05	34336	2.09	1.78	0.31	0.18	0.91	0.15	15.78	0.44
B45.45/30.60.e08.2	62.78	33884	2.25	1.85	0.40	0.21	0.92	0.19	5.55	0.86
B45.45/30.60.e08.3	63.18	36050	2.06	1.75	0.31	0.18	0.91	0.15	13.08	0.52
B45.45/30.120.e08.1	66.91	36996	2.19	1.81	0.38	0.21	0.91	0.19	16.31	0.33
B45.45/30.120.e08.2	66.54	36455	2.24	1.83	0.41	0.23	0.93	0.21	7.37	0.62
B45.45/30.120.e08.3	63.94	36302	2.21	1.76	0.45	0.25	0.93	0.22	5.39	0.76
B45.80/30.60.e08.1	64.67	37280	2.21	1.73	0.48	0.27	0.91	0.24	11.58	0.37
B45.80/30.60.e08.2	63.16	37376	2.21	1.69	0.52	0.31	0.90	0.25	17.53	0.24
B45.80/30.60.e08.3	66.38	36245	2.42	1.83	0.59	0.32	0.92	0.30	14.96	0.23
B45.80/60.60.e08.1	64.86	37124	2.24	1.75	0.49	0.28	0.92	0.24	7.03	0.55
B45.80/60.60.e08.2	68.25	36693	2.26	1.86	0.40	0.21	0.94	0.20	7.44	0.62
B45.80/60.60.e08.3	67.63	36014	2.19	1.88	0.31	0.17	0.95	0.16	11.05	0.55
B105.80/30.60.e08.1	118.29	40455	3.23	2.92	0.31	0.10	0.96	0.22	19.27	0.24
B105.80/30.60.e08.2	119.70	41948	3.08	2.85	0.23	0.08	0.91	0.16	45.12	0.15
B105.80/30.60.e08.3	127.63	40903	3.41	3.12	0.29	0.09	0.96	0.22	31.53	0.15

Table 3.8: CDZ model parameters for tests with an eccentricity of h/6

Test	f_c^*	E_c	ε_0	ε^{el}	ε^{in}	$\varepsilon^{in} / \varepsilon^{el}$	α_{fd}	γ	k	r
	N/mm^2	N/mm^2	$^0/_{00}$	$^0/_{00}$	$^0/_{00}$	[-]	[-]	mm^{-1}	[-]	mm
B45.0.0.e25.1	72.25	42174	2.16	1.71	0.45	0.26	0.85	0.24	11.20	0.41
B45.0.0.e25.2	70.75	36294	2.44	1.95	0.49	0.25	0.85	0.26	11.25	0.38
B45.0.0.e25.3	72.92	46553	1.98	1.57	0.41	0.26	0.80	0.22	7.13	0.70
B45.0.0.e25.5	76.79	35028	2.66	2.19	0.47	0.21	0.90	0.26	7.95	0.49
B45.0.0.e25.6	71.28	31210	2.50	2.28	0.22	0.09	0.96	0.11	19.64	0.45
B45.45/30.60.e25.1	62.00	35158	2.72	1.76	0.96	0.54	0.86	0.46	18.06	0.13
B45.45/30.60.e25.2	72.44	33674	2.45	2.15	0.30	0.14	0.87	0.16	40.26	0.18
B45.45/30.60.e25.3	78.23	39511	2.46	1.98	0.48	0.24	0.85	0.27	14.45	0.29
B45.45/30.120.e25.1	67.90	33770	2.67	2.01	0.66	0.33	0.93	0.34	9.70	0.30
B45.45/30.120.e25.2	69.84	37172	2.61	1.88	0.73	0.39	0.88	0.38	16.70	0.17
B45.45/30.120.e25.3	73.04	38743	2.57	1.89	0.68	0.36	0.87	0.36	12.21	0.24
B45.80/30.60.e25.1	70.96	36426	2.60	1.95	0.65	0.33	0.90	0.34	14.72	0.21
B45.80/30.60.e25.3	74.81	30939	2.71	2.07	0.64	0.31	0.92	0.35	12.68	0.23
B45.80/60.60.e25.1	75.23	38767	2.42	1.94	0.48	0.25	0.89	0.26	18.27	0.22
B45.80/60.60.e25.2	78.85	38036	2.41	2.07	0.34	0.16	0.88	0.19	19.32	0.30
B45.80/60.60.e25.3	76.89	36389	2.37	2.11	0.26	0.12	0.87	0.14	29.86	0.26
B105.80/30.60.e25.1	143.57	48175	3.51	2.98	0.53	0.18	0.92	0.43	18.04	0.13
B105.80/30.60.e25.2	144.55	46482	3.62	3.11	0.51	0.16	0.93	0.41	13.19	0.18
B105.80/30.60.e25.3	146.43	47706	3.73	3.07	0.66	0.22	0.92	0.54	15.09	0.12
B105.80/60.60.e25.1	140.91	45902	3.76	3.07	0.69	0.22	0.98	0.55	11.43	0.15
B105.80/60.60.e25.2	143.61	43725	3.89	3.28	0.61	0.18	0.95	0.49	13.05	0.15
B105.80/60.60.e25.3	146.88	49824	3.74	2.95	0.79	0.27	0.89	0.65	7.53	0.20

The model extension was derived for the normal strength tests. Many of the high strength concrete tests, especially the centric ones, could not be performed up to a deformation of 10‰. Therefore, only tendencies are given for HSC.

In the following figures, the parameters determined directly from the test results are presented graphically with the expressions for the parameters in the extended CDZ model. A comparison of the best fit in linear regression and the expressions for the parameters in the extended CDZ model is shown in appendix F. It is noted that the validity of the extended CDZ model is restricted to the scope of the tests, i.e. eccentricities up to $e/h = 1/6$ and a fiber factor $V_f \, l_f / d_f$ up to 0.675, which corresponds to the maximum fiber factor of steel wire fibers with hooked ends for the tested self-compacting concretes.

3.4.3 Extension of the CDZ Model to SCSFRC

The proposed extended CDZ model has a bilinear ascending branch and a linear descending branch of the average stress-strain relationship. An additional confinement, e.g. provided by stirrup-reinforcement or other boundary conditions, can be taken into account by an additional strain $\Delta\varepsilon$, seen Fig. 3.14. The five points defining the stress-strain relationship are shown in Fig. 3.25.

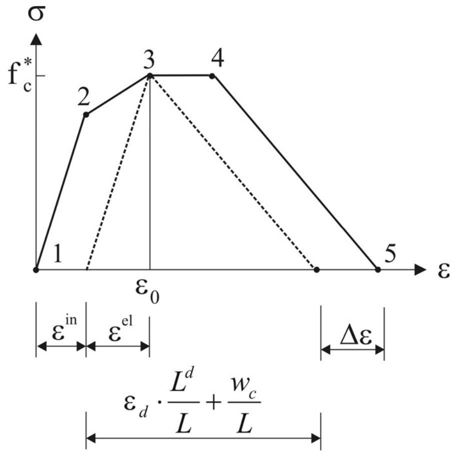

Fig. 3.25: Average stress-strain relationship in the extended CDZ model

All points of the diagram in Fig. 3.25 can be calculated according to Table 3.9. The parameters α_{fd}, f_c^*, E_c, ε_0, k, L^d, L, and w_c are explained in the following sections. Appendix E presents the other model parameters and energies, which were used in order to calculate the parameters shown in Table 3.9. Appendix E also presents alternative expressions, which were derived from the experiments in order to illustrate the effect of the fibers and the eccentricity of the load on the compressive behavior of SCSFRC prisms.

Table 3.9: Values of the extended CDZ model

Point	σ	ε
1	0	0
2	$(2\alpha_{fd}-1)f_c^*$	$(2\alpha_{fd}-1)f_c^*/E_c$
3	f_c^*	ε_0
4	f_c^*	$\varepsilon_0+\Delta\varepsilon$
5	0	$\varepsilon^{in}+\varepsilon_d\cdot\frac{L^d}{L}+\frac{w_c}{L}+\Delta\varepsilon=\left(\varepsilon_0-\frac{f_c^*}{E_c}\right)\cdot\left(1+2\alpha_{fd}\,k\cdot\frac{L^d}{L}\right)+\frac{w_c}{L}+\Delta\varepsilon$

The model was optimized to fit the centric results best because in further beam analysis, the centric relationship is used. The expressions for the model parameters were obtained from the test results by using the average results for each parameter per eccentricity. Then, the contribution of the eccentricity was included in a general formula. No additional confinement was present in the compressive tests. The stress-strain relationship derived from the experiments is therefore defined by four points.

The following pictures (Fig. 3.26 to Fig. 3.32) present the test results and the CDZ model extension in dotted lines for the centric and eccentric tests. The test results along with the best linear fits for each eccentricity as well as the model proposals are shown in appendix F.

Pre-peak Behavior

The steel fibers used in this study are assumed to contribute to the energy absorption after the peak load has been reached and to have no effect on the pre-peak behavior. Therefore, the CDZ model extension for the corresponding values neglects an influence of the steel fibers. However, in the experiments a slight influence of the fiber factor on the pre-peak behavior was observed, see appendix F.

Filling Degree α_{fd}

In contrast to conventional normal strength concrete, self-compacting normal strength concrete has a denser structure, which is more similar to that of high strength concrete being characterized by a finer pore size, a more uniform pore distribution, less flaws and a higher density [Han, 1996]. It was therefore expected that the filling degree α_{fd} for self-compacting normal strength concrete (NSC) used in the experiments would be similar to that of conventional HSC and that the filling degree for self-compacting HSC would be even higher.

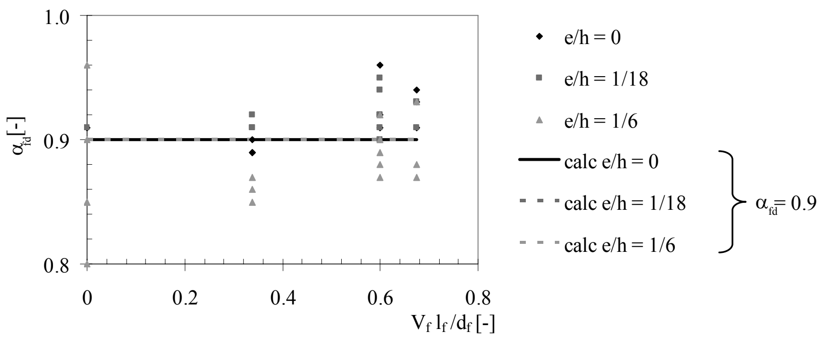

Fig. 3.26: Test results and model approach for the filling degree α_{fd}

In the tests, the filling degree α_{fd} slightly increased with increasing fiber factor. Its influence on the other model parameters was, however, very small and therefore considered negligible.

There was no clear relationship between the eccentricity and α_{fd}. The parameter α_{fd} was therefore proposed to be constant with the value 0.9 for the self-compacting normal strength concrete used in the experiments and 0.93 for the self-compacting high strength concrete (see Table 3.7 and Table 3.8).

Nominal Concrete Compressive Strength f_c^*

The nominal concrete compressive strength was calculated from the force and the assumed stress distribution shown in Fig. 3.16 with formula (3.19) where the stress σ was substituted by the strength f_c^*.

It was expected that the steel fibers have no effect on the pre-peak behavior and thus on the concrete strength because the fibers need a certain crack opening in order to be activated. In the pre-peak region, there are only micro cracks and these are too small to activate this kind of steel fibers.

Fig. 3.27 shows the nominal concrete prism strength observed in the centric test specimens and that calculated according to equation (3.19) and Fig. 3.16 for the eccentrically loaded test specimens as a function of the fiber factor. The lines represent the calculated concrete strength for all eccentricities according to equation (3.27). This calculated nominal concrete stress is calculated from the centric concrete prism strength f_c as a function of the relative eccentricity and is denoted as f_c^*.

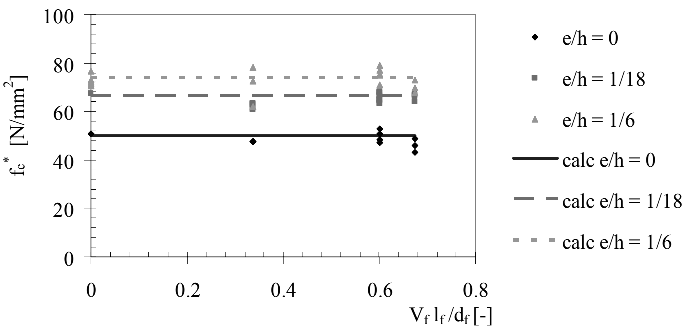

Fig. 3.27: Test results and model approach for the concrete compressive strength

The test results confirm earlier findings that the concrete compressive strength is not significantly influenced by the addition of similar types of steel fibers [e.g. Hartwich, 1986; Niemann, 2002]. Other researchers found no influence or a slight increase in compressive strength due to fiber addition [Maidl, 1995; Winterberg, 1997].

The nominal concrete strength increased with increasing eccentricity. This can be explained by the fact that redistribution of forces takes place in eccentrically loaded specimens (see Schumacher et al., 2002a). The nominal compressive strength was expressed as:

$$f_c^* = f_c - 1430(e/h)^2 + 380(e/h) \quad [\text{N/mm}^2] \tag{3.27}$$

E-modulus

Earlier research on SCC showed that the E-modulus of SCC was lower than for conventional concrete due to the higher mortar content but still in the same range of scatter [Holschemacher, 2001]. The effect of fibers on the E-modulus in regular FRC was expected to be negligible [Maidl, 1995] or only slightly decreasing the E-moduli for increasing fiber contents in the slender test specimens due to larger porosity of the FRC [Winterberg, 1998]. Fig. 3.28 shows the E-moduli of the tests.

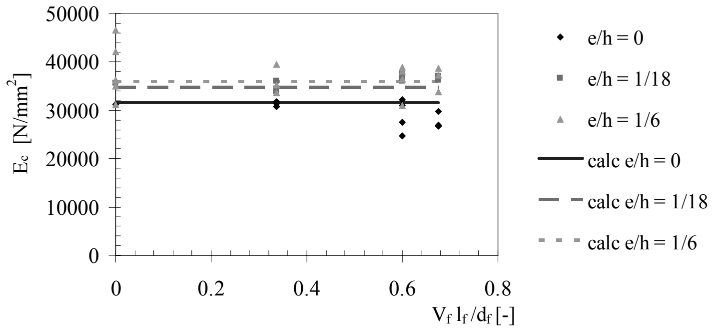

Fig. 3.28: Test results and model approach for the E-modulus

As can be seen from the test results in the figure, there was a slight tendency that the E-modulus decreased with increasing fiber factor. However, this decrease was considered to be negligible. The E-modulus turned out to be lower for SCSFRC than for conventional concrete. According to Eurocode 2, the E-modulus can be calculated as $E_{cm} = 9500 f_{cm}^{1/3}$. A reduction by 10% of this value gives a good model approach. The E-modulus was therefore expressed as:

$$E_{cm} = 0.9 \cdot 9500 f_{cm}^{1/3} = 8550 f_c^{*(1/3)} \tag{3.28}$$

Strain at Maximum Stress ε_0

It was expected that the strain on the most compressed side at maximum stress would increase with increasing eccentricity of the load.

As no influence of the fibers in the pre-peak region was expected, the strain at maximum stress for the centric tests was calculated based on an equation given in Eurocode 2. For the mixture used, a reduction factor of 0.80 was applied to fit the test results. The influence of the eccentricity was accounted for by an addition to the value for the centric tests, see equation (3.27). The strain at maximum stress was calculated as:

$$\varepsilon_0 = 0.7 f_c^{0.31} \cdot 0.8 - 7.5(e/h)^2 + 4.7\, e/h \qquad [‰] \tag{3.29}$$

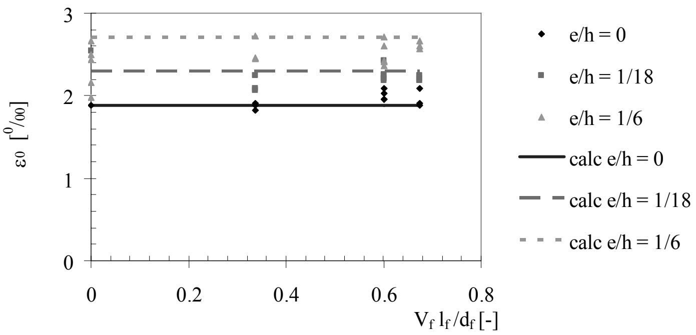

Fig. 3.29: Test results and model approach for the strain at the concrete compressive strength

Post-Peak Behavior

Earlier research has shown that the effect of steel fibers on the compressive behavior can mainly be found in an increase of ductility in the post-peak range [Hartwich, 1986; Brite Euram, 1992]. Beyond the peak, the micro cracks coalesce and form longitudinal cracks. As they open, the fibers are activated and contribute to the absorption of energy.

As explained earlier, the energy absorbed in the shear band was assumed to be constant irrespective of the fiber content. Hence, the complete fiber contribution was assigned to the longitudinal cracks. The input values for the energy absorbed in the shear band according to equation (3.10) were therefore chosen according to Markeset's (1993) proposal: w_c = 0.7 mm for NSC and 0.4 mm for HSC.

From the test results, it could be seen that the drop in the average stress-strain relationship after the peak was rather steep for the measuring length over the whole specimen. This can partly be attributed to the large measuring length which involves a large amount of stored elastic energy. In the following figures, the energies are linked to the length of the damage zone L^d and the total specimen length L^l in order to obtain the average stress-strain relationships as input for the model for calculating the rotation capacity. The phenomenon of localization was explained in section 3.2.

Damage Zone Length L^d

In Schumacher et al. (2003a), the specimens were compared with each other after testing in order to find repeating failure patterns. Markeset (1993) found a damage zone length of 2.5 times the width of the cross-section for the centric tests and 5 times the depth of the damage zone for beams under pure bending. It was therefore expected that the length of the damage zone in the centric tests would be approximately 375 mm and that it would be smaller as the eccentricity increased.

Appendix D presents the observed damage zone lengths L^d. The average damage zone length observed in the tests was somewhat higher than the 375 mm expected from Markeset's proposal for the centric tests: The average damage zone length was 410 mm for all tests (i.e. $2.73 \cdot h$) and more specifically 456 mm (i.e. $3.04 \cdot h$) for the centric tests, 442 mm (i.e. $2.94 \cdot h$) for the tests with an eccentricity of $h/18$ and 356 mm (i.e. $2.37 \cdot h$) for those with an eccentricity of $h/6$. Thus, the length of the damage zone decreased with increasing eccentricity of the load.

The coefficient of variation for various parameter combinations was nearly always in the range of 0.06-0.25. As a tendency, the addition of fibers to the self-compacting concrete mix led to slightly lower lengths of the damage zone (Table 3.10).

Table 3.10: Average damage zone lengths L^d for different mixes and eccentricities (in mm)

Mixture	B45 $e/h=0$	B45 $e/h=1/18$	B45 $e/h=1/6$	B105 $e/h=1/6$
B45.0.0	483	550	400	475
B45.45/30.60	417	500	250	-
B45.45/30.120	450	417	317	-
B45.80/30.60	467	350	325	333
B45.80/60.60	417	483	367	367

Fig. 3.30 presents the damage zone length divided by the prism length (600 mm) as a function of the fiber factor for the three eccentricities. As can be seen from the figure, the damage zone length slightly decreases with increasing fiber factor. The influence of the eccentricity determined by best fit did not show a consistent result.

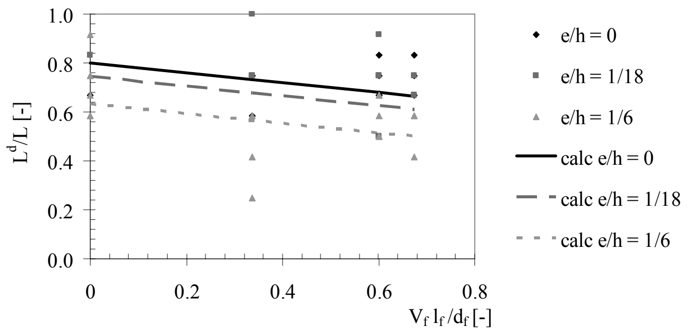

Fig. 3.30: Test results and model approach for the damage zone length

It is proposed to estimate the damage zone length divided by the specimen length, which was 600 mm in the experiments, with the following expression:

$$L^d / L = 0.8 - 0.2\, V_f\, l_f / d_f - e/h \tag{3.30}$$

Considering the scatter of the results, this slight decrease is neglected in describing the compressive behavior in the beam model in chapter 6. There, the damage zone length is not inserted explicitly, but derived from equation (3.15), where the damage zone length L^d is calculated from the damage zone depth d^l with the help of the factor k^l, which is 2.5 for pure compression and 5 for an eccentricity larger than h/6 and linearly increasing in between, see Fig. 3.31.

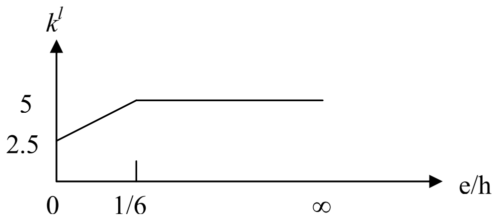

Fig. 3.31: Factor k^l depending on the relative eccentricity

Proportionality Factor k

The proportionality factor k is obtained by dividing the energy absorbed in the longitudinal cracks by the inelastic energy. It was expected that the proportionality factor k would increase with increasing fiber content [Kützing, 2000].

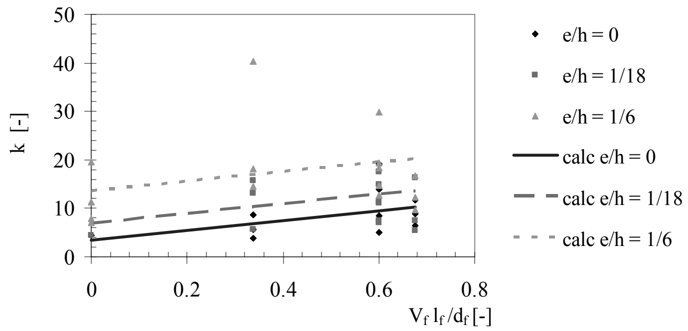

Fig. 3.32: Test results and model approach for the proportionality factor k

As can be seen from Fig. 3.32, the proportionality factor k increased with increasing fiber factor and increasing eccentricity.

As the energy absorbed in the longitudinal cracks increases with increasing fiber factor and the inelastic energy is independent of the fiber factor, the proportionality factor k also has to increase with increasing fiber factor.

The best fit of the test results for centric tests without fibers shows that the proportionality factor is 3.5 for this mixture rather than the 3.0 proposed by Markeset. This is logical because the factor α_{fd} has already been approximately 10% larger and therefore even for identical post-peak behavior, the division of the energy dissipated in the longitudinal cracks by a smaller inelastic energy should give a larger proportionality factor. Furthermore, the proportionality factor k was rather sensitive to the mixture composition, in particular to the choice of the aggregates in Markeset's tests.

The more homogeneous the mixture the less micro cracking is observed in the ascending branch of the stress-strain relationship. Therefore, the proportionality factor k increases. The proportionality factor k was expressed as:

$$k = 3.5 + 10\, V_f\, l_f / d_f + 60 (e / h) \qquad (3.31)$$

As the properties of fiber reinforced concrete strongly depend on the fiber orientation, it is logical to link the middle term of the proportionality factor k to the orientation number of the fibers. In this model, the fiber orientation is assumed to be the same in all prisms because they were manufactured in the same way. Consequently, the influence of the fiber orientation is accounted for in the term for the contribution of the fibers to the proportionality factor k. Due to the flow of the concrete, a preferred orientation can occur in the test specimens made of SCSFRC (see section 3.3.2).

Summary of the Input Values to Obtain the Stress-Strain Relationship

Table 3.11 gives an overview of the input values to obtain the stress-strain relationship of concrete in compression in the original CDZ model proposed by Markeset for plain conventional normal density concrete and in the extended model for SCSFRC. The parameters of the extended model were derived for a concrete strength of 50 N/mm^2 for plain concrete and the expressions are valid for an eccentricity of up to $e / h = 1/6$ and for a fiber factor $V_f\, l_f / d_f$ up to 0.675, which corresponds to the maximum amount of fibers that could be applied in self-compacting concrete at the given mixture compositions.

Table 3.11: Comparison of the model parameters of the original and of the extended CDZ model

Parameter	CDZ model	CDZ extension
α_{fd}	0.8	α_{fd} = 0.9 for NSSCC, 0.93 for HSSCC
f_c	f_c	$f_c^* = f_c - 1430(e/h)^2 + 380(e/h)$
E_c	E_c	$E_c = 0.9 \cdot 9500 f_c^{*(1/3)} = 8550 f_c^{*(1/3)}$
ε_0	ε_0	$\varepsilon_0 = 0.7 f_c^{0.31} \cdot 0.8 - 7.5(e/h)^2 + 4.7 e/h$
k	3.0	$k = 3.5 + 10 V_f l_f / d_f + 60(e/h)$
w_c	0.4 – 0.7 mm	w_c = 0.7 mm for NSSC, 0.4 for HSSC

In order to illustrate the effect of the fiber addition, Fig. 3.33 shows the stress-strain relationships calculated for SCC for different fiber factors ($V_f l_f / d_f$ = 0 to 0.675). The values were calculated for a concrete prism compressive strength of 50 N/mm^2 and a specimen length of 600 mm.

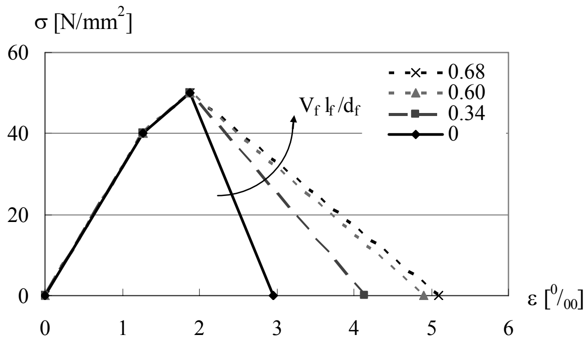

Fig. 3.33: Stress-strain relationships of concrete under uniaxial compression for different fiber factors $V_f l_f/d_f$

An additional confinement, e.g. provided by stirrup-reinforcement or other boundary conditions, can be taken into account by an additional strain $\Delta\varepsilon$, seen Fig. 3.14 and Fig. 3.25.

3.4.4 Verification of the Centric Relations by Simulating the Eccentric Tests

The stress-strain relation derived with equation (3.19) is a fictitious relation based on the assumption of the stress distribution shown in Fig. 3.16. When simulating the eccentric tests with a numerical model with these relations, the moment capacity is strongly overestimated. Due to the strain gradient in the compressive zone of a beam, both the strength and the ductility are increased with respect to the centric relations. However, the quantity might be less than assumed when deriving the relations with equation (3.19). This increase can be explained with a support of the most stressed layer by the less stressed layers when the specimen is bent. Markeset (1993) quantified the increase in concrete compressive strength by 10-30%, depending on the ratio between the width and the depth of the compression zone, increasing as this ratio increases. For the beams considered here, good agreement of the numerical simulation of some eccentric prism tests has been achieved by increasing the concrete compressive strength by 10% and using the proportionality factor k as a function of the eccentricity as derived from the eccentric tests (equation 3.31). This means that the factor k is assumed to be linearly increasing with the relative eccentricity e/h up to the experimentally verified limit of e/h = 1/6. For increasing values of e/h, the factor k is likely to increase even further. However, as this has not been experimentally verified, the factor k is kept constant from e/h = 1/6 on, see Fig. 3.34.

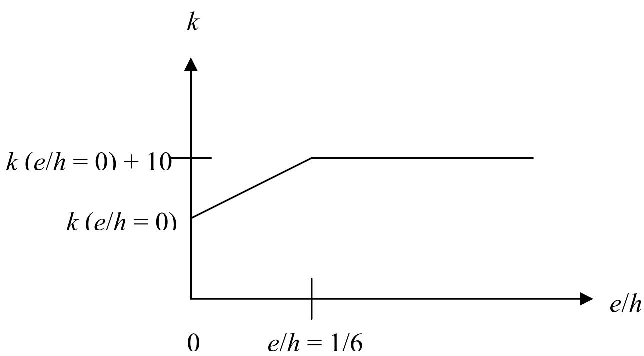

Fig. 3.34: Proportionality factor k as a function of the relative eccentricity e/h

3.5 Concluding Remarks

As a shear band was observed in nearly all centric specimens and in most of the eccentric ones it was concluded that the failure pattern was conform to that described by the CDZ model and that the CDZ model is therefore applicable for SCSFRC.

The CDZ model has been extended for steel wire fibers with hooked ends. The influence of the fibers in the pre-peak region has been neglected. This chapter showed the extension of the CDZ model to SCSFRC with a concrete strength of 50 N/mm^2. The model parameter k was expressed depending on the fiber factor and the eccentricity of the load.

The five points, as illustrated in Fig. 3.25 and Table 3.9, are used as input for the compressive behavior in the calculations of the rotation capacity of SCSFRC. In the calculations of the rotation capacity in chapter 6, the concrete compressive strength is increased by 10% in case of bending to account for the confining action from the less stressed layers on the most stressed layer and the proportionality factor k is used as a function of the eccentricity up to a relative eccentricity e/h = 1/6 and constant from there on.

4 Tensile Behavior of SCSFRC

4.1 Introduction

The tensile behavior of concrete strongly influences the bond between concrete and reinforcement and therefore the rotation capacity of members with bending reinforcement. In members without bending reinforcement, the behavior of the tension zone is fully governed by the tensile behavior of the concrete. Pondering the importance of the tensile behavior of concrete for the deformation behavior of the members and the variety of models for SFRC, this chapter focuses on the tensile behavior of SCSFRC. Firstly, some general remarks about the influence of steel fibers on the tensile behavior of concrete are given in section 4.2. Then, several methods for testing the tensile properties of concrete are presented in section 4.3 and the differences in the obtained stress-crack width relationships are discussed in section 4.4. Several research results are mentioned in order to enable the reader to find more information. A section on fiber orientation explains some of these differences (section 4.5). The model for the tensile behavior of SCSFRC which is used for the calculation of the rotation capacity in chapter 6 is presented in section 4.6.

4.2 Effect of Steel Fibers

4.2.1 Uniaxial Tensile Strength

The influence of steel fibers on the uniaxial tensile strength depends among other factors on the fiber properties and the fiber content. For the hooked-end steel fibers used in this research, it can be expected that the tensile strength is not affected by the fibers. Gettu & Barragán (2003) observed no correlation between the number of effective fibers and the peak stress in concentric tensile tests for concrete mixtures with 40 kg/m^3 hooked-end steel wire fibers with an aspect ratio of 80 and a fiber length of 60 mm. They did, however, observe a strong correlation of the number of effective fibers and the post-peak stresses. This supports the assumption that hooked-end steel fibers of usual geometry need a certain crack opening in order to become effective as is taken into account in the model of Kützing (2000).

For short straight steel fibers, on the contrary, an increase in tensile strength has been observed in the past [Marković, 2006]. This is explained by the fact that short fibers are more effective in bridging micro cracks, which develop before the peak load is reached, and therefore, the tensile strength can be increased. At the same fiber content as for large fibers, the number of short fibers and thus the bond area is much larger.

4.2.2 Post-Cracking Strength

The post-cracking strength of concrete can be considerably influenced by the type, aspect ratio, length, content and distribution of the fibers and by the concrete quality [Niemann, 2002]. For common fiber contents up to 120 kg/m^3 of hooked end steel fibers and normal or high strength concretes up to approximately 100 N/mm^2 compressive strength it is expected that the post-cracking strength is lower than the uniaxial tensile strength. The post-peak behavior is therefore characterized by softening and not by hardening.

In contrast to plain concrete, which fails rather brittle, SFRC exhibits an increased post-cracking strength. Fig. 4.1 shows the influence of different contents of steel wire fibers with hooked ends on the post-peak behavior of concrete.

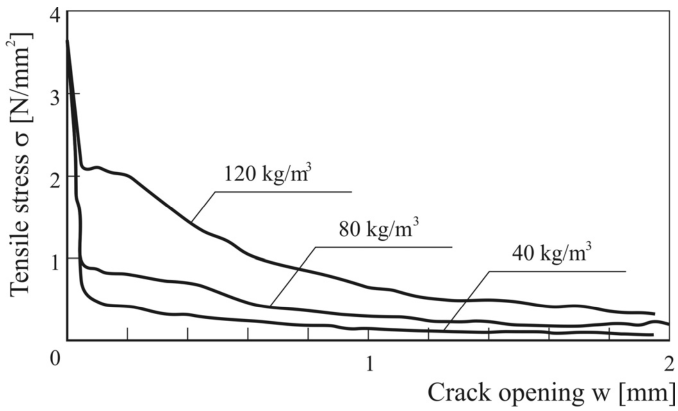

Fig. 4.1: Results of direct tensile tests on SFRC with hooked end steel fibers [Kützing, 2000]

4.3 Test Methods

There are several methods to test the tensile properties of concrete. The main categories include:

- bending tests
- splitting tests
- uniaxial tensile tests
- punching tests.

All these test methods have advantages and disadvantages. As size effects and loading conditions play an important role in the outcome of a test, most test results do not represent pure material laws but the outcome of the conditions of a test set-up.

Stroband (1998) investigated different test methods concerning the criteria:

- complexity of the test set-up
- complexity of preparing the specimens
- complexity of execution
- reproducibility of the tests
- costs per experiment
- acceptance of the test method by researchers
- complexity of processing
- reliability of the test results.

The tests Stroband investigated included the:

- four-point-bending test
- three-point-bending test
- Brazilian splitting test
- wedge-splitting test
- uniaxial tensile test.

Kooiman (2000) concluded from this investigation that the three-point-bending test and the wedge-splitting test are the most suitable test methods, the three-point-bending test being preferred in the Netherlands.

The three-point-bending test is the standard test method recommended in RILEM [Vandewalle et al., 2000]. It was therefore chosen to use the three-point-bending test in the scope of this research. Yet, it is not possible to obtain the uniaxial post-cracking behavior of SFRC directly from the three-point bending tests. Therefore, an inverse analysis had to be carried out to determine the stress-crack width relationship [Roelfstra & Wittmann, 1986]. Further analysis has proven that the stress-crack width relationship obtained with the inverse analysis as described by Kooiman (2000) and Schumacher et al. (2003b) is inappropriate for the description of the behavior in the cracks of members with combined steel fiber and conventional reinforcement. This issue is further discussed in section 4.4.

4.4 Differences in σ-w Relationships Derived from Different Types of Tests

Often, the stress-crack width relationship is defined as a bilinear softening relation in literature. In this thesis, the corresponding parameters are defined as shown in Fig. 4.2 with

σ_{ct}	concrete tensile stress
$f_{ctm,ax}$	average axial concrete tensile strength
w	crack width
w_0	critical crack width
α_{FCM}	FCM constant
β_{FCM}	FCM constant

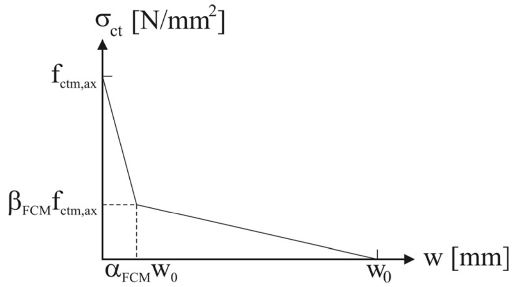

Fig. 4.2: Definition of parameters in the stress-crack width relation

4.4.1 Plain Concrete

The fracture energy of plain concrete can be uniquely derived from fracture mechanics experiments but the determination of the tensile strength and the softening relationship appear to be ambiguous. The stress-crack width relationship for the tension softening response of plain concrete cannot be established with certainty from indirect tests [Karihaloo, 1995]. The softening relationships derived from an inverse analysis are not unambiguous: from a mathematical point of view, several solutions are possible [Villmann et al., 2004]. However, considering the relationships from the uniaxial tensile test, physically sound and realistic solutions can be identified [Villmann et al., 2004]. Some typical stress-crack width relationships of plain concrete with a tensile strength of 3 N/mm^2 can be seen in Fig. 4.3. The crack width of the point at which the slope in bilinear softening relationships changes is usually found in the range of 0.02 to 0.05 mm.

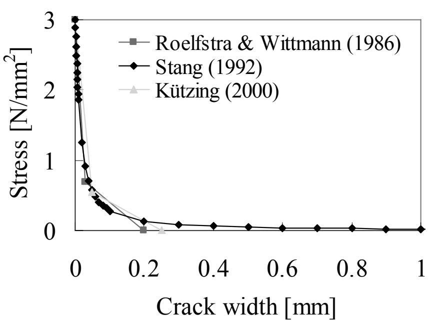

Fig. 4.3: Stress-crack width relationships for plain concrete

A first approximation of the strength and the softening parameters is directly obtained in uniaxial tensile tests. However, it is noted that the result is influenced by the test set-up, e.g. the boundary rotations [Van Mier, 1997].

Wedge splitting and bending tests allow the direct determination of the fracture energy but require an inverse analysis in order to obtain the softening parameters and the tensile strength under the assumption of a certain softening model.

The inverse analysis is described in more detail by Kooiman (2000). Automatic algorithms are available for the inverse analysis, e.g. the approach of Roelfstra & Wittmann (1986) using the discrete crack model and bilinear softening, the approach of the Japan Concrete Institute (2001) using poly-linear softening, or the approach of Villmann et al. (2004) using the discrete crack model, optimization by evolutionary algorithms and an exponential softening function.

Differences in stress-crack width relationships derived from different test methods were observed in plain concrete. Slowik & Wittmann [1992; Slowik, 1993] investigated the influence of the strain gradient, of the ligament size and of the most stressed volume on the fracture energy and the strain softening behavior of plain conventional concrete. The fracture energy depends on the specimen geometry and on the ligament size just as the tensile strength also depends on the specimen size and geometry. They found nearly identical first branches of the stress-crack opening relationships derived from direct tension tests, wedge splitting tests and three-point bending tests. However, the critical crack width w_0 was lowest for the three-point bending test (0.15-0.2 mm), somewhat larger for the wedge splitting tests (0.25 mm) and largest for the direct tensile tests (0.5 mm). The reason for this was attributed to a different stress condition around the fracture process zone. For higher strain gradients, the length of the fracture process zone decreases and the width becomes more confined. This results in a decrease of the fracture energy. Furthermore, the long tail of the relationships derived from the three-point bending tests was explained by friction at the supports and by the friction between the inclined rough crack surfaces.

It is sometimes argued in literature that the differences in stress-crack width relationships are partially due to non-local effects, namely the effect of the strain gradient. This reasoning might, however, mean that the principle of plane sections remaining plane does not completely hold true and therefore should not be applied without due consideration.

The assumption of plane sections remaining plane has been found appropriate for the three-point bending test on plain concrete [Hordijk, 1991]. However, it is questionable whether this assumption holds true for the wedge splitting test.

Good agreement of the relationships determined from different kinds of tests on plain concrete were found by Barragán (2002), Østergaard (2003) and Villmann et al. (2004).

4.4.2 SFRC Relationships and Observed Differences

A large number of relationships for the tensile behavior of SFRC has been proposed in the literature based on experimental results. Some of them are listed in Table 4.1. The table also shows the tests, from which the relationships were derived and the types of specimens which were used to verify these relationships.

Table 4.1: Stress-crack width relationships for SFRC
UTT – uniaxial tension test, WST – wedge splitting tests, 3PB – three-point bending tests, 4PB – four-point bending test
+: good, 0: not always good, - not good

Author	Year	Model		Type of tests			Tests vs. model			Agreement
		ascending branch	descending branch	UTT	Bending 3PB	4PB	UTT	Bending 3PB	4PB	test - calculation
Barros & Figueiras	1999	linear σ-ε	bilinear σ-ε		x			x		+
Kützing	2000	linear σ-ε	trilinear σ-w	x			x			0
Kooiman	2000	linear σ-ε	bilinear σ-w		x			x		+
Barragán	2002	linear σ-ε	a.o. bilinear σ-w	x	x		x			+ 1)
Schumacher et al.	2003b	linear σ-ε	bilinear σ-w		x			x		+
Sorelli	2003	linear σ-ε	bilinear σ-w	x		x	x		x	+
Meda et al.	2004	linear σ-ε	bilinear σ-w	x		x	x		x	0
Pereira et al.	2004	linear σ-ε	trilinear σ-w		x			x		+
Grünewald	2004	bilinear σ-ε	bilinear σ-w		x			x		+
Voo & Foster	2004	linear σ-ε	power function	x			x			+
Löfgren et al.	2004	linear σ-ε	bilinear σ-w	x	x		x			- 2)

1) up to 2 mm

2) different fiber orientation

The relationships for SFRC are either derived theoretically, semi-empirically or empirically. Theoretically derived models often assume randomly oriented fibers, which is seldom the case in reality.

Often, models for the tensile behavior of SFRC derived from the uniaxial tension tests consist of a concrete contribution and a fiber contribution [Vandewalle et al., 2002]. They have a steep first branch similar to plain concrete. The crack opening at the bending point in the stress-crack width relationship can usually be found in the range of 0.02 to 0.05 mm. Examples for a steep first branch can be found in Lin (1996), Kützing (2000), Groth (2000), Barragán (2002), Sorelli (2003), Cairns & Plizzari (2004), Voo & Foster (2003, 2004), Pereira et al. (2004), Meda et al. (2004).

Relationships derived from the inverse analysis of bending tests often show a less steep first branch, e.g. Kooiman (2000), Schumacher et al. (2003b), Grünewald (2004).

Fig. 4.4 shows a comparison of the stress-crack width relationships obtained for SFRC with 60 kg/m^3 steel fibers with an aspect ratio of 80 and a length of 30. The relation of Kützing (2000) was derived from uniaxial tensile tests. The relation of Kooiman was derived from the inverse analysis of three-point bending tests and was optimized in Schumacher et al. (2003b) for SCSFRC. In this respect, differences in fiber orientation can play a significant role.

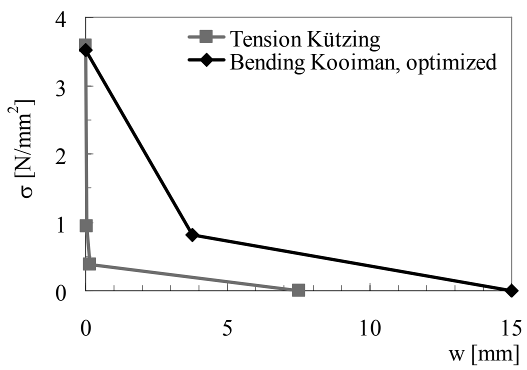

Fig. 4.4: Stress-crack width relationships for SFRC derived from different types of tests

The response of tensile tests could be simulated well with relationships derived from uniaxial tensile tests and bending tests could be simulated well with relationships derived by inverse analysis from bending test, see Table 4.1. However, if bending tests are modeled with stress-crack width relationships derived from uniaxial tensile tests, the ductility after peak load is generally underestimated. This underestimation provides a lower boundary and is satisfactory for calculating the resistance of a member because it is at the safe side. However, it does not describe the mean experimental response right after the peak very well. Hence as such it will not allow to model the deformation behavior (including cracking) correctly in general cases. Application of the stress-crack width relationships derived from the inverse analysis of three-point bending tests would lead to unrealistically low transmission lengths and thus crack distances in members with combined fiber and bar reinforcement. As the stress-crack width relationships derived from the inverse analysis of three-point bending tests substantially differed from those derived from direct tensile tests (see Fig. 4.4) it can be concluded that the stress-crack width relationships derived in the inverse analysis of three-point bending tests are not suitable to be used in applications in which the uniaxial tensile behavior is needed. Therefore they should rather be called "fictitious stress-crack width relationships". The reasons for these differences can be sought in the different fiber distribution and orientation in the bending tests compared to the uniaxial tensile tests in with respect to the main tensile loading. The quantitative relation between the results of the different stress-crack width relationships derived by the different test methods is not yet known and is therefore subject to further research. Nevertheless, a stress-crack width relationship representing the uniaxial tensile behavior should be used in modeling cracking and bond in members with steel fibers and bar reinforcement.

For the effect of changing the parameters in the concrete tensile properties on the force-deformation relationship it is referred to the parameter studies of Kooiman (2000), Elisaigh et al. (2004) and Grünewald (2004).

Fiber Distribution and Orientation in Different Types of Tests

It has been tried to explain the differences in softening relationships of SFRC for different test methods from the influences of the casting direction and the way of compaction on the orientation of the fibers compared to the direction of the principle tensile stresses in the tests considered.

Barragán (2002) compared stress-crack width relationships from the inverse analysis of beams and uniaxial tension tests on normal and high strength concretes reinforced with different types and contents of steel fibers with hooked ends. His tension test specimens were cored in longitudinal direction at mid-height of the beams where no influence of the walls on the fiber orientation was present [Barragán, 2002]. As the stress direction was the same as the preferred fiber orientation in case of the beams, whereas the fiber orientation was assumed to be 3D in case of the cores in contrast to a preferred fiber orientation in the beams, it can be expected that the second branch of the stress-crack opening relationship derived from the beam tests was less steep than that measured in the uniaxial tensile tests. Barragán concluded that more studies are needed for comparing the results of uniaxial tensile tests with those obtained from the inverse analysis of beam data [Barragán, 2002].

Fiber Distribution and Orientation Consequences

It has been tried to explain the phenomenon of different softening relationships for SFRC by analyzing test results for different directions of casting and different methods of compaction and thus for different fiber orientations with regard to the main tensile stresses in the tests [Barragán, 2002; Meda et al., 2004, Löfgren et al., 2004].

Di Prisco & Felicetti (2001) reported a change in fracture energy of concrete with the same mix design of a factor three or even more depending on the casting direction.

Ferrara et al. (2004) investigated the connection between concrete workability, fiber distribution and the mechanical properties of the SFRC. The random 3D fiber distribution, on which many relationships for the post-cracking behavior of SFRC are based, is usually not achieved in a structural element. The orientation depends on the casting process, boundary effects, the compaction method, flow etc. These factors influence the number of fibers in a cross-section and their inclination with respect to the main tensile force and finally the crack surface. The number of effective fibers in a cross-section strongly influences the post-cracking behavior [Gettu & Barragán, 2003].

Ferrara et al. (2004) concluded that there is a need for further investigating the relation between fiber distribution, workability and mechanical properties. Up to now, this is not yet fully explained.

4.5 Fiber Orientation

4.5.1 Influencing Factors and Definitions

The differences in stress-crack width relationships derived from different test methods are more pronounced for SFRC compared to plain concrete. The explanation of the different stress-crack width relationships can be sought in the distribution and the orientation of the fibers. The efficiency of a fiber depends on the bond behavior of the fiber in the matrix and the fiber orientation relative to the direction of the tensile stresses. Therefore, the fiber orientation is an important influencing factor on the post-cracking behavior of SFRC. If the fibers are randomly oriented, the mechanical properties are isotropic. However, this is seldom the case.

The fiber orientation of regular SFRC has been investigated by e.g. Stroeven (1978), Schönlin (1988), Soroushian & Lee (1990), Lin (1996) and Erdem (2002), Dupont (2003), Rosenbusch (2003) and others [Rosenbusch, 2004]. Grünewald (2004) investigated the fiber orientation of SCSFRC.

Influencing Factors

The fiber orientation is influenced by:

- wall effects
- specimen size
- casting direction
- way of compaction
- mixture composition
- mixture workability
- presence of reinforcing bars and other obstacles.

Definitions

Kameswara Rao (1979) distinguished between the fiber efficiency and the fiber effectiveness. He defined the fiber efficiency as the performance of an individual fiber as a function of the embedment length and the orientation of the fiber to the tensile load. The fiber effectiveness indicates the average value of the fiber efficiency, considering all possible orientations and embedment lengths.

When comparing fiber orientation numbers from literature one must be aware of the fact that different definitions are used.

In the following, the derivation of the theoretical orientation numbers for the 1D-, 2D-, and 3D-situation is presented. The fiber orientation number is 1 if a fiber is aligned in the direction under consideration and it is zero if the fiber is aligned perpendicular to that direction. The larger the fiber orientation number is the more effective the fibers are in that direction. The fiber orientation number can be obtained from a fiber count (e.g. manual or with image analysis) of the cross-section by equation (4.1) [Krenchel, 1975, reformulated]:

$$\eta_\varphi = N_f \cdot \frac{A_f}{V_f} \tag{4.1}$$

where:

η_φ	fiber orientation number [-]
N_f	number of steel fibers per unit area [1/mm^2]
A_f	area of the cross-section of a single fiber [mm^2]
V_f	fiber content [m^3/m^3]

1D-situation

In a 1D-situation, all fibers are oriented in the same direction. For that direction, the orientation number is 1. The fiber appears as a circle in the cross-section. Perpendicular to that direction, the orientation number is zero.

2D-situation

In the 2D-situation, the fibers appear as an ellipse in the cross-section. The fibers are considered randomly oriented in a plane, see Fig. 4.5.

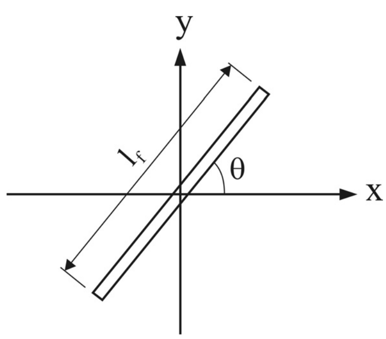

Fig. 4.5: Two-dimensional fiber orientation system [Kooiman, 2000]

The orientation angle θ can vary between zero and π. In order to determine the fiber effectiveness, the mean fiber orientation is projected on the axis that is parallel to the tensile stress (here y-axis). The effectiveness is calculated with equation (4.2):

$$\eta_{\theta 2D} = \int_0^{\pi} \frac{\sin\theta \cdot d\theta}{\pi} = \frac{2}{\pi} \cong 0.637 \qquad (4.2)$$

3D-situation

A fiber is considered randomly oriented in a sphere, see Fig. 4.6. The integration of a randomly oriented fiber over the two angles ψ and θ leads to the orientation of the fibers if they are uniformly distributed in a sphere, i.e. they have the same orientation number in each direction.

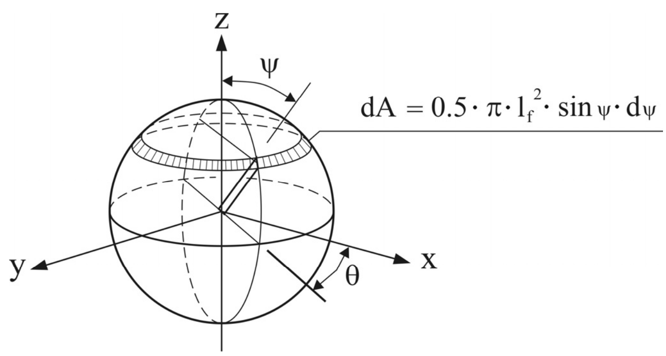

Fig. 4.6: 3D fiber orientation system: randomly oriented fibers in three dimensions [Kooiman, 2000]

The contribution of the area dA to the orientation factor is $\cos\psi dA$. Integrating this over half the sphere and dividing it by the surface of half the sphere results in:

$$\eta_{\theta 3D} = \frac{\int_0^{\pi/2} \cos\psi dA}{2\pi \cdot (\frac{l_f}{2})^2} = \frac{\int_0^{\pi/2} \pi \cdot \frac{l_f^2}{2} \cdot \sin\psi \cdot \cos\psi d\psi}{2\pi \cdot (\frac{l_f}{2})^2} = \frac{1}{2} \qquad (4.3)$$

Overview

The orientation efficiency factors and the mean embedment lengths are summarized in Table 4.2.

Table 4.2: Orientation factors and mean embedment lengths for the 1D-, 2D- and 3D-situations

	orientation factor η [–]	mean embedment length [mm]
1D	1	$\frac{1}{2} \cdot l_f$
2D	$2/\pi$	$1/\pi \cdot l_f$
3D	½	$\frac{1}{4} \cdot l_f$

4.5.2 Influence of Walls on Fiber Orientation

The fiber orientation is strongly influenced by boundaries (mould or surface), especially when the fiber length is relatively large compared to the structural dimensions. Dupont (2003) derived different orientation numbers for three distinguished zones in a rectangular cross-section as shown in Fig. 4.7.

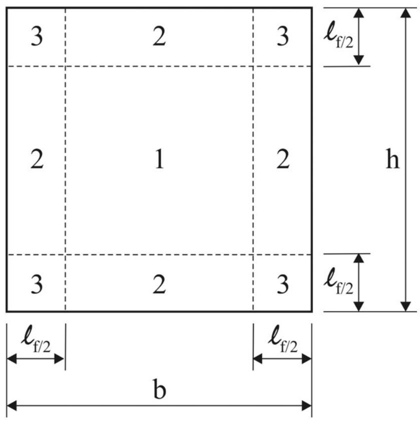

Fig. 4.7: Cross-section of a beam divided into three different zones [Dupont, 2003]

The average orientation over the cross-section can be calculated with equation (4.4)

$$\eta = \frac{[\eta_1 \cdot (b - l_f)(h - l_f) + \eta_2 \cdot [(b - l_f)l_f + (h - l_f)l_f] + \eta_3 \cdot l_f^2]}{b \cdot h} \tag{4.4}$$

For the bulk, Dupont assumed the above mentioned 3D-orientation of 0.5, for one boundary 0.6 and in the corners 0.84. Inserting these values into equation (4.4) results in the following average orientation numbers η for the fiber lengths 30 and 60 mm and the cross-section dimensions 150 by 150 mm and 150 by 300 mm, which present dimensions used in the scope of this thesis:

Table 4.3: Average fiber orientation numbers η for different specimens and fiber dimensions

	Unit	Example 1	Example 2	Example 3	Example 4
b	mm	150	150	150	150
l_f	mm	30	30	60	60
h	mm	300	150	300	150
η_1	-	0.5	0.5	0.5	0.5
η_2	-	0.6	0.6	0.6	0.6
η_3	-	0.84	0.84	0.84	0.84
η	-	0.53	0.55	0.57	0.60

4.5.3 Influence of Casting and Compaction on Fiber Orientation

The production process, the concrete composition and the geometry of a structure have a significant influence on the mechanical properties of SFRC. Due to a preferred orientation of the fibers, the mechanical properties can be different in different directions [Rosenbusch, 2004]. Different fiber orientations in different directions have been observed for regular SFRC [Lin, 1996] as well as for SCSFRC [Grünewald, 2004]. In contrast to plain concrete, SFRC can therefore not generally be assumed as isotropic but the different material properties, which can be found in different loading directions, should be accounted for in calculation models. This would require more complicated calculation models unless a uniform 3D-distribution of the fibers can be ensured. This anisotropy presents the main difference in the model approach between plain and fiber reinforced concrete. If the fiber orientation is included in models for SFRC, phenomena often attributed to the scatter of material properties can be physically explained.

Fibers are found to have a preferred orientation perpendicular to the direction of casting in vibrated concrete (see also Fig. 4.8) [Rosenbusch, 2003]. However, the quantification of the effect of the influencing factors on the mechanical properties remains difficult and is not yet fully understood (compare Ferrara et al., 2004). In SCSFRC, the fibers have a preferred orientation parallel to the flow direction.

The tensile properties were investigated as a function of the position and the direction of the fibers in members by several researchers, e.g. Lin (1996), Kooiman (2000), Barragán (2002), Rosenbusch (2003). Grünewald (2004). An example of the differences between the stress-crack width relationship obtained from cores drilled horizontally and vertically, respectively, can be seen in Fig. 4.8.

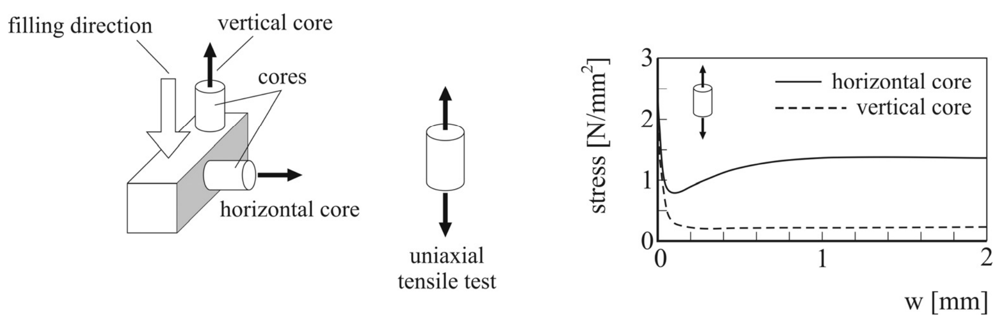

Fig. 4.8: Extraction of the cores and the stress-crack width responses of the cores in UTT [Barragán, 2002; Rosenbusch, 2003]

Toutlemonde (2004) investigated a tunnel segment made of SFRC and compared the stress-crack width relationships obtained from cores drilled at different places in the element. He observed a very large scatter in the stress-crack width relationships obtained from cores from different positions and directions (e.g. forces at 0.5 mm crack width varying from 1 to 30 kN in the same element), see Fig. 4.9.

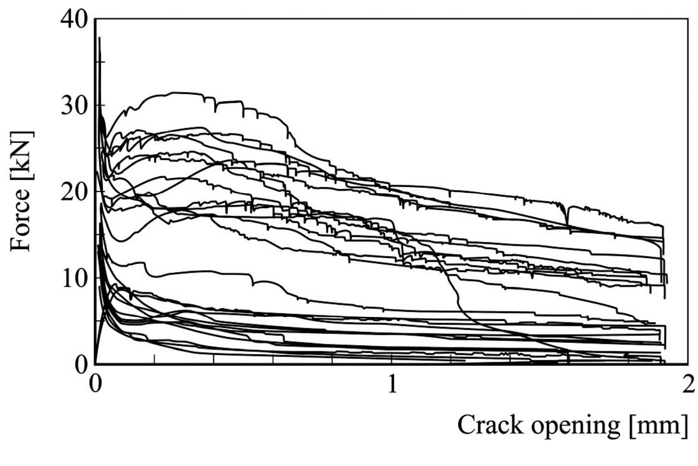

Fig. 4.9: Force-crack width relationships from cores drilled from a tunnel segment [Toutlemonde, 2004]

This large scatter due to the inhomogeneity in fiber distribution and orientation related to the casting process led Quiertant et al. (2001) to the conclusion that the fibers were unable to control the crack propagation and the post-cracking behavior in the investigated member, leading to failure in one major crack and brittle structural behavior.

An extreme example of the influence of the casting direction on the mechanical properties can be seen in Fig. 4.10. Note that this figure shows the test results of an ultra-high-performance concrete with smaller fibers than the hooked-end steel fibers usually referred to in this thesis.

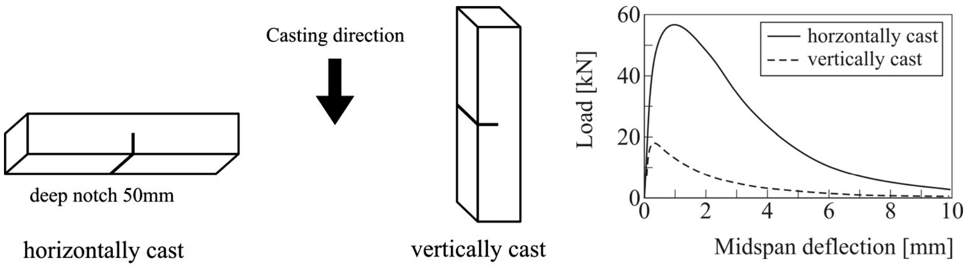

Fig. 4.10: Comparison of the load-deflection relationships for vertically and horizontally cast beams by averaged load-deflection curves [Stiel et al., 2004]

4.6 Modeling the Tensile Behavior

The model of Kützing (2000) describes the softening of SFRC. It takes into account the

- slope of the first branch observed in uniaxial tension tests
- fiber content (with no fibers as a lower boundary)
- fiber orientation
- bond properties of the fibers
- shape and maximum size of the aggregates.

Therefore, this model with some modifications described below is the most suitable for application in the calculation of the rotation capacity in chapter 6.

In the following sections, the original model is described and the modifications for calculating the bond behavior and the rotation capacity are motivated.

4.6.1 The Model of Kützing (2000)

The trilinear softening relationship proposed by Kützing (2000) was derived from direct tension tests on conventional normal and high strength concrete with a fiber content up to 120 kg/m^3. The relationship is divided into the three sections shown in Fig. 4.11.

In section I, the fibers are not active yet and the concrete contribution is responsible for the stress transfer. The concrete contribution is described by a formula developed by Remmel (1994). In section II, the matrix as well as the fibers carry the loads. With increasing crack width, the load bearing capacity of the concrete decreases. In section III, the fibers carry the load without any contribution of the concrete.

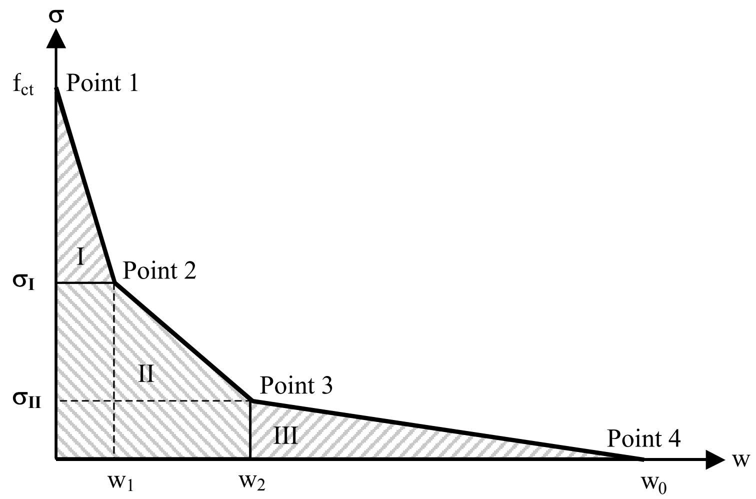

Fig. 4.11: Trilinear softening relationship for SFRC [Kützing, 2000]

The four points according to Fig. 4.11 can be calculated as described below. Point 1 is estimated as the uniaxial tensile strength of the concrete. It is calculated as:

$$f_{ct} = 2.12 \cdot \ln(1 + \frac{f_c}{10}) \tag{4.5}$$

with f_c being the cylinder compressive strength in N/mm^2. This relationship is valid for normal as well as for high strength concrete [Remmel, 1994].

Slipping of the fibers is assumed to start at a crack width w_I, which is fixed at 50 μm in the analyses. The stress at point 2 is calculated as follows:

$$\sigma_I = f_{t2} \cdot (1 - \frac{0.05}{w_2}) + \eta_{Vol\,SF} \cdot \eta_\theta \cdot \sigma_\tau \cdot (1 - \frac{0.05}{w_0}) \tag{4.6}$$

where:

f_{t2} [N/mm^2] =	$0.17\cdot(1+0.6\cdot f_{ct}) \leq 0.60$ for gravel with a maximum diameter of 8 mm
	$0.20\cdot(1+0.6\cdot f_{ct}) \leq 0.70$ for gravel with a maximum diameter of 16 mm
	$0.24\cdot(1+0.6\cdot f_{ct}) \leq 0.85$ for crushed aggregates
w_2 [mm] =	0.16 for round aggregates [Remmel, 1994]
$\eta_{Vol\,SF}$ [%]	volumetric fiber ratio
η_θ [-]	fiber orientation
	according to the definition of Schnütgen (1975) and Kützing (2000)
	$\eta_{3D} = 0.30$
	$\eta_{2D} = 0.45$

σ_τ [N/mm^2] the fiber stress during fiber pull-out, i.e. $\sigma_\tau = 4 \cdot \frac{w_0}{d_f} \cdot \tau_m = \frac{l_f}{d_f} \cdot \tau_m$

τ_m [N/mm^2] bond strength
w_0 [mm] average bond length of the hooked end fibers, i.e. approximately 0.25 times the fiber length
d_f [mm] fiber diameter
l_f [mm] fiber length

The stress at point 3 is calculated as:

$$\sigma_{II} = \eta_{VolSF} \cdot \eta_\theta \cdot \sigma_\tau \cdot (1 - \frac{w_2}{w_0}) \tag{4.7}$$

4.6.2 Modifications for the Application in SCSFRC

Tensile Strength

In the original model, the tensile strength of the concrete was calculated from the compressive cylinder strength. In our tests, the compressive strength was determined by cube tests. The cylinder strength is assumed to be 0.85 times the cube strength. In case of SCC, the tensile strength determined with the formula of Remmel (1994) is increased by 10%. This increase is based on the findings of Holschemacher (2001), who found increased spitting tensile strengths for SCC compared to conventional concrete of the same compressive strengths.

If splitting tensile tests were performed, the axial tensile strength was calculated from the splitting tensile strength by multiplying the splitting tensile strength of the plain concrete with the factor 0.9.

Fiber Orientation

The stress-crack width relationships according to the model of Kützing (2000) were first calculated for a 3D-orientation according to his definition of the fiber orientation and then multiplied by a factor accounting for the present fiber orientation. This factor was $\eta_\varphi / \eta_{\varphi 3D}$ with η_φ obtained from optical analysis or motivated assumptions based on boundary effects and fiber length.

Bilinear Model

In the trilinear model of Kützing (2000), the first branch represents the contribution of the concrete before the fibers are activated, the second branch represents the combined contribution of concrete and steel fibers and the third branch represents the fiber contribution. In the proposed modification, this relationship was simplified to a bilinear relationship by extending the first and third branch and calculating the intersection point, see Fig. 4.12. The post-peak ductility is slightly underestimated by this simplification but it is considered to be acceptable.

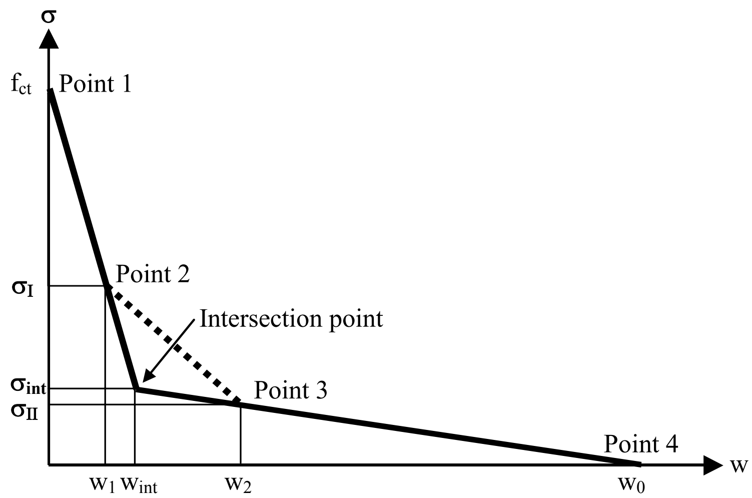

Fig. 4.12: Bilinear softening relationship for SFRC

The intersection points were calculated with equations (4.8) and (4.9). The values α_{FCM} and β_{FCM} are calculated with equations (4.10) and (4.11).

$$w_{\text{int}} = \frac{w_0 \cdot \dfrac{\sigma_{II}}{w_0 - w_2} - f_{ct}}{\dfrac{\sigma_{II}}{w_0 - w_2} - \dfrac{f_{ct} - \sigma_I}{w_1}} \tag{4.8}$$

where:
w_{int} [mm] crack width at the intersection point

$$\sigma_{\text{int}} = f_{ct} - \frac{f_{ct} - \sigma_I}{w_1} \cdot w_{\text{int}} \tag{4.9}$$

where:
σ_{int} [N/mm^2] stress at the intersection point

$$\alpha_{FCM} = \frac{w_{\text{int}}}{w_0} \tag{4.10}$$

$$\beta_{FCM} = \frac{\sigma_{\text{int}}}{f_{ct}} \tag{4.11}$$

The parameters for the stress- crack width relations are shown in Table 4.4 and Fig. 4.13. Furthermore, Fig. 4.13 shows the differences between the trilinear and the bilinear relationships. The tensile strengths were determined with equation (4.5) and then increased by 10%. The required cylinder strength was obtained by multiplying the compressive strengths found in cube tests (i.e. 55 N/mm^2 for the B45 and 115 N/mm^2 for the B105, see appendix C) with the factor 0.85. The other values were determined with equations (4.6) to (4.11).

Table 4.4: Parameters for concrete in tension

Parameter		B45.45/30.60	B45.45/30.120	B45.80/30.60	B105.80/30.60
f_{ct}	[N/mm^2]	4.05	4.05	4.05	5.54
α_{FCM}	[-]	0.0076	0.0077	0.0077	0.0075
β_{FCM}	[-]	0.09	0.18	0.16	0.20
w_0	[mm]	7.5	7.5	7.5	7.5
σ_I	[N/mm^2]	0.82	1.19	1.10	1.58
σ_{II}	[N/mm^2]	0.36	0.72	0.64	1.10
σ_{int}	[N/mm^2]	0.37	0.73	0.65	1.12
w_1	[mm]	0.05	0.05	0.05	0.05
w_2	[mm]	0.16	0.16	0.16	0.16
w_{int}	[mm]	0.057	0.058	0.058	0.056

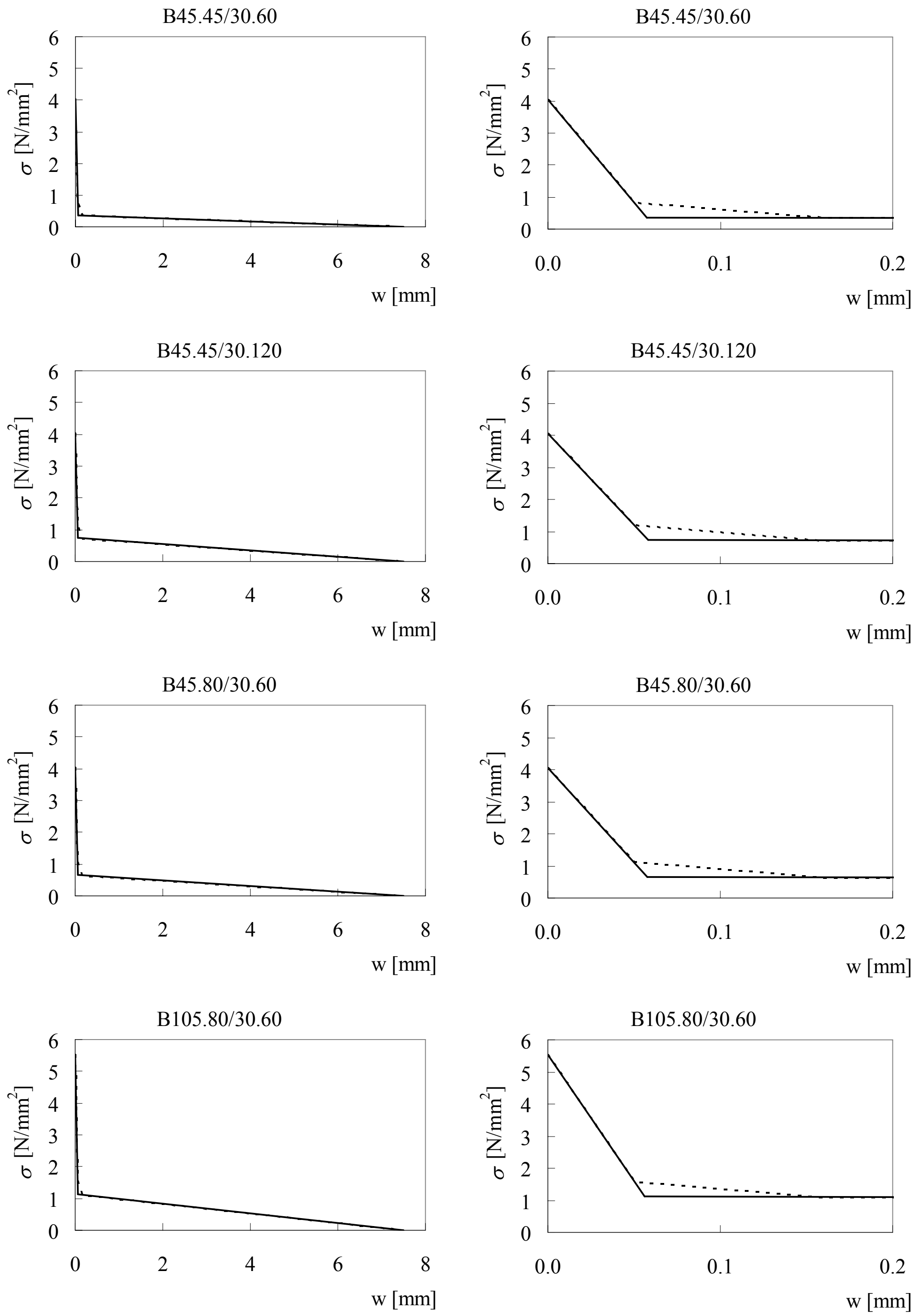

Fig. 4.13: Comparison of the trilinear softening model of Kützing (2000) (points) and the bilinear approximation (straight line) for different mixtures

4.7 Concluding Remarks

The tensile properties of concrete can be determined with different kinds of tests. The main categories include bending, splitting, uniaxial tensile and punching tests. Relationships derived by inverse analysis of bending tests can significantly differ from relationships observed in uniaxial tensile tests of the same mixtures. The reasons for these differences can be sought in the different fiber distribution and orientation in the bending tests compared to the uniaxial tensile tests with respect to the main tensile loading.

The modified model of Kützing (2000) will be used for calculating the bond behavior and the rotation capacity in the following chapters. It was adapted with regard to axial tensile strength (depending on the mixture and not necessarily on the compressive strength), fiber orientation, and complexity (bilinear instead of trilinear relationship).

The stress-crack width relationship is not a pure material property but depends on boundary conditions such as specimen size, strain gradient, wall effects, direction of load application, casting direction etc. The variation of the distribution and the orientation of the fibers within the specimens leads to variations in the stress-crack width relationship within the specimens. There can be a large scatter in fiber distribution and orientation due to the influence of the casting process. This needs to be taken into account when modeling the cracking behavior of SFRC.

5 Bond Behavior of Ribbed Bars in Concrete

5.1 Introduction

The bond behavior of ribbed bars in conventional concrete is thoroughly described in earlier publications by other authors, e.g. *fib* bulletin 1 (1999), *fib* bulletin 10 (2000), Bigaj (1999), Noghabai (1998), and Alvarez (1998). In the scope of this thesis, the bond model of Den Uijl & Bigaj (1996) was extended to SCSFRC.

In this chapter, definitions and some general remarks on the bond behavior of ribbed bars in concrete are given (section 5.2). The bond model of Den Uijl & Bigaj (1996) is summarized in section 5.2.4. A literature survey on the effect of fibers on the bond behavior of ribbed bars in concrete is presented in section 5.3. The numerical simulation of the confinement capacity is described in section 5.4. A proposal for the modification of the bond model of Den Uijl & Bigaj (1996) to SFRC is given in section 5.4.2. The performed pull-out tests are described and evaluated in section 5.5. The proposed bond model is verified against experimental results in section 5.6. Finally, concluding remarks are given in section 5.7.

5.2 Bond of Ribbed Bars in Plain Concrete

5.2.1 Definitions

In the following sections, frequently used terms are defined. It is noted that when talking about bond in the scope of this chapter, the bond of ribbed steel bars used as tensile reinforcement is meant, unless indicated differently.

Adhesion

Adhesion is the bond between steel and concrete caused by chemical and physical effects. No slip between steel and concrete occurs unless the adhesion is destroyed by bond stresses exceeding the threshold value. Failure of the adhesive bond occurs at very small displacements. Therefore adhesion plays a minor role in the bond behavior of ribbed bars [*fib* bulletin 1, 1999].

Rib Bearing and Wedging Action

After breaking of the adhesive bond, the force transfer is mainly governed by bearing of the ribs against the concrete. This evokes the so-called wedging effect. Concentrated forces in front of the ribs cause cone-shaped cracks starting from the top of the ribs, see Fig. 5.1 (left).

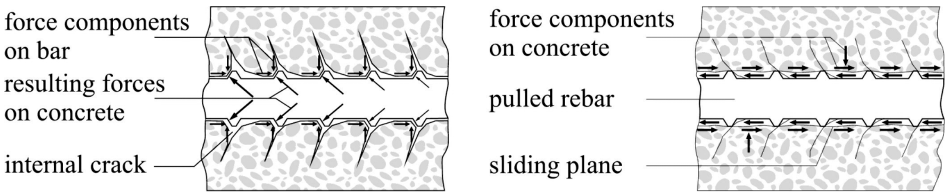

Fig. 5.1: Splitting failure (left) [after: Goto, 1971] and pull-out failure after formation of a sliding plane (right) [Den Uijl & Bigaj, 1996]

The concrete keys between the ribs transfer the forces into the surrounding concrete. The keys are bent and at higher bond stresses, the concrete in front of the ribs is crushed. The resulting forces on the concrete can be decomposed into components parallel to the bar axis and perpendicular to it. The sum of the parallel components equals the bond force. The perpendicular components induce circumferential tensile stresses in the surrounding concrete, which can result in radial cracks.

It is noted that even if there are no splitting cracks visible on the surface of the member, splitting cracks can often be found in the vicinity of the bar.

Friction

In case of pull-out failure, the concrete keys are sheared off and a sliding plane around the bar is created. The force transfer mechanism changes from rib bearing to friction of the cylindrical sliding plane. The magnitude of the friction is governed by the geometrical and material properties of the reinforcing bar and the concrete and possibly by confinement. If the loading is continued the sliding plane is smoothened due to wear and compaction of the concrete.

Passive Confinement

Passive confinement is generated by the concrete around a bar (effective cover, tensile properties) and, if present, by transverse reinforcement. The effectiveness of passive confinement depends on the mode of the force transfer. For rib bearing, the increase of the bond strength is proportional to the confining stress generated by the surrounding concrete and the transverse reinforcement. For friction, the bond strength cannot be further increased by the provided passive confinement.

Active Confinement

Active confinement results from loads transverse to the bar. Active confinement increases the bond strength both for rib bearing and for friction. It is noted that the presence of tensile stresses perpendicular to the bar may result in a negative contribution to the confinement and may therefore cause a decrease in bond strength.

Failure Modes

Two types of bond failure can be distinguished: splitting failure and pull-out failure. The force transfer of the steel into the concrete is illustrated in Fig. 5.1 for both failure modes. The failure mode depends on the confinement provided by the surrounding concrete, confining reinforcement and external pressure. For given bar geometry and mechanical characteristics, when no active confinement is provided in the structure, the bond failure mode depends on the (effective) concrete cover thickness [Bigaj, 1999]. Fig. 5.2 shows the different failure patterns (steel bars and the concrete after failure) for both failure modes. In case of pull-out failure, wear of the concrete is clearly visible on the bottom picture, which is not the case for splitting failure. The different failure modes lead to different types of response in the bond stress-slip relationships.

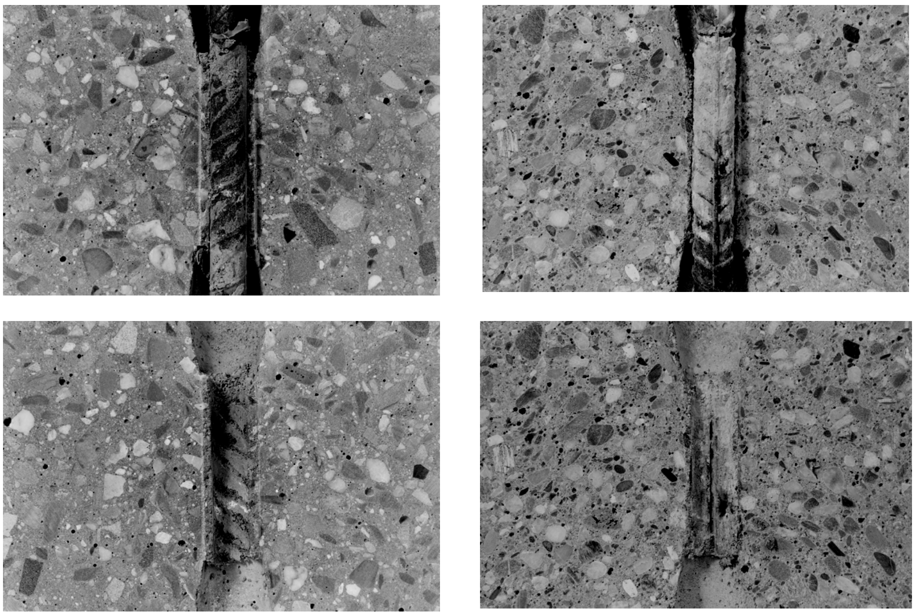

Fig. 5.2: Rebar and concrete after splitting failure (left) and pull-out failure (right) [Sule, 2003]

Splitting Failure

If the radial cracks propagate through the entire concrete cover they will be visible as splitting cracks at the concrete surface. The maximum bond stress follows from the maximum possible confinement provided by the surrounding concrete. The bond stress drops suddenly after the first splitting crack has been formed. The load bearing mechanism remains generally the same, i.e. bearing of the ribs against the concrete and wedging action govern the bond behavior.

Pull-Out Failure

When the confinement capacity is large enough to prevent the growth of the radial cracks throughout the entire concrete cover, the bar is pulled out of the concrete. The concrete keys are sheared off and a sliding plane around the bar is created. The influence of rib height and rib distance on the shearing off of the concrete corbels is described in Rehm (1961). After shearing off of the concrete keys, the force transfer mechanism changes from rib bearing to friction of the cylindrical sliding plane. Contraction of the reinforcing bar results in a reduction of the radial compressive stress. In particular, contraction of the bar after yielding results in a considerable reduction of the radial stress and a reduction of the bond strength for pull-out failure [Bigaj, 1999].

5.2.2 Influencing Factors

The main influencing factors on the bond behavior, in particular strength, stiffness, ductility and failure mode, are summarized in *fib* bulletin 1 (1999) and *fib* bulletin 10 (2000). A general bond model shall capture the effect of these factors. The most important influencing factors are:

- mechanical properties of steel and concrete
- bar surface geometry
- bar diameter
- concrete cover thickness
- position of the bar during casting
- state of stress in the bar
- state of stress in the surrounding concrete
- boundary restraint.

Other influencing factors include [*fib* bulletin 1, 1999; *fib* bulletin 10, 2000]:

- active (loading) and passive (reinforcement) confinement
- concrete ductility (matrix quality)
- load-time history / fatigue behavior
- environmental effects (rust, steel corrosion, temperature of the environment)
- maximum aggregate size
- bar spacing
- embedment length.

Concerning the scope of this thesis, the influence of the concrete properties on the bond behavior are particularly relevant. The effect of the self compaction of the concrete on the bond strength is reported contradictory in literature [König et al., 2003]. The results ranged from lower bond strength for SCC over similar bond strength up to higher bond strength compared to conventional concrete. The influence of the rebar position (casting and loading in the same direction, opposite or perpendicular) on the bond strength and on the bond ductility was reported to be less pronounced in SCC than in conventional concrete [König et al., 2003].

König et al. (2003) reported a higher initial bond stiffness and a more ductile bond behavior of SCC. As SCC has a larger splitting tensile strength than conventional concrete of the same compressive strength [Holschemacher, 2001], splitting failure is less likely to occur.

The influence of steel fibers on the bond behavior will be discussed later in this chapter.

5.2.3 General Bond Models Based on the Hydraulic-Pressure Analogy

An overview over existing models for bond can be found in *fib* bulletin 10 (2000) or in Noghabai (1995). In particular, the models based on the hydraulic-pressure analogy will be discussed here because a similar type of modeling will be proposed in this thesis for SCSFRC.

Tepfers (1979) described the resulting forces from the rib bearing in an anchorage zone with the so-called thick-walled-cylinder model. According to this approach, the bond forces can be subdivided into radial (σ_r) and tangential (τ) components. The radial components are in balance with the tangential tensile stresses σ_t. The radial compressive stresses can be regarded as a hydraulic pressure p_b inside a thick-walled cylinder. The angle θ (see Fig. 5.3) depends on the geometrical properties of the ribs, on the additional confinement and on the chosen confinement model.

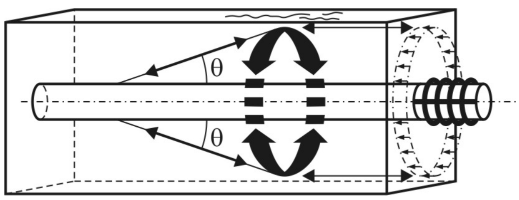

Fig. 5.3: Schematic representation of how the radial components of the bond forces are balanced against tensile stress rings in the concrete in an anchorage zone [Tepfers, 1979]

According to Tepfers (1979), the bond resistance can be calculated as:

$$\tau_b = \sigma_r / \tan\theta \tag{5.1}$$

Tepfers (1979) gave a lower bound solution assuming that cracking occurs in a perfectly brittle material with elastic material behavior and an upper bound solution assuming plastic material behavior of concrete. To describe bond failure more realistically, Tepfers (1979) also assumed a partly-cracked-elastic concrete ring. Most test results lay between the partly-cracked-elastic and the plastic solution (Tepfers, 1979).

More advanced models based on the hydraulic-pressure analogy, e.g. Van der Veen (1990), Rosati and Schumm (1992), Gambarova et al. (1994), Noghabai (1995), or Den Uijl & Bigaj (1996), include the softening behavior of concrete in the partly-cracked-elastic stage. Only the model of Den Uijl & Bigaj (1996) also considers the radial deformations of both, the steel and the concrete ring.

5.2.4 The Bond Model of Den Uijl & Bigaj (1996)

The bond model of Den Uijl & Bigaj is thoroughly described in Den Uijl & Bigaj (1996) and Bigaj (1999). It is a general bond model for ribbed bars based on concrete confinement delivered by the concrete surrounding the reinforcing bar. The model takes into account the:

- bond failure mode
- mechanisms of force transfer from the ribbed bar to the surrounding concrete
- capacity of the concrete to resist radial forces, i.e. the confinement capacity
- concrete compressive strength
- concrete toughness
- state of stresses and contraction of reinforcement (which is especially important after yielding)
- bar diameter and geometry
- member geometry
- boundary effects (e.g. cone pull-out).

Limitations of the Model

The model does not directly take into account:

- active confinement
- additional passive confinement, e.g. given by transverse reinforcement
- variation of the rib geometry
- variation of the effective rib area f_R.

These latter aspects are included in a more recent extension of this model by Mayer (2002).

Input for the Model [Bigaj, 1999]

Input parameters for the bond model of Den Uijl & Bigaj are:

- steel characteristics
- concrete characteristics
- rebar geometry (bar diameter and rib distance)
- concrete cover thickness and bar spacing (effective cover).

Calculation of the Confinement Capacity

The confinement capacity plays a decisive role for the ultimate bond resistance and the mode of bond failure [Bigaj, 1999]. The model is based on the radial stress versus radial displacement relationship at the interface, which is subdivided into three stages [Bigaj, 1999], see Fig. 5.4.

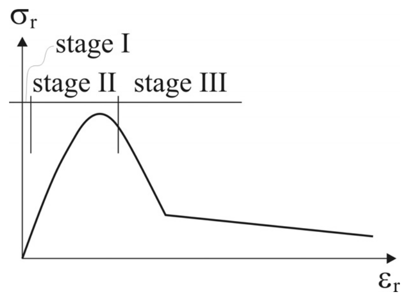

Fig. 5.4: Confining capacity estimated with the thick-walled-cylinder model (stage I: uncracked, stage II: partially cracked, stage III: entirely cracked) [Bigaj, 1999]

In stage I, the tangential tensile stress at the interface reaches the concrete tensile strength. In stage II, radial cracks start at the interface between concrete and steel and grow through the concrete cover. In stage III, the cracks open further. The concrete is considered entirely cracked. The further behavior depends on the bond failure mechanism, which is decisively influenced by the concrete confinement capacity [Bigaj, 1999]. In case of splitting failure (see section 5.2.1), the load bearing mechanism remains generally the same as in stage II. The Poisson effect as well as wear and compaction are considered negligible in case of splitting failure. In case of pull-out failure, the failure mechanism changes from bearing of the ribs into friction (see section 5.2.1). The Poisson effect as well as wear and compaction of the sliding plane cannot be neglected then, especially when the steel yields. In the model, the displacement of a ribbed bar is conceived as the displacement of a conical bar in the concrete, see Fig. 5.5. The transition of the cone bearing mechanism into the frictional mechanism occurring in case of pull-out failure is accounted for by a reduction of the cone angle φ.

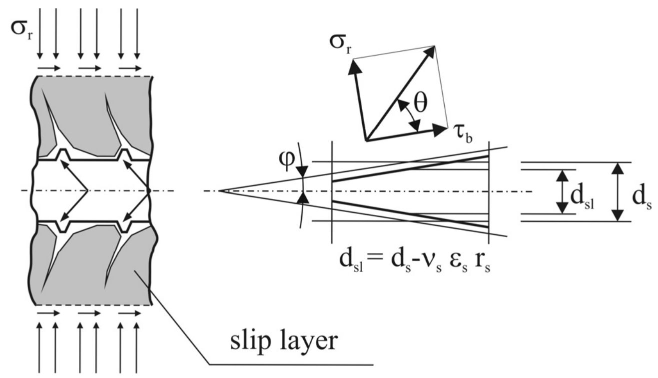

Fig. 5.5: Bond model formulation – modeling steps [Bigaj, 1999]

Effective concrete cover c_{eff}

The wall thickness of the concrete ring is equal to the effective concrete cover thickness c_{eff},. The effective concrete cover c_{eff} is calculated according to Bigaj (1999) as:

$$c_{eff} = \frac{1}{m}\sum_{i=1}^{m}[c_i \chi(c_i) + c_{eff,\max}(1-\chi(c_i))] \tag{5.2}$$

where:

- c_{eff} effective concrete cover
- $c_{eff,max}$ maximum effective concrete cover to be taken into account
- m number of equally spaced directions to be taken into account, here m = 4
- c_i cover thickness in any of the m directions
- $\chi(c_i)$ indicator function, defined as $\chi(c_i) = 1$ if $c_i \leq c_{eff,max}$ and $\chi(c_i) = 0$ if $c_i > c_{eff,max}$

The maximum effective concrete cover is defined as:

$$c_{eff,\max} = \frac{c_{i,\min} + r_s}{\cos(\alpha_s)} - r_s \tag{5.3}$$

where:

- $c_{i,min}$ smallest concrete cover to be taken into account
- α_s angle between the critical splitting plane and normal to the closest concrete surface (α_s = 45-60º)
- r_s bar radius

The effective concrete cover, the cover thickness in the different directions and the angle between the critical splitting plane and normal to the closest concrete cover are shown in Fig. 5.6. If the effective concrete cover is equal to or larger than 3.0 d_s pull-out failure is expected for concrete without fibers.

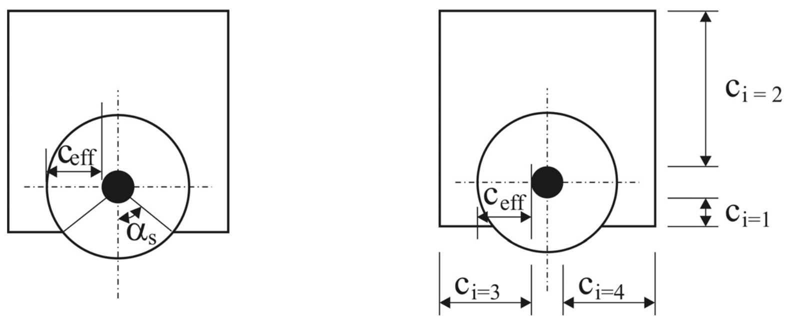

Fig. 5.6: Illustration of the concrete covers and the angle α_s

Relationship between slip δ and radial stress σ_r

Practically, in case of splitting failure the cone angle remains the same and the entire confinement capacity curve (Fig. 5.7 left) is followed. In case of pull-out failure, the reduction of the cone angle results in only partially following the ascending branch of the confinement capacity curve (Fig. 5.7 right), first following it upward and then downward. The calculation procedure of the curves in Fig. 5.7 is given in Den Uijl & Bigaj (1996) and Bigaj (1999).

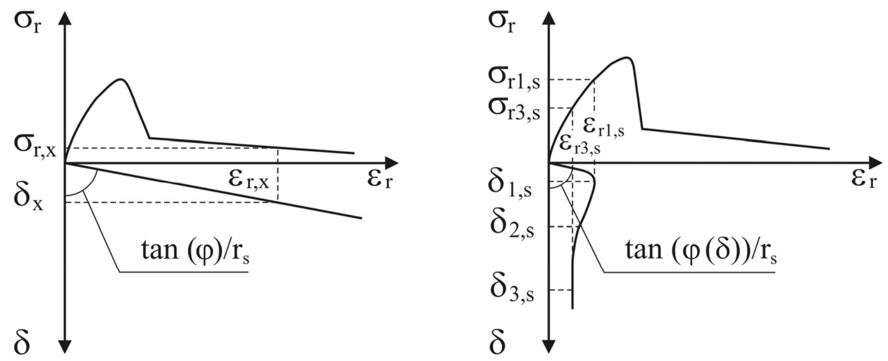

Fig. 5.7: Relationship between slip δ and radial stress σ_r for splitting bond failure (left) and for pull-out bond failure (right) [Bigaj, 1999]

The bond stress τ_b can be calculated from the radial compressive stress by:

$$\tau_b = \sigma_r \cot(\theta) \qquad [\text{N/mm}^2] \qquad (5.4)$$

where:

$\cot(\theta)$ coefficient of friction [-]

σ_r response of the surrounding concrete to the radial displacement of the interface [N/mm^2]

Calculation of the Transmission Length L_t

The transmission length L_t is defined as the length required to develop the concrete tensile strength in a cross-section. The steel and concrete stress development along the transmission length depends on the bond between steel and concrete. The differential equation of bond is solved with finite difference calculations. This procedure is done in the following steps. In the model, the transmission length is subdivided into 50 elements with a finite length Δx. Such an element is shown in Fig. 5.8.

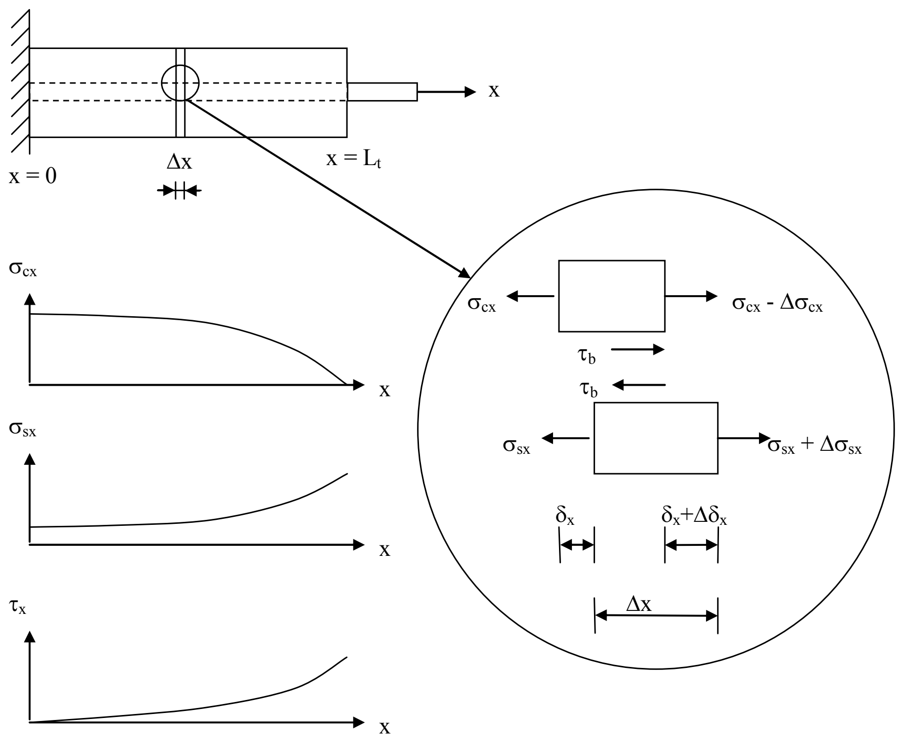

Fig. 5.8: Equilibrium of stresses in a bar element and concrete stresses, steel stresses and bond stresses along the transmission length

The boundary conditions are:

- The total force along the transmission length is constant.
- The slip δ_x at the beginning of the transmission length (x = 0) is zero.
- The concrete stress at the beginning of the transmission length (x = 0) is equal to the uniaxial tensile strength.
- The concrete stress at the end of the transmission length ($x = L_t$) is equal to zero for conventional concrete.

The total force T in the tensile member is calculated as:

$$T = f_{ct}\, A_{c,eff}\, (1 + n_E\, \omega_s) \tag{5.5}$$

where:

T	Total force in the tensile member [N]
f_{ct}	Concrete tensile strength [N/mm^2]
$A_{c,eff}$	Effective concrete area [mm^2]
n_E	Ratio of the E-moduli of steel and concrete E_s / E_c [-]
ω_s	Mechanical reinforcement ratio [-]

Equilibrium of forces and compatibility of deformations has to be satisfied in each element. The steel stress at position x = 0 is calculated as:

$$\sigma_{s,0} = f_{ct} \cdot \frac{E_s}{E_c} \tag{5.6}$$

From the steel and concrete stresses, the elongations of the steel and the concrete can be calculated. The increase in slip over the element can be calculated as:

$$\Delta\delta_x = \varepsilon_{sx} \cdot \Delta x - \varepsilon_{cx} \cdot \Delta x \tag{5.7}$$

where:

ε_{sx}	steel strain
ε_{cx}	concrete strain

The bond stress τ_b is derived from the slip δ_x and the steel strain. With this bond stress, the differences in steel and concrete stresses can be calculated, using the equilibrium of forces. The increase of the steel stress can be calculated by:

$$\Delta\sigma_{sx} = \frac{\tau_b \cdot U_s \cdot \Delta_x}{A_s} \tag{5.8}$$

where:

$\Delta\sigma_{sx}$	change in steel stress
τ_b	bond stress
U_s	circumference of the reinforcing bar
A_s	cross-section of the reinforcing bar

As the steel stress is increased, the concrete stress is decreased:

$$\Delta\sigma_{cx} = \frac{\tau_b \cdot U_s \cdot \Delta_x}{A_c} \tag{5.9}$$

where:

$\Delta\sigma_{cx}$	change in concrete stress

In the iterative calculation procedure, the transmission length is computed when the solution satisfies the boundary conditions. The slip at the end of the transmission length follows from the integration of the differences of steel and concrete strains.

Calculation of the Average Crack Distance s_{cr}

For a fully developed crack pattern, the average crack distance s_{cr} is assumed to be 1.3 times the transmission length. This factor was derived by Kreller (1989) and Bigaj (1999) for members in bending.

Calculation of Stress and Strain Distribution in an Element between Two Subsequent Cracks

As in the calculation of the transmission length, the differential equation of bond in the calculation of the stress and strain distribution in an element between two subsequent cracks is performed with finite difference calculus. The steel strain at the beginning of the element between two subsequent cracks is given as input. The boundary conditions are:

- The total force along the tensile element is constant.
- The concrete stress at the beginning and at the end of the element between two subsequent cracks is equal to zero for conventional concrete.

In the iterative calculation procedure, the slip is altered until the boundary conditions are met.

5.3 Bond of Ribbed Bars in a SFRC Matrix

5.3.1 General Considerations

In order to investigate the effect of steel fibers on the bond behavior, it is useful to take an indirect approach and analyze in how far steel fibers affect the major influencing factors on bond behavior.

The steel fibers are expected to affect the concrete properties (and therefore the confinement capacity) as well as the behavior of the boundary (cone pull-out, which can be prevented or retarded by fibers crossing the cracks). The influence of steel fibers on the bond behavior is schematically illustrated in Fig. 5.9.

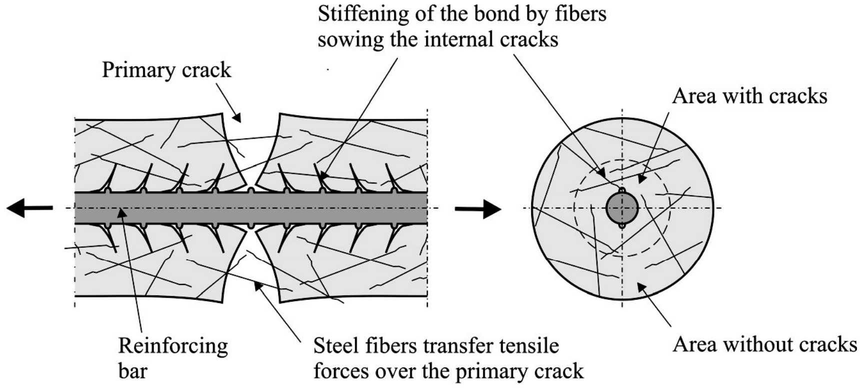

Fig. 5.9: Steel fibers in a cracked concrete cross-section [Hartwich, 1986; Pfyl, 2003]

As can be seen in Fig. 5.9, the steel fibers bridge the internal cracks, which form at small displacements when the ribs bear against the concrete [Pfyl, 2003]. Splitting cracks along the bar occur if the confinement capacity of the concrete around the bar is exceeded due to too large tangential stresses caused by the wedging effect of the displaced bar. Also these cracks can be bridged by the fibers.

The magnitude of the force transmitted by a steel fiber depends on the bond between fiber and matrix, the concrete tensile strength, the shape of the fiber ends, the fiber tensile strength, and the fiber geometry (see Marković et al., 2002; Van Gysel, 2000; Pfyl, 2003).

The bond strength of a single fiber can be assumed based on experiments reported in literature (e.g. Kützing, 2000) or determined in tests. Single fiber pull-out tests on the mixtures used in the scope of this research were performed by Marković et al. (2002).

As always in SFRC, the fiber distribution and orientation also have to be considered when it comes to bond behavior. Unintentional fiber concentrations or a certain fiber orientation due to e.g. wall effects or disturbances lead to significantly different material behavior. The scatter of the results increases with increasing fiber size and the workability and compactability of the concrete also influence the bond behavior [Bigaj-van Vliet, 2001].

In order to extend the bond model of Den Uijl & Bigaj to the bond of reinforcing bars in SFRC, the effect of fibers on the bond stress–slip relationship and on the behavior of tensile elements (i.e. concentrically loaded reinforced concrete tensile bars) needs to be investigated. Literature provides a range of data on both. The results of a literature survey are presented in the following section.

5.3.2 Literature Survey

A thorough survey of existing literature about the bond of ribbed reinforcing steel bars embedded in SFRC was carried out by Bigaj-van Vliet (2001). For pull-out tests with a short embedment length she summarized existing literature on the effect of fiber volume, bar diameter, concrete cover thickness, fiber shape, bar position, bar geometry, matrix strength, embedment length, confinement on bond strength, bond stiffness, bond ductility and failure propagation, and structural response. For tensile element tests, evidences were summarized with regard to the effect of fiber volume, fiber shape, matrix strength on the tension stiffening effect, failure propagation, and structural response. For beam tests, the results of Harajli (1992) on the effect of specimen type on bond ductility were reviewed. Noghabai (1998) reported about tests on thick-walled concrete rings, tie elements and beams on normal and high strength concretes with four types of steel fibers.

Table 5.1 shows the effect of the addition of hooked-end steel wire fibers to conventional concrete on the bond strength, bond stiffness and bond ductility in the case of splitting or pull-out failure. The following symbols will be used to indicate the tendencies the researchers found for an increased fiber volume fraction for the parameters they investigated:

- ++ significantly increased
- \+ increased
- 0 no pronounced difference
- nc no clear agreement
- na not available

Table 5.1: Summary of the influence of the addition of hooked-end steel fibers on the bond behavior

		Bond properties at						
		splitting failure			pull-out failure			
Researcher	Year	strength	stiffness	ductility	strength	stiffness	ductility	likeliness of pull-out failure
Hartwich	1986	++	0	++	0	0	++	0
Samen Ezeldin & Balaguru	1989/90	++	0	+	0	na	+	na
Harajli	1992	na	na	na	+	+	+	na
Soroushian et al.	1994	na	na	na	+	+	+	na
Harajli et al.	1995	0	na	+	na	na	na	na
Hota & Naaman	1997	+	0	+	na	na	na	na
Plizzari	1999	+	+	+	+	na	+	na
De Bonte	2000	0	0	+	+	0	0	na
Literature survey Bigaj-van Vliet (summary of the above)	2001	+	nc	+	nc	nc	nc	0
Dupont et al.	2002	na	0	+	+	0	+	na
Plizzari et al.	2002	+	na	+	na	na	na	na
Weiße NSC	2002	0	0	+	0	0	0	+
Weiße HSC	2002	+	0	++	na	na	na	na
Pfyl	2003	na	na	na	na	+	na	na

It is noted that the specimen geometry and way of manufacturing were different or often not well reported in the literature and that these factors play an important role for fiber distribution and fiber orientation and thus for the tensile properties of the concrete. The existing studies on the effect of hooked-end steel fibers on the bond behavior of ribbed bars in concrete are hardly comparable due to variations in mechanical and geometrical bar, steel fiber and concrete matrix properties and partly reported contradictory results. Therefore, it was decided to systematically investigate the influence of the addition of different kinds and amounts of steel fibers on the local bond behavior of ribbed bars in SCC.

5.4 Modeling Bond Behavior of Ribbed Bars in SCSFRC

5.4.1 Numerical Simulation of the Confinement Capacity

Problem Statement

The fibers were not uniformly distributed in the specimens (see section 5.5.3). It was therefore questioned whether the confinement capacity could be increased due to fiber addition even if there were only a few fibers in the cover. In order to investigate this phenomenon, a numerical simulation of the confinement capacity was carried out.

Numerical Model

In order to investigate the influence of the fiber distribution around a bar on the bond behavior, 2D non-linear simulations were carried out with the FE program ATENA (Červenka Consulting, Prague). The model includes a 10 mm steel bar (region 1) a 1 mm thick boundary layer (region 2) and two concrete regions around the bar, see Fig. 5.10 (left). The boundary between region 3 (concrete cover) and 4 (bulk) was arbitrarily chosen as the line from the center of the bar to a point 20 mm from the symmetry line on the edge of the specimen.

The following concrete properties were assumed:

- cube compressive strength 50 N/mm^2,
- tensile strength 3.3 N/mm^2 and
- fracture energy 100 N/m for the reference mixture (further indicated as mixture A),
- fracture energy 1000 N/m for fiber mixture 1 (further indicated as mixture B) and
- fracture energy 2000 N/m for fiber mixture 2 (further indicated as mixture C).

The latter values were estimated on the basis of a trilinear softening behavior developed by Kützing (2000) for the mixtures used in the pull-out tests. The boundary layer indicated by area 2 in Fig. 5.10 had the same compressive strength as the concrete indicated by area 3 and 4, but a very low tensile strength and fracture energy. The loading consisted of gradually increasing the bar diameter and thus simulating the wedging effect.

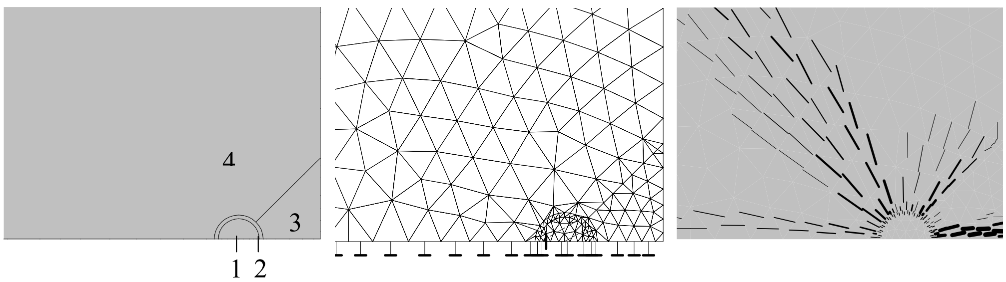

Fig. 5.10: left: overview over the areas with different material properties in the FE simulations
middle: FE net and boundary conditions
right: cracks > 0.001 mm

Results of the Numerical Simulation

The stress presented in Fig. 5.11 and in Fig. 5.12 is the average stress at the section in the middle of the steel bar as a function of the expansion of the bar. The identification in the figures, e.g. c15AA, indicates concrete cover thickness, fracture energy of the bulk and fracture energy of the cover. The fracture energies of the bulk and the cover are indicated by the mixture abbreviations A, B, and C.

c15AA
- G_f cover
- G_f bulk
- cover thickness

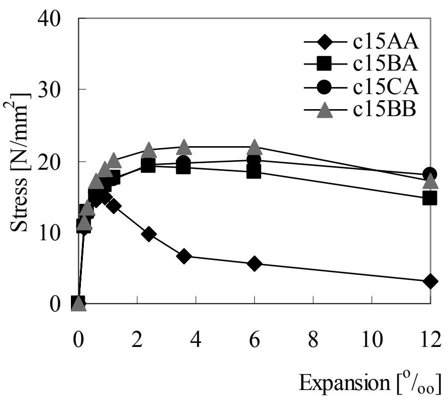

Fig. 5.11: Confinement capacity simulation for a concrete cover of 15 mm

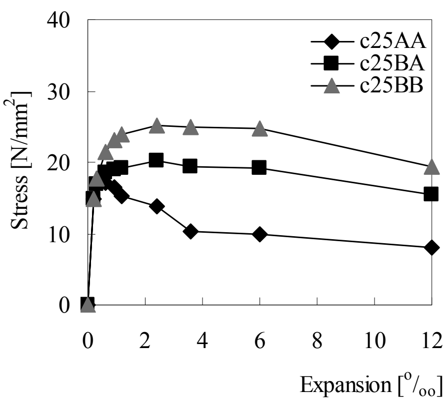

Fig. 5.12: Confinement capacity simulation for a concrete cover of 25 mm

From Fig. 5.11 and Fig. 5.12, it can be seen that the fibers in the bulk (area 4 in Fig. 5.10) are mainly responsible for the increase in confining capacity. Contrary to what might have been expected, the fibers in the bulk cause a significant increase in confining capacity, even if there are no fibers present in the concrete cover (area 3 in Fig. 5.10). The increase in splitting resistance due to the addition of fibers in the bulk is more pronounced for a concrete cover of 15 mm than for a concrete cover of 25 mm. The fibers present in the concrete cover cause a further increase in confinement capacity, see Fig. 5.11 and Fig. 5.12. The increase is more pronounced for the larger concrete cover as a larger area is influenced by the addition of fibers.

Conclusion

The confinement capacity is increased due to fiber addition, even if only few fibers are present in the concrete cover region.

5.4.2 Modification of the model of Den Uijl & Bigaj for SCSFRC

The changes and extensions that need to be made in order to use the bond model of Den Uijl & Bigaj (1996) for SCSFRC are described in the following. Some of the input parameters of the existing bond model have to be adapted to the material properties of SCSFRC in order to simulate the bond behavior of the SCSFRC specimens. The model itself was also adapted to account for stress transfer across the primary crack in SCSFRC.

For the practical application of the present research project, i.e. tunneling, pull-out failure is expected to be relevant because of the small bar diameters and the large concrete covers used ($c_{eff}/d_s \geq 3.0$), which result in a sufficiently large confinement capacity to prevent splitting failure. The extension of the model for SCSFRC is valid for pull-out bond failure.

Concrete Behavior in Tension (Parameters w_0, α_{FCM} and β_{FCM})

As the post-cracking tensile properties of concrete change significantly due to fiber addition, the input values for w_0, α_{FCM} and β_{FCM} need to be changed in the model to reflect the material properties of SFRC in uniaxial tension. As explained in chapter 4, the properties of SCSFRC in uniaxial tension can be derived from uniaxial tensile tests or from an inverse analysis of three-point bending or wedge splitting tests. The input values are illustrated in Fig. 5.13.

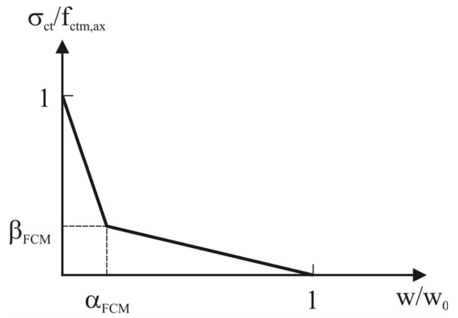

Fig. 5.13: Bilinear tensile softening relationship for concrete in tension [Den Uijl & Bigaj, 1996]

In the model of Den Uijl & Bigaj, w_0 is assumed to be 0.2 mm, α_{FCM} was fixed at 0.14 and β_{FCM} at approximately 0.25, depending on the concrete strength [Bigaj, 1999]. For SCC, the same values as for plain regular concrete are taken, i.e. w_0 is assumed to be 0.2 mm, α_{FCM} to 0.14 and β_{FCM} to approximately 0.25. For SCSFRC, the relation presented in chapter 4.6 is used (modified relation of Kützing, 2000).

SFRC is be anisotropic due to heterogeneous fiber distribution and orientation (see section 4.5). The stress-crack width relationship that is relevant for the confinement capacity around the steel bar can be significantly different from the stress-crack width relationship relevant for transferring forces across the cracks in other regions of the structural members [Rosenbusch, 2003].

Hence, the model of the post-cracking behavior of SFRC in tension used for estimating the confinement capacity may be different from the model used for assessing the force transfer over the primary cracks (see section 4.5). In this respect it should also be noticed that while the confinement capacity can best be captured with average material properties around the bar, primary cracks along the bar occur at the weakest cross-section. In the following, the model for the post-cracking behavior of SFRC in tension is discussed, which is found suitable for the estimation of the confinement capacity. The model used for assessing the force transfer across the primary cracks in case of SFRC will be discussed in section 5.6.2 and Table 5.10.

It should be realized that changing the tensile softening parameters w_0, α_{FCM} and β_{FCM} has no effect on the bond stress-slip relationship obtained with the bond model of Den Uijl & Bigaj in case of pull-out failure, but it does influence the results in case of splitting failure.

Threshold Value τ_{b1}

As it is less likely to have splitting failure when self-compacting concrete is used because it has a larger tensile splitting strength than regular plain concrete, the criterion for splitting occurrence needs to be modified. In the existing model for plain concrete, this criterion is given by the critical bond stress τ_{b1} being five times the concrete tensile strength [Bigaj, 1999]. If the ratio τ_{b1}/f_{ct} increases it is more likely that pull-out failure occurs. As will be further discussed in section 5.6.1 an increase of τ_{b1} by 5% was considered for SCC.

Number of Radial Cracks n_{rad}

In the existing model, good simulation results for conventional concrete were obtained with the number of radial cracks fixed to three [Bigaj, 1999]. Research by Noghabai (1998) showed that in NSC as well as HSC the number of radial cracks can be two or more. For SFRC, it is likely that the number of radial cracks is larger than for conventional concrete. However, as a first approximation, because of the pronounced softening behavior of the SCSFRC used in the tests, no modifications were made with regard to the number of cracks.

Concrete Cone Pull-Out

It is assumed that in case of plain concrete, a cone-shaped part of the concrete breaks off at the point where the bar reaches the concrete surface or the primary cracks. The contribution of the fibers is indicated in Fig. 5.9. The phenomenon is described for plain concrete in *fib* bulletin 1 (1999). In the bond model of Den Uijl & Bigaj (1996), this phenomenon is captured by reducing the effective concrete cover in the vicinity of the loaded ends depending on an angle ψ_{cpo}, which is assumed to be 40° for plain concrete, see Fig. 5.14.

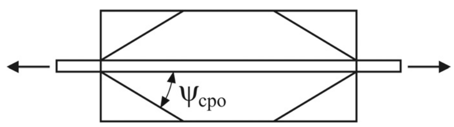

Fig. 5.14: Definition of the angle ψ_{cpo}

It is assumed for SFRC that the outbreaking plane (cone pull-out) is less pronounced or even not present at all because the fibers bridge the cracks and keep the concrete together. Therefore, the angle ψ_{cpo} is increased to 89°. An upper boundary would be 90°, which indicates no cone pull-out at all. For numerical stability, this case is calculated with an angle of 89°.

Stress Transfer across the Primary Cracks

One of the main differences between the cracking behavior of plain concrete and SFRC is that in the latter case stresses are transmitted across the cracks by the fibers, whereas the post-cracking strength of conventional concrete is zero for crack widths larger than 0.2 mm. This phenomenon is illustrated in Fig. 5.15 and Fig. 5.16. The magnitude of the stress that is transmitted across the crack by the steel fibers (σ_{cf}) depends on the crack width as given by the σ-w relationship.

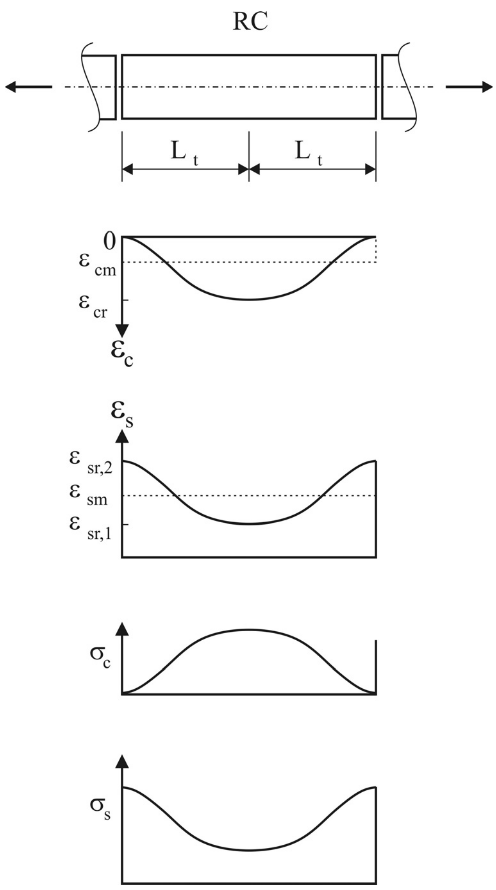

Fig. 5.15: Stresses in a member of reinforced plain concrete after cracking

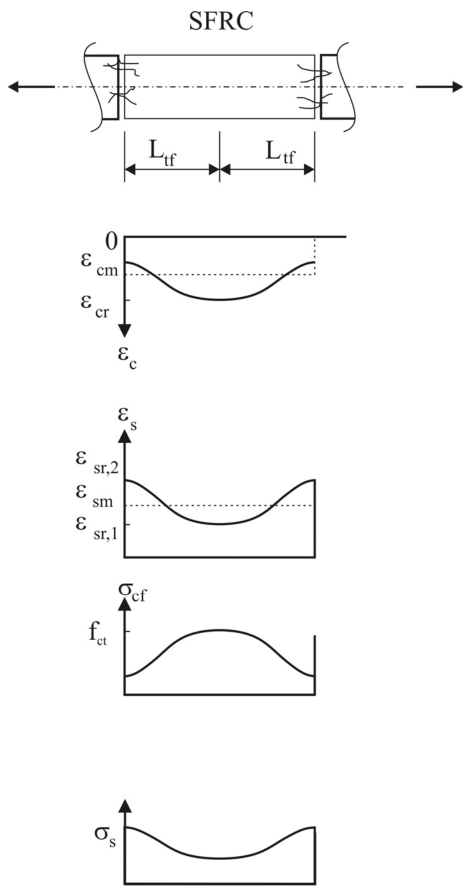

Fig. 5.16: Stresses in a member of SFRC after cracking

The concrete stress in the crack σ_c is neglected in the original model because for a fully developed crack pattern, the stress is in fact zero for conventional concrete, see Fig. 5.15. In SFRC, however, the concrete transmits the stress σ_{cf} across the crack, see Fig. 5.16. This stress is included as a starting value, which depends on the crack width, in the modified model. Because of this stress transmission across the crack less stress is to be transmitted by bond to reach the tensile strength and therefore the transmission length and thus the crack spacing is reduced.

Calculation of the Transmission Length L_t

Most boundary conditions for calculating the transmission length presented in section 5.2.4 are still valid. However, in SFRC, the concrete stress at the end of the transmission length is not zero as for conventional concrete, but has a value, which depends on the crack width. To find L_t, the transmission length is varied until the boundary conditions are met, as previously described.

An example for the steel stresses, concrete stresses and bond stresses along the transmission length is given in Fig. 5.17. These stresses were calculated for the tensile zone of a beam with two reinforcing bars with a diameter of 10 mm, a beam width of 150 mm, a concrete cover of 25 mm, a concrete compressive strength of 50 N/mm^2 and 60 kg/m^3 steel fibers. The calculated transmission length was 73.46 mm.

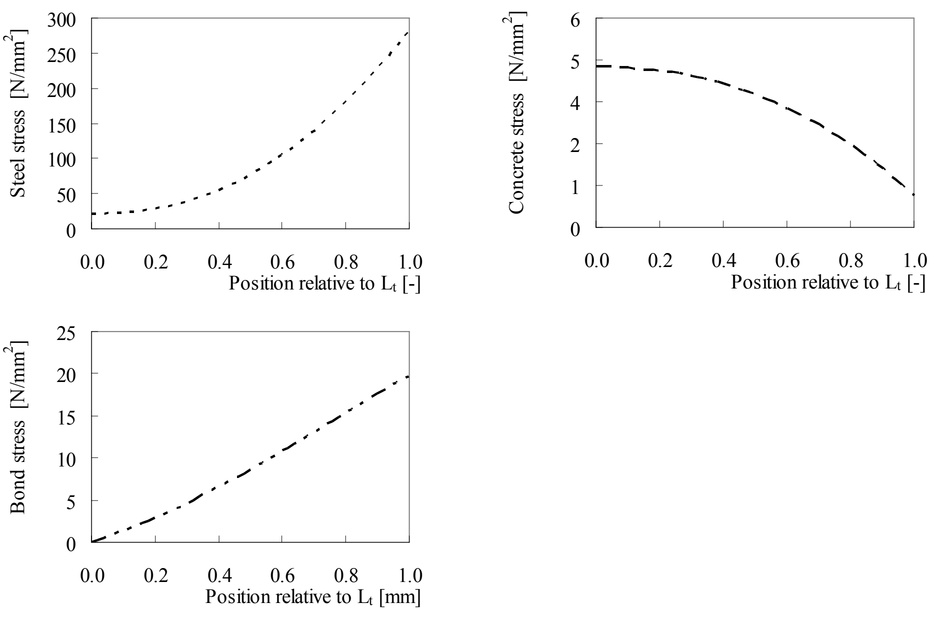

Fig. 5.17: Steel stresses, concrete stresses and bond stresses along the transmission length (here, the end of the transmission length corresponds to the crack surface)

Calculation of Stress and Strain Distribution in an Element between Two Subsequent Cracks

The tensile member force is not necessarily steadily increasing with increasing elongation in the steel yielding range in SFRC in contrast to RC. Therefore, the steel stress is no longer used as input value for the calculation of the stress and strain distribution in an element between two subsequent cracks. As the slip is steadily increasing, it was chosen as input in the calculation of the stress and strain distribution in an element between two subsequent cracks.

It is assumed that the slip at a crack is equal to half the crack width. The average concrete strain between two cracks is equal to the crack width divided by the crack spacing.

The differential equation of bond in the calculation of the stress and strain distribution in an element between two subsequent cracks is solved with finite difference calculus. Most boundary conditions for calculating the transmission length presented in section 5.2.4 are still valid. However, in SFRC, the concrete stress at the beginning of the element between two subsequent cracks is not equal to zero but depends on the crack width. The calculation is performed in the following steps: For a predefined slip, the steel stress in the first crack is varied in a number of iterations until equilibrium of forces is found and the tensile forces at both cracks are equal, taking into account that the calculated slip in the second crack corresponds to the concrete stress at that crack.

5.4.3 Localization of Deformations in One Crack

It has also been observed by other researchers that the plastic deformations may localize in only one crack in SFRC [Espion et al., 1993; Pfyl & Marti, 2001; Pfyl, 2003; Eligehausen et al., 2003; De Pauw & Tearwe, 2004; Fehling & Leutbecher, 2005; Löfgren, 2005; Jungwirth, 2006; Shionaga, 2006]. On the other hand, in the range usually considered for the serviceability, the addition of fibers indeed leads to smaller crack widths, smaller crack spacings, a larger number of cracks, and a stiffer behavior of tension elements [Abrishami & Mitchell, 1997; Bischoff, 2000; Bischoff, 2003; Eligehausen et al., 2003]. Hereafter, it is explained that the localization may result in a reduced deformation capacity.

Cracking of the structural member can develop in two ways. If the overall behavior is softening, the deformation localizes in one single large crack. If the overall behavior is hardening, the deformation localizes in several large cracks, leading to a larger total deformation capacity than in the previous case.

Whether the deformation localizes in one crack or is distributed over more cracks depends on the section properties and the strength distribution. A section that exhibits softening will result in localization of the deformation in one crack. To obtain localization of the deformation in more cracks the section must exhibit hardening and the hardening ratio must be large enough to allow for the development of the yield stress in more cracks taking into account the statistical strength variation. Due to the statistical variation in tensile strength and post-peak material properties of SFRC, there will be stronger and weaker cross-sections. Therefore, a cross-section needs a minimum amount of hardening and a maximum scatter to guarantee hardening of the member. The percentages are not yet clarified and is subject to further research. A first assumption of this is that the ratio of the force at ultimate load in the tensile member or tensile chord divided by the force at the onset of steel yielding T_u/T_y should at least be 1.05 in order to obtain multiple cracking. Due to the statistical variation of the concrete properties, a ratio lower than this value is likely to result in localization of the deformations in one single large crack. For the engineering practice this might mean that the added load bearing capacity of the SFRC leads to an increased T_y, whereas the T_u remains at the same level or is increased less significantly. This increases the probability of crack localization.

Parameter Study

To further investigate this phenomenon, a parameter study was carried out. A steel reinforcement ratio $\rho_s = A_s / A_c = 0.01227$ (d_s = 10 mm) was assumed in the first place. In order to illustrate the combined effect of the amount of reinforcing bars and steel fibers, the reinforcement ratio was also assumed to be 0.00785 (d_s = 8 mm) and 0.01767 (d_s = 12 mm), respectively, for the steel hardening ratios 1.05 and 1.20. The steel properties are given in Table 5.2.

Table 5.2: Steel properties

f_{su}/f_{sy} [-]	f_{sy} [N/mm^2]	f_{su} [N/mm^2]	E_s [N/mm^2]	ε_{su} [%]
1.20	500	600	200000	10
1.15	500	575	200000	10
1.10	500	550	200000	10
1.05	500	525	200000	10

The concrete cross-section was 80×80 mm. A concrete with an E-modulus E_c of 34000 N/mm^2 was assumed. The tensile properties of the concrete are given in Table 5.3. The variation of the fiber content was captured by varying the parameter β_{FCM} similar to the model proposed in chapter 4.

Table 5.3: Concrete tensile properties

Fiber content [kg/m^3]	f_{ct} [N/mm^2]	α_{FCM} [-]	β_{FCM} [-]	$\beta_{FCM} f_{ct}$ [N/mm^2]	w_0 [mm]
0	3.0	0.0067	0.001	0.003	7.5
60	3.0	0.0067	0.2	0.6	7.5
120	3.0	0.0067	0.4	1.2	7.5

The cases analyzed are denoted with an identifying number, giving the hardening ratio of the steel in percent and the fiber content in kg/m^3. For example, the case Var105.120 means: a hardening ratio of 1.05, i.e. an ultimate steel strength of 525 N/mm^2 and a fiber content of 120 kg/m^3, represented by the value $\beta_{FCM} = 0.4$.

Fig. 5.18 shows the tensile member force versus crack width relations obtained with the bond model.

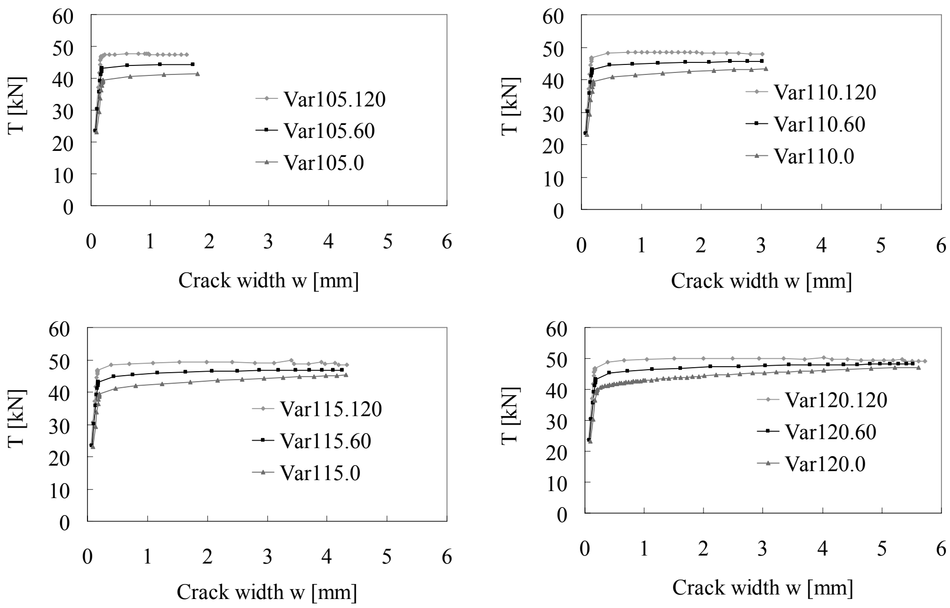

Fig. 5.18: Relation of tensile member force and crack width for different steel hardening ratios and fiber contents for a reinforcement ratio of 0.01227 (d_s = 10 mm)

It can be seen that the members with steel fibers show a lower hardening ratio of the tensile member than the members without fibers. This becomes even clearer when the tensile member force at ultimate steel stress T_u divided by the tensile members force at the onset of steel yielding T_y is displayed as a function of the fiber content as shown in Fig. 5.19 or as a function of the steel hardening ratio in Fig. 5.20. In the following, the ratio T_u/T_y is called the hardening ratio of the tensile member.

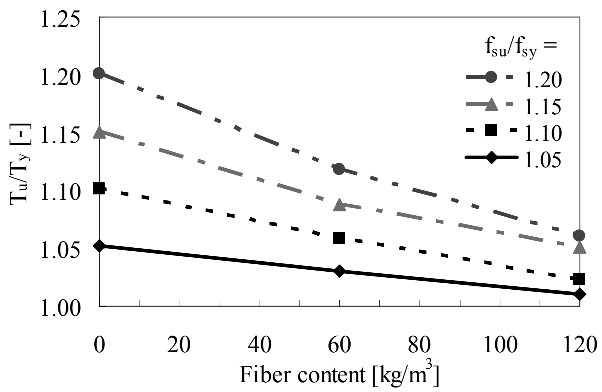

Fig. 5.19: Hardening ratio of the tensile member as a function of the fiber content for different steel hardening ratios for a reinforcement ratio of 0.01227 (d_s = 10 mm)

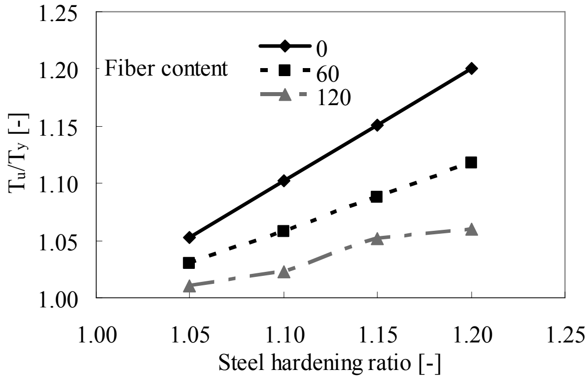

Fig. 5.20: Hardening ratio of the tensile member as a function of the steel hardening ratio for different fiber contents for a reinforcement ratio of 0.01227 (d_s = 10 mm)

The variation of the reinforcement ratio leads to the tensile member force versus crack width relations shown in Fig. 5.21.

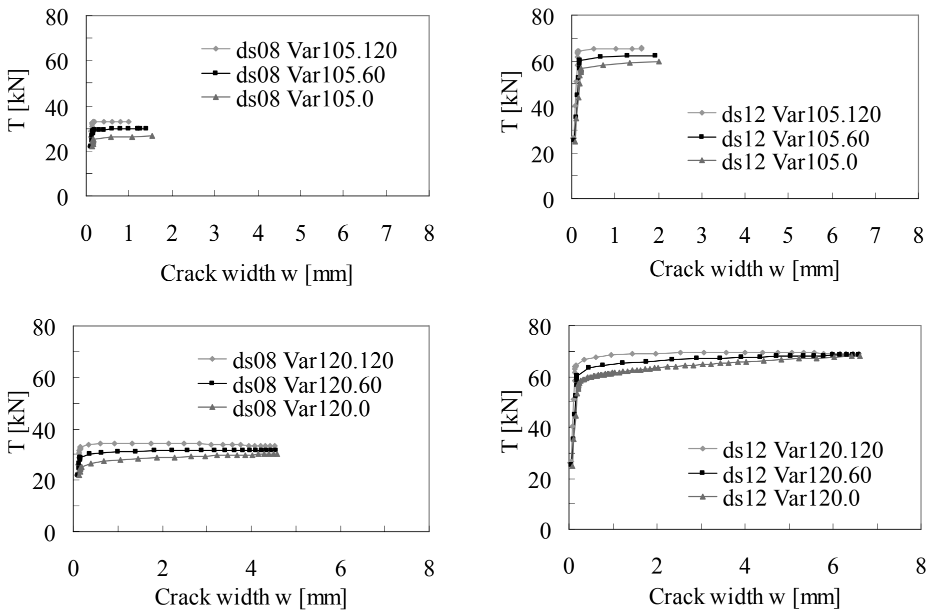

Fig. 5.21: Relation of tensile member force and crack width for different steel hardening ratios, fiber contents and reinforcement ratios

The maximum force of the tensile member increases with increasing reinforcement ratio and with increasing fiber content. The maximum crack width increases with increasing hardening ratio of the reinforcing bars and with increasing reinforcement ratio.

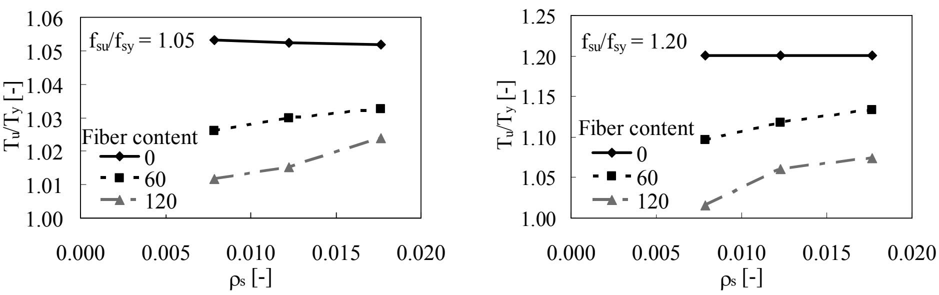

Fig. 5.22: Hardening ratio of the tensile member as a function of the fiber content and the steel reinforcement ratio for the steel hardening ratio 1.05 (left) and 1.20 (right)

The hardening ratio of the tensile member decreases with increasing fiber content. The variation of the reinforcement ratio showed that this decrease is more pronounced for smaller steel reinforcement ratios, irrespective of the steel hardening ratio. Localization of the deformations in one crack is thus most likely to occur in members with a low steel bar reinforcement ratio and a large steel fiber content.

The tensile strength of the concrete is not constant, but has a large scatter (approximately ± 30%). Since in the tensile members, the equilibrium of forces must be valid in any arbitrary cross-section, the sum of the forces carried by the steel rebar and by the steel fibers must be equal in any cross-section. This means that if in a cross-section with low tensile strength the deformations are already large, the deformations in neighboring cross-sections at the same load level are much smaller.

Fig. 5.23 illustrates the difference in crack width for members with a steel hardening ratio of 1.05 and a variation of the concrete tensile strength along the member of ± 30%. As the maximum force in a tensile member is determined by the weakest cross-section, the crack widths in the stronger cross-sections are found at the same load level. It can be seen that there is a pronounced difference in crack width between the assumed weakest link with an assumed concrete tensile strength of 30% below average compared to the crack width for the average concrete tensile strength.

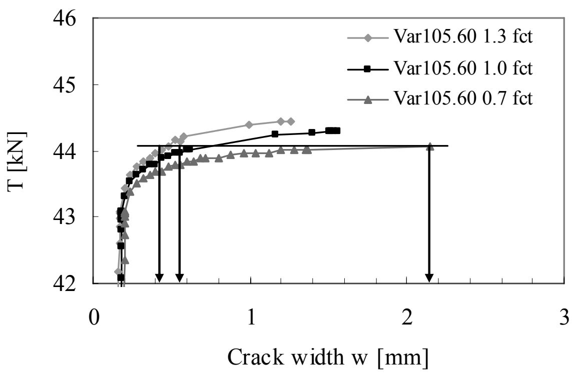

Fig. 5.23: Relation between tensile member force and crack width for steel hardening ratio f_{su}/f_{sy} = 1.05 and a ± 30% variation of the concrete tensile strength ρ_s = 0.01227

Likewise, the steel fiber distribution and orientation influence the localization process. Because the steel fibers are not necessarily homogeneously distributed and oriented, the stress-crack width properties of the SFRC can vary along the tensile member. Since the equilibrium of forces must be valid in any arbitrary cross-section in the tensile members, the sum of the forces carried by the steel rebar and by the steel fibers must be equal in any cross-section. This means that if in a cross-section with few or unfavorably oriented fibers the deformations are already large, the deformations in a neighboring cross-section at the same load level are much smaller.

Fig. 5.24 illustrates the difference in crack width for members with a steel hardening ratio of 1.05 and a variation of the fiber content along the member of ± 10%. As the maximum force in a tensile member is determined by the weakest cross-section, the crack widths in the stronger cross-sections are found at the same load level. It can be seen that there is a pronounced difference in crack width between the assumed weakest link with an assumed fiber content of 10% below average compared to the crack width for the average fiber content.

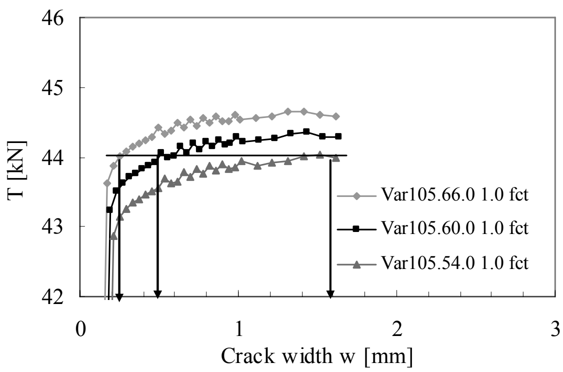

Fig. 5.24: Relation between tensile member force and crack width for steel hardening ratio f_{su}/f_{sy} = 1.05 and a ± 10% variation of the fiber content ρ_s = 0.01227

It is noted that in slab-type structures (b/h>5) it is to be expected that redistribution takes place over the width of the structure and that this localization is therefore less pronounced or not present.

5.5 Pull-out Tests with Short Embedment Length

Tests were performed in order to extend the confinement-based model of Den Uijl & Bigaj (1996) to describe the local bond behavior of ribbed bars embedded in SFRC.

The tests have been published earlier in Schumacher et al. (2002b) and Schumacher et al. (2002c).

5.5.1 Experimental Program

Deformation controlled pull-out tests were performed on reinforcing bars embedded in plain and fiber reinforced self-compacting concrete over a short embedment length. Table 5.4 gives an overview of the experimental program. The influence of the following parameters on the bond behavior was investigated:

- fiber volume
- fiber aspect ratio
- concrete cover
- way of manufacturing (cast and sawn specimens)
- concrete compressive strength.

The concrete cover was obtained by direct moulding (cast specimens) or by sawing a part of the specimen after hardening (sawn specimens indicated by the letter “s”) to separate the concrete cover effect and the wall effect, which refers to the distribution of the fibers near a moulded face of the concrete member. The fiber length was 30 mm.

The pull-out tests were performed at an age of 28 ± 1 days. For any combination of test parameters, two specimens were tested.

The specimen identification (e.g. B45.80/30.60.c35.1) is composed of the concrete compressive strength class, fiber type, amount of fibers in kg/m^3, concrete cover thickness and repetition number.

Table 5.4: Experimental program of the pull-out tests

Concrete strength class	Fiber type $(l_f/d_f)/l_f$	Aspect ratio [-]	Fiber amount [kg/m^3]	Concrete cover[1)] [mm]
B45			0	15, 25, 35, 95
B45	80/30	80	60	15, 15s, 25, 25s, 35, 95
B45	45/30	45	60	35
B45	45/30	45	120	35
B105				35
B105	80/30	80	60	35

[1)] s = sawn outer face

Standard specimens were made of the same mixtures to measure the E-modulus (100 × 100 × 400 mm prisms), the compressive strength and the splitting tensile strength (150 mm cubes) at an age of 28 days, see appendix C.

5.5.2 Specimens

Pull-out tests were performed on single 10 mm diameter ribbed bars embedded along three times the bar diameter (i.e. 30 mm) in 200 mm cubes, see Fig. 5.25. The specimens, which were bound to be sawn, were cast in moulds 45 mm (i.e. 1.5 times the fiber length) larger than the desired specimen size at the side of the smallest concrete cover. The loading direction was the same as the casting direction.

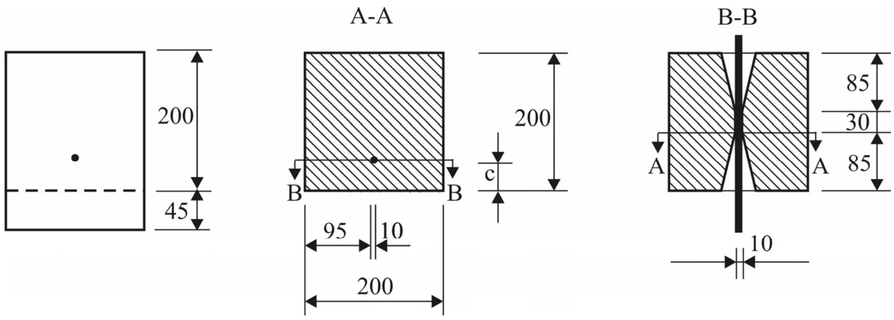

Fig. 5.25: Geometry of the test specimens for the pull-out tests (dimensions in mm)

5.5.3 Material Properties

Concrete Composition

The concrete composition, the mixing procedure, finishing and curing were identical with that described in chapter 3. The concrete was filled into the center of the moulds with hand shovels.

Standard Test Results

The standard tests were performed in the same way as described in chapter 3. The average results and the standard deviations of these tests are given in Table 5.5. All results are given in appendix C.

Table 5.5: Results of standard tests (average and standard deviation)

Mixture	Cube strength [N/mm^2]	Splitting tensile strength [N/mm^2]	E- Modulus [kN/mm^2]
B45.0.0	51.8 (3.6)	3.77 (0.24)	33.0 (2.6)
B45.80/30.60	51.8 (3.4)	5.41 (0.68)	34.3 (0.6)
B45.45/30.60	52.2 (2.3)	5.59 (0.05)	38.0 (3.0)
B45.45/30.120	55.5 (2.3)	7.30 (0.30)	36.4 (0.5)
B105.0.0	105.8 (4.0)	5.77 (0.22)	43.3 (1.2)
B105.80/30.60	114.4 (6.2)	11.6 (0.25)	44.1 (0.7)

Reinforcing Steel Properties

Hot rolled FeB500 HWL reinforcing steel was used. The bar diameter was 10 mm. The effective rib area f_R was measured to be between 0.059 and 0.085 (average 0.071) in standard tests according to the German code DIN 488. According to ENV 10080, the minimum effective rib area f_R for a bar with 10 mm diameter is 0.052.

The stress-strain response of the reinforcing steel was also determined in tensile tests. Table 5.6 gives the yield stress f_{sy}, the tensile strength f_{su}, the ratio f_{su}/f_{sy}, the effective rib area f_R, and the E-modulus.

Table 5.6: Results of standard tests on reinforcing steel bars 10mm, average and (standard deviation)

f_{sy} [N/mm^2]	f_{su} [N/mm^2]	f_{su}/f_{sy} [-]	f_R	E- modulus [N/mm^2]
589	662	1.12	0.071	207667
(11)	(8)	(0.01)	(0.006)	(1337)

Variation of Concrete Properties within Specimens

For self-compacting concrete without fibers, Weiße (2001) showed that the direction of casting the pull-out test specimens does not significantly influence the bond stress–slip relationship. His test results for bars pulled out in the direction of casting, opposite to it or perpendicular to it were nearly identical.

For steel fiber reinforced self-compacting concrete, however, the direction of casting may influence the fiber orientation and distribution and therefore the pull-out behavior. To get an impression of the fiber distribution in the present tests, the specimens with fibers were sawn open after testing and the number of fibers in an area of 15 × 30 mm next to the reinforcing bar was counted manually (see Table 5.7) at both sides of the bar, as indicated in Fig. 5.26.

Fig. 5.27 shows the number of fibers counted in the areas A and B for the mixture with 60 kg/m^3 fibers with an aspect ratio of 80. Remarkably, no significant difference between the sawn and the cast specimen was observed. Therefore, the values for the sawn and cast specimens were averaged.

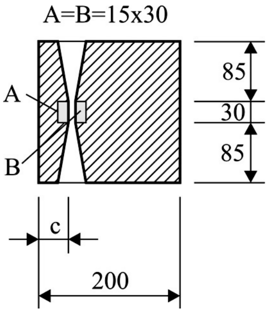

Fig. 5.26: Area where fibers were counted (dimensions in mm)

Specimen	Number of fibers in area			
	Specimen 1		Specimen 2	
Test	A1	B1	A2	B2
B45.80/30.60.c15.1/2	2	48	3	35
B45.80/30.60.c15.1s/2s	1	40	3	29
B45.80/30.60.c25.1/2	6	21	6	19
B45.80/30.60.c25.1s/2s	8	19	14	29
B45.80/30.60.c35.1/2	11	27	6	30
B45.80/30.60.c95.1/2	27	32	17	20
B45.45/30.60.c35.1/2	5	8	4	13
B45.45/30.120.c35.1/2	11	35	6	22

Table 5.7: Number of fibers in an area of 15 × 30 mm (see Fig. 5.26) next to the steel bar

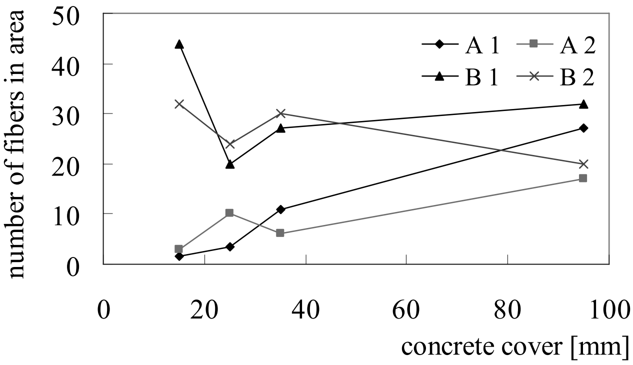

Fig. 5.27: Number of fibers in the area A and B for test 1 and 2

From Table 5.7 it can be concluded that the number of fibers present in the concrete cover (A-section) is smaller than in the bulk (B-section). For the specimens with a concrete cover of 15 mm, the ratio was on average 1:20, for those with a concrete cover of 25 and 35 mm it was on average 1:3, and for the specimens with a concentric bar it was approximately 1:1.2 which indicates a scatter in the fiber distribution of approximately 20%.

The inhomogeneous fiber distribution can be explained by the effect of blocking when the fresh concrete flows and comes across a steel bar. The concrete was filled in with hand shovels at side B for all specimens except for the concentric ones. Hence, there was a "shadow side" with respect to filling when it comes to the fiber distribution.

Probably more fibers would have flown to the side of the smaller concrete cover if the specimens had been cast into the direction perpendicular to the loading direction. Such a situation could be compared to the fiber orientation observed in the beams cast in horizontal position, which will be described in detail in chapter 6. In case of the beams, the concrete was poured into the mould and could flow along the bottom of the mould under the reinforcing bars and the fibers were well distributed in the concrete cover.

The difference in manufacturing methods is also likely to be a reason for the contradictions found in the literature survey by Bigaj-van Vliet (2001), see section 5.3.2.

5.5.4 Experimental Set-up

The pull-out tests were performed in a test set-up similar to that of Rehm (1961) and to RILEM (1970). The bar was pulled in the casting direction and the slip was measured at the non-loaded end of the specimens, see Fig. 5.28. The test set-up is shown in Fig. 5.29. The tests were carried out displacement-controlled at a speed of 0.01 mm/s.

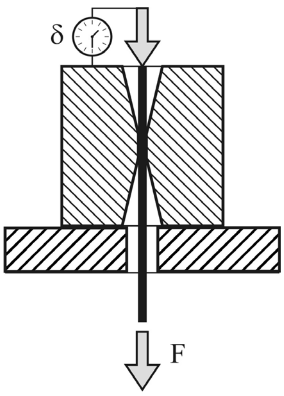

Fig. 5.28: Measuring the slip in the pull-out tests

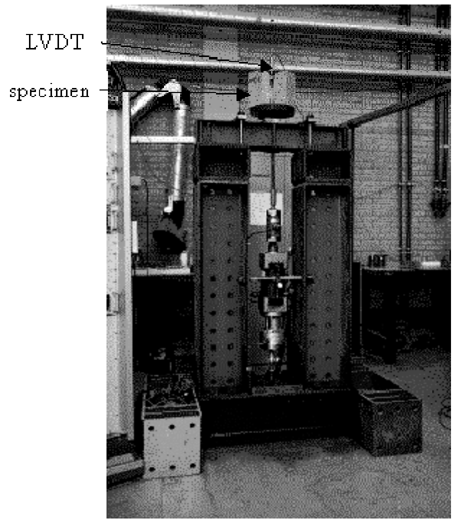

Fig. 5.29: Pull-out test set-up [Sule, 2003]

5.5.5 Test Results

Data Processing

In the following, the test results are given as graphs of the mean bond stress τ_b and the slip δ at the unloaded end of the specimen. The bond stress τ_b is calculated by dividing the measured force by the contact area. In pull-out tests, the embedment length decreases as the bar is pulled out of the concrete because part of the embedded length is not surrounded by concrete any more and the part of the steel bar that is then pulled into the area that had previously been surrounded by concrete has not been embedded and therefore can move freely, see Fig. 5.30. Therefore, the contact area decreases proportionally to the decreasing embedded length. For small slips compared to the embedment length, the error made by neglecting this phenomenon is negligible. However, if the slip is one third of the original embedment length the error made is 33%. Therefore, the bond stress was calculated as:

$$\tau_b = \frac{P}{\pi \cdot d_s \cdot (l_{bond,initial} - \delta)} = \frac{l_{bond,initial}}{l_{bond,initial} - \delta} \cdot \frac{P}{\pi \cdot d_s \cdot l_{bond,initial}} \qquad (5.10)$$

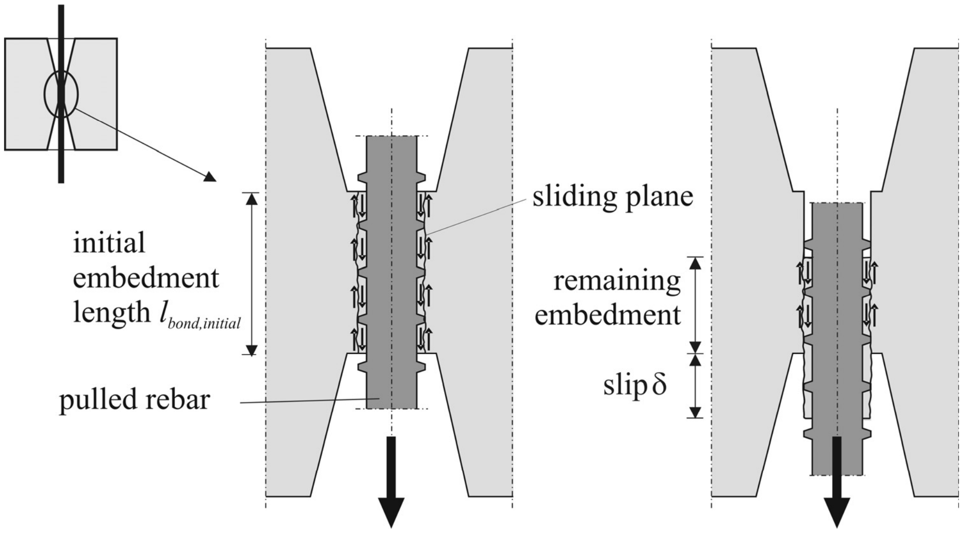

Fig. 5.30: Change of the real embedment length in a pull-out test

Test Results

The average results and the upper and lower boundaries of the pull-out tests with pull-out failure of all test specimens of the reference mixture for the B45 and of all tests with the mixture B45.80/30.60 are shown in Fig. 5.31.

Note that usually in plain concrete the scatter in pull-out tests is rather large compared to tests of the compressive or the splitting tensile strength. The relatively large scatter is predominantly caused by inhomogeneities in the material such as the position of aggregates and pores at the concrete-steel interface, the local strength of the cement paste, local differences in the steel surface (especially the effective rib area f_R), position of the lugs with respect to the embedment, etc.

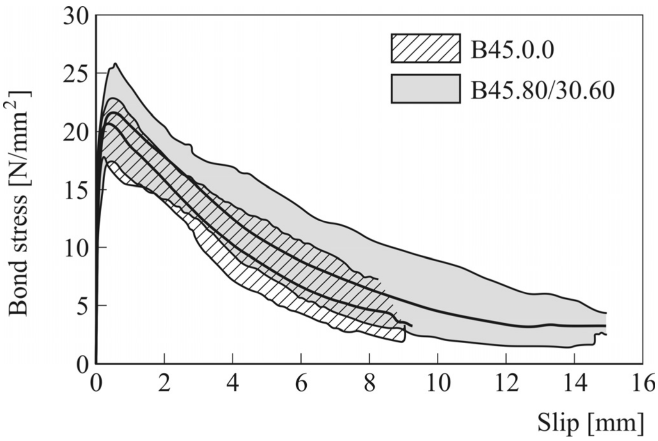

Fig. 5.31: Comparison of the pull-out behavior of plain SCC and SCC with 60 kg/m³ steel fibers 80/30

As can be seen from Fig. 5.31, the fibers on average slightly increased the bond ductility in case of pull-out failure. From the peak load on, the resistance of the SFRC specimens was approximately 2 N/mm² higher than that of the plain SCC specimens. The descending branches decreased with the same slope. However, it can be seen that the average response of the specimens with fibers was in the upper range of scatter of the test specimens without fibers and the average response of the specimens without fibers was between the average and the lower boundary of those with fibers. All test results can be found in appendix G.

To explain why fibers are not significantly effective in case of pull-out failure, a close look at Fig. 5.7 is taken. In case of splitting failure, the entire confinement capacity curve is followed and an increase in confinement capacity will result in an increase in bond ductility (see Fig. 5.7, left). In case of pull-out failure, however, the radial strains remain within the ascending branch of the confinement capacity curve, first upward, then downward, (see Fig. 5.7, right). As shown in section 5.4, the fibers only have an influence for strains exceeding this range. Therefore, the fibers are not activated in the inner cracks and do not influence the confinement capacity in case of pull-out failure.

However, when slipping, the lugs of the steel bars can be “blocked” by neighboring fibers, which then work as a dowel and result in a slightly more ductile bond behavior. These steel fibers obstruct the movement of the reinforcing bar when it is pulled out of the concrete (see Fig. 5.32). Yet, only a few fibers are effective in this way and therefore, this influence is neglected in the modification of the bond model.

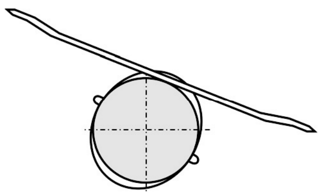

Fig. 5.32: Dowel action of the ribs of the reinforcing bar on the steel fibers

5.6 Model Validation

5.6.1 Modeling of Pull-out Tests with Short Embedment Length in SCC and SCSFRC

Effective Concrete Cover

The bond failure mode is directly dependent on the effective concrete cover. Bigaj (1999) concluded on the basis of a numerical simulation for conventional concrete that splitting failure occurs up to an effective concrete cover c_{eff} of 3.0 times the bar diameter d_s and beyond that, pull-out failure is likely to occur:

$c_{eff} \geq 3.0\ d_s$ pull-out failure
$c_{eff} < 3.0\ d_s$ splitting failure.

In order to judge whether splitting failure can take place, the effective concrete cover c_{eff} is calculated according to Bigaj (1999) for a bar diameter of 10 mm and various smallest concrete covers c_1 (see Table 5.8). The concrete covers c_2, c_3 and c_4 are larger than $4 \cdot d_s = 40$ mm and therefore 40 mm is assumed in the calculations. The angle between the critical splitting plane and that normal to the closest concrete surface α_s can be chosen between 45° and 60°. For the sake of comparison, a simple rule of thumb is also given in which c_{eff} is calculated as:

$$c_{eff} = 0.25 \cdot (c_1 + c_2 + c_3 + c_4) \tag{5.10}$$

where:
$c_i \leq 4\ d_s$ and c_i being the concrete cover as shown in Fig. 5.6.

Table 5.8: Effective concrete covers for different values of the smallest concrete cover

Smallest cover c [mm]	c_{eff} for $\alpha_s = 45°$ [mm]	c_{eff} for $\alpha_s = 60°$ [mm]	c_{eff} according to rule of thumb [mm]
15	21.21	30.00	33.75
25	34.32	36.25	36.25
35	38.75	38.75	38.75
95	40.00	40.00	40.00

Therefore, for a bar diameter of 10 mm depending on the arbitrary choice of the angle α_s, even for the smallest concrete cover of 15 mm it is not evident on the basis of the c_{eff}/d_s ratio whether splitting or pull-out failure will occur. For all larger concrete covers, pull-out failure is evidently expected, since $c_{eff} \geq 3.0\ d_s = 30$ mm.

Influence of SCC and SCSFRC on the Bond Failure Mode

As the splitting tensile strength of self-compacting concrete is higher than that of conventional concrete with the same compressive strength [Holschemacher, 2001] and as the tendency to splitting failure decreases with increasing concrete tensile strength, it was expected that splitting failure was not likely to occur in the tests, even for the plain SCC test specimens. In the tests performed, only one of the test specimens of plain SCC with a concrete cover of 15 mm showed a thin splitting crack along the bar. All other specimens clearly showed pull-out failure.

As shown in section 5.4.1, the addition of steel fibers increases the confining capacity. The fiber reinforced specimens are therefore even less likely to fail due to splitting bond failure.

Input Parameters

The bond stress-slip relationships of the performed pull-out tests were simulated with the bond model presented in section 5.4.2.

The post-peak behavior of the SCSFRC in tension was modeled with the model proposed in section 4.6. The post-peak behavior of the SCSFRC in the pull-out tests was calculated based on the assumption of a 3D fiber orientation.

Table 5.9 shows the input parameters used to simulate the pull-out tests. The tensile strength and the other values of the stress-crack width relation of the SCSFRC were derived from the compressive strength of the mixtures reported in appendix C, Table C3, as explained in section 4.6. The values for α_{FCM}, β_{FCM} and w_0 for the SCC were used as proposed in Bigaj (1999) for plain concrete.

Table 5.9: Input parameters for simulating the pull-out tests

Parameter		B45.0.0	B45.45/30.60	B45.45/30.120	B45.80/30.60
$f_{c,cube}$	[N/mm^2]	52	52	56	52
f_{ct}	[N/mm^2]	3.9	3.9	4.1	3.9
α_{FCM}	[-]	0.14	0.0076	0.0077	0.0077
β_{FCM}	[-]	0.23	0.093	0.180	0.165
w_0	[mm]	0.2	7.5	7.5	7.5
τ_{b1}/f_{ct}	[-]	5.25	5.25	5.25	5.25

Comparison of Pull-Out Tests with Simulation Results

The results of the simulation (‘sim’) with the standard input parameters as defined in section 5.4.2 are compared to the average test results of the different concretes in Fig. 4.13.

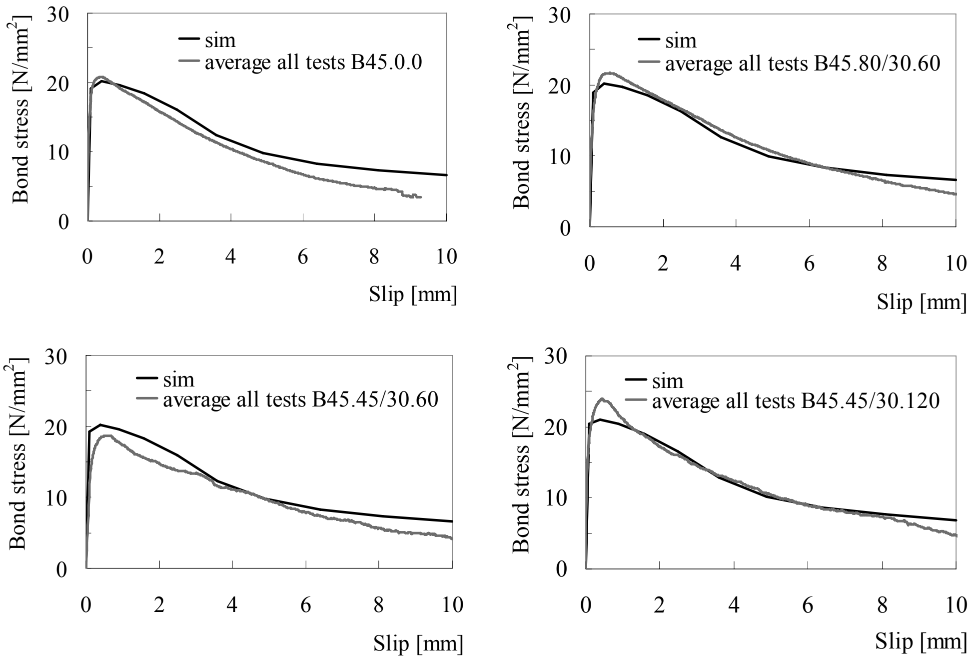

Fig. 5.33: Comparison of simulation of the pull-out tests and average experimental results

It can be seen that the simulations with the bond model fit the average test results very well considering the scatter of the test results as shown in Fig. 5.31 and appendix G.

5.6.2 Modeling the Behavior of Tensile Elements in SFRC

General Remarks on Tensile Elements

The response of a tensile element can be used to model the tensile zone of a reinforced concrete beam in flexure. The behavior of the tensile element follows from the behavior of the concrete and the rebar in uniaxial tension and the bond between the two. It was described in section 5.4.

Comparison of Simulations with Proposed Model and Tensile Tests of Pfyl (2003)

The tensile elements chosen for comparison with the bond model were taken from Pfyl & Marti (2001) and Pfyl (2003). Pfyl tested tensile elements made of SFRC and ordinary concrete with a total length of 2000 mm. All elements were reinforced with four steel bars with a diameter of 8 mm. The concrete cover was 26 mm. The test specimens denoted by T100 contained the minimum reinforcement according to the Swiss standard SIA 162 (1993), the test specimens denoted by T75 had a larger concrete cross-section so that the tensile element contained 75% of the minimum reinforcement. The tensile elements were made of concrete without and with 30 and 60 kg/m^3 hooked-end steel fibers with an aspect ratio of 65, a length of 35 mm, and a tensile strength of 1250 ± 150 N/mm^2. The geometry of the test specimens can be seen in Fig. 5.34. The identification of the specimens, e.g. T100.30, consists of:

- T — tensile element
- 100 or 75 — percentage of minimum bar reinforcement
- 0; 30 or 60 — steel fibers in kg/m^3.

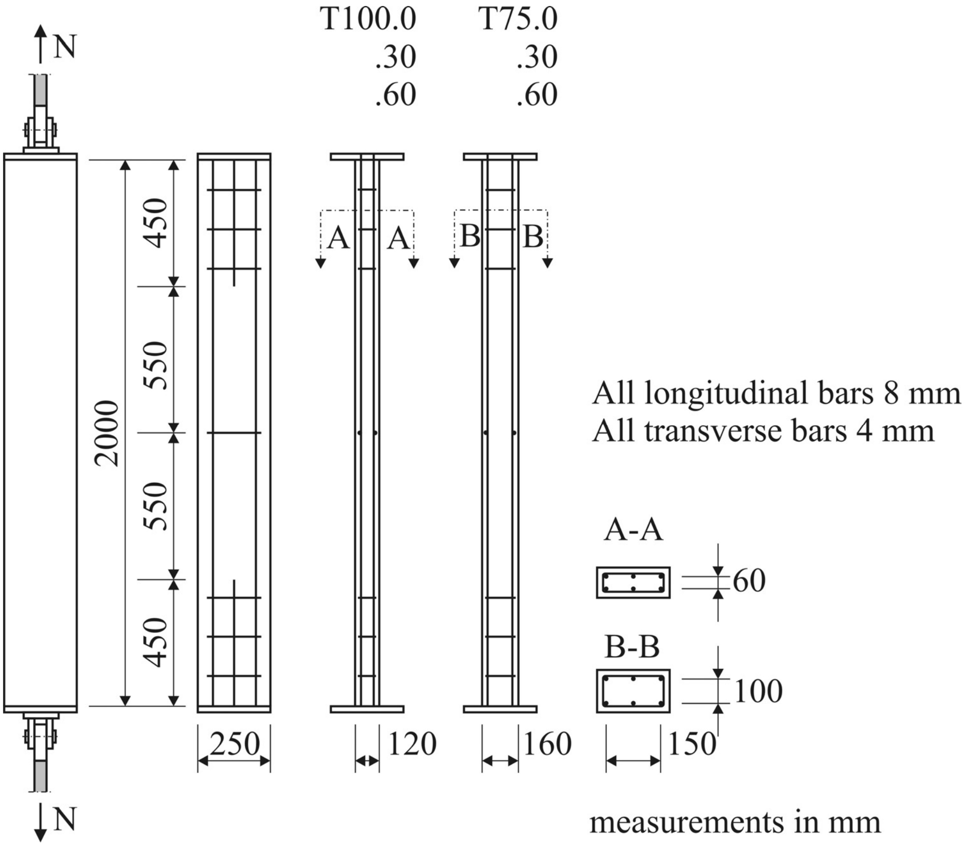

Fig. 5.34: Tensile test specimens [Pfyl, 2003]

The crack patterns and the crack widths at the last measured load step before failure can be seen in Fig. 5.35. The figure includes the widths of cracks that were at least 1 mm. The widths of the smaller cracks as well as crack widths at other load steps can be found in Pfyl & Marti (2001). The deformations of the SFRC specimens localized in one large primary crack whereas for the specimens without fibers, several primary cracks showed similar crack widths.

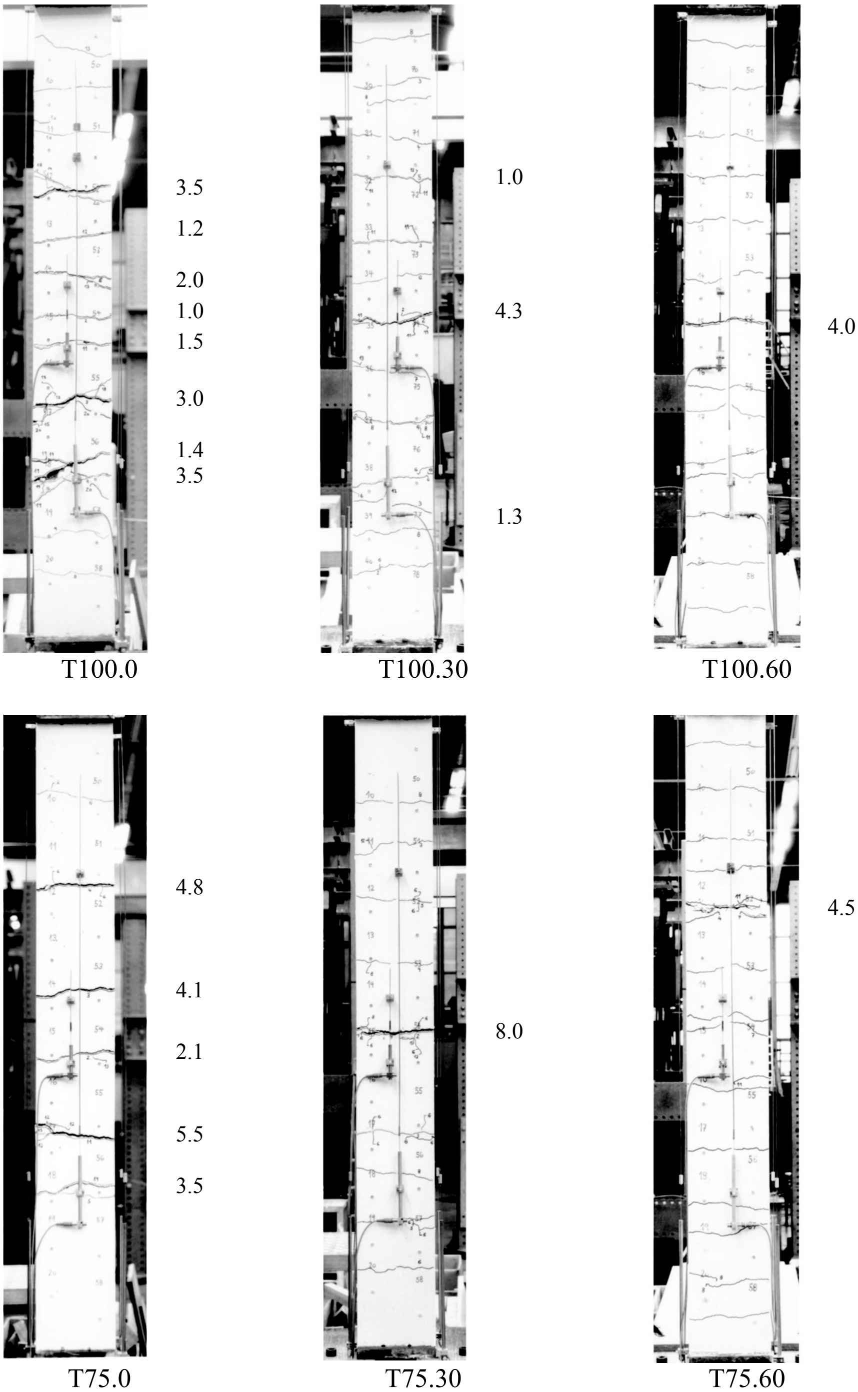

Fig. 5.35: Crack patterns after testing with crack widths at the last measured load step in mm [Pfyl & Marti, 2001]

Table 5.10 shows some of the input parameters for the bond model used to simulate the tensile elements. The tensile properties were modeled as proposed in chapter 4 with the exception of the tensile strength, which was calculated from the experimental results at load step 2 directly after cracking as the lower boundary (*lb*) value and from the average of all load steps as the average value (*ave*) with:

$$\sigma_c = \frac{N}{A_c\,(1 + n_E \omega_s)} \tag{5.11}$$

This is similar to the approach of calculating the first crack with the 5% fractile of the concrete tensile strength $f_{ctm,ax}$.

The factor β_{FCM} was adapted to result in the same stress level that would have been obtained with the model proposed in chapter 4. One element between two subsequent cracks was calculated with the lower boundary value of the concrete tensile strength $f_{ct,lb}$. The other elements between two subsequent cracks within the measuring length of 1000 mm in the center of the specimens were calculated with the average value of the concrete tensile strength $f_{ct,ave}$. The total elongation was calculated as:

$$\Delta L = w_{lb} + \frac{1000 - s_{cr,lb}}{s_{cr,ave}} \cdot w_{ave} \tag{5.12}$$

where:

ΔL	total elongation over the measuring length of 1000 mm [mm]
$s_{cr,lb}$	crack spacing calculated with lower boundary concrete tensile strength [mm]
$s_{cr,ave}$	crack spacing calculated with average concrete tensile strength [mm]
w_{lb}	crack width calculated with lower boundary concrete tensile strength [mm]
w_{ave}	crack width calculated with average concrete tensile strength [mm]

The fiber orientation was assumed to be influenced by the boundaries, leading to a preferred fiber orientation parallel to the sides of the tensile elements. This was included in the parameters by multiplying the input parameter β_{FCM} with the factor 0.7/0.5 in the direction of stress transfer over the cracks and 0.43/0.5 in the direction relevant for the confinement capacity. These factors represent preferred fiber orientations as will be shown in chapter 6. The other input parameters such as the concrete properties in compression and the steel properties were taken from Pfyl & Marti (2001). The specimen was subdivided into elements from one crack to the next. The length of such an element between two subsequent cracks was calculated with the bond model.

Table 5.10: Input parameters for simulating tensile tests

Parameter		T100.0	T75.0	T100.30	T75.30	T100.60	T75.60
τ_{b1}/f_{ct}	[-]	5	5	5	5	5	5
α_{FCM}	[-]	0.14	0.14	0.0066	0.0066	0.0067	0.0067
w_0	[mm]	0.2	0.2	8.75	8.75	8.75	8.75
$f_{ct,lb}$	[N/mm^2]	1.73	1.62	2.37	1.77	2.37	2.47
$\beta_{FCM,lb}$ crack	[-]	0.36	0.39	0.16	0.21	0.32	0.31
$\beta_{FCM,lb}$ confinement	[-]	0.36	0.39	0.09	0.12	0.19	0.18
$f_{ct,ave}$	[N/mm^2]	2.96	2.44	3.26	2.72	3.34	3.16
$\beta_{FCM,ave}$ crack	[-]	0.21	0.26	0.12	0.14	0.23	0.24
$\beta_{FCM,ave}$ confinement	[-]	0.21	0.26	0.07	0.08	0.13	0.14

In Fig. 5.36, the results of the simulations with the input parameters presented in Table 5.10 are compared with the test results of Pfyl. The simulation results up to the symbol “×” (point 1) in the figures represent the simulations with the average steel properties. The simulation results beyond up to the symbol “○” (point 2) in the figures represent the simulations with an increase in ultimate steel strength from 588 to 605 N/mm^2 and an increase in ultimate steel strain from 7.8 to 10%. The specimens failed due to rupture of one or more reinforcing bars.

Table 5.11 shows the crack widths calculated for the crack with the lower bound tensile strength and a crack with the average tensile strength for the steel stress values 588 (×) and 605 (○) N/mm^2. For the sake of comparison, the crack widths measured in the last load step in the experiments are given.

Table 5.11: Calculated (lb and ave) and measured crack widths in [mm]

Parameter	T100.0	T75.0	T100.30	T75.30	T100.60	T75.60
w_{lb} ×	3.2	3.4	2.4	3.2	2.4	4.4
w_{lb} ○	6.0	6.4	4.4	6.0	4.4	4.4
w_{loc} test	3.5	5.5	4.3	8.0	4.0	4.5
w_{ave} ×	1.9	2.4	1.4	0.95	0.65	0.19
w_{ave} ○	3.5	4.4	2.0	1.2	0.4	0.2
w_{next} test	3.0	4.8	1.0	0.30	0.15	0.15

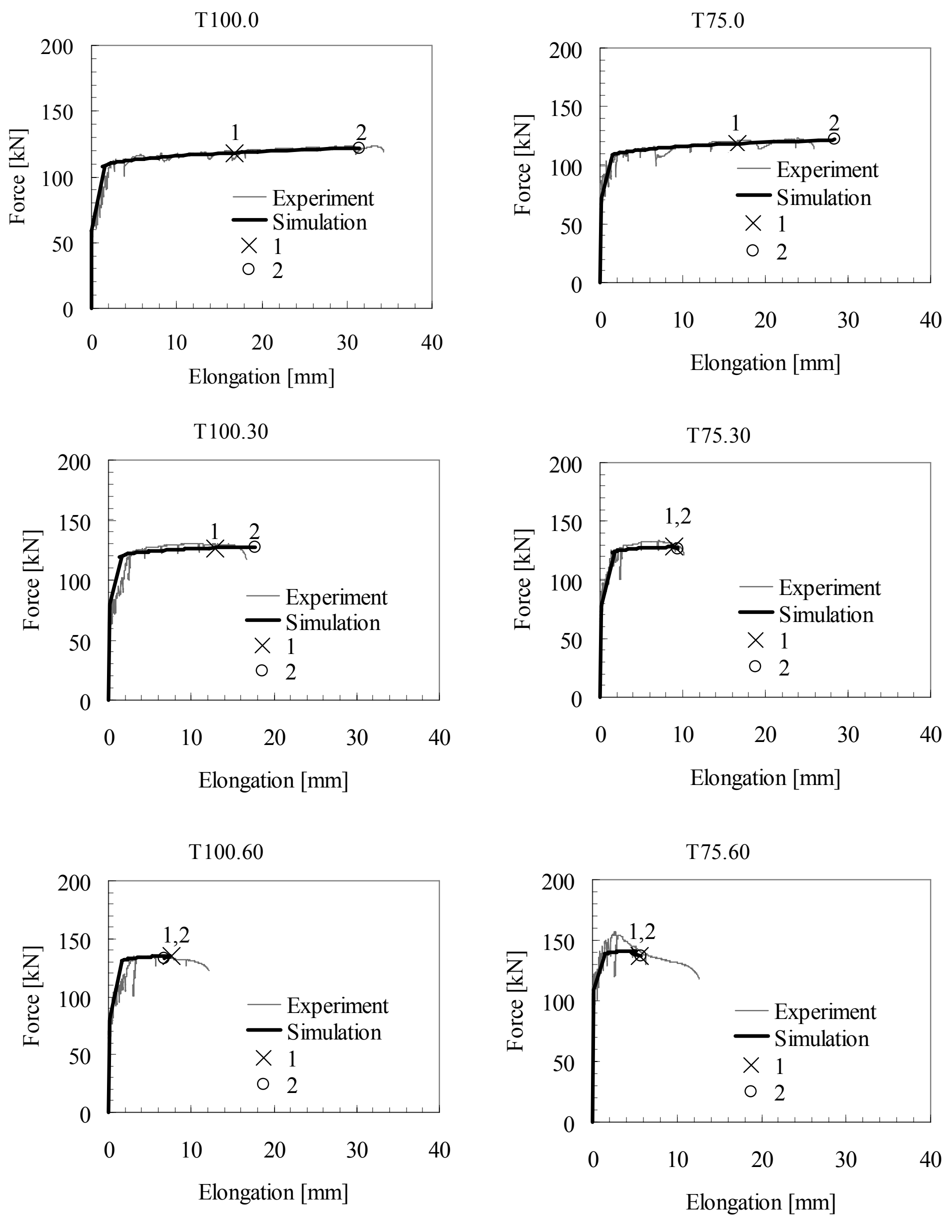

Fig. 5.36: Comparison of test results of Pfyl (2003) with simulation results

The calculations capture well the phenomenon of localization and large crack opening in only one crack in the fiber reinforced specimens. This is more pronounced for larger fiber contents.

From the model and the combined load bearing capacity of the steel (constant 4 bars d_s = 8 mm) plus the SFRC it is understandable that the total load carried by a tensile element with combined reinforcement is larger for SFRC than for concrete without steel fibers (compare the specimens with varying fiber content).

It is noted that in the experiments the steel strains were not measured in detail along the steel bars.

To sum up the major findings from the analysis of the tensile elements, it is important to keep in mind for the further analysis of beams that in case of SFRC, deformations may localize in one single crack. This phenomenon is attributed to the overall softening behavior of the members with steel fibers in the first place and to the scatter of the material properties of SFRC in the second place.

5.7 Concluding Remarks

The main goal of the study described in this chapter was to gain more insight into the effect of steel fibers on the bond behavior. It was found that:

- The addition of steel fibers slightly influenced the bond behavior in case of pull-out bond failure and that it is expected to have a pronounced effect for splitting bond failure.
- The confinement capacity is increased due to fiber addition, even if only few fibers are present in the concrete cover region.
- In case of the simulated behavior of SFRC tensile bars, the deformations localized in one single crack. This phenomenon is attributed to the overall softening behavior of the tensile bar and the scatter of the material properties of SFRC.
- For bar diameters and concrete covers usual in tunneling practice, pull-out failure is expected rather than splitting failure.

Regarding modeling of bond with the proposed model it was concluded that:

- It was shown that, after modifying single input parameters, the bond model of Den Uijl & Bigaj can be used to describe the bond behavior of SCSFRC with satisfactory agreement of experimental and simulation results considering the scatter in test results of pull-out tests and the bond behavior of SFRC in case of tension stiffening tests.
- The proposed bond model can therefore be used to model the tension stiffening and the rotation capacity of SFRC members.
- The analytical bond model of Den Uijl & Bigaj considers the fracture characteristics of concrete by using the stress-crack opening relationship of plain concrete in tension as input. The results obtained with the modified model agreed well with the test results for SFRC. The influence of steel fibers on the bond behavior is considered by using the stress-crack opening relationship for the SFRC in tension as input in the existing model. For this, the model parameters α_{FCM}, β_{FCM} and w_0 were adapted.
- The concrete cone pull-out is expected to be less pronounced for SFRC compared to concrete without fibers. The cone angle ψ_{cpo} is therefore fixed at 89° for SFRC in contrast

to 40° for concrete without fibers. Note that assuming an angle of 89° would be on the conservative side considering the calculation of the rotation capacity.

- Apart from changing the cone angle ψ_{cpo}, the contribution of the fibers in case of pull-out failure are neglected in the model because the experiments showed that the fibers did not influence bond stiffness and bond strength and only slightly influenced the bond ductility in case of pull-out bond failure. From the modeling approach of Den Uijl & Bigaj it is explained that the fibers should not have an influence in pull-out failure.
- In order to include the effect of the different matrix characteristics of SCC on the bond behavior, the parameter τ_{b1}, which determines whether splitting or pull-out failure occurs, was set 5 % higher than for regular concrete.
- The main influence of steel fibers on the tension stiffening behavior in case of pull-out failure lies in their contribution to the stress transfer across the cracks.
- The addition of steel fibers leads to a reduction in crack spacing and to an increased load bearing capacity.
- The addition of steel fibers leads to stiffer member behavior and smaller crack widths in the SLS.
- Depending on the combination of steel fibers (amount, geometry, orientation, bond properties) and reinforcing bars (amount, hardening properties), localization of the deformations in one large crack can occur. The member deformation capacity can thereby be reduced.
- Differently than in RC, for SFRC, the hardening ratio of the tensile member decreases with increasing fiber content due to the softening behavior of the SFRC. The variation of the reinforcement ratio showed that this decrease is more pronounced for smaller steel reinforcement ratios. Localization of the deformations in one crack is most likely to occur in members with a low member hardening ratio, i.e. members with a low steel bar reinforcement ratio and a for large steel fiber content.

6 Rotation capacity of SCSFRC

6.1 Introduction

The use of nonlinear design methods offers possible cost savings, such as savings in the cross-section, in the amount of steel, the volume of soil excavation and in transportation costs. In order to make use of redistribution of forces, it has to be guaranteed that the deformation capacity provided by the structure is higher than a certain required level. The structure only fulfills the safety requirements if the assumed plastic hinges can deform as desired and no premature failure occurs.

The addition of steel fibers increases concrete ductility in tension as well as in compression [Ortu, 2000]. This suggests that it improves as well the rotation capacity of plastic hinges in concrete structures. It should be questioned, however, whether the addition of fiber reinforcement in RC leads to an overall increased rotation capacity. A possible decrease in the overall deformation capacity of RC members manufactured with SFRC would lead to an unsafe design if for plastic design the same procedures are adapted as for ordinary RC.

This chapter provides a calculation model in order to determine the effect of steel fibers on the rotation capacity. The compressive, tensile and bond behavior have been described in the previous chapters and models were proposed. They form the basis for modeling the bending behavior of structural elements. In the following, the tests on RC beams with and without steel fibers are described in section 6.2. The model for calculating the rotation capacity of members with combined steel fiber and bar reinforcement is presented in section 6.3 and compared with test results in section 6.4. Section 6.5 presents the concluding remarks concerning the testing and calculating the rotation capacity.

6.2 Beam Tests

The goal of the test series described in this chapter was to validate the calculation model for the rotation capacity of beams made of steel fiber reinforced concrete, which is proposed in section 6.3. The behavior of a continuous tunnel lining between two subsequent points of inflection is simulated by tests on beams subjected to bending or a combination of bending and compression. This simplification is justified because the point of zero moment and the point of inflection are identical and therefore the rotations at the end of the cut out beam are identical with those in the real structure. In the particular case of curved beams or tunnel segments, the simplification by a one-span straight beam is justified because the differences in load-deformation behavior are approximately 5% [Hemmy, 2003].

The eccentricity of the normal force and the amount of longitudinal reinforcement are decisive parameters in determining whether the failure mode is concrete crushing or steel rupture, see Fig. 6.1. The figure qualitatively shows the rotations Θ for different reinforcement ratios ω_s.

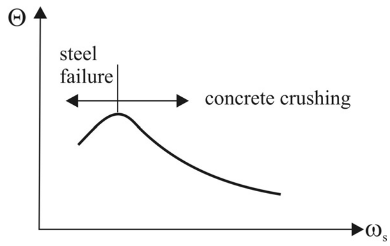

Fig. 6.1: Failure modes depending on the reinforcement ratio (schematic)

The bending tests without normal force were intended to verify the calculation model for steel failure, whereas the bending tests with normal force were intended to verify it for concrete failure. In tunneling, eccentricities e/d of up to 1.0 are usual. Pure bending, i.e. $e/d \rightarrow \infty$, is rather unusual. The combination of normal force and moment influences the failure mode. In an experiment it is possible to increase the normal force and the bending force proportionally, which leads to a constant eccentricity in the tests. In the scope of this research it was chosen to have a constant normal force and a varying bending load. This corresponded to $e/d = \infty$ for the tests without normal force and $0 < e/d < 0.70$ for the tests with normal force. Basically, both approaches of load application lead to the same point of failure on the moment-normal force interaction diagram.

6.2.1 Test Program

Beam tests on self-compacting normal strength concrete (B45) were performed on 3000 mm long, 300 mm deep and 150 mm wide beams with longitudinal reinforcement consisting of two ribbed bars with a diameter of 10 mm but without shear reinforcement. Forces, deformations and crack development were monitored.

As only four tests were carried out, the tests have the character of case studies intended to verify the model, rather than allowing for a statistical verification.

Test Parameters

The chosen test parameters are given in Table 6.1.

Table 6.1: Test program

Test	Concrete grading	Fiber type	Fiber content [kg/m^3]	N [kN]	Failure mode[1)] expected
B45.0.0.N400	B45	-	0	-400	c
B45.0.0.N0	B45	-	0	0	s
B45.80/30.60.N400	B45	80/30	60	-400	c
B45.80/30.60.N0	B45	80/30	60	0	s

[1)] c = concrete crushing, s = steel rupture

The concrete strength class was chosen to be in the range of NSC because at present, tunnel linings are usually made of normal strength concrete rather than high strength concrete.

The reinforcement ratio was chosen to be low (2 bars with a bar diameter of 10 mm, $\rho_s = 0.349\%$), leading to specimen failure in the compressive zone when the normal force was applied and to failure due to steel rupture when no extra normal force was applied. Usually, in tunnel linings, reinforcement is present at both the inner and outer side of the ring or segment because the side subjected to tensile forces changes along the circumference of the ring. However, in the experiments, it was decided not to use longitudinal reinforcement at the compressive side.

It was chosen to test the reference mixture without fibers and one mixture with fibers. The mixture with 60 kg/m^3 fibers ($l_f/d_f = 80$, $l_f = 30$ mm, $d_f = 0.375$ mm) was chosen because it represents a potential fiber volume that is applied in tunnel structures. The normal force applied in the tests was calculated to be roughly the one acting in a 10 m diameter tunnel at 30 m below ground level.

6.2.2 Specimen Geometry and Reinforcement Layout

Geometry of the Test Specimens

All specimens had a specified

- beam height h of 300 mm
- beam width b of 150 mm
- concrete cross-section A_c of 45000 mm^2
- total beam length l_0 of 3000 mm
- span l of 2850 mm
- slenderness l/h of ~10.

Due to insufficient stiffness of the mould, the actual dimensions of the specimens slightly differed. The span was also slightly different in the experiments. The actual values are given in Table 6.2.

Table 6.2: Measurements of the test specimens [in mm]

Test	Width at supports	Width at mid-span	Length	Height	Span
B45.0.0.N400	150	156	3000	300	2850
B45.0.0.N0	150	156	3000	300	2850
B45.80/30.60.N400	150	156	3000	300	2870
B45.80/30.60.N0	150	152	3000	300	2855

Reinforcement Layout of the Test Specimens

The details of the longitudinal reinforcement can be seen in Fig. 6.2 and in Fig. 6.3. It was kept in place by rebar spacers in the vertical direction and by steel bars in two places at a third of the beam length. The ends of the bars were held in the proper position by welded steel plates that also provided the required anchorage capacity.

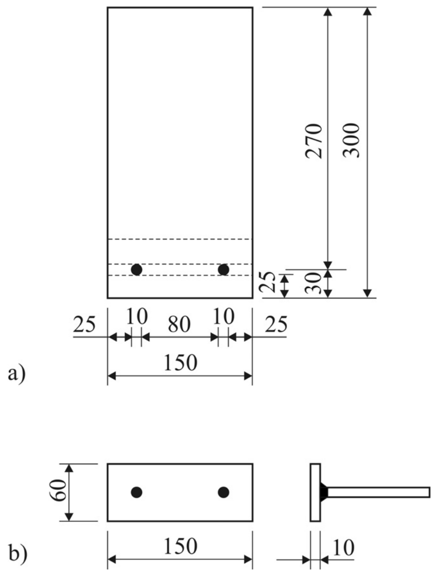

Fig. 6.2: Reinforcement layout (measurements in mm) a) Positions in cross-section b) End anchorage by means of welded steel plates

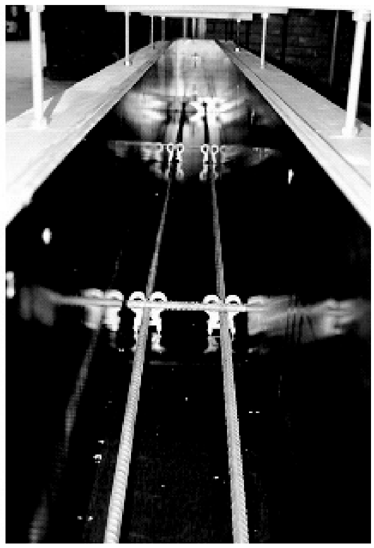

Fig. 6.3: Reinforcement in the mould

6.2.3 Materials

Concrete

Mixtures and Specimen Production

The mixture composition of the self-compacting normal strength concrete used in the beam tests and the control tests, the mixing procedure, and the finishing were identical with those described in chapter 3 for the compressive tests. As the required concrete volume for the beam and the standard test specimens exceeded the capacity of the mixer, the concrete was mixed in two batches of 95 liter each. The properties of the concrete in the fresh state are given in appendix B.

The concrete of the first batch was poured from the mixer into two wheel barrows. The beams were filled up to approximately half of the beam height from the ends of the mould. Then the same procedure was followed for the second batch.

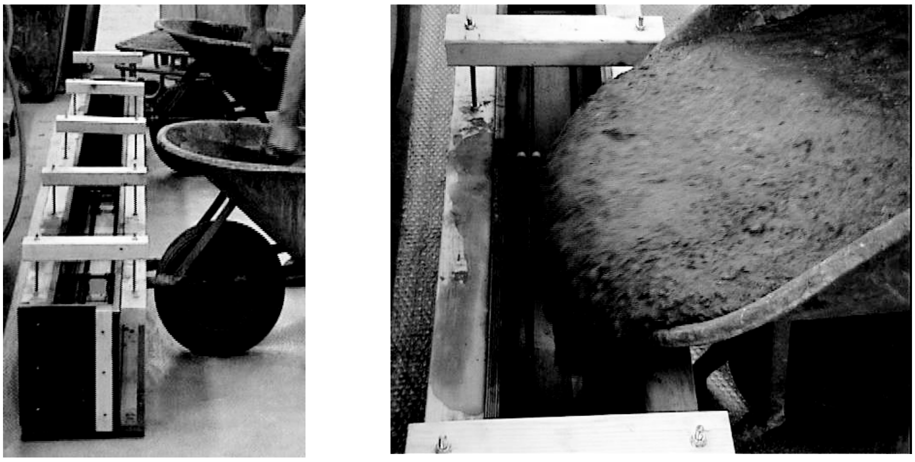

Fig. 6.4: Filling of the beam mould: place (left) and filling (right)

After the concrete had been placed, the moulds were covered with a plastic sheet. The specimens were demoulded after five days and placed in a fog room at approximately 95% RH and 20°C. One week before testing, the beams were stored in the laboratory at about 18°C and 60% RH. After the surface had dried, they were painted with white chalk in order to enable easy crack detection during the tests.

Standard Test Results

The standard tests to determine the strength properties were performed in the same way as described in chapter 3. The mean results and the standard deviations of these tests are given in Table 6.3. Note that the prisms were only used to determine the prism compressive strength. The E-modulus was assumed to be the same as observed in previous tests on the same mixtures (see chapter 3 and 5). A complete overview of the data for all test specimens is given in appendix C.

Table 6.3: Results of standard tests (averages and standard deviations)

Mixture for test	Cube strength [N/mm^2]	Splitting tensile strength [N/mm^2]	Prism strength [N/mm^2]
B45.0.0.N400	55.34 (0.93)	5.16 (0.16)	53.27 (0.51)
B45.0.0.N0	54.27 (1.31)	5.06 (0.15)	51.34 (1.22)
B45.80/30.60.N400	54.51 (1.52)	6.09 (0.40)	49.61 (0.20)
B45.80/30.60.N0	54.86 (0.73)	5.76 (1.05)	49.25 (0.37)
Average	54.75	5.48	50.87

The cube compressive strength was nearly identical for all four mixtures, whereas the prism compressive strength was lower for the SCSFRC specimens compared to the SCC specimens. The ratio of prism compressive strength to cube compressive strength was 0.95 and 0.96 for the SCC specimens and 0.90 and 0.91 for the SCSFRC specimens. Furthermore, the splitting tensile strength of the SCSFRC was larger than that of the SCC.

Steel Fibers

The steel wire fibers used in the experiments had hooked ends, an aspect ratio of 80 and a fiber length of 30 mm. They were collated and had a minimum tensile strength of at least 2000 N/mm^2.

Reinforcing Steel

Hot rolled FeB500 HWL reinforcing steel was used. The effective rib area f_R was determined to be between 0.063 and 0.065 (average 0.064) in standard tests according to the German code DIN 488. According to ENV 10080, the minimum effective rib area f_R for a bar with 10 mm diameter is 0.052.

The stress-strain response of the reinforcing steel was determined experimentally. Table 6.4 gives the yield stress f_{sy}, tensile strength f_{su}, the hardening ratio f_{su}/f_{sy}, the ultimate steel strain ε_{su} measured over 10 times the bar diameter, the effective rib area f_R, and the E-modulus.

It is noted that the steel properties determined for the naked bars are dominated by the weakest cross-section in the measuring range. Hence, the steel properties in the crack are likely to be better, because the location of the crack is determined by the concrete properties and it is unlikely that the weakest cross-sections of the concrete and the steel coincide.

Table 6.4: Results of the standard tests on the reinforcing steel bars

Test	f_{sy} [N/mm^2]	f_{su} [N/mm^2]	f_{su}/f_{sy} [-]	ε_{su} [$^0/_0$]	d_s [mm]	A_s [mm^2]	f_R
1	567	643	1.13	11.4	10.06	79.5	0.065
2	569	643	1.13	12.1	10.09	80.0	0.063
3	577	649	1.12	12.2	10.07	79.6	0.064
Average	571	645	1.13	11.9	10.07	79.7	0.064

The results of the standard steel tests can be seen in Fig. 6.5.

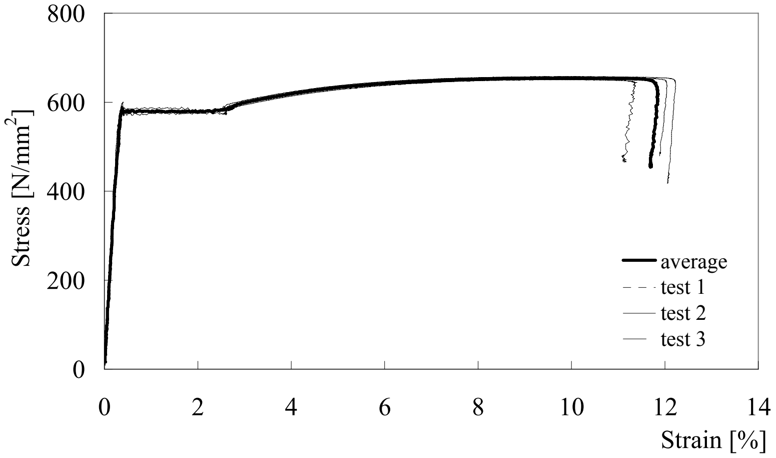

Fig. 6.5: Stress-strain behavior of the reinforcing steel tested on three bars

In the following, the stress-strain behavior of the reinforcing steel is described by the four points given in Table 6.5.

Table 6.5: Material input for the reinforcing steel for further calculations

σ [N/mm^2]	ε [-]
0	0
571	$3.4 \cdot 10^{-3}$
585	$27.0 \cdot 10^{-3}$
645	$118.9 \cdot 10^{-3}$

6.2.4 Fiber Distribution and Fiber Orientation within the Specimens

For steel fiber reinforced self-compacting concrete, the direction of casting may influence the fiber distribution and orientation, and therefore the bending behavior. In order to obtain detailed information on the fiber distribution and fiber orientation in the present tests, some cross-sectional saw cuts were made after testing and pictures were taken of the sawing faces, see Fig. 6.6. After sawing, no additional treatment, e.g. polishing, was applied.

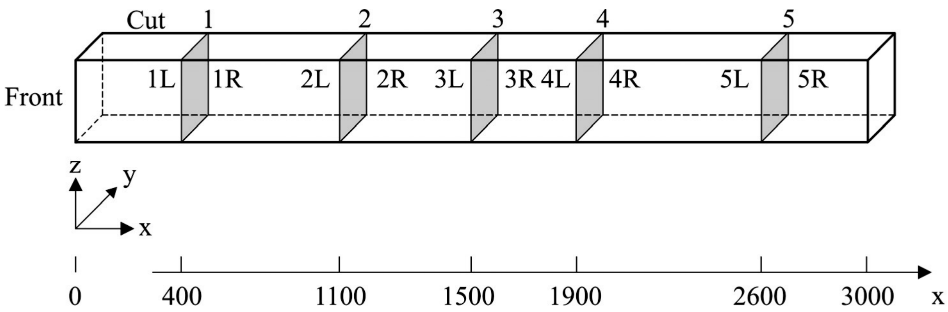

Fig. 6.6: Identification of the saw cuts of the SCSFRC beams

The pictures were taken in a dark room using a camera flash so the fibers reflected the flash and became very well visible. An example of such a picture is shown in Fig. 6.7.

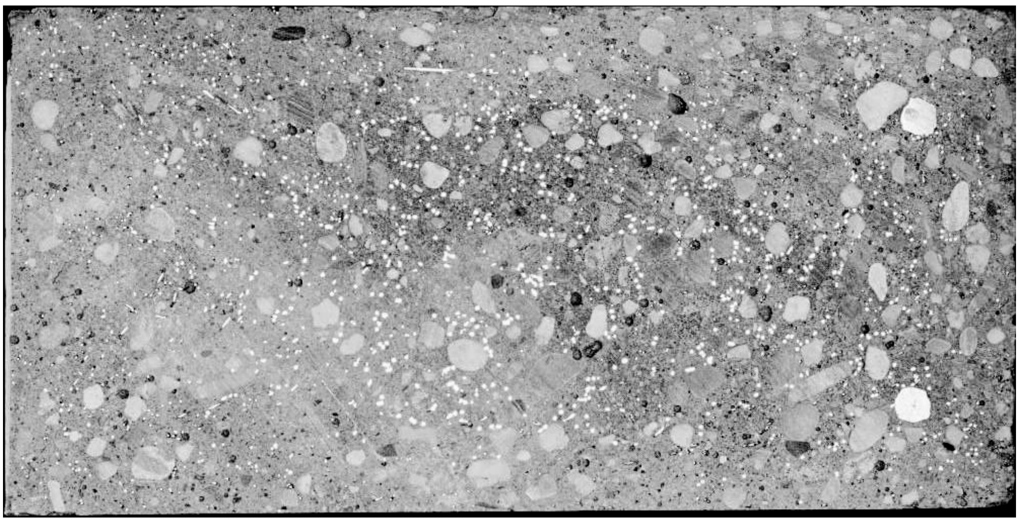

Fig. 6.7: Example of a picture used in the optical analysis (N0 3L turned by 90°)

These pictures were analyzed with the optical analysis program Optimas. Areas of a certain color (fibers) were identified according to predefined threshold values for the colors. The fibers are identified as ellipses and information on their major and minor axis lengths is provided by the software. Due to the flash, the fiber cross-section in some cases appeared smaller or larger in the pictures than they were in reality. Therefore, only those ellipses, which had a minor axis between 0.5 and 3.0 times the real fiber diameter, were taken into account in the further analysis. This did, however, not influence the calculated fiber orientation. From the lengths of the axes and the angle with respect to the principal axes of the ellipse, the fiber orientation in the different directions were determined. The number of fibers in the cross-sections was also counted.

Fiber Distribution and Accuracy of Optical Analysis

The number of fibers in the cross-sections along the beam length can be seen in Fig. 6.8 and Fig. 6.9. According to equation (4.1), the number of fibers assuming a 3D distribution with a fiber orientation factor of 0.5 should be 3.40 per cm^2. The figures show the number of fibers determined from the pictures taken to the left and right hand side and their average.

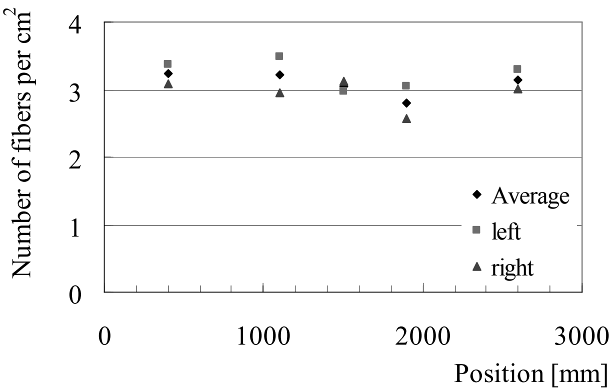

Fig. 6.8: Number of fibers in beam B45.80/30.60.N0

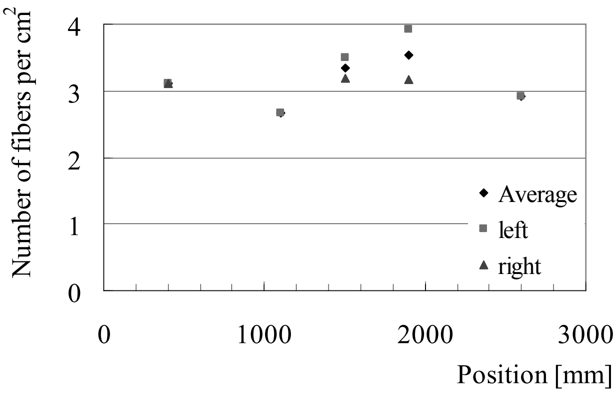

Fig. 6.9: Number of fibers in beam B45.80/30.60.N400

The scatter in the number of fibers found in a single cross-section was rather large. The observed scatter can be considered a result of the accuracy of the observed fiber distribution and orientation. The number of fibers observed in the different cross-sections varied from 2.57 to 3.93 fibers per cm^2. On the average, the observed number of fibers in a picture was slightly lower than the number of fibers expected for a 3D distribution. This can be explained by the fact that the fibers near the edges of the cross-section were not reflected well and therefore not recognized in the optical analysis. The observed number of fibers did not systematically change over the length of the beam.

Fiber Orientation along the Beam Length

To further confirm the 3D distribution of the fibers, an analysis of the fiber orientation numbers was done. The fiber orientation as defined in chapter 4 along the beam length can be seen in Fig. 6.10 and Fig. 6.11.

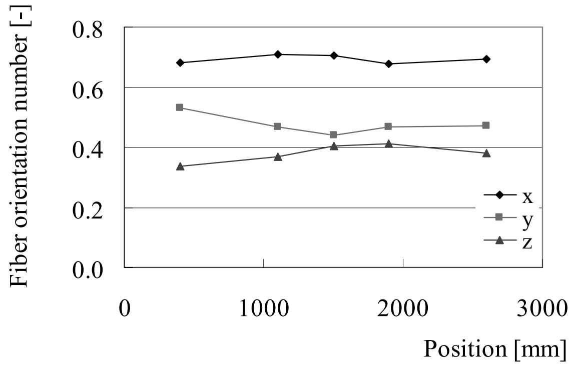

Fig. 6.10: Fiber orientation in beam B45.80/30.60.N0

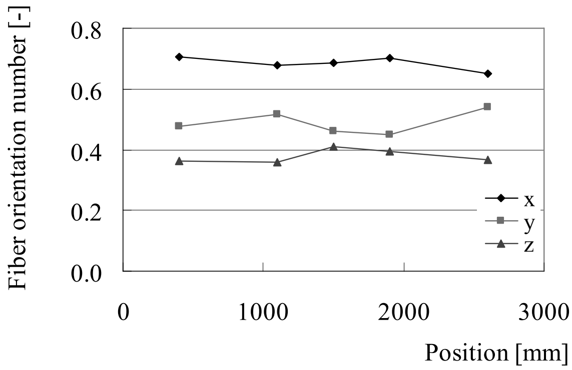

Fig. 6.11: Fiber orientation in beam B45.80/30.60.N400

As can be seen from the figures, the observed fiber orientations did not significantly nor systematically change along the length of the beam. The fibers had a preferred orientation parallel to the x-axis as shown in Fig. 6.10 and Fig. 6.11, which can be attributed to the wall effect of the formwork during casting and the flow direction of the concrete. Therefore, the orientation number in the x-direction is significantly higher than in the y- and z-direction (on average 0.68 in x-direction in contrast to 0.48 and 0.38 in y- and z-direction, respectively).

The orientation in the x-direction is significant for the tensile behavior of the beams, whereas the orientation of the y- and z-direction is significant for the tensile forces perpendicular to the compressive force in the compressive zone of the beams. For further analysis, the orientation number used is 0.68 in the x-direction and 0.43 in the y- and z-direction.

Fiber Distribution and Fiber Orientation over the Beam Height

In addition to the analysis over the beam length, the pictures of beam B45.80/30.60.N0, which were taken to the left hand side (N0 L) were analyzed over the height of the beam. Each quarter of the beam height was analyzed separately and compared with the results over the total beam height. As an example, the analysis of the cross-section in the middle of the beam is shown in Fig. 6.12 and Fig. 6.13.

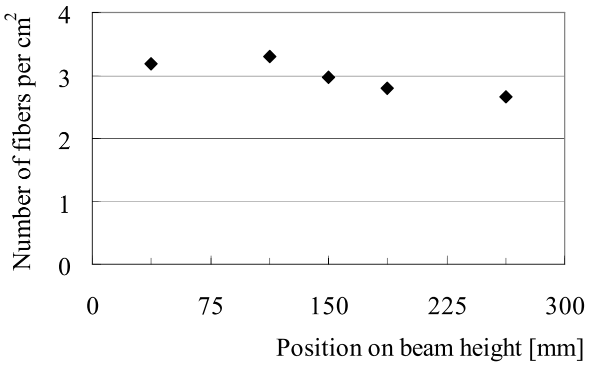

Fig. 6.12: Number of fibers over the beam height in the middle of beam B45.80/30.60.N0

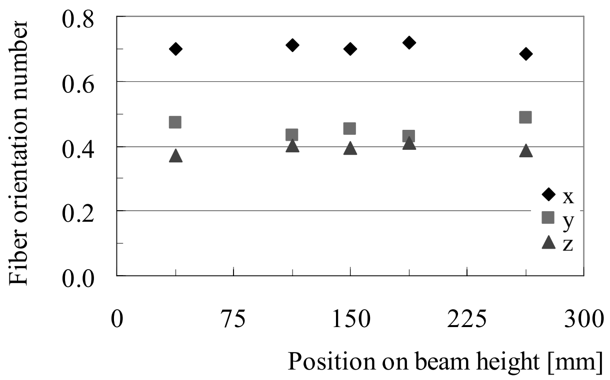

Fig. 6.13: Fiber orientation over the beam height in the middle of beam B45.80/30.60.N0

Although a tendency of more fibers in the top half of the specimen and less in the bottom half seems to apply in the analyzed picture, this tendency is not pronounced and is within the scatter of the cross-section. As this phenomenon was not investigated in detail, it is assumed that the number of fibers as well as the fiber orientations do not significantly or systematically vary over the beam height. Therefore, the concrete properties were assumed to be constant over the beam height.

Fiber Distribution and Fiber Orientation around the Steel Bars

The flash was not reflected well near the specimen edges in most cases. Steel fibers were slightly visible on the photographs but were not reflected well and therefore not captured using the threshold values for the colors. A separate analysis of a picture (N0 3L, see Fig. 6.7), in which the area around the steel bars did well reflect the flash light (picture N0 3L left bar, see Fig. 6.14), was performed. The number of fibers per cm^2 and the fiber orientations are shown in Table 6.6. The orientation was approximately the same as in the whole cross-section. It was therefore chosen to assume the same fiber distribution and fiber orientation in the vicinity of the steel bars as in the remaining concrete cross-section.

Table 6.6: Comparison of the properties around a bar with the whole cross-section for cut N0 3L

Picture	Fibers per cm^2	η_x	η_y	η_z
N0 3L	2.98	0.70	0.45	0.39
N0 3L left bar	3.67	0.71	0.46	0.41

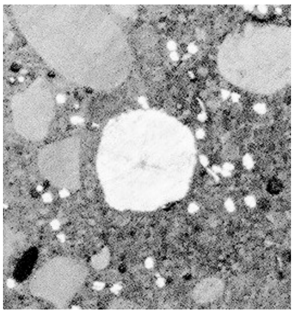

Fig. 6.14: Detail of fiber distribution around a steel bar (N0 3L left bar)

6.2.5 Experimental Set-Up

Load Frame

The test- set-up is shown in Fig. 6.15 and Fig. 6.16. The figure shows the front side of the specimen with the free support at the left hand side and the horizontally fixed support at the right hand side. The load application is explained in the following sections. The position along the beam length was measured from left (x = 0) to right (x = 3000 mm) at the front side.

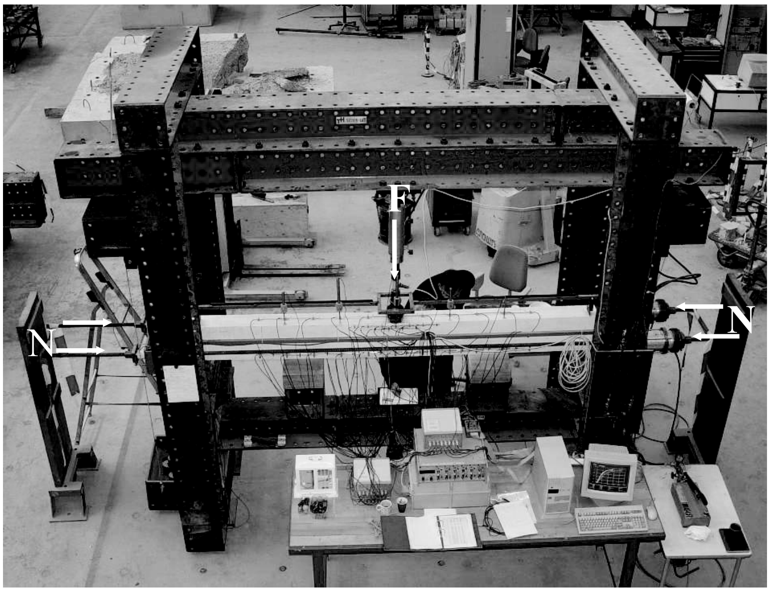

Fig. 6.15: Test set-up with test specimen and measuring devices

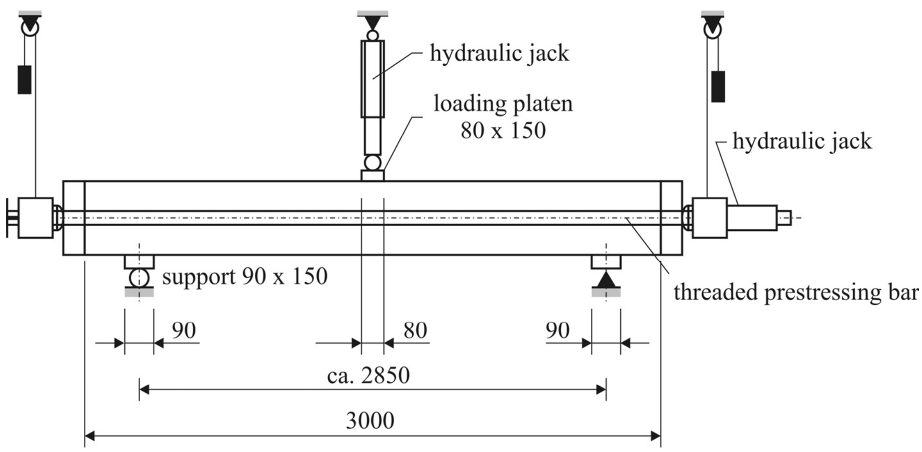

Fig. 6.16: Drawing of the test set-up (measurements in mm)

Boundary Conditions

The loading platen was 80 mm wide. The 90 mm wide supports consisted of line hinges. The support at the left hand side could freely move in the horizontal direction, the support at the right hand side was fixed. The vertical load introduction and the supports are illustrated in Fig. 6.17 to Fig. 6.19.

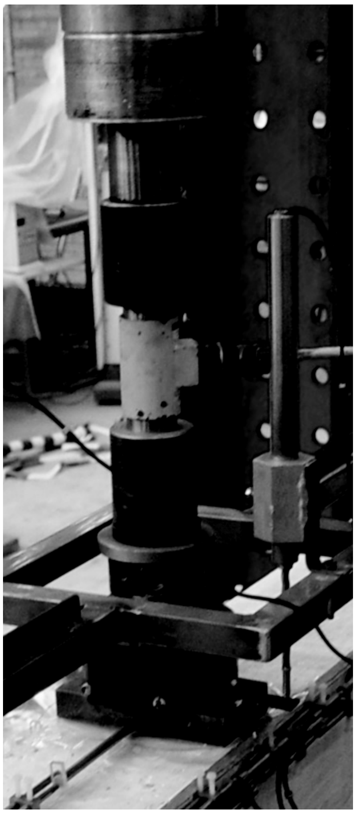

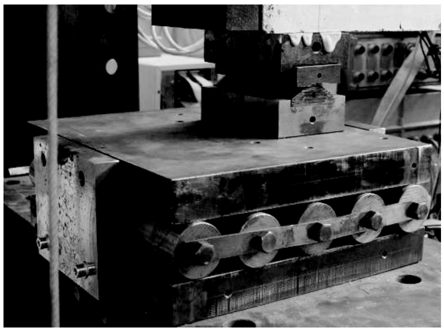

Fig. 6.17: Fixed support

Fig. 6.18: Load introduction at mid-span

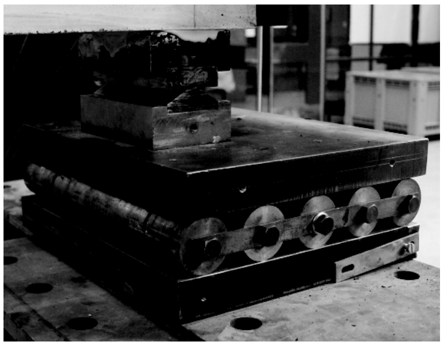

Fig. 6.19 Roller support

Application of the Normal Force

The normal force was approximately constant throughout the tests. Therefore, a set-up was chosen in which the normal force could be controlled independently of the transverse load at mid-span and adjusted if necessary. The application of the normal force is illustrated in Fig. 6.20 and Fig. 6.21.

The normal force was applied as external prestressing with hinges between the loading platens and the hydraulic jacks and load cells, respectively. The weights of the steel parts were counter-balanced to prevent transverse forces at the beam ends.

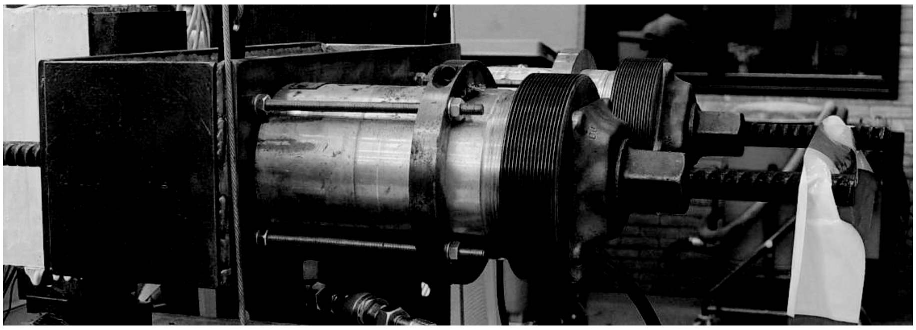

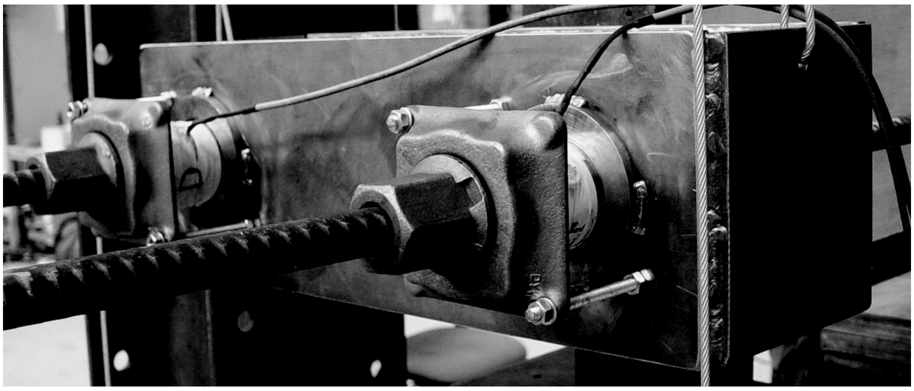

Fig. 6.20: Test set-up for applying the normal force (top: hydraulic jack, bottom: load cell)

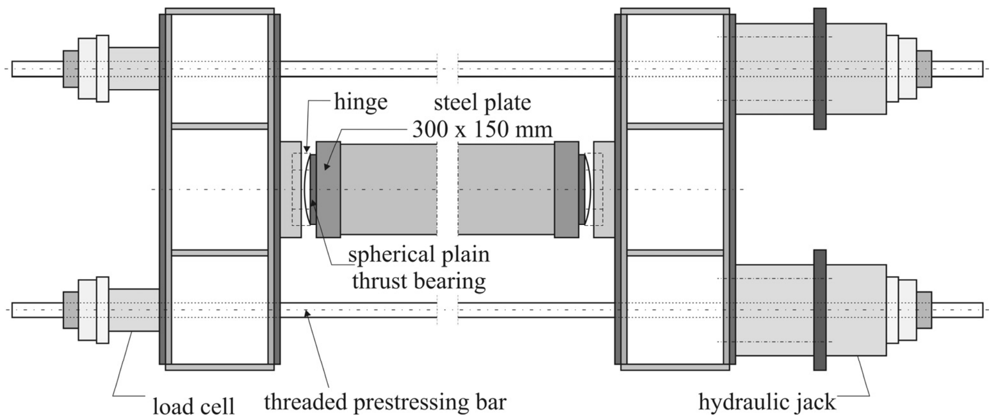

Fig. 6.21: Set-up for applying the normal force

Measurements

The following measurements were used to assess the information needed to calculate the beam rotation from the experiments:

- local strains
- deflections
- crack widths and crack lengths
- loads.

Local Strains

The compressive zone in the middle of the beam had to be thoroughly investigated because localization of failure was expected to occur there. Over a total length of 2000 mm, the compressive strains were measured at the top of the specimen by LVDT09 to LVDT18. At both sides of the specimen, the strains were measured in two rows (see Fig. 6.22 and Table 6.7).

The deformations at the level of the reinforcing bars were measured at each side of the specimen. The tensile deformations were also measured at the bottom of the specimen.

The arrangement of the strain measuring devices allowed the determination of the place and magnitude of the localization of deformations.

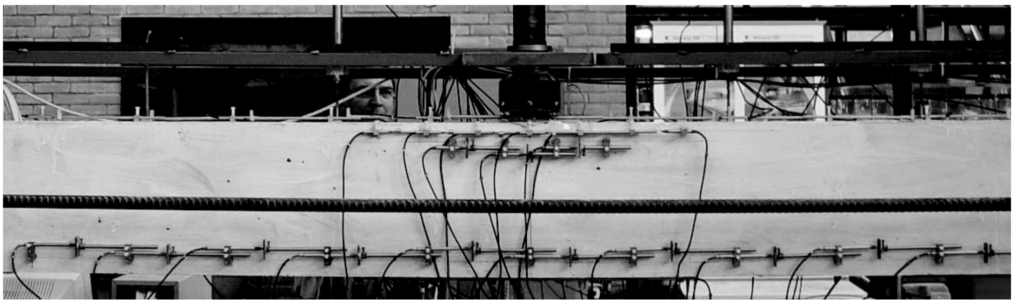

Fig. 6.22: LVDT's on the back side of the beam and measuring frame for deflection measurements

The LVDT's at the back side of the beam can be seen in Fig. 6.22. An overview over the position of the measuring devices for the local strains can be seen in Table 6.7. The values for the length and the middle of the section correspond to the values on the x-axis in Fig. 6.6. The range and the sensitivity of the LVDTs can be found in appendix H. The accuracy was 0.1%.

Table 6.7: Numbering and position of the LVDTs

<table>
<tr><td>Length of the section [mm]</td><td>200</td><td>200</td><td>200</td><td>100</td><td>100</td><td>50</td><td>50</td><td>50</td><td>50</td><td>50</td><td>50</td><td>50</td><td>50</td><td>100</td><td>100</td><td>200</td><td>200</td><td>200</td></tr>
<tr><td>Middle of the section [mm]</td><td>600</td><td>800</td><td>1000</td><td>1150</td><td>1250</td><td>1325</td><td>1375</td><td>1425</td><td>1475</td><td>1525</td><td>1575</td><td>1625</td><td>1675</td><td>1750</td><td>1850</td><td>2000</td><td>2200</td><td>2400</td></tr>
<tr><td>Place</td><td colspan="18">Number of the LVDT</td></tr>
<tr><td>Compression zone top</td><td>9</td><td>10</td><td>11</td><td colspan="2">12</td><td colspan="4">13</td><td colspan="4">14</td><td colspan="2">15</td><td>16</td><td>17</td><td>18</td></tr>
<tr><td>Compression zone front face top</td><td colspan="4"></td><td>19</td><td colspan="2">20</td><td colspan="2">21</td><td colspan="2">22</td><td colspan="2">23</td><td>24</td><td colspan="4"></td></tr>
<tr><td>Compression zone front face lower</td><td colspan="6"></td><td colspan="2">25</td><td colspan="2">26</td><td colspan="2">27</td><td colspan="6"></td></tr>
<tr><td>Compression zone rear face top</td><td colspan="4"></td><td>33</td><td colspan="2">32</td><td colspan="2">31</td><td colspan="2">30</td><td colspan="2">29</td><td>28</td><td colspan="4"></td></tr>
<tr><td>Compression zone rear face lower</td><td colspan="6"></td><td colspan="2">36</td><td colspan="2">35</td><td colspan="2">34</td><td colspan="6"></td></tr>
<tr><td>Tensile zone front face</td><td>37</td><td>38</td><td>39</td><td colspan="2">40</td><td colspan="4">41</td><td colspan="4">42</td><td colspan="2">43</td><td>44</td><td>45</td><td>46</td></tr>
<tr><td>Tensile zone rear face</td><td>56</td><td>55</td><td>54</td><td colspan="2">53</td><td colspan="4">52</td><td colspan="4">51</td><td colspan="2">50</td><td>49</td><td>48</td><td>47</td></tr>
<tr><td>Tensile zone bottom</td><td colspan="4"></td><td colspan="3">57</td><td colspan="4">58</td><td colspan="3">59</td><td colspan="4"></td></tr>
</table>

Deflections

With LVDT04 to LVDT08, the deflections were measured at mid-span and in a distance of 400 and 800 mm from mid-span to both sides. The deflections were measured with respect to the supports. The LVDTs were fixed to a frame that was placed at the top of the beam, its supports coinciding with the supports of the beam. The rotations of the beam were also calculated from these deflections in order to have a check for the rotations calculated from the strains.

Crack Widths and Crack Heights

The crack widths were approximately measured at every load step with a crack ruler. The crack heights were drawn at the back side of the beam with the numbers indicating the load steps at which they were detected.

Loads

The load was increased in steps of 5 kN until the predicted maximum load was almost reached. Thereafter, loading was continued by increasing stepwise the deflection at mid-span. The duration of the tests was between 1.5 and 4.5 hours. The criteria for the measurements were steps in time, load or deformation (whichever reached the criterion first). 550 to 950 measurement scans were recorded per test.

6.2.6 Test Results and Discussion

Cracking Behavior

The developed crack pattern in the middle 1200 mm of the beams can be seen in Fig. 6.23 to Fig. 6.26. The pictures were taken at the back side of the specimens after testing. For better visibility, the cracks were marked with a black line directly next to the actual cracks. The numbers indicate the load steps. In the following, the crack widths at the final load step before failure are presented. The crack widths for all load steps can be found in appendix J.

Specimen B45.0.0.N400

In specimen B45.0.0.N400, a total number of 14 cracks was observed in the middle 1200 mm measuring length. This results in an average crack distance s_{cr} of 92.3 mm, see Fig. 6.23 and Table 6.8. The specimen failed due to concrete crushing. The deformations localized in two large cracks.

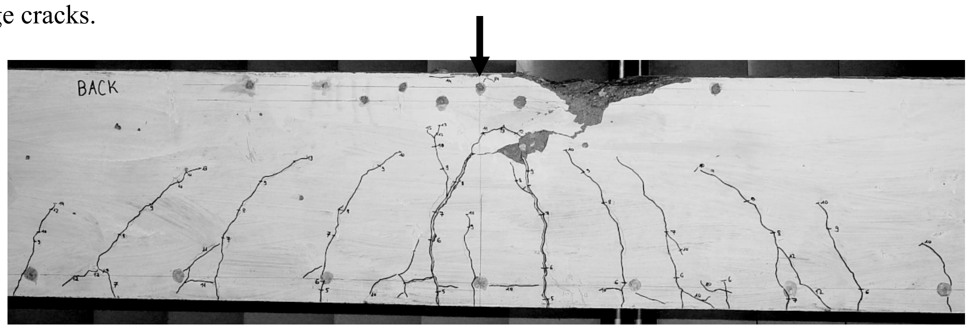

Fig. 6.23: Crack pattern of specimen B45.0.0.N400

Table 6.8: Crack widths w_i [mm], crack lengths a_i [mm] and crack opening angles $\Theta_{cr,i}$ [mrad] for the cracks in order of appearance from left to right at the final load step for B45.0.0.N400

No	1	2	3	4	5	**6**	7	**8**	9	10	11	12	13	14
w_i	0.05	0.25	0.35	0.35	<	**2**	0.1	**2.3**	0.35	0.3	<	0.35	0.2	<
a_i	130	170	180	220		**220**	120	**220**	200	190		170	150	90
$\Theta_{cr,i}$	0.4	1.5	2.0	1.6		**9.1**	0.8	**10.5**	1.8	1.6		2.1	1. 3	

Specimen B45.0.0.N0

In specimen B45.0.0.N0, a total number of 18 cracks was observed in the middle 1200 mm measuring length. This results in an average crack distance s_{cr} of 70.6 mm, see Fig. 6.24 and Table 6.9. This test was the only test with obvious secondary cracking, i.e. cracking at larger deformations long after the primary crack pattern had developed (see appendix J). Up to failure it was not clear whether the specimen would fail due to concrete crushing or steel rupture. Finally, the specimen failed due to concrete crushing. The deformations localized in four large cracks.

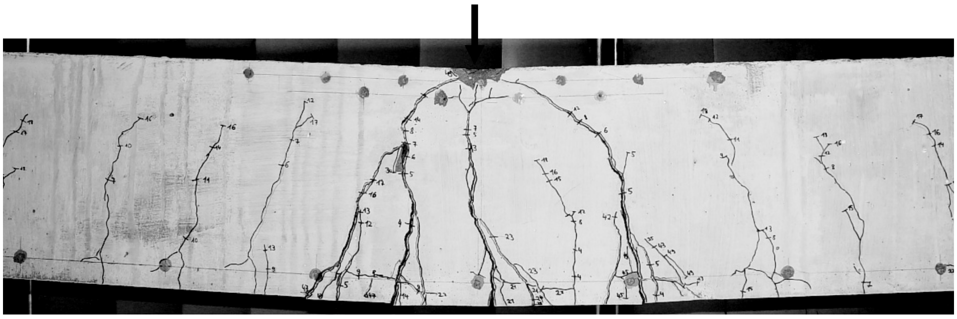

Fig. 6.24: Crack pattern of specimen B45.0.0.N0

Table 6.9: Crack widths w_i [mm], crack lengths a_i [mm] and crack opening angles $\Theta_{cr,i}$ [mrad] for the cracks in order of appearance from left to right at the final load step for B45.0.0.N0

No.	1	2	3	4	5	**6**	**7**	8	**9**	10	11	12	**13**	14	15	16	17	18
w_i	0.2	0.25	0.2	0.2	0.1	**4**	**5.5**	0.6	**4.5**	1	0.15	1	**4**	1	<	0.35	0.2	0.2
a_i	230	230	210	250	60	**280**	**280**	280	**260**	260	180	280	**280**	280		250	200	210
$\Theta_{cr,i}$	0.9	1.1	1.0	0.8	1.7	**14.3**	**19.6**	2.1	**17.3**	3.9	0.8	3.6	**14.3**	3.6		1.4	1	1.0

Specimen B45.80/30.60.N400

In specimen B45.80/30.60.N400, a total number of 32 cracks was observed in the middle 1200 mm measuring length. This results in an average crack distance s_{cr} of 38.7 mm, see Fig. 6.25 and Table 6.10. The specimen failed due to concrete crushing. The deformations localized in one large crack.

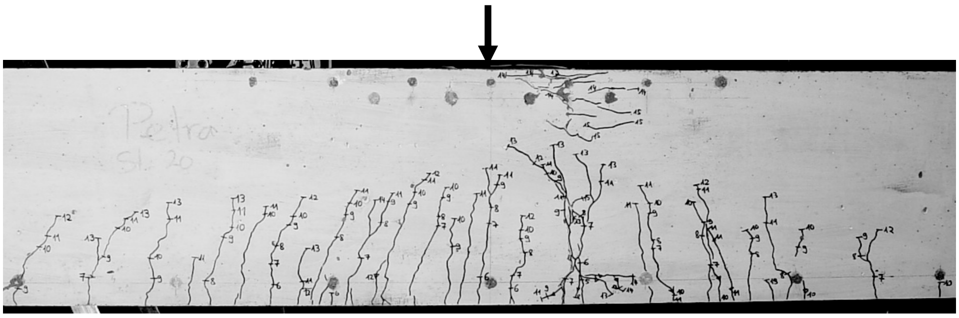

Fig. 6.25: Crack pattern of specimen B45.80/30.60.N400

Table 6.10: Crack widths w_i [mm], crack lengths a_i [mm] and crack opening angles $\Theta_{cr,i}$ [mrad] for the cracks in order of appearance from left to right at the final load step for B45.80/30.60.N400

No.	1	2	3	4	5	6	7	8	9	10	11	12	13	14	15	16
w_i	<	0.1	<	<	<	0.05	<	<	<	<	<	<	<	<	<	0.05
a_i		120				120										100
$\Theta_{cr,i}$		0.8				0.4										0.5

No.	17	18	19	**20**	21	22	23	24	25	26	27	28	29	30	31	32
w_i	<	<	<	**3.1**	<	<	<	<	<	<	<	<	<	<	0.05	<
a_i				**200**		150									100	
$\Theta_{cr,i}$				**15.5**											0.5	

Specimen B45.80/30.60.N0

In specimen B45.80/30.60.N0, a total number of 23 cracks was observed in the middle 1200 mm measuring length. This results in an average crack distance s_{cr} of 54.5 mm, see Fig. 6.26 and Table 6.11.

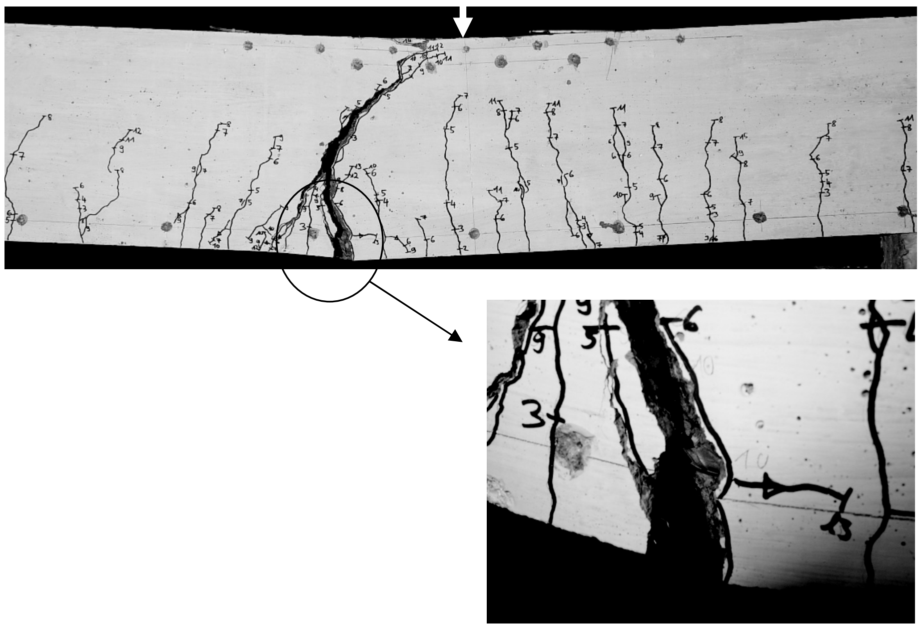

Fig. 6.26: Crack pattern of specimen B45.80/30.60.N0

Table 6.11: Crack Crack widths w_i [mm], crack lengths a_i [mm] and crack opening angles $\Theta_{cr,i}$ [mrad] for the cracks in order of appearance from left to right at the final load step for B45.80/30.60.N0

No.	1	2	3	4	5	6	7	8	9	**10**	11	12	13	14	15	16	17	18	19	20	21	22	23
w_i	0.05	0.1	0.05	<	0.05	<	<		<	**14**	0.05	<	0.1	0.05	0.05	0.05	0.05	0.05	<	<	0.05	0.1	0.05
a_i	170	160	180		160					**280**	130		230	100	210	200	200	200			150	160	160
$\Theta_{cr,i}$	0.3	0.6	0.3		0.3					**50.0**	0.4		0.4	0.5	0.2	0.3	0.3	0.3			0.3	0.6	0.3

It can be seen that the crack spacing in the SCSFRC was much smaller than that of the SCC. The average crack distances found at the end of the tests are summarized in Table 6.12. These values already include secondary cracking. The average crack distance in the primary crack pattern was larger. The specimen failed due to rupture of a steel bar. The deformations localized in one large crack.

Table 6.12: Number of cracks n_{cr} and average crack distances [mm] in the 1200 mm center region

Test	n_{cr} [-]	average crack distance s_{cr} [mm]
B45.0.0.N400	14	92
B45.0.0.N0	18	71
B45.80/30.60.N400	32	39
B45.80/30.60.N0	23	54

Crack Spacing in the Various Tests

The crack distance observed in the SCSFRC beams was 0.42 times that for SCC in case of $N = 0$ and 0.77 times that for SCC in case of $N = -400$ kN.

The reduced crack spacing due to fiber addition can be explained by the fact that stresses are transferred across the cracks by the fibers and therefore, the concrete tensile strength is reached again within a shorter transmission length, see chapter 5.

The observed tendency roughly corresponds with the recommendation by Dupont & Vandewalle (2003) to reduce the calculated crack spacing of SFRC by 50/aspect ratio of the fibers compared to conventional concrete for comparable fiber contents, which would result in a reduction factor of 50/80 = 0.625 in the present study.

Crack Opening

In the SCC beams, several cracks had the same crack widths initially. Later, the deformations localized in two and four cracks for the beams with and without normal force, respectively with crack widths up to 1 mm in neighboring cracks.

In the SCSFRC beams, localization of the deformations in one crack could be observed as soon as the first crack reached a crack width of 0.05 mm (the smallest crack width that could be quantified). The neighboring cracks only had crack widths up to 0.1 mm at failure.

This localization of the deformations in one single crack in case of SCSFRC is attributed to the overall softening behavior of the SCSFRC specimens. The scatter of the fiber distribution and orientation in SCSFRC also plays a role in this. Due to the contribution of the fibers to the transmission of forces across the cracks, the reinforcing bars are less likely to yield in the cracks other than the dominant crack. For more information, see section 6.3.

Load Bearing Capacity

An overview of the maximum forces and mid-span deflections as well as the failure modes observed in the tests is given in Table 6.13. The moment at mid-span was calculated from the transverse and normal forces, taking into account the dead weight of the concrete, the effect of 2nd order theory and the friction in the hinge over which the normal force was applied:

$$M = \frac{F \cdot l^2}{4} + N \cdot u_{v,LVDT06} + M_{dead\_weight} - N \cdot \mu \cdot r_h \tag{6.1}$$

where:

$u_{v,LVDT06}$ deflection measured at mid-span
μ coefficient of friction assumed to be 0.2 based on Schneider (1994)
r_h radius of the hinge 0.065 m (see Fig. 6.21)

With the assumed coefficient of friction of 0.2, the moment due to friction in the hinge results in 5.2 kNm. Assuming the coefficient of friction between 0.1 and 0.3 would result in a moment due to friction of 2.6 to 7.8 kNm.

Table 6.13: Overview over the maximum forces and deflections

Test	Fmax [kN]	$u_{v,LVDT06}$ at Fmax [mm]	M at Fmax [kNm]	N at Fmax [kN]	$u_{v,LVDT06}$ at failure [mm]	Failure mode [1)]
B45.0.0.N400	94.2	13.4	71.5	-410.6	24.2	c
B45.0.0.N0	36.2	55.0	27.0	0	60.1	c
B45.80/30.60.N400	103.4	12.9-14.4	76.1	-409.1	18.3	c
B45.80/30.60.N0	40.9	9.9-25.9	30.4	0	41.7	s
N400 ratio SCSFRC/SCC	1.10		1.07		0.75	
N0 ratio SCSFRC/SCC	1.13		1.13		0.70	

[1)] c = concrete crushing, s = steel rupture

From Table 6.13 it can be seen that the fiber reinforced specimens carried approximately 10% higher loads but had approximately 30% lower total deflections at maximum load. The ratio of the moments is not as large as that of the applied vertical forces because in the calculation of the moment the contribution due to dead weight is assumed to be the same in all cases.

The increase of the maximum load and the decrease of the maximum deformation due to fiber addition are discussed in the following section.

Deformation Capacity

Fig. 6.27 and Fig. 6.28 show the moment – mid-span deflection curves of the four beam tests.

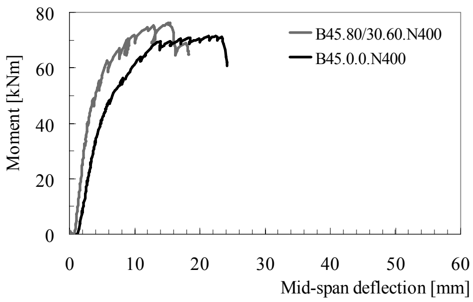

Fig. 6.27: Moment-deflection curves for B45.0.0.N400 and B45.80/30.60.N400

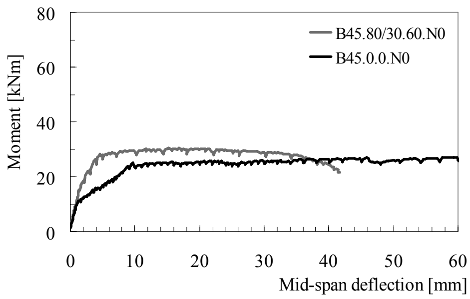

Fig. 6.28: Moment-deflection curves for B45.0.0.N0 and B45.80/30.60.N0

From the obtained information, several aspects are worth considering:

- cracked stiffness
- deflection at maximum load
- deflection at the last load step
- rotation capacity.

The observations from the four tests are summarized and discussed in the following.

Stiffness

The cracked SCSFRC specimens are stiffer than those made of SCC. The main reason for this is that in the former case, the fibers bridge the cracks and thus contribute to the load transfer. Hence, at the same load level, the steel carries the total load minus the contribution of the fibers. This results in lower average steel stresses and strains, smaller crack widths and a higher stiffness compared to concrete without fibers at the same load level.

Deflection at Maximum Load

The magnitude of the deflection at maximum load is highly sensitive to the method of defining the maximum load. In case of a plateau it is more useful to define a range in which the maximum is reached and render the corresponding deflections of the upper and lower boundary of the range. These boundaries are shown in Fig. 6.29. For further information about the load steps, see appendix I.

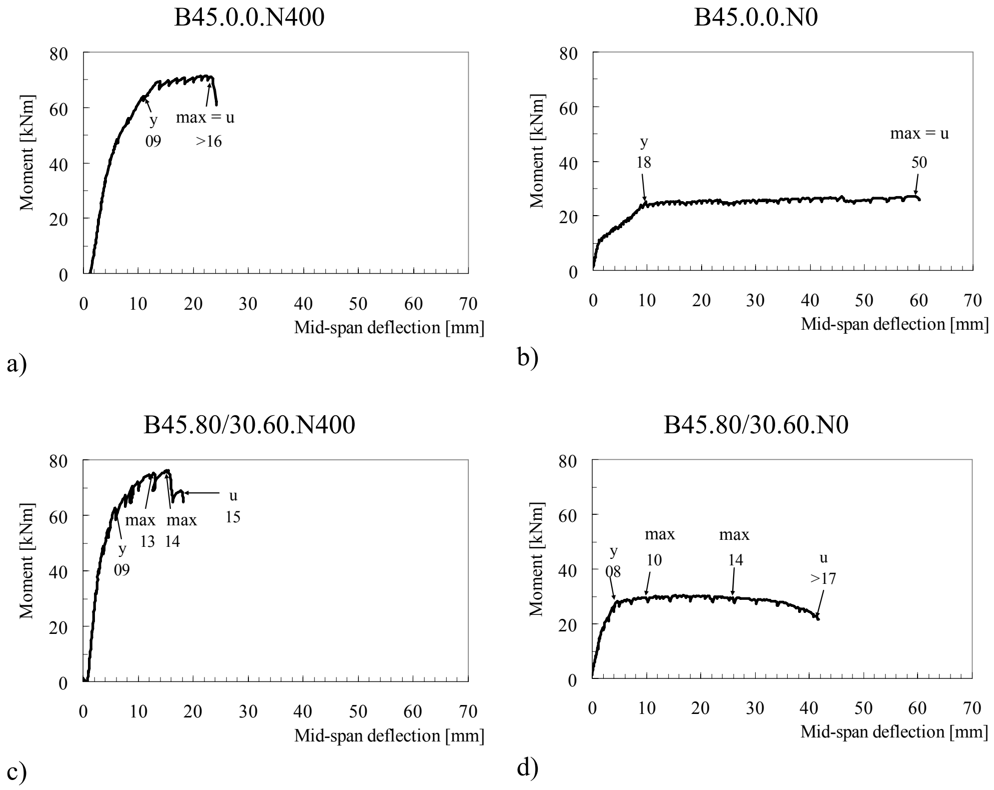

Fig. 6.29: Moment versus mid-span deflection curves indicating the load step (e.g. 09), the onset of yielding of the reinforcing bar (y), the maximum moment (max), and the ultimate moment (u)

In the tests with a normal force, the SCSFRC specimens had approximately 30% smaller deflections at maximum load than the SCC ones.

In the tests without normal force, the plastic deformations are larger than in the tests with normal force. For the tests without normal force, the deflections at maximum moment cannot unambiguously be indicated. Therefore, a range of deflections is given over which the moment practically equals the maximum.

The explanation for the localization in one large crack rather than several large cracks is the overall softening or hardening behavior in a cross-section. In case of RC, overall hardening behavior can be expected in a cross-section due to the hardening of the reinforcing steel. Hence, yielding of the reinforcing steel can also be reached in a neighboring crack. In case of SFRC, however, the softening of the SFRC can be dominant, resulting in an overall softening behavior of the cross-section in spite of the hardening of the reinforcing steel. The remaining tensile force is insufficiently large to build up the force that is necessary to further open a neighboring crack.

The scatter in material properties of the SFRC determines – in combination with the magnitude of the moment – the position of the cross-section in which the cracks form. Due to the scatter, it is likely that the neighboring cracks have a larger fiber contribution (higher fiber concentration) than the first crack and that this fiber contribution leads to a stronger resistance against crack opening.

Rotations

An overview over the rotations measured with the different methods is given in Table 6.14. The rotations have been calculated on the basis of:

- deflections (measured by LVDT06 at mid-span)
- strains (average of the tensile strains at the front and the back of the specimens at the level of the reinforcing bars and the compressive strains measured at the top, indicated by Ctop)

The rotations calculated from the deflections at mid-span are indicated as LVDT06 in Table 6.14. The rotations calculated from the compressive strains at the top and the tensile strains at the front and back of the specimen at the level of the reinforcing bars are indicated as Ctop TZ average front/back in Table 6.14. The exact position of the measuring devices is given in Table 6.7.

Table 6.14: Measured rotations

Test	Load level	Θ LVDT06 [mrad]	Θ Ctop TZ average front/back [mrad]	Θ average [mrad]
B45.0.0.N400	Fy	19	18	19
	Fmax = Fu	33	33	33
	Fu - Fy	14	14	14
B45.0.0.N0	Fy	14	15	14
	Fmax = Fu	84	81	83
	Fu - Fy	70	66	68
B45.80/30.60.N400	Fy	8	11	10
	Fmax 13	18	22	20
	Fmax 14	20	24	22
	Fu	25	29	27
	Fmax 13-Fy	10	11	10
	Fmax 14-Fy	12	13	12
	Fu - Fy	17	18	17
B45.80/30.60.N0	Fy	7	9	8
	Fmax 10	14	17	15
	Fmax 14	36	38	37
	Fu	58	59	59
	Fmax 10 - Fy	7	8	8
	Fmax 14 - Fy	30	29	29
	Fu - Fy	52	50	51

The SCSFRC specimen that was tested without normal force had a lower rotation capacity ($\Theta_{max} - \Theta_y$) than that made of SCC. The rotation capacity was 8/68 = 12% to 29/68 = 43% of that of the SCC specimen. The rotation at ultimate load minus the rotation at the onset of yielding ($\Theta_u - \Theta_y$) was 51/68 = 75% of that of the SCC specimen.

For the specimens tested with a normal force, the rotation capacity ($\Theta_{max} - \Theta_y$) of the SCSFRC specimen was 10/14 = 71% to 12/14 = 86% of that of the SCC one. However, the rotation at ultimate load minus that at the onset of yielding ($\Theta_u - \Theta_y$) of the SCSFRC specimen was 17/14 = 121% of that of the SCC one. So, depending on the definition of the rotation capacity and on the criteria that belong to it, different conclusions can be drawn regarding the effect of the fiber addition on the rotation capacity. The increase in the tests with normal force is due to the increase in ductility of concrete in compression when fibers are added, as explained in chapter 3. The decrease of the rotation capacity in the tests without normal force is explained with the localization of failure in only one large crack when fibers are added in contrast to large crack openings of several cracks in case of concrete without steel fibers.

6.3 Modeling the Rotation Capacity of SFRC

In conventional design of RC members, e.g. Eurocode 2 (1992), ductile steel failure is aimed at. Modeling the bending behavior of structural elements is based on uniaxial constitutive relationships. In the proposed model, this has been achieved by using the general approaches followed by Langer (1987) and Bigaj (1999) and - where necessary - by taking into account the differences in material input and modeling for SCC and SCSFRC compared to conventional concrete. The model takes into account:

- material properties (concrete strength and ductility, steel strength and ductility, bond behavior)
- geometry (height, width, slenderness, longitudinal reinforcement ratio)
- type of loading (moment or moment plus normal force).

The program can be applied in case of:

- in-plane bending without and with normal force
- rectangular cross-section
- steel bar reinforcement in the tensile and compressive zone.

Description of the Model

The general procedure for the calculation of the behavior for hinge type A, see Fig. 1.6, can be summarized in the following steps. These steps are further described and explained in the sections 6.3.1 to 6.3.7.

Step 1: The material properties and the cross-sectional dimensions are specified.
Step 2: The average crack distance s_{cr} is determined assuming a fully developed primary crack pattern.
Step 3: The steel and concrete strain in the cracks of the tie are determined.
Step 4: The concrete strains in the compressive zone of cracks are determined.
Step 5: The average curvature in an element between two subsequent cracks is determined.
Step 6: The rotation is calculated at different load levels.
Step 7: The plastic rotation is calculated.

6.3.1 Material and Geometry Input (Step 1)

Material Input

The model used for the calculation of the rotation capacity is based on the assumptions for the compressive behavior given in chapter 3, for the tensile behavior in chapter 4 and for the bond behavior in chapter 5. Furthermore, the following assumptions were made in the scope of the rotation calculation procedure:

- Only ribbed bar reinforcement with an effective rib area f_R according to ENV 10080 is considered.
- The loading history and the time-dependent behavior of the material is not considered.

Steel

The steel properties are simplified by a 4-point polygon, see Fig. 6.30. In the simulations, the steel properties are taken from standard tests, if available.

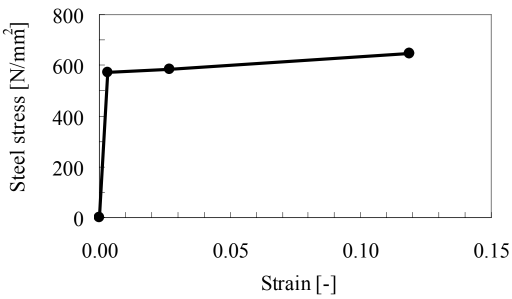

Fig. 6.30: Example of the input of the steel properties

Concrete in Tension

The concrete properties in tension are described as 4-point polygon relations, with a linear ascending branch (stress-strain relation, see Fig. 6.31, left) and a bilinear descending branch (stress-crack width relation, see Fig. 6.31, right).

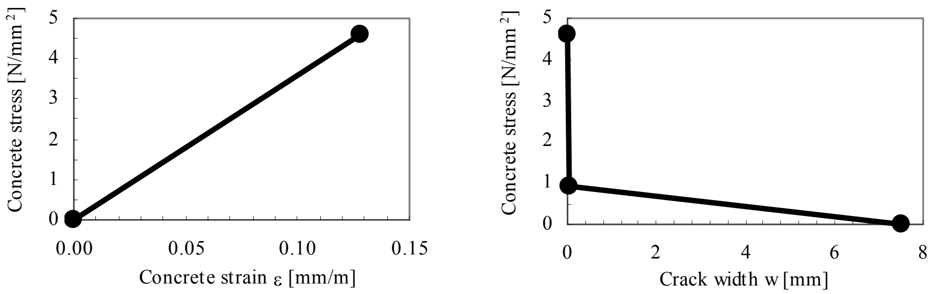

Fig. 6.31: Example of the input of the properties of concrete in tension

As explained in chapter 4, due to the anisotropy of the SFRC, the properties of concrete in tension are explicitly defined in two distinct directions: parallel and transverse to the beam axis. This provides the possibility to take into account the fiber orientation within the specimen. In this way a distinction is made between the influence of the fibers on the confinement capacity on the one hand and on the load transfer across the cracks on the other hand.

For assessing the confinement of the ribbed bars, the average concrete properties around a bar are relevant.

For the contribution of the concrete in the cracks and along the beam, the statistical variation of the concrete tensile properties might be taken into account by varying the input parameters.

The stress-strain relation is obtained by dividing the crack width of the stress-crack opening relation by the average crack distance.

Concrete in Compression

The properties of concrete in compression are specified as a 5-point polygon, see Fig. 6.32.

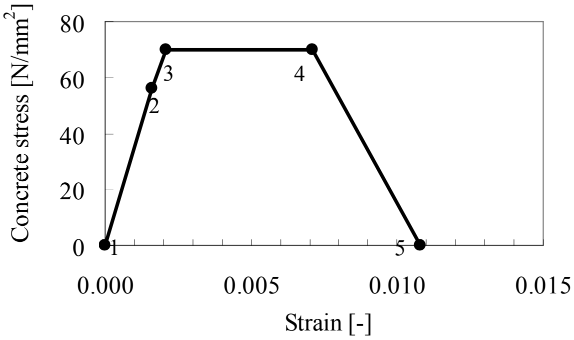

Fig. 6.32: Example of the input of the properties of concrete in compression

For the sake of simplicity, the ascending branch of the stress-strain relationship is assumed to be bilinear with a bending point at 75% of the maximum compressive load, which is taken from the standard tests on prisms (100×100×400 mm).

Due to the strain gradient of in the compressive zone of a beam (internal confinement), the concrete compressive strength was increased by 10% and the proportionality factor *k* for the largest eccentricity of the compressive tests in chapter 3 was used for the calculations of the rotation capacity. To account for the confining action of the loading platen in the region with the maximum moment (external confinement), the concrete confinement was accounted for by increasing the prism compressive strength by another 10%, resulting in a factor 1.2 for the concrete compressive strength.

The confinement in the zone under the loading platen is taken into account by an additional strain, see section 3.4.3. For numerical stability, the stress is not taken constant in the zone under the loading platen but it slightly decreases according to equation (6.2)

$$\sigma_4 = 0.999 \cdot \sigma_3 \tag{6.2}$$

Geometry Input

The model is developed for rectangular cross-sections. The geometry of the specimen is specified by its width, depth, distance from bottom to the center of gravity of the reinforcing bars, total length of the specimen, distance between the supports, steel bar reinforcement diameter (all in mm) and number of steel bars.

6.3.2 Average Crack Distance s_{cr} (Step 2)

In the model for the rotation capacity, the transmission length L_t and the average crack distance s_{cr} are calculated with the bond model presented in section 5.4.2. The average crack distance s_{cr} is assumed to be 1.3 times the transmission length.

In the model for the rotation capacity it is assumed that the first crack forms in the cross-section at the load axis and that the subsequent cracks form symmetrically to both sides in the average crack distance s_{cr}. The number of cracks is therefore uneven. The possibility of no crack directly under the load but two cracks immediately next to it as had been investigated by Bigaj (1999) has not been considered in this model. The present approach represents a lower bound approach.

6.3.3 Steel and Concrete Strains in the Tie (Step 3)

For the calculation of the steel and concrete strain distribution in a tensile element between two subsequent cracks, the differential equation of bond is performed with finite difference calculus. The procedure is described for tension members in section 5.4.2. For the calculation of bending members, the boundary condition regarding the tension chord force is changed. The boundary conditions are now:

- The difference in tension chord forces at both ends of an element between two subsequent cracks is correlated to the moment gradient. The tensile chord force T_1 at the position along the beam with a larger moment is larger than the tensile chord force T_2 at the position with the smaller moment. The difference between the two is the shear force S. It is uniformly distributed over the length of the element, see Fig. 6.33.
- The concrete stress at the beginning and at the end of the element between two subsequent cracks are a function of the slip.

The calculation is performed in the following steps: For a predefined slip, the steel stress in the first crack is varied in a number of iterations until equilibrium of forces is found and the tension chord forces at both ends of the element between two subsequent cracks satisfy the relation depending on the moment gradient, taking into account that the calculated slip in the second crack corresponds to the concrete stress at that crack. The steel strain is then calculated from the steel stress and the concrete strain at the height of the reinforcing bars is calculated by dividing the crack width w, which is twice the slip δ, by the crack distance s_{cr}.

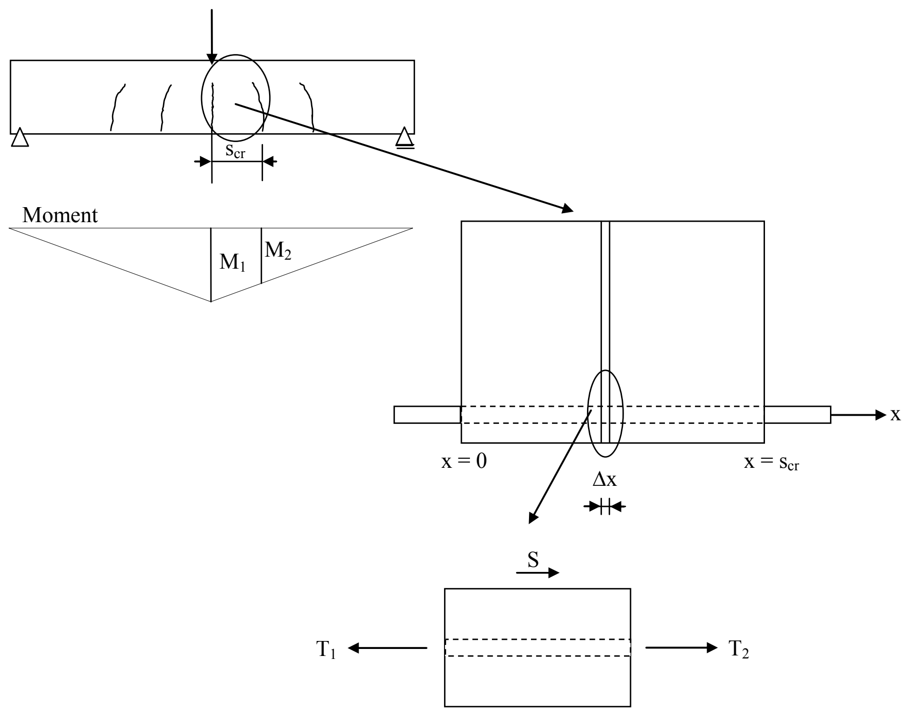

Fig. 6.33: Illustration of the shear force in an element between two subsequent cracks due to a moment gradient

6.3.4 Concrete Strains in the Compression Zone in the Cross-Section of the Cracks (Step 4)

For each set of the previously calculated steel strains and concrete strains at the height of the reinforcing bar, the concrete strains in the compressive zone at the cracks are calculated in an iterative procedure in a cross-sectional analysis with the help of a layer model. The cross-section is divided into n_l layers ($n_l = 100$) from top to bottom. The strain distribution over the beam height and the corresponding moment and curvature are calculated in the following steps:

- The strain distribution in the concrete is assumed linear in the compressive zone from the most compressed fiber to the neutral axis.
- The position of the neutral axis is determined by a linear connection of the concrete strain in the most stressed fiber with the previously determined steel strain.
- The concrete strain in the tensile zone is assumed to be linear from zero at the neutral axis up to the previously calculated concrete strain at the height of the reinforcing bar.
- For each layer the normal force is calculated from the strains and the material input.
- The concrete strain in the compressive zone is varied until equilibrium of inner and outer forces (normal force and moment) is found.
- The curvature is calculated from the concrete strain in compression and the steel strain.

It is noted that for SFRC, the steel and the fiber reinforced concrete contribute to the stress transfer in the tensile zone, whereas the concrete contribution in concrete without fibers is negligible. This strain distribution is illustrated in Fig. 6.34.

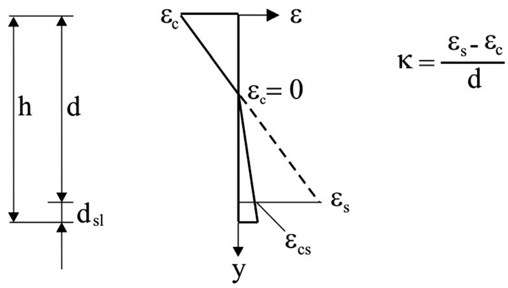

Fig. 6.34: Strain distribution of concrete and steel in the crack

For each set of steel and concrete strains at the height of the reinforcing bar, the moment and the curvature are calculated for the given dimensions and material properties, rendering the ascending and descending branch of the moment-curvature relation.

The failure criteria are related to the strains at the top (concrete crushing) and at the height of the bar reinforcement (steel rupture). Steel failure is assumed to occur when the steel strain reaches the ultimate steel strain. Concrete failure is assumed to occur when the strain in the mostly compressed layer reaches the maximum concrete compressive strain. Whichever happens first, determines the failure mechanism.

It is noted that the calculation of the strain ε_5 (see Fig. 6.32) depends on the damage zone length (see equation 3.12) and that the calculation is therefore an iterative procedure. In every step of calculating the moment-curvature relation (see section 6.3.4), the damage zone length L^d is first assumed to be zero and the stress-strain relation is calculated. With this relation, the cross-sectional analysis is done, which yields the damage zone depth d^l and the new damage zone length L^d. The previous damage zone length is compared with the new one. In case of disagreement, the new one is used to calculate the stress-strain relation and perform the cross-sectional analysis. This procedure is followed until agreement of the previous and the new damage zone length is reached.

6.3.5 Average Curvature in an Element between Two Subsequent Cracks (Step 5)

The average curvature in an element between two subsequent cracks is determined by the difference between average steel strain in the element and the concrete compressive strain in the crack divided by the effective height of the cross-section. Fig. 6.35 qualitatively shows the real concrete and steel strain distribution in a beam element between two subsequent cracks in dotted lines. The concrete compressive strain in the crack and the average steel strain in the element, which are used for the calculation of the average curvature of the element, are shown as straight lines.

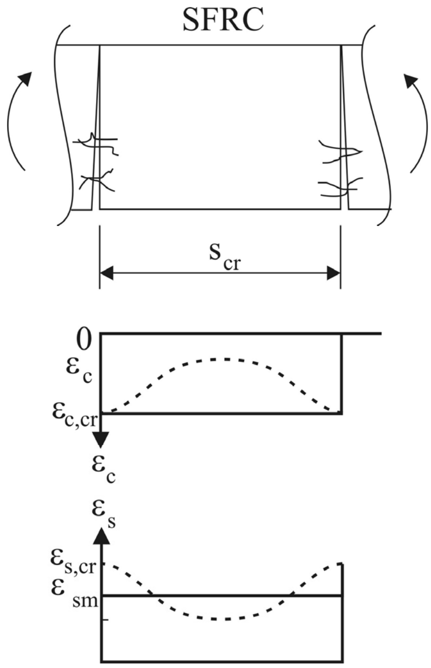

Fig. 6.35: Beam element between two subsequent cracks and concrete and steel strain distribution along the element for the calculation of the average curvature (straight lines)

It is noted that this procedure can lead to an overestimation of the curvature because in reality, the concrete strains in the compressive zone between the cracks are lower. This overestimation is considered acceptable because in case of steel failure, the main contribution to the curvature is found in the large steel strains (at failure approximately 100‰ compared to approximately 4‰ for concrete). In case of concrete failure, the damage zone was found to be larger than the crack spacing and therefore extends into the element. Thus the concrete strain is constant for the length of the plastic hinge and the assumption is correct.

6.3.6 Total Rotation of the Beam (Step 6)

The total rotation of the beam is the integration of the curvature along the beam according to:

$$\Theta = \int_0^l \kappa \, dx \tag{6.4}$$

This is obtained by multiplying the average curvature of each element between two subsequent cracks from step 5 with the average crack distance s_{cr}. These rotations are added in order to obtain the rotation of the beam.

6.3.7 Calculation of the Rotation Capacity (Step 7)

The rotation capacity was defined in chapter 2 as the difference between the total rotation at maximum load minus the rotation at the onset of steel yielding according to:

$$\Theta_{pl} = \Theta_{tot} - \Theta_{el} \tag{6.5}$$

For comparison, the total rotation at failure minus the rotation at the onset of steel yielding is also calculated and presented in section 6.4.

6.4 Comparison of Model and Experiments

The following phenomena are considered the central issues in modeling the effect of steel fibers on the rotation capacity of reinforced concrete members:

- load transfer in a crack in case of SCSFRC
- localization of the deformations in one large crack
- the scatter of the SCSFRC tensile strength and post-peak strength
- the effective crack distance.

The model was developed on the basis of the model of Bigaj (1999). An essential difference between RC and SFRC is the significant stress transfer across the cracks in case of SFRC. Therefore, assumptions are necessary for the distribution of tensile forces over the steel fiber concrete and the reinforcing bars. In case the contribution of the steel fibers is overestimated, the contribution of the bars is underestimated and thus the rotation is also underestimated and vice versa.

The model for rotation capacity includes many factors, which refer to the material properties, the geometry and the static system, see chapter 2. These influencing factors are used as input for calculating the rotation capacity. Some of these parameters, e.g. the material properties, are subjected to scatter. These input parameters and their variation are explained in the following section.

In the simulations, the input parameters related to the material properties were varied in the realistic range in order to find a parameter combination that fits the test results well on average.

The criteria that were used to check whether the simulation gives satisfactory results were the attainment of:

- maximum moment
- number of cracks in which the deformations localize
- crack distance
- rotation at the beginning of steel yielding
- rotation at maximum load
- rotation at ultimate load.

6.4.1 Input Parameters

Steel Properties

The average values of the stress-strain relationship of steel shown in Table 6.5 were used as input parameters.

Concrete in Tension

An axial tensile strength of 0.9 times the splitting tensile strength of the SCC was used for the SCSFRC.

The tensile behavior of the SCC was modeled with the model proposed in Bigaj (1999). The tensile behavior of the SCSFRC was modeled with the model proposed in chapter 4.6. The model parameters, which were used for the calculation of the rotation capacity, are shown in Table 6.15. To account for the variation of tensile properties along the beam, the crack in the middle was calculated assuming 0.7 $f_{ctm,ax}$. The value of β_{FCM} was adjusted to obtain the same second branch of the bilinear softening relationship as in the original set of data with the average tensile strength.

Table 6.15: Input parameters for concrete in tension

Parameter	Value at cracks with 1.0 $f_{ctm,ax}$	Value at crack with 0.7 $f_{ctm,ax}$
α_{FCM}	0.0075	0.0075
w_{int}	0.056 mm	0.056 mm
w_0	$0.25 \cdot l_f = 7.5$ mm	$0.25 \cdot l_f = 7.5$ mm
$f_{ctm,ax}/f_{ct,sts}$	0.9	0.9·0.7 = 0.63
$\beta_{FCM,3D}$	0.14	0.14/0.7 = 0.200
$\beta_{FCM,crack}$	0.20 = 0.14·0.7/0.5 [1)]	0.20/0.7 = 0.286
$\beta_{FCM,confinement}$	0.12 = 0.14·0.43/0.5[1)]	0.12/0.7 = 0.171

[1)] Value for fiber orientation derived from optical analysis of the beam cuts, see section 6.2.4

Concrete in Compression

Due to the strain gradient of in the compressive zone of a beam, the concrete compressive strength was increased by 10% and the proportionality factor k for the largest eccentricity of the compressive tests in chapter 3 was used for the calculations of the rotation capacity. To account for the confining action of the loading platen in the region with the maximum moment, the concrete confinement was accounted for by increasing the prism compressive strength by another 10%, resulting in a factor 1.2 for the concrete compressive strength, and by adding a strain $\Delta\varepsilon_{peak}$ of 0.010. It is noted that this increased confinement is not generally present in a structure and that calculation results based on this confinement would lead to an overestimation of the rotation capacity in cases where the confinement is not present.

Overview of the Input File

The input parameters for the simulations of the test reported in section 6.2 are shown in Table 6.16. The geometry of the test specimens was taken from Table 6.2 and the reinforcement layout was taken from Fig. 6.2. The concrete cover was 25 mm.

Table 6.16: Input parameters for the calculation of the rotations

Parameter		B45.0.0.N0	B45.0.0.N400	B45.80/30.60.N0	B45.80/30.60.N400
Load					
N	[kN]	0	-400	0	-400
Concrete tension confinement					
f_{ct}	[N/mm^2]	4.6	4.6	4.6	4.6
α_{FCM}	[-]	0.14	0.14	0.0075	0.0075
β_{FCM}	[-]	0.22	0.22	0.12	0.12
w_0	[mm]	0.2	0.2	7.5	7.5
Concrete tension in crack					
f_{ct}	[N/mm^2]	4.6	4.6	4.6	4.6
α_{FCM}	[-]	0.14	0.14	0.0075	0.0075
β_{FCM}	[-]	0.22	0.22	0.2	0.2
w_0	[mm]	0.2	0.2	7.5	7.5
Concrete compression					
f_c/k_{fc}	[N/mm^2]	-51	-51	-50	-50
E_c	[N/mm^2]	35000	35000	36000	36000
k	[-]	13.5	13.5	19.5	19.5
r	[mm]	1.25	1.25	1.01	1.01
k_{fc}	[-]	1.2	1.2	1.2	1.2
$\Delta\varepsilon_{peak}$	[‰]	10	10	10	10

6.4.2 Calculation Results

The calculation results obtained with the input parameters given in section 6.4.1 are summarized in this section.

Maximum Moments

Table 6.17 shows the maximum moments observed in the tests and those obtained in the calculations. The simulated maximum moments agree well with the measured ones.

Table 6.17: Maximum moment in tests and calculations

Test	M_{max} measured [kNm]	M_{max} calculated [kNm]
B45.0.0.N400	72	73
B45.80/30.60.N400	76	77
B45.0.0.N0	27	28
B45.80/30.60.N0	30	30

Number of Large Cracks

The number of the cracks with deformation localization was observed to be 2 to 4 in the beams with SCC and 1 for the tests with SCSFRC. Table 6.18 shows the number of cracks that had a crack width of at least 1 mm at the final load step.

Table 6.18: Number of cracks with crack openings larger than 1 mm before failure

Test	measured [-]	calculated [-]
B45.0.0.N400	2	1
B45.80/30.60.N400	1	1
B45.0.0.N0	4	3
B45.80/30.60.N0	1	1

As can be seen in the table, the number of cracks in which the deformations localized was correctly captured for the SCSFRC specimens and underestimated by one for the SCC specimens. The reason for the different number of cracks can be sought in the way the calculation model is set-up: It is assumed that one crack forms in the center of the beam and that the other cracks form symmetrically to both sides in a distance s_{cr} from this center crack (see also section 6.3.2). The number of cracks in the model is therefore always an uneven number. In the simulation of the experiments, the number of cracks is underestimated for the tests without steel fibers, which provides a conservative estimation.

Crack Distances

The comparison of the measured and computed average crack distances are shown in Table 6.19. The bond model calculates the stress distribution for the primary crack pattern. At later load stages, secondary cracking occurred in the tests. This is neglected in the calculations.

Table 6.19 shows the average crack distances measured after the tests, i.e. including secondary cracking.

Table 6.19: Number of cracks n_{cr} and average crack distances (including secondary cracking) in the 1200 mm center region

Test	n_{cr} [-]	Average crack distance measured [mm]	Average crack distance calculated [mm]
B45.0.0.N400	14	92.3	94
B45.80/30.60.N400	32	38.7	91
B45.0.0.N0	18	70.6	94
B45.80/30.60.N0	23	54.2	91

At the beginning of steel yielding in case of the SCSFRC specimens, there is no inclination of the cracks visible and there is only one crack in which the deformations localize.

It is noted that the calculated crack distances for the SFRC specimens are larger than the measured ones. The calculation of the crack width is very sensitive to the slope of the first branch in the stress-crack width relationship of the concrete. Slight changes would result in a more realistic crack width. However, if the deformations localized in one crack, the average crack spacing loses its significance for the determination of the plastic rotations. In addition to this, an overestimation of the crack spacing usually results in an underestimation of the rotations. The deviation of calculated and measured crack spacings for the SFRC specimens has therefore been found acceptable.

Rotations at Different Load Steps

Table 6.20 and Fig. 6.36 show the measured and calculated rotations at the onset of yielding, at maximum load and at ultimate load. Due to a plateau at maximum loading in the fiber reinforced specimens, the rotation of the maximum load and the rotation capacity are given as a range in the tables as well as in the figures. The calculated rotations agree well with the measured ones.

Table 6.20: Measured and calculated rotations at onset of yielding (y), maximum load (max) and ultimate load (u)

Test	$\Theta_{measured}$ at F_y [mrad]	$\Theta_{calculated}$ at F_y [mrad]	$\Theta_{measured}$ at F_{max} [mrad]	$\Theta_{calculated}$ at F_{max} [mrad]	$\Theta_{measured}$ at F_u [mrad]	$\Theta_{calculated}$ at F_u [mrad]
B45.0.0.N400	19	19	33	27	33	27
B45.80/30.60.N400	10	16	20-22	26	27	26
B45.0.0.N0	14	14	83	68	83	68
B45.80/30.60.N0	8	13	15-37	22	59	54

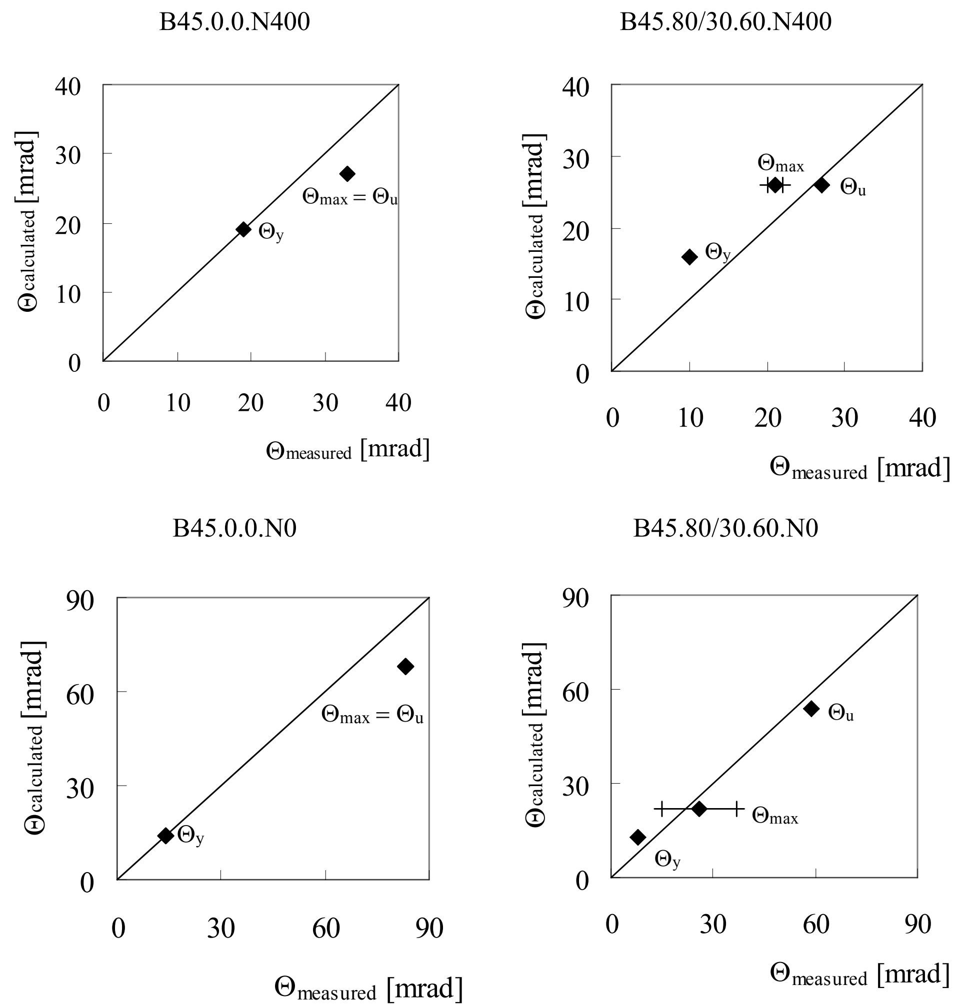

Fig. 6.36: Comparison of calculated and measured rotations at different load steps

Rotation Capacity and Rotation at Ultimate Load minus Rotation at the Onset of Steel Yielding

With these rotations, the rotation capacity (Θ_{max}–Θ_y) and the difference between the rotation at ultimate load and the rotation at the onset of steel yielding (Θ_u–Θ_y) were calculated. The values are given in Table 6.21 and illustrated in Fig. 6.37.

The influence of steel fibers on the difference of the rotations at ultimate load minus the rotations at the onset of steel yielding has also been investigated because in cases in which a hinge mechanism is not completed yet and in which the structures allow for redistribution of forces at decreasing load bearing capacity in the earlier hinges, the descending branch of the moment-curvature relation is also of interest.

Table 6.21: Rotation capacity and difference between rotation at ultimate load and rotation at the onset of steel yielding from the tests and the calculations

Test	$\Theta_{max}-\Theta_y$ measured [mrad]	$\Theta_{max}-\Theta_y$ calculated [mrad]	$\Theta_u-\Theta_y$ measured [mrad]	$\Theta_u-\Theta_y$ calculated [mrad]
B45.0.0.N400	14	8.6	14	8.6
B45.80/30.60.N400	10-12	9.1	17	9.1
B45.0.0.N0	68	55	68	55
B45.80/30.60.N0	8-29	9.4	51	41

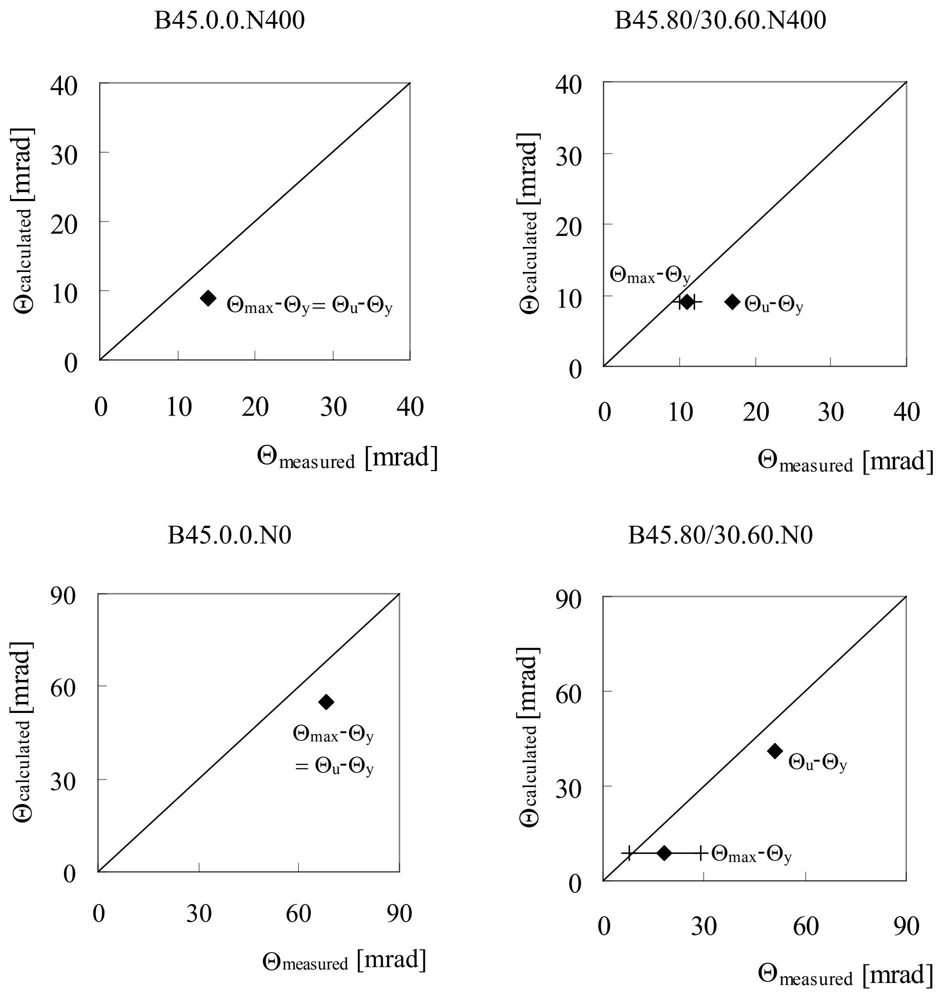

Fig. 6.37: Comparison of calculated and measured rotation capacity and difference between rotation at ultimate load and rotation at the onset of steel yielding

Agreement experiment and model

The rotation capacity of the beams ($\Theta_{max}-\Theta_y$) observed in the experiments is slightly underestimated by the calculation model presented in section 6.3. The rotations at ultimate load minus the rotations at the onset of steel yielding obtained in the calculations are underestimated.

Effect of fibers in the tests without normal force (from B45.0.0.N0 to B45.80/30.60.N0)

For the investigated parameters, the experiments as well as the numerical calculation results show that the overall rotation capacity in the tests without normal force was significantly decreased when fibers were added. This phenomenon had already been observed for linear members by other researchers, see section 5.4.2.

The rotation at ultimate load minus the rotation at the onset of steel yielding in the tests without normal force was decreased when fibers were added in both the experiment as well as the calculation. The decrease was not more pronounced in the calculation than in the experiment.

Effect of fibers in the tests with normal force (from B45.0.0.N400 to B45.80/30.60.N400)

For concrete failure, the experimentally observed rotation capacity slightly decreased due to the fiber addition. The experimental and calculation results seem contradictory. However, the difference is not significant. It should be understood that in compressive failure, the two phenomena of increased deformation capacity in compression and localization of the deformations in one large crack counteract.

The rotation at ultimate load minus the rotation at the onset of steel yielding was slightly increased in the experiments due to the fiber addition. This increase is attributed to the increase in concrete ductility due to fiber addition, see chapter 3.

6.5 Concluding Remarks

The experiments and the simulations showed that in case of SCSFRC, localization of the deformations in one crack was observed compared to localization in several cracks for SCC, leading to reduced total deformations. This was an important result. The reduction in total deformation can be dangerous because it can lead to less ductile failure, and therefore it has to be kept in mind in elastic design with redistribution of forces or plastic design of concrete structures.

The localization of failure in one large crack in the SCSFRC specimens and thus the reduction in total deformation is mainly attributed to the fact that for the fiber reinforced specimens, the softening of the SFRC dominates the hardening of the reinforcing steel so that the hardening ratio of the tie is decreased and localization is more likely to occur. The scatter of the properties of the SFRC also plays a role in this, but a minor one. Due to the scatter of the properties of SFRC, which results in a larger contribution to load bearing in the cracks next to the first crack, it is impossible to build up the stresses necessary to obtain plastic steel strains and thus large deformations in the neighboring cracks.

The addition of steel fibers led to:

- smaller crack spacings
- smaller crack widths, deflections, and curvatures in the range of elastic steel strains
- an increase in maximum moment
- localization of deformations in one large crack
- smaller deformations in the ultimate load step (less plastic deformations)
- cracks but no spalling in the compressive zone.

The rotation capacity of the fiber reinforced specimens was smaller than for the ones without fibers due to the localization of the deformations in one single crack in case of SCSFRC.

In some cases it may be desired to capture the complete behavior including the descending branch of the moment-rotation curve. In this case, the rotation at the ultimate load step minus the rotation at the beginning of steel yielding was smaller for the SCSFRC specimen compared to the SCC one in case of steel failure due to the localization of deformations in one crack, but it was slightly larger in case of concrete crushing due to the increased concrete ductility.

Only four tests were performed. The experimental validation of the model is therefore limited to these four tests. More calibration is recommended.

7 Application in Tunneling: Parameter Study

In case of tunnels, usually, relatively large normal forces and small bending moments act on the tunnel lining. From previous research [Hemmy, 2003] it was concluded that a combination of traditional and fiber reinforcement could be very useful for tunnel segments. The fibers can be used to replace reinforcing bars (for reinforcement in the cover, 3-D reinforcement, reducing crack widths, increasing the resistance against impact loading), whereas traditional reinforcing bars can be placed in areas where larger tensile forces are expected (controlled transfer of forces; required position of the reinforcement is known). By using the combined reinforcement, cost savings can be achieved in two ways: either by reducing the thickness of the elements or by reducing the amount of traditional reinforcement.

The effect of steel fibers on reinforced concrete beams and tension members has been described in chapter 5 and chapter 6. In the previous chapter, a model to calculate the rotation capacity of SCSFRC members has been developed and validated against beam tests. The purpose of this parameter study is to give more insight into the influence of steel fibers on the rotations and on the rotation capacity for structural dimensions usual in tunnel linings.

As pointed out in chapter 2, the rotation capacity of reinforced concrete members depends on a large number of influencing factors, among which the material properties, the geometry of the structure and the reinforcement layout. The variation of a single parameter in itself can lead to an increase or reduction in rotation capacity depending on the circumstances (e.g. the amount of steel reinforcement). As the influence of the single parameters on the rotation capacity is already difficult to capture, the problem becomes even more complex when several of these parameters are subjected to variation and when a positive effect of changing one parameter is suppressed by the change in another. Parameter studies can provide information on the interaction of the single input parameters and their influences on the rotations and the rotation capacity.

7.1 Parameter Choice

The parameter study is based on the cross-section of the beams introduced in chapter 6 (b = 150 mm, h = 300 mm, d = 255 mm, span l = 2850 mm). A statically determinate beam over one span is used to simulate the part in a statically indeterminate beam over multiple spans or in a tunnel ring with changing bending moments, which is located between two points of zero moment. This simplification is justified as explained in section 6.2. The study is limited to normal strength concrete. Only beams with longitudinal tensile and compressive reinforcement and without shear reinforcement or other confining reinforcement apart from the steel fibers are considered. The steel properties are shown in Table 7.1.

Table 7.1: Material input for the reinforcement steel

σ [N/mm^2]	ε [-]
0	0
571	$3.4 \cdot 10^{-3}$
585	$27 \cdot 10^{-3}$
665	$150 \cdot 10^{-3}$

The main variables in this series of simulations are:

- amount of steel fibers: none, 60 and 120 kg/m^3
- amount of traditional reinforcement: 2 d_s 8 mm, 2 d_s 10 mm, 2 d_s 12 mm at top and bottom side
- normal compressive force: none, 100, 200, 400 kN.

Amount of Steel Fibers

The concrete properties are shown in Table 7.2. They were chosen similar to the concrete properties of the tests reported in chapter 6, Table 6.16. The amount of steel fibers is taken into account by the stress-crack width relation of the concrete in tension. The fiber orientation is taken into account by the difference in stress-crack width relation in the crack and in the plane perpendicular to the beam axis.

Table 7.2: Material input for concrete

Parameter		B45.0.0	B45.80/30.30	B45.80/30.60
Concrete tension for confinement around the reinforcing bar				
f_{ct}	[N/mm^2]	4.6	4.6	4.6
α_{FCM}	[-]	0.0075	0.0075	0.0075
β_{FCM}	[-]	0.001	0.06	0.12
w_0	[mm]	7.5	7.5	7.5
Concrete tension in crack				
f_{ct}	[N/mm^2]	4.6	4.6	4.6
α_{FCM}	[-]	0.0075	0.0075	0.0075
β_{FCM}	[-]	0.001	0.1	0.2
w_0	[mm]	7.5	7.5	7.5
Concrete compression				
f_c	[N/mm^2]	-50	-50	-50
E_c	[N/mm^2]	36000	36000	36000
k	[-]	13.5	16.5	19.5
r	[mm]	1.25	1.13	1.01

Amount of Traditional Reinforcement

The analysis is performed for mechanical reinforcement ratios ω_s ranging from 0.03 to 0.07. This amount is based on the tests presented in chapter 6. Different diameters of bars are used in the variation in order to show the effect of choosing a smaller of larger bar diameter. The reinforcement layouts shown in Table 7.3 were considered. The concrete covers were defined in section 5.2.4. The same reinforcement was modeled in the tension as well as in the compression zone.

Table 7.3: Reinforcement layout and ratio and concrete covers

Reinforcement layout	2 d_s 8 mm	2 d_s 10 mm	2 d_s 12 mm
Mechanical reinforcement ratio ω_s [-]	0.03	0.05	0.07
c_1 [mm]	32	40	42
c_2 [mm]	32	40	42
c_3 [mm]	32	40	39
c_4 [mm]	32	40	48
Smallest cover to surface c [mm]	32	40	39

Amount of Normal Compressive Force

Based on the experiments presented in chapter 6, the normal force was chosen to vary between 0 and 400 kN. The values 100 kN and 200 kN were chosen to study the effect of smaller normal forces.

7.2 Simulation Results

This section presents the basic findings from the simulations. The influence of the normal compressive force and the steel fibers on the rotations is given as a function of the mechanical reinforcement ratio ω_s, which was calculated as:

$$\omega_s = \frac{A_s}{b\,d} \cdot \frac{f_{sy}}{f_c} \tag{7.1}$$

The rotations were calculated for different load steps:

- u ultimate
- max maximum
- y beginning of yielding of the reinforcing bars.

The rotation capacity is defined as the rotation at the maximum load minus that at the onset of yielding. Furthermore, the rotation at ultimate load minus that at the onset of yielding is given as discussed in chapter 6. According to the currently used definition of the rotation capacity, the descending branch can only serve as a safety margin. It cannot be used in the design, e.g. to reduce the cross-section.

The results of the calculations are strongly dependent on the failure criterion in the compressive zone. In the results presented below, failure in compression was supposed to occur when the most compressed fiber reached a strain of 50‰. This value had been observed locally in the experiments.

The identification of the parameter simulations is identical to the identification of the test specimens in chapter 6. It consists of:

- the concrete compressive strength class
- the fiber aspect ratio [-]
- the fiber length [mm], the fiber content [kg/m^3] and
- the normal compressive force [kN].

Fig. 7.1 to Fig. 7.8 allow to compare the influence of steel fibers on the rotations at constant normal forces. The rotation capacity as well as the differences between rotation at the ultimate load step and the rotation at the onset of steel yielding are given here. The rotations at the beginning of steel yielding, maximum load and ultimate load are given in appendix K.

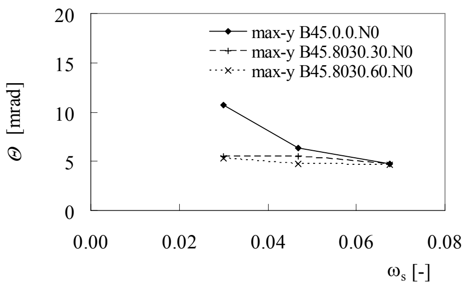

Fig. 7.1: Rotation capacity for N = 0

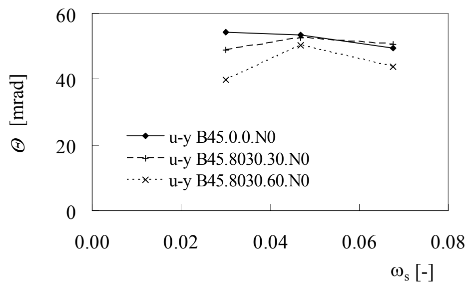

Fig. 7.2: Rotation at ultimate load minus rotation at the onset of steel yielding for N = 0

Fig. 7.1 shows the effect of steel fibers on the rotation capacity in absence of a normal compressive force. For the sake of comparison, Fig. 7.2 shows the effect of steel fibers on the difference between the rotations at ultimate load and those at the beginning of steel yielding.

For low reinforcing steel bar ratios, the rotation capacity from the SCSFRC calculations are smaller than those from the SCC calculations. This phenomenon was explained in chapter 5 and chapter 6 with the overall softening behavior in a cross-section in which the hardening of the reinforcing steel is outweighed by the softening of the SFRC and the resulting localization of the deformations in one large crack in SCSFRC compared to localization of the deformations in several large cracks for SCC. In case of larger reinforcement ratios, the steel fibers hardly influence the rotations.

The simulation results with normal force are shown in Fig. 7.3 to Fig. 7.8.

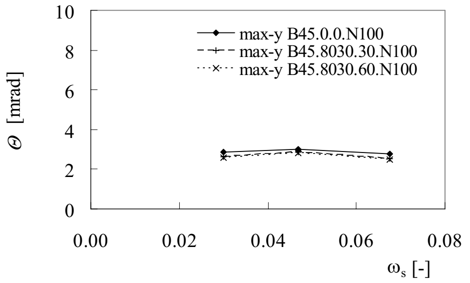

Fig. 7.3: Rotation capacity for N = 100 kN

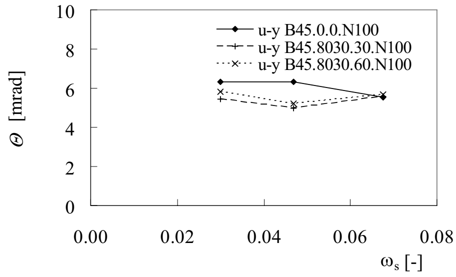

Fig. 7.4: Rotation at ultimate load minus rotation at the onset of steel yielding for N = 100 kN

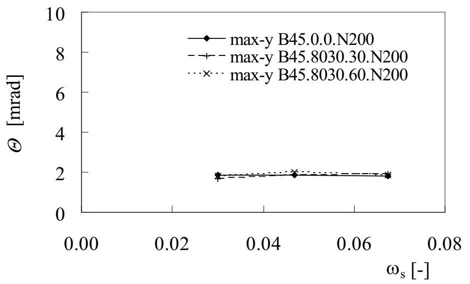

Fig. 7.5: Rotation capacity for N = 200 kN

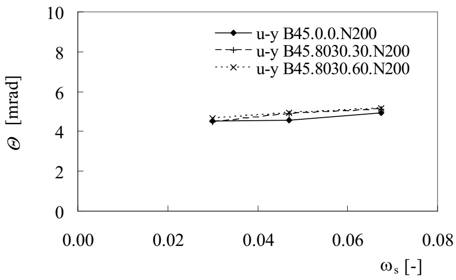

Fig. 7.6: Rotation at ultimate load minus rotation at the onset of steel yielding for N = 200 kN

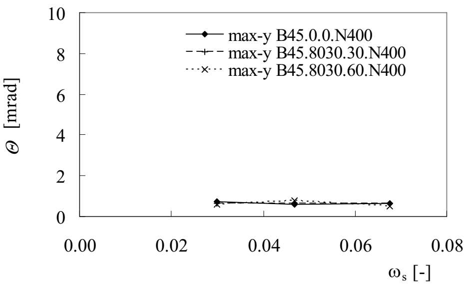

Fig. 7.7: Rotation capacity for N = 400 kN

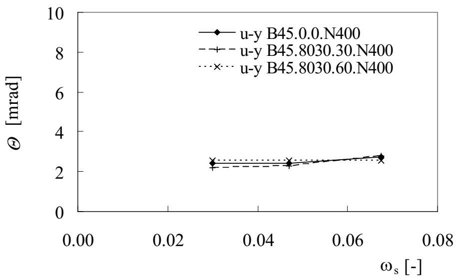

Fig. 7.8: Rotation at ultimate load minus rotation at the onset of steel yielding for N = 400 kN

The larger the normal compressive force is, the smaller the rotations are. The lower boundary value of the rotations is zero for uniaxial compression. This is because the onset of steel yielding, maximum load and ultimate load will lay closer together as the normal force increases, resulting in nearly identical rotations for the three stages and therefore in nearly no rotation capacity.

The increase of the ductility of concrete in compression leads to an increase in rotations at ultimate load minus rotations at the onset of steel yielding in case of large normal forces.

The moment at the ultimate load step was between 74 and 98% of that at maximum loading.

It is noted that the addition of steel fibers leads to an increase in load bearing capacity at the beginning of steel yielding, at the level of maximum load and at the level of ultimate load. The redistribution of forces depends on the load bearing capacity as well as on the rotation capacity. If a larger load bearing capacity is present, less rotation capacity is required in order to achieve the same level of overall structural load bearing capacity.

7.3 Link to Tunneling

Influence of Member Width

The localization of the deformations in one large crack in SFRC that has been observed in tension members and beams is expected not to be as pronounced in plane-like structures such as slabs and tunnel segments. Due to the larger width of these structures, the scatter of material properties along the structural element is less pronounced. With increasing beam width, the scatter of SFRC decreases [Erdem, 2002]. This reduction in scatter leads to more homogeneous material properties and allows for redistribution of stresses over the width of a structural element. It therefore can prevent the localization of the deformations in only one crack and thereby lead to multiple cracking. In cases, in which the softening of the SFRC is not significantly dominating the hardening behavior of the RC, an increased deformation capacity can be expected.

In the proposal for the German guideline for SFRC [DAfStb, 2005], this phenomenon is captured by a factor κ_b for the centric post-peak stresses of the SFRC. The factor depends on the width and the height of the cross-section and results in an increase of post-peak tensile strengths if the width of a member is larger than three times the height. It results in a reduction of the post-peak tensile strength if the width is less than three times the height. The same phenomenon is addressed in the DBV guideline for SFRC [DBV, 2001]. There, the post-peak tensile stresses of the SFRC were increased by approximately one third compared to the small beams for material tests. It is not completely clear whether this leads to multiple cracking or still to localization of the deformations in one large crack. Both are possible. Scatter over the width of the beam is not explicitly included in the model presented in this thesis. An increase of the tensile strength of the SFRC in the input file is a possible way to account for that.

Furthermore, a normal compressive force reduces the scatter of the test results. This can be ascribed to the fact that the scatter of the concrete properties in tension is larger than that in compression. Erdem (2002) therefore proposed a reduction of the safety factor in case of the presence of normal forces.

7.4 Concluding Remarks

The findings of the parameter study correspond well with the trends observed in chapter 6. For a combination of a small reinforcing bar ratio and fiber reinforcement, the overall softening behavior is dominant and the deformations localize in one large crack. The rotation capacity of the fiber reinforced concrete is lower than that of reinforced plain concrete for the cases calculated without normal force and for N = 100 kN. For the combinations with larger normal forces (N = 200 kN, N = 400 kN), the rotation capacity is slightly larger for cases with steel fibers than without steel fibers due to the increased ductility of the SCSFRC in compression and the resulting activation of deformations in the tensile zone.

The presence of normal compressive forces generally decreases the rotation capacity. The lower boundary value for the rotations is zero in case of uniaxial compression. The upper boundary value follows from the simulations without normal force.

8 Conclusions and Suggestions for Further Research

8.1 Conclusions

In the present research project, the effect of steel fibers on

- the compressive behavior and tensile behavior of SCSFRC (chapter 3 and 4)
- the bond behavior of reinforcing bars in SCSFRC (chapter 5) and
- the rotation capacity of members with combined fiber and bar reinforcement (chapter 6)

has been investigated. Conclusions have been drawn with respect to the influence of steel fibers on plain concrete on the one hand and on reinforced concrete on the other hand.

8.1.1 Conclusions Concerning the Addition of Steel Fibers to Plain Concrete

Anisotropy

The effect of steel wire fibers with hooked ends on the mechanical properties of concrete strongly depends on the fiber orientation. The fiber orientation is influenced by

- wall effects, size of the specimen
- casting direction
- way of casting
- mixture composition, workability of the fresh concrete
- restraints at flow, such as reinforcing bars.

Fibers are usually not perfectly 3D oriented. Therefore, in contrast to plain concrete, SCSFRC cannot automatically be assumed to be an isotropic material. The direction dependent properties have to be considered in modeling SCSFRC if the principal tensile stresses in different directions in a member are considered.

Compressive Behavior

The effect of the volume of steel fibers with various aspect ratios on the compressive behavior of concrete prisms subjected to centric or eccentric compressive loading was investigated experimentally. The Compressive Damage Zone (CDZ) Model, which had been developed by Markeset (1993) for plain concrete, has been extended for steel fiber reinforced concrete considering the volume and aspect ratio of the fibers. In the extended model, the effect of the fibers was captured by a proportionality factor k, which was 3 for conventional concrete. For plain SCC, a value of 3.5 is proposed. The effect of the fibers is included in an additive term of 10 times the fiber factor $V_f l_f / d_f$. This results in the proportionality factor

$$k = 3.5 + 10 \cdot V_f \cdot \frac{l_f}{d_f} \tag{8.1}$$

The influence of different fiber factors on the concrete ductility in compression is illustrated in Fig. 8.1.

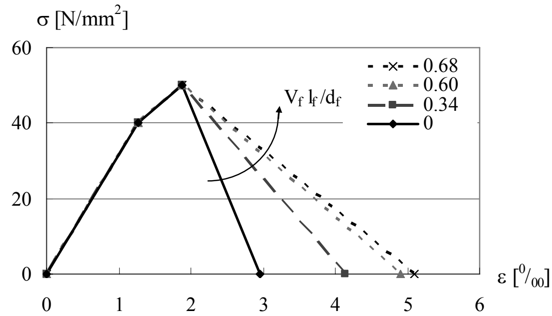

Fig. 8.1: Effect of steel fibers on the compressive behavior for different fiber factors $V_f\, l_f/d_f$

In members subjected to bending, the addition of steel fibers leads to an increase in load bearing capacity after the cracking moment. Due to the softening behavior of the SCSFRC, deformations usually localize in one region.

Tensile Behavior

The stress-crack width relationship is not a pure material property, but it depends on boundary conditions such as specimen size, strain gradient, wall effects, direction of load application, casting direction etc. The variation of fiber distribution and orientation leads to variations in the stress-crack width relationship within the specimens. There can be a large scatter in fiber distribution and orientation due to the influence of the casting process. This needs to be taken into account when modeling the cracking behavior of SFRC.

The addition of steel wire fibers with hooked ends to plain concrete leads to an increase in concrete ductility in tension. The tensile strength is not significantly altered by the fiber addition. The modified model of Kützing (2000) was used for calculating the bond behavior and the rotation capacity in this study. It was adapted with regard to axial tensile strength (depending on the mixture and not necessarily on the compressive strength), fiber orientation, and complexity (bilinear instead of trilinear relationship). The influence of the fiber content on the stress-crack width relationship is illustrated in Fig. 8.2.

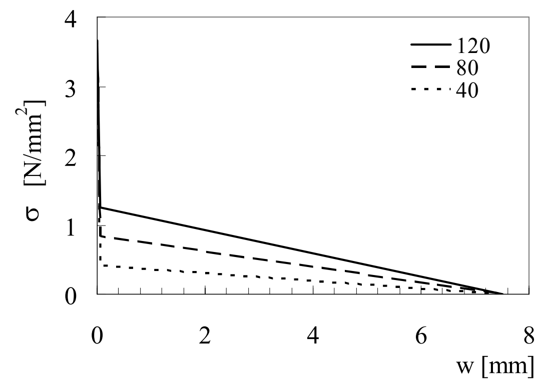

Fig. 8.2: Effect of fibers on the tensile behavior for different fiber contents [in kg]

8.1.2 Conclusions Concerning the Addition of Steel Fibers to Reinforced Concrete

Anisotropy

In reinforced concrete structures, the tensile properties in the cracks as well as around a reinforcing bar need to be considered. Due to a varying fiber orientation the tensile properties are direction dependent. In this study, the tensile properties in the direction along the member axis and an average of the tensile properties perpendicular to it were considered separately in modeling. The tensile properties along the member axis represented the tensile behavior in the cracks, whereas the average of the tensile properties perpendicular to it represented the tensile behavior necessary to evaluate the confinement capacity of the concrete surrounding a reinforcing bar.

Bond Behavior

After modifying single input parameters, the analytical bond model of Den Uijl & Bigaj (1996) has been used to describe the bond behavior of SCSFRC with satisfactory agreement of experimental and simulation results considering the scatter in test results of pull-out tests and the bond behavior of SFRC in case of tension stiffening tests. The model considers the fracture characteristics of concrete by using the stress-crack opening relationship of plain concrete in tension as input. The influence of steel fibers on the bond behavior in case of pull-out bond failure is considered by

- adapting the model parameters α_{FCM}, β_{FCM} and w_0 for the stress-crack opening relationship for the SFRC in tension
- considering the anisotropy
- adapting the cone angle, which represents the concrete cone pull-out, to 89° for SFRC in contrast to 40° for concrete without fibers.

It was found that:

- for bar diameters and concrete covers usual in tunneling practice, pull-out failure is expected rather than splitting failure.
- the addition of steel fibers slightly influences the bond behavior in case of pull-out bond failure and is expected to have a pronounced effect in case of splitting bond failure.
- the confinement capacity is increased due to fiber addition, even if only a few fibers are present in the concrete cover region.
- the main influence of steel fibers on the tension stiffening behavior in case of pull-out failure lies in their contribution to the stress transfer across the cracks.
- the addition of steel fibers leads to a reduction in crack spacing and to an increased load bearing capacity.
- the addition of steel fibers leads to stiffer member behavior and smaller crack widths in the SLS.
- depending on the combination of steel fibers (amount, geometry, orientation, bond properties) and reinforcing bars (amount, hardening properties), localization of the deformations in one large crack can occur. The member deformation capacity can thereby be reduced.
- in a reinforced tensile member without fibers, the deformations localize in various cracks. However, in a reinforced tensile member with fibers, the deformations may localize in only one crack due to the fact that the hardening behavior of the reinforcing bars is superseded by the softening behavior of the SFRC.

Rotation Capacity

In the experiments performed, the addition of steel fibers led to:

- smaller crack spacings
- smaller crack widths, deflections, and curvatures in the range of elastic steel strains
- an increase in maximum moment
- localization of deformations in one large crack
- smaller deformations in the ultimate load step
- cracks but no spalling in the compressive zone.

Due to the advantages in the SLS, the addition of steel fibers is beneficial in tunnel linings.

The experiments and the simulations showed that in case of SCSFRC, localization of the deformations in one crack was observed compared to localization in several cracks for SCC, leading to reduced total deformations. This was an important result. The reduction in total deformation can be dangerous when it leads to brittle failure, and therefore it has to be kept in mind in elastic design with redistribution of forces or plastic design of concrete structures.

The localization of failure in one large crack in the SCSFRC specimens and thus the reduction in total deformation is mainly attributed to the fact that for the fiber reinforced specimens, the softening of the SFRC dominates the hardening of the reinforcing steel so that the hardening ratio of the tie is decreased and localization is more likely to occur. The scatter in the properties of the SFRC also plays a role in this respect, but a minor one. Due to the scatter of the properties of SFRC, which results in a larger contribution to load bearing in the cracks next to the first crack, it is impossible to build up the stresses necessary to obtain plastic steel strains. Thus, large deformations will not be obtained in the neighboring cracks.

The rotation capacity is usually defined as the rotation at maximum load minus the rotation at the onset of steel yielding. The rotation capacity of the fiber reinforced specimens was smaller than for the ones without fibers due to the localization of the deformations in one single crack in case of SCSFRC.

In some cases it may be desired to capture the complete behavior including the descending branch of the moment-rotation curve. In those cases, the rotation at the ultimate load step minus the rotation at the beginning of steel yielding is of interest. Both in the beam tests and the simulations, this difference was smaller for the SCSFRC specimen compared to the SCC one in case of steel failure due to the localization of deformations in one crack, but it was slightly larger in case of concrete crushing due to the increased concrete ductility.

The findings of the parameter study correspond well with chapter 6. For a combination of a small reinforcing bar ratio and fiber reinforcement, overall softening behavior is dominant and the deformations localize in one large crack. The rotation capacity of the fiber reinforced concrete is decreased compared to reinforced plain concrete. For the parameter combinations with large normal forces, the rotation capacity is slightly larger for the combinations with steel fibers than that of the combinations without steel fibers due to the increased ductility of the SCSFRC in compression and the resulting activation of deformations in the tensile zone.

Parameter Study

The findings of the parameter study correspond well with the trends observed in chapter 6. For a combination of a small reinforcing bar ratio and fiber reinforcement, the overall softening behavior is dominant and the deformations localize in one large crack. The rotation capacity of the fiber reinforced concrete is lower than that of reinforced plain concrete for the cases calculated without normal force and for N = 100 kN. For the combinations with larger normal forces (N = 200 kN, N = 400 kN), the rotation capacity is slightly larger for cases with steel fibers than without steel fibers due to the increased ductility of the SCSFRC in compression and the resulting activation of deformations in the tensile zone.

The presence of normal compressive forces generally decreases the rotation capacity. The lower boundary value for the rotations is zero in case of uniaxial compression. The upper boundary value follows from the simulations without normal force.

8.2 Suggestions for Further Research

Tensile Behavior and Average Crack Spacing

The stress-crack width relationship of concrete in tension is not a pure material property but depends on boundary conditions such as:
- specimen (size, shape)
- way of manufacturing (mixture composition, wall effects, casting direction)
- loading conditions (direction of load application, strain gradient).

The variation of the distribution and the orientation of the fibers within the specimens leads to variations in the stress-crack width relationship within the specimens. There can be a large scatter in fiber distribution and orientation due to the influence of the casting process. This needs to be taken into account when modeling the cracking behavior of SFRC. The influence of the production method on the fiber distribution and orientation is not yet completely clear. For further research it is recommended to systematically link the mixture composition, way of manufacturing and boundary effects to the fiber distribution and orientation, and considering the state of stresses in the test specimens, to explain the results of uniaxial tension tests and three-point bending tests and the link between them. These conclusions are in line with other recent publications, e.g. Barragán (2002), Rosenbusch (2003) and Ferrara et al. (2004).

As long as the link between the stress-crack width relations obtained with different test methods is not yet completely clear, the test method for determining the relation for a specific case should be as close as possible to the state of stresses in the real structure.

It is noted that the calculated crack distances for the SFRC specimens are larger than the measured ones. The calculation of the crack width is very sensitive to the slope of the first branch in the stress-crack width relationship of the concrete. Slight changes would result in a more realistic crack width. However, if the deformations localized in one crack, the average crack spacing loses its significance for the determination of the plastic rotations. In addition to this, an overestimation of the crack spacing usually results in an underestimation of the rotations. The deviation of calculated and measured crack spacings for the SFRC specimens has therefore been found acceptable. This should be refined in future research.

Model for Rotation Capacity

The model for the rotation capacity was verified for a limited number of tests. The model should be validated against more experimental results.

In this model, only beams with rectangular cross-section were covered. The model should be extended to other cross-sections

The model considers a descending branch in the moment-curvature relationship of deformation controlled tests up to a significant load drop either due to failure of the compressive zone or due to rupture of the first steel bar. At that point, the tests were stopped. However, if deformation-controlled tests are run even further, a further rotation can be assumed at a much lower load level, the maximum of which is governed by the load bearing capacity of the SCSFRC.

However, a practical value of the allowable reduction in load carrying capacity in the descending branch in the plastic hinge is approximately 5 to 10%.

It should be kept in mind that the reduction in load carrying capacity in one hinge must be smaller than the reserves that can be activated in other hinges to avoid collapse.

Consequences for Design Rules

The design rules for the redistribution of cross-sectional actions in RC depend on the hardening ratio f_{su}/f_{sy} and the ultimate strain ε_{su} of the reinforcing steel. For RC members without fibers, the hardening ratio of the tensile member is approximately the same as the hardening ratio of the naked reinforcing steel. For SFRC, however, the hardening ratio of a tensile member is smaller than the hardening ratio of the naked reinforcing steel due to the softening behavior of the SFRC. This might mean that the design rules concerning redistribution of cross-sectional actions derived for RC can be adapted to SFRC by introducing the hardening ratio of the tensile member T_u/T_y rather than the hardening ratio of the naked steel f_{su}/f_{sy} as a decisive parameter. This should be quantified and worked out more thoroughly in future research.

In order to prevent premature localization of the deformations in one crack and thus reduced deformation capacity, the reinforcing steel needs to have a sufficiently large hardening ratio, preferably no yielding plateau and thus continual hardening and a sufficiently large amount of reinforcing steel should be present to compensate for the softening behavior of the SFRC.

It is noted that the addition of steel fibers leads to an increase in load bearing capacity at the beginning of steel yielding, at the level of maximum load and at the level of ultimate load. The redistribution of forces depends on the load bearing capacity as well as on the rotation capacity. If a larger load bearing capacity is present, less rotation capacity is required in order to achieve the same level of redistribution.

References

Abrishami, H.H., Mitchell, D. (1997). Influence of steel fibers on tension stiffening, *ACI Structural Journal*, Vol. **94**, No. 6, pp. 769-776.

Akkermann, J. (2000). *Rotationsverhalten von Stahlbeton-Rahmenecken*, Dissertation, Schriftenreihe des Instituts für Massivbau und Baustofftechnologie, Universität Karlsruhe, Heft 39.

Alvarez, M. (1998). *Einfluss des Verbundverhaltens auf das Verformungsvermögen von Stahlbeton*, Institut für Baustatik und Konstruktion, ETH Zürich, IBK Bericht Nr. 236, Birkhäuser Verlag, Basel, July 1998, 182 pp.

Bachmann, H. (1967). *Zur plastizitätstheoretischen Berechnung statisch unbestimmter Stahlbetonbalken*, Dissertation ETH Zürich, Switzerland. (after: CEB, 1998; Langer, 1997)

Bachmann, H. (1970). Influence of shear and bond on rotational capacity of reinforced concrete beams, IABSE Publications Vol. 30-II, Zürich, Switzerland, pp. 11-28.

Baker, A.L.L. (1956). The ultimate load theory applied to the design of reinforced and prestressed concrete frames, Concrete Publications, London. (after: CEB, 1998; Ortu, 2000)

Barragán, B.E. (2002). *Failure and toughness of steel fiber reinforced concrete under tension and shear*, Doctoral Thesis, Universitat Politècnica de Catalunya, Barcelona, Spain.

Barros, J.A.O., Figueiras, J.A. (1999). Flexural behaviour of SFRC: Testing and modeling, *Journal of Materials in Civil Engineering*, November 1999, pp. 331-339.

Bazant, Z.P. (1989). Identification of strain-softening constitutive relation from uniaxial tests by series coupling model for localization, *Cem. and Conc. Res.*, Vol. **19**, pp. 973-977 (after: Markeset, 1993).

Bekaert (2000). *Dramix® Steel wire fibres for tunnelling*, Product information.

Bigaj-van Vliet, A.J., Mayer, U. (1998). Round Robin analysis of available rotation capacity of plastic hinges – Evaluation, *CEB Bulletin* No. 242, pp. 143-156.

Bigaj, A.J. (1999). *Structural Dependence of Rotation Capacity of Plastic Hinges in RC Beams and Slabs*, PhD thesis, Delft University of Technology.

Bigaj-van Vliet, A.J. (2001). *Bond of deformed reinforcing steel bars embedded in steel fiber reinforced concrete – State-of-the-art report*, Delft Cluster, Oct. 2001, 65 pp.

Bischoff, P. (2000). Comparison of tension stiffening for plain and steel fibre reinforced concrete, *Proceedings of the Fifth International RILEM Symposium Fibre-Reinforced Concretes (FRC)*, Rossi, P. and Chanvillard, G. (eds.), RILEM Publications S.A.R.L.

Bischoff, P. (2003). Tension stiffening and cracking of steel fiber-reinforced concrete, *Journal of Materials in Civil Engineering*, March/April 2003, Vol. **15**, Issue 2, pp. 174-182.

Blom, C.B.M. (2002). *Design philosophy of concrete linings for tunnels in soft soils*, PhD thesis, Delft University of Technology, The Netherlands.

Bonte, F. de (2000). *Hechtsterkte bij staalvezelbeton*, MSc Theis, Katholieke Universiteit Leuven, Belgium, pp. 140.

Brite Euram Task Report P-89-3275 (1992). *Failure mechanics of fibre-reinforced concrete and pre-damaged structures*, Institut für Massivbau und Baustofftechnologie, Universität Karlsruhe, Germany.

Bühler, A.; Eibl, J. (1991). *Untersuchung des Einflusses verschiedener Stahlparameter auf die mögliche plastische Rotation bei Stahlbetonplatten*, Versuchtsbericht, Institut für Massivbau und Baustofftechnologie, Universität Karlsruhe, Germany.

Cairns, J., Plizzari, G. (2004). Bond behaviour of conventional reinforcement in fibre reinforced concrete, *Sixth RILEM Symposium on Fibre-Reinforced Concretes (FRC) - BEFIB 2004*, Varenna (LC), Italy, 20-22 September, 2004, pp. 321-330.

CEB (Comité Euro-International du Béton) (1993). *CEB-FIP Model Code 1990*, CEB Bulletin d'Information, N. 213/214, Comitée Euro-International du Béton, Lausanne, pp. 273.

CEB (1998). *Ductility of reinforced concrete structures, Synthesis report and individual contributions*, Bulletin 242, Lausanne, Switzerland.

Cosenza, E.; Greco, C.; Manfredi, G. (1991). Theoretical evaluation of inelastic rotations and displacements in the reinforced concrete monodimensional elements (in Italian), Atti dell'Accademia Nazionale dei Lincei, serie IX, Volume II, Fascicolo 3 (after: CEB, 1998).

Cosenza, E.; Greco, C.; Manfredi, G. (1992). *Evaluation of plastic rotations in r.c. beams: comparison between theoretical and experimental results*, Technical Report n. 28, Structural Division, Istituto di Ingegneria Civile, Università di Salerno. (after: CEB, 1998)

COB/CUR L500 (2000). *Toetsingsrichtlijn voor het ontwerp van boortunnels voor weg- en railinfrastructuur,* (http://www.cob.nl).

DAfStb (Deutscher Ausschuss für Stahlbeton) (2005). *Richtlinie "Stahlfaserbeton"* (21. Entwurf). Ergänzung zu DIN 1045, Teile 1 – 4, März 2005.

DBV (Deutscher Beton- und Bautechnik-Verein e.V.) (2001). *Merkblatt "Stahlfaserbeton"*, Oktober 2001.

Delibes Liniers, A. (1987). Microcracking of concrete under compression and its influence on tensile strength, *Materials and Structures*, **20**, pp. 111-116.

Di Prisco, M., Felicetti, R., Iorio, F., Gettu, R. (2001). On the identification of SFRC tensile constitutive behaviour, *Proceedings of the fourth international conference on fracture mechanics of concrete and concrete structures* / Cachan / France / 28 May - 1 June 2005, pp. 541-548.

Dietrich, J. (1992). *Zur Qualitätsprüfung von Stahlfaserbeton für Tunnelschalen mit Biegezugbeanspruchung*. Dissertation, Technisch-wissenschaftliche Mitteilungen des Instituts für Konstruktiven Ingenieurbau der Ruhr-Universität Bochum, TWM 92-4.

Dilger, W. (1966). *Veränderlichkeit der Biege- und Schubsteifigkeit bei Stahlbetontragwerken und ihr Einfluß auf Schnittkraftverteilung und Traglast bei statisch unbestimmter Lagerung*, Deutscher Ausschuß für Stahlbeton, Heft 179, Ernst & Sohn, Berlin, Germany.

DIN 488 (1984). *Betonstahl*, Beuth Verlag GmbH, Berlin, Germany.

Dupont, D.; Vandewalle, L.; De Bonte, F. (2002). Influence of steel fibres on local bond behaviour, in: *Bond in concrete – from research to standards*, Balázs, G. et al. (ed.), pp. 783-790.

Dupont, D. (2003). *Modelling and experimental validation of the constitutive law (σ-e) and cracking behaviour of steel fibre reinforced concrete*, PhD Thesis Katholieke Universiteit Leuven, Belgium.

Dupont, D.; Vandewalle, L. (2003). Calculation of crack widths with the σ-e method, Test and design methods for steel fibre reinforced concrete – Background and experiences – *Proceedings of the RILEM TC 162-TDF Workshop*, Eds. B. Schnütgen and L. Vandewalle, Bochum, Germany.

Eifler, H. (1969). *Bericht über die Vorversuche für die Ermittlung des Werkstoff- und Verbundverhaltens im Bereich plastischer Gelenke von Stahlbetonplatten bei statischer Belastung*, Bundesanstalt für Materialprüfung (BAM), Az.: 2.2/11 9311, Berlin, Germany. (after: CEB, 1998)

Eifler, H. (1983). *Verbundverhalten zwischen Beton und geripptem Betonstahl sowie sein Einfluß auf inelastische Verformungen biegebeanspruchter Stahlbetonbalken*, Dissertation Technische Universität Berlin, Germany.

Eligehausen, R., Mayer, U., Lettow, S. (2003). *Mitwirkung des Betons zwischen den Rissen in Stahlbetonbauteilen*, Abschlussbericht zum DFG-Forschungsvorhaben EL 72/8-1+2, Universität Stuttgart, Germany.

Elsaigh, W.A., Robberts, J.M.; Kearsley, E.P. (2004). Modelling non-linear behaviour of steel fibre reinforced concrete, in: *Sixth RILEM Symposium on Fibre-Reinforced Concretes (FRC) - BEFIB 2004*, Varenna (LC), Italy, 20-22 September, 2004.

ENV 10080 (1994). *Steel for the reinforcement of concrete*.

Erdem, E. (2002). *Probabilistisch basierte Auslegung stahlfasermodifizierter Betonbauteile auf experimenteller Grundlage*, Dissertation Ruhr-Universität Bochum, Germany.

Espion, B.; Devillers, J.-J.; Halleux, P. (1993). De l'utilisation de fibres métalliques comme armature complémentaire de poutres en béton armé soumises à flexion, *Materials and Structures*, **26**, 479-485.

Eurocode 2 (1992). *Planung von Stahlbeton- und Spannbetontragwerken*. ENV 1992-1-1: 1991.

Falkner, H., Teutsch, M. (2006). Stahlfaserbeton – Anwendungen und Richtlinie, *Betonkalender 2006: Turmbauwerke und Industriebauten*, Eds. K. Bergmeister and J.-D. Wörner, Ernst & Sohn, Berlin.

Fehling, E., Leutbecher, T. (2005). *Structural behaviour of UHPC under tension, using steel fibres and bar reinforcement*, unpublished presentation.

Ferrara, L., Meda, A., Lamperti, T., Pasini, F. (2004). Connecting fibre distribution, workability and mechanical properties of SFRC: An industrial application to precast elements, in: *Sixth RILEM Symposium on Fibre-Reinforced Concretes (FRC) - BEFIB 2004*, Varenna (LC), Italy, 20-22 September, 2004.

fib bulletin 1 (1999). *Structural concrete, Textbook on behaviour, design and performance, Updated knowledge of the CEB/FIB Model Code 1990*, Lausanne. Switzerland.

fib bulletin 10 (2000). *Bond of reinforcement in concrete*, Lausanne. Switzerland.

Gambarova, P.G., Rosati, G.P., Schumm, C.E. (1994). An elasto-cohesive model for steel-concrete bond, *Proc. Europe-US Workshop on Fracture and Damage in Quasibrittle Structures*, Ed. by Z. Bazant, Z. Bittnar, M. Jirasek and J. Mazars, Prague (Czech Republic), pp. 557-566 (after: *fib* bulletin 10, 2000).

Gettu, R., Barragán (2003). Direct tension test and interpretation, *RILEM Proceedings PRO 31 Test and Design Methods for Steel Fibre Reinforced Concrete – Background and Experiences, Proceedings of the RILEM TC 162-TDF Workshop*, Edited by B. Schnütgen and L. Vandewalle.

Glerum, A. (1992). Within the next ten years doubling tunnel kilometres, *De Ingenieur* no. 11, pp. 4-7 (in Dutch) (after: De Waal, 2000).

Goto, Y. (1971). Cracks Formed in Concrete around Deformed Tension Bars, *ACI Journal*, Vol. **68**, No. 4, pp. 241-251.

Graubner, C.A. (1989). *Schnittgrößenverteilung in statisch unbestimmten Stahlbetonbalken unter Berücksichtigung wirklichkeitsnaher Stoffgesetze – Baustoffbedingte Abweichungen von elastizitätstheoretischen und plastizitätstheoretischen Lösungen*, Dissertation, TU München, Germany.

Grimm, R. (1997). *Einfluss bruchmechanischer Kenngrössen auf das Biege- und Schubtragverhalten hochfester Betone*. Deutscher Ausschuss für Stahlbeton, Heft 477, Beuth Verlag GmbH Berlin / Wien / Zürich.

Groth, P. (2000). *Fibre reinforced concrete - Fracture mechanics applied on self-compacting concrete and energetically modified binders*, Doctoral Thesis, Department of Civil and Mining Engineering, Luleå University of Technology, Sweden.

Grübl, P., Weigler, H., Karl, S. (2001). *Beton*, Ernst & Sohn Verlag, Berlin Germany.

Grünewald, S.; Walraven, J.C. (2002a). High strength self-compacting fibre reinforced concrete: Behaviour in the fresh and the hardened state, *Proc. 6th Int. Symposium on Utilization of High Strength/High Performance Concrete*, Leipzig, Germany, pp. 977-989.

Grünewald, S.; Walraven, J.C. (2002b). *Self-compacting fibre reinforced concrete – orientation and distribution of steel fibres in beams*. Stevinrapport no. 25.5-02-33, Delft University of Technology, Netherlands.

Grünewald, S. (2004). *Performance-based design of self-compacting fibre reinforced concrete*, PhD Thesis, Delft University of Technology, The Netherlands.

Gysel, A. van (2000). *Studie van het uittrekgedrag van staalvezels ingebed in een cementgebonden matrix met toepassing op staalvezelbeton onderworpen aan buiging*, Universiteit Gent, Doctoral Thesis, Academiejaar 1999-2000.

Han, N. (1996). *Time Dependent Behaviour of High Strength Concrete*, PhD thesis, Delft University of Technology, The Netherlands.

Harajli, M.H. (1992). Local bond-slip behavior of reinforcing bars embedded in fiber reinforced concrete, *Proceedings of international conference: Bond in concrete – From research to practice*, Riga, 1992, pp. 7.87-7.97. (after: Bigaj-van Vliet, 2001).

Harajli, M.H., Hout, M., Jalkh, W. (1995). Local bond stress-slip behavior of reinforcing bars embedded in plain and fiber concrete, *ACI Materials Journal*, Vol. **92**, No. 46, pp. 343-354.

Hartwich, K. (1986). *Zum Riss- und Verformungsverhalten von stahlfaserverstärkten Stahlbetonstäben unter Längszug*, Dissertation, TU Braunschweig, Institut für Baustoffe, Massivbau und Brandschutz, Heft 72, Germany.

Hemmy, O. (2002). *Tunnelbauwerke aus Stahlfaserbeton*, Heft 164 IBMB Braunschweiger Bauseminar 2002, Germany.

Hemmy, O. (2003). *Zum Gebrauchs- und Tragverhalten von Tunnelschalen aus Stahlfaserbeton und stahlfaserverstärktem Stahlbeton*. Dissertation TU Braunschweig, Germany.

Hemmy, O., Falkner, H. (2004). Neue Konstruktionsprinzipien bei Tunnelinnenschalen, *Beton- und Stahlbetonbau*, **99**, Heft 2, pp. 89-96.

Herzog, M. (1999). *Elementare Tunnelbemessung*, Werner Verlag, Germany.

Hillerborg, A., Modéer, M., Peterson, P.E. (1976). Analysis of crack growth in concrete by means of fracture mechanics and finite elements, *Cement and Concrete Research*, **6**, pp. 773-782.

Hillerborg, A. (1988). Fracture mechanics concepts applied to moment capacity and rotational capacity of reinforced beams, *Proc. Int. Conf. Fracture and damage mechanics of concrete and rock*, Vienna, 233-240.

Holschemacher, K. (2001). Bemessungsrelevante Eigenschaften von selbstverdichtenden Betonen, *Selbstverdichtender Beton* (Editors: König, Holschemacher, Dehn), Bauwerk Verlag GmbH, Berlin, Germany, pp. 129 – 143.

Hordijk, D.A. (1991). *Local approach to fatigue of concrete*, PhD-thesis, Faculty of Civil Engineering, Delft University of Technology, The Netherlands.

Hota, S., Naaman, A.E. (1997). Bond stress-slip response of reinforcing bars embedded in FRC matrices under monotonic and cyclic loading, *ACI Structural Journal*, Vol. **94**, No. 5, pp. 525-537.

Hsu, T.T.C., Slate, F.O., Sturman, G.M., and Winter, G. (1963). Microcracking of plain concrete and the shape of the stress-strain curve, *Journal of the American Concrete Institute*, Proc., Vol. **60**, No. 2, pp. 209-224.

IFT Info (2004). *Beton- und Stahlbetonbau*, **99**, Heft 2.

Janßen, P. (1983). *Tragverhalten von Tunnelausbauten mit Gelenktübbings*. Dissertation Technische Universität Braunschweig, Germany.

Japan Concrete Institute (2001). Determination of tension softening diagram of concrete, *JCI-TC992 Test Method for Fracture Property of Concrete*, Draft (after: Villmann et al., 2004).

Jungwirth, J. (2006). *Zum Tragverhalten von zugbeanspruchten Bauteilen aus Ultra-Hochleistungs-Faserbeton*, Dissertation No. 3429 (2006), École Polytechnique Fédérale de Lausanne, Switzerland.

Kameswara Rao, C.V.S. (1979): Effectiveness of random fibres in composites, *Cement and Concrete Research*, **9**, pp. 685-693.

Karihaloo, B.L. 1995, *Fracture mechanics and structural concrete*, Longman Scientific & Technical, England.

Kooiman, A.G. (2000). *Modelling steel fibre reinforced concrete for structural design*, PhD-thesis, Department of Concrete Structures, Faculty of Civil Engineering, Delft University of Technology, The Netherlands.

König, G., Pommerening, D., Tue, N.V. (1999). *Nichtlineares Last-Verformungs-Verhalten von Stahlbeton- und Spannbetonbauteilen, Verformungsvermögen und Schnittgrößenermittlung*, Deutscher Ausschuß für Stahlbeton, Heft 492, Beuth Verlag GmbH, Berlin.

König, G., Holschemacher, K., Dehn, F., Weiße, D. (2003). Bond of reinforcement in self-compacting concrete (SCC) under monotonic and cyclic loading, *3rd International symposium on self-compacting concrete*, 17-20 August 2003, Reykjavik, Iceland.

Kreller, H. (1989). *Zum nichtlinearen Trag- und Verformungsverhalten von Stahlbetonstabtragwerken unter Last- und Zwangeinwirkung*, Dissertation, Universität Stuttgart, Institut für Werkstoffe im Bauwesen, 1989/4, Germany.

Krenchel, H. (1975): *Fibre spacing and specific fibre surface, Fibre reinforced cement and concrete*, Edited by Neville, The Construction Press, UK, pp. 69-79.

Kützing, L. (2000). *Tragfähigkeitsermittlung stahlfaserverstärkter Betone*. B.G.Teubner Stuttgart Leipzig Wiesbaden.

Langer, P., (1987). *Verdrehfähigkeit plastizierter Tragwerksbereiche im Stahlbetonbau*, Dissertation, Universität Stuttgart, Institut für Werkstoffe im Bauwesen, 1987/1, Germany.

Langer, P., (1997). *Verdrehfähigkeit plastizierter Tragwerksbereiche im Stahlbetonbau*, Deutscher Ausschuß für Stahlbeton, Heft 484, Beuth Verlag GmbH, Germany, pp. 129-198.

Li, L., (1997). *Rotationsfähigkeit von plastischen Gelenken im Stahl- und Spannbetonbau*, Deutscher Ausschuß für Stahlbeton, Heft 484, Beuth Verlag GmbH, Germany, pp. 45-126.

Lin, Y.-Z. (1996). *Tragverhalten von Stahlfaserbeton*, Dissertation, Schriftenreihe Heft 28, Institut für Massivbau, Universität Karlsruhe, Germany.

Löfgren, I., Stang, H., Olesen, J.F. (2004). Wedge splitting test – A test to determine fracture properties of FRC, in: *Sixth RILEM Symposium on Fibre-Reinforced Concretes (FRC) - BEFIB 2004*, Varenna (LC). Italy, 20-22 September, 2004, pp. 379-388.

Löfgren, I. (2005). *Fibre-reinforced concrete for industrial construction – a fracture mechanics approach to material testing and structural analysis*, PhD Thesis, Chalmers University of Technology, Sweden.

Maidl, B.R. (1995). *Steel fibre reinforced concrete*, Ernst & Sohn Verlag, Berlin, Germany, pp. 291.

Markeset, G. (1993). *Failure of concrete under compressive strain gradients*. Dr.ing. Thesis 1993: 110, The Norwegian Institute of Technology, Trondheim, Norway.

Markeset, G. (1995). Softening of concrete in compression – Localization and size effects, *Cement and Concrete Research*, Vol. **25**, No. 4, pp. 702-708.

Marković, I., Grünewald, S., Walraven, J.C., Mier, J.G.M. van (2002). Characterization of Bond Between Steel Fibres and Concrete – Conventional Fibre Reinforced Versus Self-Compacting Fibre Reinforced Concrete, in: *Bond in Concrete – from research to standards*, Balázs, G. et al. (ed.), pp. 520-528.

Marković, I. (2006). *High-Performance Hybrid-Fibre Concrete – Development and Utilisation*, PhD Thesis, Delft University of Technology, The Netherlands.

Mayer, U. (2002). *Zum Einfluss der Oberflächengestalt von Rippenstählen auf das Trag- und Verformungsverhalten von Stahlbetonbauteilen*, Dissertation, Institut für Werkstoffe im Bauwesen, Universität Stuttgart, Germany.

Meda, A., Plizzari, G.A., Sorelli, L. (2004). Uni-axial and bending test for the determination of fracture properties of fiber reinforced concrete, *Proceedings of the Fifth International Conference on Fracture Mechanics of Concrete and Concrete Structures*, Edited by V.C. Li, C.K.Y. Leung, K. J. Willam, S.L. Billington, pp. 1163-1170.

Meyer, J. (1997). *Ein Beitrag zur Untersuchung der Verformungsfähigkeit von Bauteilen aus Beton unter Biegedruckbeanspruchung*, Dissertation, Leipzig, Germany.

Mier, J.G.M. van (1984). *Strain-softening of concrete under multiaxial loading conditions*, Ph.D. thesis, Eindhoven University of Technology, The Netherlands.

Mier, J.G.M. van (1997). *Fracture process of concrete: Assessment of material parameters for fracture models*, CRC Press, Boca Raton, Florida, USA.

Mitchell, D., Abrishami, H.H., Mindess, S. (1996). The effect of steel fibers and epoxy-coated reinforcement on tension stiffening and cracking of reinforced concrete, *ACI Materials Journal*, Jan.-Feb., 1996, pp. 61-68.

NEN 5968 (1988). *Beton en Mortel - Bepaling van de druksterkte van proefstukken*, Nederlands Normalisatie-instituut (NNI), Delft, The Netherlands.

NEN 5969 (1988). *Beton en Mortel - Bepaling van de splijtsterkte van proefstukken*, Nederlands Normalisatie-instituut (NNI), Delft, The Netherlands.

Niemann, P. (2002). *Gebrauchsverhalten von Bodenplatten aus Beton unter Einwirkung infolge Last und Zwang*, Dissertation, TU Braunschweig, Germany.

Noghabai, K. (1995). *Splitting of concrete in the anchoring zone of deformed bars – A fracture mechanics approach*, Licenciate Thesis 1995:26L, Luleå University of Technology, Luleå, Sweden, 131+46 pp.

Noghabai, K. (1998). *Effect of tension stiffening on the performance of concrete structures – experimental, analytical and computational studies*, Doctoral Thesis 1998:21, Luleå University of Technology, Luleå, Sweden.

Ortu, M. (2000). *Rißverhalten und Rotationsvermögen von Stahlfaserbeton für Standsicherheitsuntersuchungen im Tunnelbau*, VDI Reihe 4 Nr. 164, Düsseldorf: VDI Verlag 2000, Germany.

De Pauw, P; Tearwe, L. (2004). The effect of steel fibres on the rotation capacity of post-tensioned high strength concrete beams, *Sixth RILEM Symposium on Fibre-Reinforced Concretes (FRC) - BEFIB 2004*, Varenna (LC), Italy, 20-22 September, 2004, pp. 1027-1034.

Pecce, M. (1998). Experimental evaluation of rotation capacity of HPC beams, *CEB Bulletin 242*, pp. 197-210.

Pereira, E.N.B., Barros, J.A.O.; Ribeiro, A.F.; Camões, A. (2004). Post-cracking behaviour of self-compacting steel fibre reinforced concrete, in: *Sixth RILEM Symposium on Fibre-Reinforced Concretes (FRC) - BEFIB 2004*, Varenna (LC), Italy, 20-22 September, 2004.

Pfyl, Th., Marti, P. (2001). *Versuche an stahlfaserverstärkten Stahlbetonelementen*, Institut für Baustatik und Konstruktion, ETH Zürich, Switzerland, IBK Bericht Nr. 268, Birkhäuser Verlag, Basel, 137 pp.

Pfyl, Th. (2003). *Tragverhalten von Stahlfaserbeton*, Dissertation ETH Nr. 15005, Zürich, Switzerland.

Plizzari, G.A. (1999). Bond and splitting crack development in normal and high strength fiber reinforced concrete, *Proceedings of 13th Eng. Mechanics Division Conference – EMD 99*, Baltimore.

Plizzari, G.A.; Lundgren, K.; Balázs, G.L. (2002). Bond and Splitting in Fibre Reinforced Concrete Under Repeated Loading, in: *Bond in Concrete – from research to standards*, Balázs, G. et al. (ed.), pp. 221-229.

Pölling, R. (2000). *Eine praxisnahe, schädigungsorientierte Materialbeschreibung von Stahlbeton für Strukturanalysen*, Dissertation, Ruhr-Universität Bochum, Germany.

Pommerening, D. (1996). *Ein Beitrag zum nichtlinearen Materialverhalten und zur Schnittgrößenermittlung im Massivbau*, Dissertation, TH Darmstadt, Germany.

Popovics, S. (1973). A numerical approach to the complete stress-strain curve of concrete, *Cem. and Conc. Res.*, Vol. **3**, pp. 583-599 (after: Markeset, 1993).

Quiertant, M., Seignol, J.F., Toutlemonde, F. (2001). Mechanical performance of RC and SFRC tunnel lining segments, *Fracture mechanics of concrete structures*, de Borst et al. (eds.), Swets & Zeitlinger, Lisse.

Rehm, G. (1961). *Über die Grundlagen des Verbundes zwischen Stahl und Beton*, Deutscher Ausschuss für Stahlbeton, Heft 138, Ernst & Sohn, Germany.

Remmel, G. (1994). *Zum Zug- und Schubtragverhalten von Bauteilen aus hochfestem Beton*, Deutscher Ausschuß für Stahlbeton, Heft 444, Beuth Verlag, Berlin, Germany.

RILEM/ CEB/ FIB committee (1970). Tests and specifications of reinforcements for reinforced and pre-stressed concrete, Bond test for reinforcing steel, 2. Pullout test, *Materials and Structures*, Research and Testing 3, 15, pp. 175-178.

Roelfstra, P.E., Wittmann, F.H. (1986). Numerical method to link strain softening with failure of concrete, Fracture Toughness and Fracture Energy of Concrete. Ed. F.H. Wittmann, Elsevier, pp. 163-175 (after: Den Uijl & Bigaj, 1996).

Römer, T. (1998). *Zur bruchmechanischen Modellierung des Druckversagens von Beton*, Unpublished thesis, HTWK Leipzig, Germany.

Rosenbusch, J. (2003). *Zur Querkrafttragfähigkeit von Balken aus Stahlfaserverstärktem Stahlbeton*, Dissertation, TU Braunschweig, Germany.

Rosenbusch, J. (2004). Einfluß der Faserorientierung auf die Beanspruchbarkeit von Bauteilen aus Stahlfaserbeton, *Beton- und Stahlbetonbau,* **99**, Heft 5, pp. 372-377.

Rosati, G.P., Schumm, C.E. (1992). Modelling of local bar-to-concrete bond in R.C. beams, *Proc. Int. Conf. "Bond in Concrete: from Research to Practice", CEB-RTU (Riga Technical University)*, Riga (Latvia), 12.34 12.34 (after: *fib* bulletin 10, 2000).

Rüsch, H., Kordina, K., Stöckl, S. (1966). *Festigkeit der Biegedruckzone – Vergleich von Prismen- und Balkenversuchen*, Deutscher Ausschuss für Stahlbeton, Heft 190, Verlag W. Ernst u. Sohn.

Samen Ezeldin, A., Balaguru, P.N. (1989). Bond behavior of normal and high-strength fiber reinforced concrete, *ACI Materials Journal*, Vol. **86**, No. 5, pp. 515-524.

Samen Ezeldin, A., Balaguru, P.N. (1990). Bond performance of reinforcing bars embedded in fiber reinforced concrete and subjected to monotonic and cyclic loads, *Proceedings of ASCE on Serviceability and Durability of Construction Materials*, pp. 145-154.

Schneider, K.-J. (1994). *Bautabellen für Ingenieure: mit europäischen und nationalen Vorschriften*, 11. Aufl., Werner Verlag GmbH, Düsseldorf, Germany.

Schnütgen, B. (1975). *Das Festigkeitsverhalten von mit Stahlfasern bewehrtem Beton unter Zugbeanspruchungen*, Dissertation, Ruhr-Universität Bochum, Technisch-wissenschaftliche Mitteilung Nr. 75-8, 1975.

Schönlin, K. (1988). Ermittlung der Orientierung, Menge und Verteilung der Fasern in faserbewehrtem Beton, *Beton- und Stahlbetonbau*, **83**, Heft 6, pp. 168-171.

Schumacher, P., Braam, C.R., Walraven, J.C. (2002a). Compressive behavior of steel fiber reinforced high strength concrete, *Proc. 6th Int. Symposium on Utilization of High Strength/High Performance Concrete*, Leipzig, Germany, pp. 1377-1390

Schumacher, P., Bigaj-van Vliet, A., Braam, C.R., Uijl, J.A. den, Walraven, J.C. (2002b). "Bond of reinforcing bars in self-compacting steel fiber reinforced concrete" in: *Bond in concrete – from research to standards*, Balázs, G. et al. (ed.), pp. 823-830.

Schumacher, P., Bigaj-van Vliet, A., Braam, C.R., Walraven, J.C. (2002c). "Bond of reinforcing bars in self-compacting steel fiber reinforced concrete", *Beiträge aus der*

Befestigungstechnik und dem Stahlbetonbau, Festschrift zum 60. Geburtstag von Prof. Dr.-Ing. R. Eligehausen, (Editors: S. Lettow, J. Hofmann), ibidem Verlag Stuttgart, Stuttgart 2002.

Schumacher, P., Uijl, J.A. den, Braam, C.R., Walraven, J.C. (2003a). *Self-compacting steel fiber reinforced concrete prisms under compressive loading*, Stevinreport 25.5-03-11, Delft University of Technology, The Netherlands.

Schumacher, P.; Uijl, J.A. den; Walraven, J.C. (2003b). *Fracture energy determined from three-point bending tests on self-compacting steel fiber reinforced concrete*, Stevinreport 25.5-03-18, Delft University of Technology, The Netherlands.

Shionaga, R. (2006). Structural behavior of high performance fiber reinforced concrete in tension and bending, *6th International PhD symposium in civil engineering*, Zürich, August 23-26, 2006, Switserland.

SIA (1993). Norm SIA 162, *Betonbauten*, Schweizerischer Ingenieur- und Architekten-Verein, 1989, update 1993, 85 pp.

Sigrist, V. (1995). *Zum Verformungsvermögen von Stahlbetonträgern*, Dissertation ETH Zürich, Switserland.

Sint, A. (2002). *Duktilität von Biegebauteilen bei Versagen der Betondruckzone*. Dissertation Universität Leipzig, Germany.

Slowik, V. & Wittmann, F.H. (1992). *Influence of strain gradient on fracture energy*. In Z.P. Bažant (ed.) FraMCoS-a, Breckenridge (USA), June 1992: 424-429.

Slowik, V. (1993). Influence of size of specimen and strain gradient on the experimentally determined fracture energy, Numerical Models in Fracture Mechanics of Concrete, Wittmann (ed.), Balkema, Rotterdam, ISBN 90 5410 353 1.

Sorelli, L. (2003). *Some studies on the assessment of the fracture toughness of fiber reinforced concrete with an emphasis on hybrid fiber systems*, PhD Thesis University of Brescia, Italy, pp. 372.

Soroushian, P., Lee, C.-D. (1990). Distribution and Orientation of Fibers in Steel Fiber Reinforced Concrete, *ACI Materials Journal*, Sept-Oct 1990, pp. 433-439.

Soroushian, P., Mirza, F., Alhozaimy, A. (1994). Bonding of confined steel fiber reinforced concrete to deformed bars, *ACI Materials Journal*, Vol. **91** (2), 1994, pp. 141-149.

Stang, H. (1992). Evaluation of properties of cementitious fiber composite materials, in *'High Performance Fiber Reinforced Cement Composites'*, Vol. I, E & FN Spon, London, pp. 388-406 (after: Østergaard, 2003).

Stiel, T., Karihaloo, B.L., Fehling, E. (2004). Effect of Casting Direction on the Mechanical Properties of CARDIFRC®, *Ultra High Performance Concrete (UHPC)*, Proceedings of the International Symposium on Ultra High Performance Concrete, Eds. M. Schmidt, E. Fehling, C. Geisenhanslüke, Kassel, Germany, 2004, pp. 481-494

Stroband. J. (1998). *Onderzoek naar standaardiseering van een beproevingsmethode voor staalvezelbeton*, Stevin Report 25.5-98.14, Delft University of Technology, The Netherlands, 41 pp.

Stroeven, P. (1978): Morphometry of fibre reinforced cementitious materials – Part 1: Efficiency and spacing in idealized structures, *Materials and Structures*, Vol. **11**, No. 61, pp. 31-37.

Sule, M.S. (2003). *Effect of reinforcement on early-age cracking in high strength concrete*, PhD Thesis, Delft University of Technology, The Netherlands.

Tepfers, R. (1979). Cracking of concrete cover along anchored deformed reinforcing bars, *Magazine of Concrete Research*, Vol. **31**, No. 106, pp. 3-12.

Teutsch, M. (2006). Einsatz von Stahlfaserbeton im Tunnelbau, *Beton- und Stahlbetonbau*, Mai 2006, pp. 311-321.

Toutlemonde, François (2004). *Contribution à la connaissance et à la maîtrise de quelques non-linéarités du comportement mécanique des bétons et de leur effet sur le fonctionnement des structures, assortie de quelques réflexions méthodologiques*, LCPC, France, ISSN 1161-028X.

Uijl, J.A. den, Bigaj, A.J. (1996). A bond model for ribbed bars based on concrete confinement, *Heron*, Vol. **41**, No. 3, pp. 201-226.

Vandewalle et al. (2000). Recommendation of RILEM TC162-TDF: Test and design methods for steel fibre reinforced concrete: Bending test, *Materials and Structures*, Vol. **33**, 2000, pp. 3-5.

Vandewalle et al. (2002). Recommendation of RILEM TC162-TDF: Test and design methods for steel fibre reinforced concrete: Design of steel fibre reinforced concrete using the σ-w method: principles and applications, *Materials and Structures*, Vol. **35**, 2002, pp. 262-178.

Veen, C. van der (1990). *Cryogenic bond stress-slip relationship*, PhD Thesis, Delft University of Technology, The Netherlands.

Villmann, B., Villmann, Th., Slowik, V. (2004). Determination of softening curves by backward analyses of experiments and optimization using an evolutionary algorithm, *Fracture Mechanics of Concrete Structures*, Li et al. (eds.), 2004 Ia-FraMCos, ISBN 0 87031 135 2, pp. 439-445.

Vonk, R. (1992). *Softening of concrete loaded in compression*, PhD Thesis, Eindhoven, The Netherlands.

Voo, J.Y.L., Foster, S.J. (2003). *Variable Engagement Model for Fibre Reinforced Concrete in Tension*, The University of New South Wales, Sydney 2052 Australia.

Voo, J.Y.L., Foster, S.J. (2004). Tensile-Fracture of Fibre-Reinforced Concrete: Variable Engagement Model, *Sixth RILEM Symposium on Fibre-Reinforced Concretes (FRC) - BEFIB 2004*, Varenna (LC), Italy, 20-22 September, 2004, pp. 875-884.

Waal, R.G.A. de (2000). *Steel fibre reinforced tunnel segments for the application in shield driven tunnel linings*, PhD thesis, Delft University of Technology, The Netherlands.

Weiße, D. (2001). Einfluss des Betonalters auf die Festigkeits-, Formänderungs- und Verbundkennwerte. 1. Leipziger Fachtagung „Innovationen im Bauwesen", *Selbstverdichtender Beton*, Bauwerk Verlag GmbH, Berlin, Germany, pp. 145-164.

Weiße, D. (2002). Verbundverhalten der Bewehrung in Stahlfaserbeton. 2. Leipziger Fachtagung „ Innovationen im Bauwesen", *Faserbeton*, Bauwerk Verlag GmbH, Berlin, Germany, pp. 77-88.

Winterberg, R. (1997). *Einfluß von Stahlfasern auf die Durchlässigkeit von Beton*, Deutscher Ausschuß für Stahlbeton, Heft 483, Beuth Verlag GmbH, Berlin, Germany.

Winterberg, R. (1998). *Untersuchungen zum Reißverhalten von Stahlfaserbeton und stahlfaserverstärktem Stahlbeton*, Dissertation, Technisch-wissenschaftliche Mitteilungen TWM 98-3, Institut für Konstruktiven Ingenieurbau, Ruhr-Universität Bochum, Germany

Østergaard, L. (2003). *Early-age fracture mechanics and cracking of concrete*, PhD Thesis, Lyngby, Denmark.

Appendices

Appendix A: Identification of the Mixtures and Test Specimens

The concrete mixtures are denoted with a code, referring to:

- the concrete compressive strength
- the fiber geometry and
- the amount of steel fibers in kg/m^3.

An overview over the names is given in Table A1.

Table A1:Mixture identification

Mixture identification	Intended compressive strength [N/mm^2]	Fiber geometry Aspect ratio / length [-] / [mm]	Fiber content [kg/m^3]
B45.0.0	45	-	0
B45.45/30.60	45	45/30	60
B45.45/30.120	45	45/30	120
B45.80/30.60	45	80/30	60
B45.80/60.60	45	80/60	60
B105.0.0	105	-	0
B105.80/30.60	105	80/30	60
B105.80/60.60	105	80/60	60

The codes of the prism tests refer to:

- mixture identification
- eccentricity of the load (e00 = centric, e08 = 8.33mm = $h/18$, e25 = 25mm = $h/6$)
- number of the individual test.

To give an example, test specimen B45.45/30.60.e08.2 means:

- concrete compressive strength: designed to be a B45
- fiber type: loose, hooked ends, aspect ratio 45, length 30 mm, minimum tensile strength of 1000 N/mm^2
- amount of steel fibers: 60 kg/m^3
- eccentricity of the load: e08 = 8.33mm = $h/18$
- number of the individual test: 2nd test with this parameter combination.

The codes of the pull-out tests refer to:

- mixture identification
- concrete cover in mm and the casting method (no index: directly cast, s = sawn)
- number of the individual test.

To give an example, test specimen B45.45/30.60.c15s.2 means:

- concrete compressive strength: designed to be a B45
- fiber type: loose, hooked ends, aspect ratio 45, length 30 mm, minimum tensile strength of 1000 N/mm^2
- amount of steel fibers: 60 kg/m^3
- concrete cover = 15 mm; sawn specimen
- number of the individual test: 2nd test with this parameter combination.

The codes of the beam tests refer to:

- mixture identification
- normal compressive force in kN.

To give an example, test specimen B45.80/30.60.N400 means:

- concrete compressive strength: designed to be a B45
- fiber type: collated, hooked ends, aspect ratio 80, length 30 mm, minimum tensile strength of 1000 N/mm^2
- amount of steel fibers: 60 kg/m^3
- normal compressive force N = 400 kN.

Appendix B: Properties of the Concrete in the Fresh State

Mixtures for the Prism Tests

Table B1: Results of the concrete tests in the fresh state (n.m. = not measured)

Mix	Slump flow [mm]		t_{50} time [s]		Temperature [ºC]
B45.0.0	760	690	1.9	3.3	25
B45.45/30.60	740	650	2.7	4.1	23
B45.45/30.120	640	650	3.9	4.2	24
B45.80/30.60	600	590	4.0	2.5	26
B45.80/60.60	580	650	2.6	3.0	26
B105.0.0	610	570	8.4	5.3	n.m.
B105.80/30.60	620	660	8.6	6.3	n.m.
B105.80/60.60	610	580	6.8	5.8	n.m.

Mixtures for the Beam Tests

After mixing, the concrete properties in the fresh state were tested in order to judge whether the self-compacting concrete would satisfy the requirements. If the slump turned out too low, approximately 10% of the superplasticizer HR were added and the concrete was tested again. The results of the final mixtures are summarized in Table B2. The temperature of the fresh concrete was between 20 and 25°C.

Table B2: Results of the concrete tests in the fresh state

Mixture for test	t_{50} mix 1 [sec]	Slump mix 1 [mm]	t_{50} mix 2 [sec]	Slump mix 2 [mm]	Air content Mix 2 [%]
B45.0.0.N400	3.54	660	2.78	750	2.9
B45.80/30.60.N400	5.72	730	3.41	710	3.6
B45.0.0.N0	3.56	820	2.62	790	3.0
B45.80/30.60.N0	3.25	795	5.84	780	2.4

Mixture for test	Temperature mix 1 [°C]	Temperature mix 2 [°C]	Temperature room [°C]	Vol. mass mix 2 [kg/m^3]
B45.0.0.N400	25	25	21	2280
B45.80/30.60.N400	22	22	Ca. 19	2278
B45.0.0.N0	23	23	19	2369
B45.80/30.60.N0	19	19	16	2310

Appendix C: Results of the Standard Tests

Mixtures for the Prism Tests

Table C1: Results of the standard tests

Mix	Age at testing	Cube compressive strength [N/mm^2]		Tensile splitting strength[1)] [N/mm^2]		Modulus of elasticity [×1000 N/mm^2]	
	[days]	Single test results	Mean value	Single test results	Mean value	Single test results	Mean value
B45.0.0	28	53.63 53.43 55.87	54.31	4.74 4.50 4.93	4.72	35.57 37.90 37.63	37.03
B45.45/30.60	28	52.59 58.92 55.49	55.67	6.73 5.51 5.27	5.84	37.47 36.07 38.79	37.44
B45.45/30.120	28	54.49 55.17 59.46	56.37	6.84 6.72 6.87	6.81	40.2 38.89 37.71	38.93
B45.80/30.60	28	51.96 61.19 55.20	56.12	6.55 6.81 6.27	6.54	37.59 38.65 37.94	38.06
B45.80/60.60	28	62.28 61.28 58.52	60.69	7.00 6.76 6.35	6.70	38.08 38.20 38.11	38.13
B105.0.0	35	118.34 117.57 109.78	115.23	5.48 5.98 5.50	5.65	44.03 43.92 44.30	44.08
B105.80/30.60	28	115.95 118.31 115.81	116.69	11.29 11.71 12.07	11.69	43.17 43.26 42.64	43.02
B105.80/60.60	28	115.84 115.32 118.78	116.65	12.28 13.13 11.71	12.37	43.51 42.72 43.33	43.19

[1)]measured perpendicular to the casting surface

Table C2: Compressive strengths

Mix	Age at testing	Compressive strength cubes [N/mm^2]		Compressive strength small prisms [N/mm^2]		Compressive strength large prisms [N/mm^2]	
	[days]	Single test results	Mean value	Single test results	Mean value	Single test results	Mean value
B45.0.0	28	53.63 53.43 55.87	54.31	47.68 51.63 47.42	48.91	50.80 51.08 49.42	50.43
B45.45/30.60	28	52.59 58.92 55.49	55.67	46.94 49.62 50.75	49.10	47.66 47.42 47.72	47.60
B45.45/30.120	28	54.49 55.17 59.46	56.37	50.93 50.55 51.83	51.10	46.09 42.95 48.71	45.92
B45.80/30.60	28	51.96 61.19 55.20	56.12	52.71 50.23 50.96	51.30	53.11 52.70 52.93	52.82
B45.80/60.60	28	62.28 61.28 58.52	60.69	52.62 50.86 50.70	51.39	47.02 50.89 48.29	48.73
B105.0.0	35	118.34 117.57 109.78	115.23	99.85 102.57 104.00	102.14	106.41	
B105.80/30.60	28	115.95 118.31 115.81	116.69	99.53 103.23 100.38	101.05	100.38	
B105.80/60.60	28	115.84 115.32 118.78	116.65	103.45 101.03 105.60	103.36		

small prism / cube = 0.85-0.91; average 0.89; general model 0.85
large prism / cube = 0.80-0.94; average 0.87; general model 0.85

It is noted that the decrease in prism compressive strength due to fiber addition can be explained by the fiber orientation. In the cubes, a more or less uniform 3D-orientation of the fibers is likely whereas in the prisms, the fibers are likely to be oriented in the direction of the flow. This is an advantage in the cracks in bending tests but a disadvantage in compressive tests. There, the fibers are not in the direction to cross and therefore transmit the tensile forces perpendicular to the compressive force but rather serve as weak points where cracks can initiate.

Mixtures for the Pull-out Tests

Table C3: Results of the standard tests (standard deviation)

Mix	Age at testing [days]	Compressive cube strength [N/mm^2]		Tensile splitting strength [N/mm^2]		Modulus of elasticity [×1000 N/mm^2]	
		Single test results	Mean value	Single test results	Mean value	Single test results	Mean value
B45.0.0	28	53.41 54.19 47.64	51.75 (3.57)	3.56 4.03 3.72	3.77 (0.24)	35.00 30.14 33.95	33.03 (2.56)
B45.45/30.60	28	54.63 50.19 51.82	52.21 (2.25)	5.64 5.54 5.59	5.59 (0.05)	36.50 41.46 36.17	38.04 (2.96)
B45.45/30.120	28	52.87 56.51 57.18	55.52 (2.32)	7.47 7.55 6.93	7.32 (0.34)	36.07 36.93 36.17	36.39 (0.47)
B45.80/30.60	28	49.04 50.77 55.68	51.83 (3.44)	4.87 5.18 6.17	5.41 (0.68)	33.88 34.14 35.00	34.34 (0.59)
B105.0.0	28	104.71 102.42 110.16	105.76 (3.98)	5.57 5.72 6.01	5.77 (0.22)	42.62 42.55 44.70	43.29 (1.22)
B105.80/30.60	28	120.28 107.91 115.00	114.40 (6.21)	11.48 11.45 11.90	11.61 (0.25)	43.57 43.81 44.93	44.10 (0.73)

Mixtures for the Beam Tests

Table C4: Results of the standard tests (standard deviation)

Mixture for test	Compressive strength cube [N/mm^2]		Tensile splitting strength [N/mm^2]		Compressive strength prism [N/mm^2]	
	Single test results	Mean value (st dev)	Single test results	Mean value (st dev)	Single test results	Mean value (st dev)
B45.0.0.N0	55.42 52.84 54.56	54.27 (1.31)	5.05 4.92 5.21	5.06 (0.15)	50.86 50.43 52.73	51.34 (1.22)
B45.0.0.N400	55.44 56.22 54.36	55.34 (0.93)	5.33 5.13 5.01	5.16 (0.16)	53.15 53.82 52.83	53.27 (0.51)
B45.8030.60.N0	54.63 54.27 55.67	54.86 (0.73)	5.16 5.16 6.97	5.76 (1.05)	49.67 49.09 48.99	49.25 (0.37)
B45.8030.60.N400	53.01 56.04 54.49	54.51 (1.52)	5.65 6.18 6.43	6.09 (0.40)	49.43 49.83 49.57	49.61 (0.20)

Appendix D: Damage Zone Lengths L^d in Prism Tests

Mix	e	no.	Ld [mm]	Coefficient of variation
Average			410	
B45.0.0	00	1	400	
B45.0.0	00	2	600	0.21
B45.0.0	00	3	450	
B45.0.0	08	1	550	
B45.0.0	08	2	600	0.09
B45.0.0	08	3	500	
B45.0.0	25	1	350	
B45.0.0	25	2	350	
B45.0.0	25	3	550	0.22
B45.0.0	25	4	300	
B45.0.0	25	5	400	
B45.0.0	25	6	450	
B45.45/30.60	00	1	350	
B45.45/30.60	00	2	450	0.14
B45.45/30.60	00	3	450	
B45.45/30.60	08	1	450	
B45.45/30.60	08	2	600	0.17
B45.45/30.60	08	3	450	
B45.45/30.60	25	1	150	
B45.45/30.60	25	2	250	0.40
B45.45/30.60	25	3	350	
B45.45/30.120	00	1	500	
B45.45/30.120	00	2	450	0.11
B45.45/30.120	00	3	400	
B45.45/30.120	08	1	400	
B45.45/30.120	08	2	400	0.07
B45.45/30.120	08	3	450	
B45.45/30.120	25	1	350	
B45.45/30.120	25	2	250	0.18
B45.45/30.120	25	3	350	
B45.80/30.60	00	1	450	
B45.80/30.60	00	2	450	0.06
B45.80/30.60	00	3	500	
B45.80/30.60	08	1	450	
B45.80/30.60	08	2	300	0.25
B45.80/30.60	08	3	300	
B45.80/30.60	25	1	300	
B45.80/30.60	25	2	no pic	
B45.80/30.60	25	3	350	
B45.80/60.60	00	1	450	
B45.80/60.60	00	2	400	0.07
B45.80/60.60	00	3	400	
B45.80/60.60	08	1	450	
B45.80/60.60	08	2	550	0.12
B45.80/60.60	08	3	450	
B45.80/60.60	25	1	300	
B45.80/60.60	25	2	400	0.15
B45.80/60.60	25	3	400	
B105.0.0	00	1	600	
B105.0.0	00	2	not perf	
B105.0.0	00	3	not perf	
B105.0.0	08	1	not perf	
B105.0.0	08	2	not perf	
B105.0.0	08	3	not perf	
B105.0.0	25	1	400	
B105.0.0	25	2	550	
B105.0.0	25	3	no pic	
B105.80/30.60	00	1	450	
B105.80/30.60	00	2	not perf	
B105.80/30.60	00	3	not perf	
B105.80/30.60	08	1	450	
B105.80/30.60	08	2	300	0.25
B105.80/30.60	08	3	300	
B105.80/30.60	25	1	300	
B105.80/30.60	25	2	400	0.17
B105.80/30.60	25	3	300	
B105.80/60.60	00	1	not perf	
B105.80/60.60	00	2	not perf	
B105.80/60.60	00	3	not perf	
B105.80/60.60	08	1	no pic	
B105.80/60.60	08	2	no pic	
B105.80/60.60	08	3	no pic	
B105.80/60.60	25	1	350	
B105.80/60.60	25	2	350	0.08
B105.80/60.60	25	3	400	

Appendix E: Prism Test Results Energies

Test	W^{el}	W^{in}	$W^{s}\cdot L^{d}/L$	L^{d}/L	W^{s}	$G^{l}\cdot 1/L$	W^{d}	$W^{s}\cdot L^{d}/L+G^{l}\cdot 1/L$
	N/mm^2	N/mm^2	N/mm^2	[-]	N/mm^2	N/mm^2	N/mm^2	N/mm^2
B45.0.0.e00.1	0.040	0.013	0.031	0.667	0.046	0.030	0.044	0.061
B45.45/30.60.e00.1	0.038	0.015	0.076	0.583	0.130	0.029	0.091	0.105
B45.45/30.60.e00.2	0.037	0.018	0.048	0.750	0.064	0.028	0.067	0.076
B45.45/30.60.e00.3	0.037	0.015	0.067	0.750	0.089	0.029	0.082	0.096
B45.45/30.120.e00.1	0.039	0.014	0.077	0.833	0.092	0.028	0.091	0.105
B45.45/30.120.e00.2	0.037	0.014	0.093	0.750	0.124	0.026	0.107	0.119
B45.45/30.120.e00.3	0.048	0.011	0.102	0.667	0.153	0.029	0.113	0.131
B45.80/30.60.e00.3	0.043	0.019	0.089	0.833	0.107	0.032	0.108	0.121
B45.80/60.60.e00.1	0.046	0.011	0.122	0.750	0.163	0.028	0.133	0.150
B45.80/60.60.e00.2	0.043	0.016	0.096	0.667	0.144	0.031	0.112	0.127
B45.80/60.60.e00.3	0.046	0.010	0.094	0.667	0.141	0.029	0.104	0.123

Test	W^{el}	W^{in}	$W^{s}\cdot L^{d}/L$	L^{d}/L	W^{s}	$G^{l}\cdot 1/L$	W^{d}	$W^{s}\cdot L^{d}/L+G^{l}\cdot 1/L$
	N/mm^2	N/mm^2	N/mm^2	[-]	N/mm^2	N/mm^2	N/mm^2	N/mm^2
B45.45/30.60.e08.1	0.054	0.017	0.206	0.750	0.275	0.037	0.223	0.243
B45.45/30.60.e08.2	0.058	0.023	0.127	1.000	0.127	0.038	0.150	0.165
B45.45/30.60.e08.3	0.055	0.018	0.174	0.750	0.232	0.038	0.192	0.212
B45.45/30.120.e08.1	0.061	0.023	0.253	0.667	0.379	0.040	0.277	0.293
B45.45/30.120.e08.2	0.061	0.026	0.126	0.667	0.189	0.040	0.151	0.166
B45.45/30.120.e08.3	0.056	0.027	0.108	0.750	0.144	0.038	0.134	0.146
B45.80/30.60.e08.1	0.056	0.028	0.243	0.750	0.324	0.039	0.271	0.282
B45.80/30.60.e08.2	0.053	0.030	0.259	0.500	0.518	0.038	0.289	0.297
B45.80/30.60.e08.3	0.061	0.036	0.269	0.500	0.538	0.040	0.305	0.309
B45.80/60.60.e08.1	0.057	0.030	0.156	0.750	0.208	0.039	0.185	0.195
B45.80/60.60.e08.2	0.063	0.026	0.175	0.917	0.191	0.041	0.201	0.216
B45.80/60.60.e08.3	0.064	0.020	0.167	0.750	0.223	0.041	0.187	0.208
B105.80/30.60.e08.1	0.173	0.035	0.502	0.750	0.669	0.043	0.537	0.545
B105.80/30.60.e08.2	0.171	0.025	0.559	0.500	1.118	0.043	0.583	0.602
B105.80/30.60.e08.3	0.199	0.035	0.559	0.500	1.118	0.046	0.594	0.605

Test	W^{el}	W^{in}	$W^{s}\cdot L^{d}/L$	L^{d}/L	W^{s}	$G^{l}\cdot 1/L$	W^{d}	$W^{s}\cdot L^{d}/L+G^{l}\cdot 1/L$
	N/mm^2	N/mm^2	N/mm^2	[-]	N/mm^2	N/mm^2	N/mm^2	N/mm^2
B45.0.0.e25.1	0.062	0.027	0.179	0.583	0.307	0.043	0.207	0.222
B45.0.0.e25.2	0.069	0.029	0.193	0.583	0.331	0.042	0.222	0.235
B45.0.0.e25.3	0.057	0.024	0.158	0.917	0.172	0.044	0.182	0.202
B45.0.0.e25.5	0.084	0.032	0.171	0.667	0.256	0.046	0.203	0.217
B45.0.0.e25.6	0.081	0.015	0.218	0.750	0.291	0.043	0.233	0.261
B45.45/30.60.e25.1	0.055	0.051	0.229	0.250	0.916	0.037	0.280	0.266
B45.45/30.60.e25.2	0.078	0.019	0.315	0.417	0.755	0.043	0.333	0.358
B45.45/30.60.e25.3	0.077	0.032	0.271	0.583	0.465	0.047	0.303	0.318
B45.45/30.120.e25.1	0.068	0.042	0.235	0.583	0.403	0.041	0.277	0.276
B45.45/30.120.e25.2	0.066	0.045	0.314	0.417	0.753	0.042	0.359	0.356
B45.45/30.120.e25.3	0.069	0.044	0.311	0.583	0.533	0.044	0.355	0.355
B45.80/30.60.e25.1	0.069	0.041	0.305	0.500	0.610	0.043	0.347	0.348
B45.80/30.60.e25.3	0.077	0.044	0.325	0.583	0.557	0.045	0.369	0.370
B45.80/60.60.e25.1	0.073	0.032	0.295	0.500	0.590	0.045	0.327	0.340
B45.80/60.60.e25.2	0.082	0.023	0.301	0.667	0.451	0.047	0.325	0.348
B45.80/60.60.e25.3	0.081	0.017	0.343	0.667	0.514	0.046	0.361	0.389
B105.80/30.60.e25.1	0.214	0.070	0.631	0.500	1.262	0.052	0.701	0.683
B105.80/30.60.e25.2	0.225	0.069	0.603	0.667	0.904	0.052	0.672	0.655
B105.80/30.60.e25.3	0.225	0.089	0.674	0.500	1.348	0.053	0.764	0.727
B105.80/60.60.e25.1	0.216	0.095	0.635	0.583	1.089	0.051	0.730	0.686
B105.80/60.60.e25.2	0.236	0.083	0.629	0.583	1.079	0.052	0.711	0.681
B105.80/60.60.e25.3	0.216	0.104	0.522	0.667	0.783	0.053	0.626	0.575

Appendix F: CDZ Model Extension

The main text of the thesis only presents the parameters necessary to determine the stress-strain relationship of concrete in compression. However, in the calculation, some steps were necessary in order to obtain these parameters. These steps include the determination of the inelastic and elastic strain, the inelastic and elastic energy, the energy absorbed in the longitudinal cracks, the energy absorbed in the shear band and the CDZ model parameters r and γ. The steps are presented in this appendix. Furthermore, the information presented here is useful in order to illustrate the effect of steel fiber addition and the eccentricity of the load on the compressive behavior of SCSFRC prisms.

Some of the parameters in the model increased linearly with increasing eccentricity of the load. Others, however, showed an increase that could be more realistically represented with a quadratic equation, i.e. a low eccentricity already led to a large change in the parameter and a further increase of the eccentricity only led to relatively small increases. This tendency was already observed by Markeset (1993) for the concrete compressive strength.

Depending on whether the effect of the eccentricity of the loading on the test results could be more realistically represented by a line or a quadratic equation in the parameter-eccentricity diagrams, it was chosen to express the parameters with a linear or quadratic approach, respectively. The following form of the expressions for the model parameters was chosen:

[parameter] = [parameter for centric tests on plain concrete] + slope$\cdot V_f l_f/d_f$ + factor a$\cdot(e/h)^2$ + factor b$\cdot(e/h)$

The model extension is based on the experiments with the B45 with the mixture composition as shown in Table 3.3. It can therefore not automatically be used for other kinds of concrete or other strengths. As the original CDZ model was valid for NSC and HSC, it can be assumed that the extension of the CDZ is also valid for concrete up to B105. However, the expressions with the form [parameter] = [parameter for centric tests on plain concrete] + slope$\cdot V_f l_f/d_f$ + factor a$\cdot(e/h)^2$ + factor b$\cdot(e/h)$ more accurately describe the performed tests but these expressions are only valid for the concrete mix used in the experiments and cannot be considered a general rule.

The following pictures present the test results and the model proposals in dotted lines for the centric and eccentric tests along with the best linear fits for each eccentricity.

Pre-Peak Behavior

As mentioned in chapter 3.4, the steel wire fibers used in this study were assumed to contribute to the energy absorption after the peak load has been reached and to have no effect on the pre-peak behavior. Therefore, the CDZ model extension for the corresponding values neglects an influence of the steel fibers. However, in the experiments a slight influence of the fiber factor on the E-modulus, the strain at maximum stress and the elastic strain was observed. This is shown in the alternative expressions that were derived from the tests on the B45, which better fit the test results but are less practical to use. These expressions for the pre-peak region are not used in the further calculations.

The concrete compressive strength, the E-modulus and the strain at maximum stress are the independent factors and the elastic and inelastic strain as well as the elastic and inelastic energy are calculated from them in the original as well as in the extended CDZ model. Therefore, if the fiber addition had no influence on the compressive strength, the E-modulus and the strain at maximum stress, it also had no influence on the elastic and inelastic strain as well as the elastic and inelastic energy. In the alternative expressions, the influence of the fiber addition on the E-modulus and the strain at maximum stress was taken into account. Therefore, the alternative expressions for the elastic strain also depends on the fiber factor. The inelastic strain and energy were not affected by the fiber addition.

Ultimate Nominal Concrete Compressive Stress f_c^*

The ultimate nominal concrete compressive stress is defined as $f_c^* = F_u / h^2 \cdot (1 + 6 \cdot e / h)$, see equation (3.19). The test results and the best fits are presented in Fig. F.1, along with the model proposal according to equation (3.27).

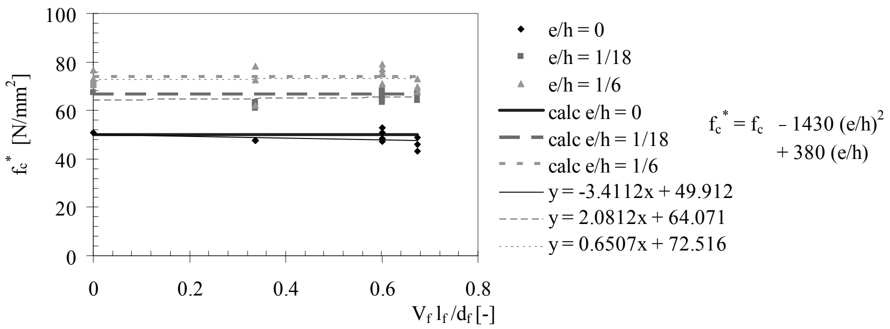

Fig. F.1: Test results, best fits and model approach for the concrete compressive strength

E-modulus

The model proposal for the E-modulus is presented and explained in section 3.4.3. Alternatively, the E-modulus can better be described as slightly decreasing with increasing fiber factor. This can be calculated with equation (F.1) for the performed tests:

$$E_c = 0.9 \cdot 9500 \, f_c^{*(1/3)} - 4000 \, V_f \, l_f / d_f \qquad \text{(F.1)}$$

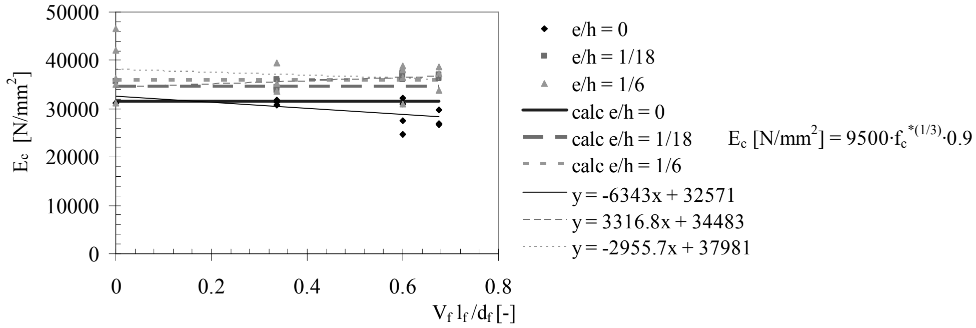

Fig. F.2: Test results, best fits and model approach for the E-modulus

The Strain at Maximum Stress ε_0

The model proposal for the strain at maximum stress is presented and explained in section 3.4.3. However, the tests showed a slightly increasing strain at maximum stress with increasing fiber factor as some researchers have already observed in the past [Erdem, 2002].

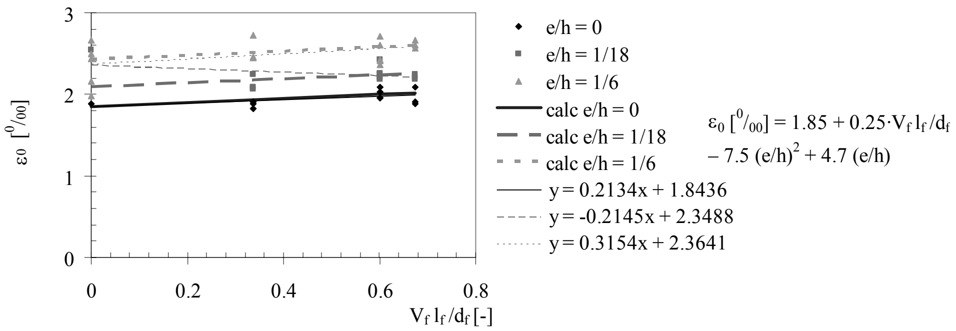

Fig. F.3: Test results, best fits and proposed expression for the strain at the concrete compressive strength

As a tendency, the strain at maximum stress increased with increasing fiber factor. The strain at maximum stress also increased with increasing eccentricity of the loading. The strain at maximum stress ε_0 was expressed as:

$$\varepsilon_0 = 1.85 + 0.2\, V_f\, l_f / d_f - 7.5 (e/h)^2 + 4.7\, e/h \qquad [‰] \qquad \text{(F.2)}$$

The Elastic Strain ε^{el}

Fig. F.4 shows the test results and the results obtained with equation (3.1). Contrary to the slight increase of elastic strain with increasing fiber factor for the centric specimens, the elastic strain is modeled as a function of the compressive strength and the E-modulus. The elastic strain increased with increasing eccentricity.

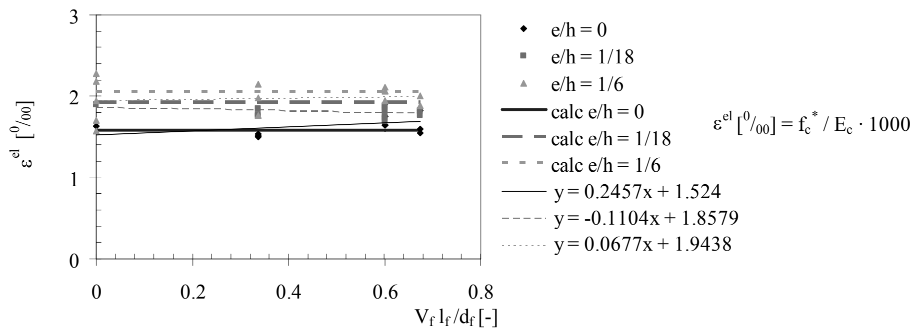

Fig. F.4: Test results and CDZ model approach for the elastic strain

In order to illustrate the effect of the fiber addition and the eccentricity (Fig. F.5), the elastic strain ε^{el} was expressed as:

$$\varepsilon^{el} = 1.55 + 0.25\, V_f\, l_f / d_f - 7.5(e/h)^2 + 3.5(e/h) \quad [‰] \qquad \text{(F.3)}$$

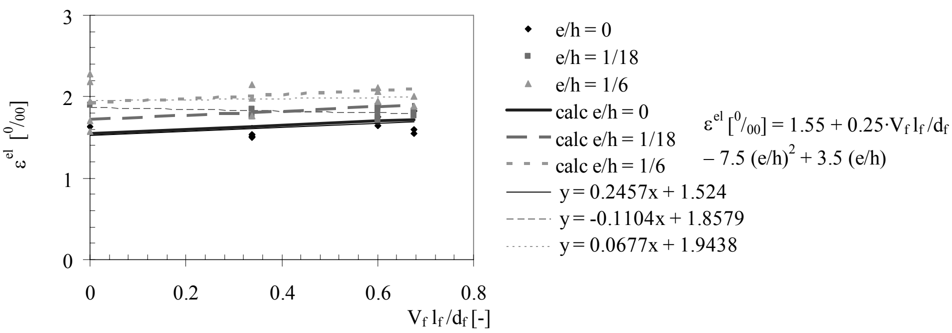

Fig. F.5: Test results, best fits and model approach for elastic strain

The Inelastic Strain ε^{in}

Fig. F.6 shows the inelastic strains observed in the tests and the CDZ model results calculated with equation (3.5).

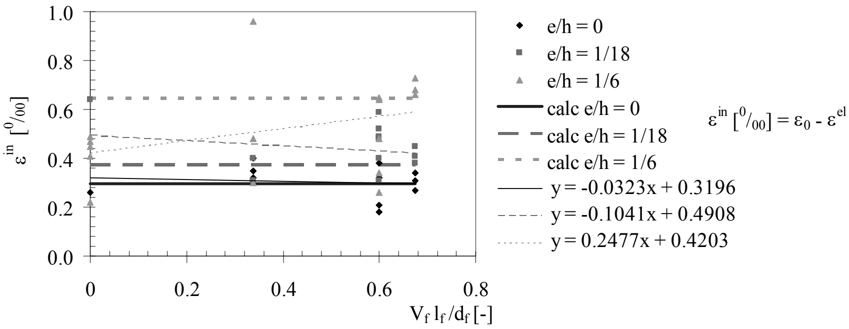

Fig. F.6: Test results and CDZ model for the inelastic strains

In order to illustrate the effect of the eccentricity, the inelastic strain ε^{in} was alternatively expressed as:

$$\varepsilon^{in} = 0.3 + 1.2(e/h) \quad [‰] \tag{F.4}$$

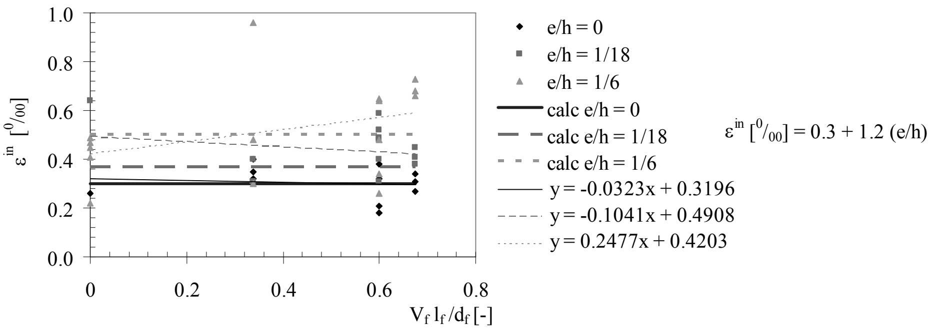

Fig. F.7: Test results, best fits and model approach for the inelastic strain

Fig. F.7 shows no clear influence of the fiber addition on the inelastic strain. In the model, however, the influence of the fiber factor on the inelastic strain is considered to be negligible. The inelastic strain increased with increasing eccentricity.

The Elastic Energy W^{el}

According to the CDZ model, the elastic energy W^{el} was calculated with equations (3.1) and (3.2), which were reformulated as

$$W^{el} = 0.5\, f_c\, \varepsilon^{el} \tag{F.5}$$

The rest results and the elastic energy obtained with equation (F.5) are shown in Fig. F.8.

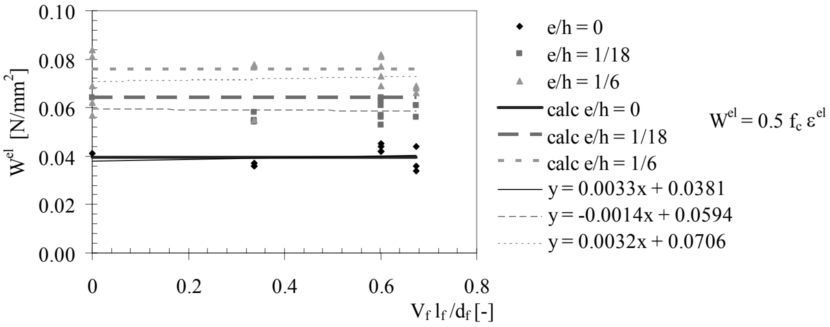

Fig. F.8: Test results and CDZ model approach for the elastic energy

In order to illustrate the influence of the eccentricity of the loading, the elastic energy W^{el} was alternatively expressed as:

$$W^{el} = 0.04 - 1.35(e/h)^2 + 0.4(e/h) \tag{F.6}$$

The approximation according to this expression is shown in Fig. F.9.

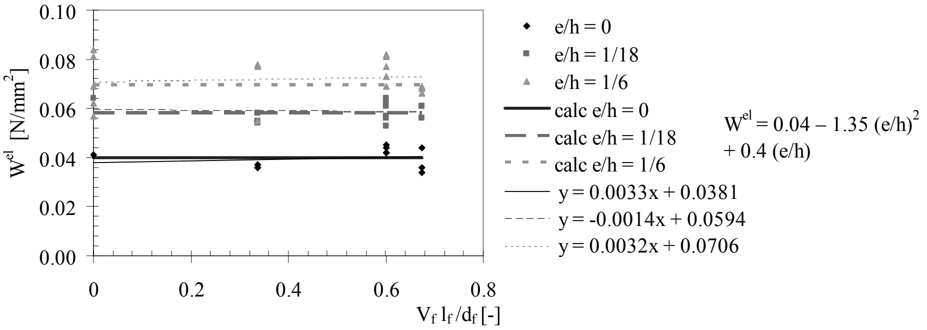

Fig. F.9: Test results, best fits and model approach for the elastic energy

The Inelastic Energy W^{in}

According to the CDZ model, the inelastic energy W^{in} was calculated with equation (3.4), which was reformulated as

$$W^{in} = \alpha_{fd} \, f_c^* \, \varepsilon^{in} \qquad \text{(F.7)}$$

The test results and the inelastic energy obtained with equation (F.7) is shown in Fig. F.10.

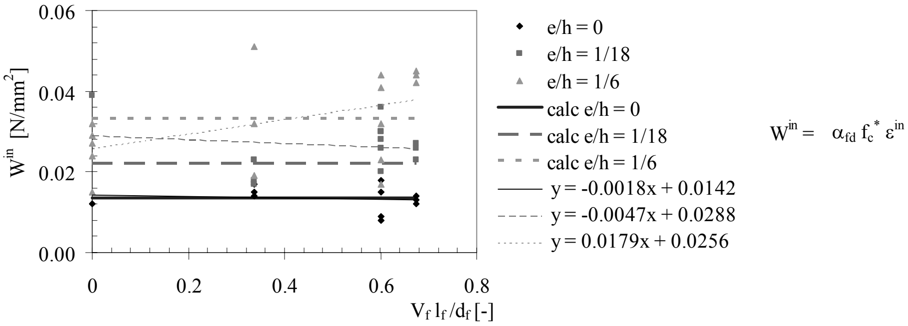

Fig. F.10: Test results and CDZ model approach for the inelastic energy

In order to illustrate the influence of the fiber addition and the eccentricity of the loading, the inelastic energy W^{in} was alternatively calculated as:

$$W^{in} = 0.015 - 1.0(e/h)^2 + 0.3(e/h) \qquad \text{(F.8)}$$

The approximation according to this expression is shown in Fig. F.11.

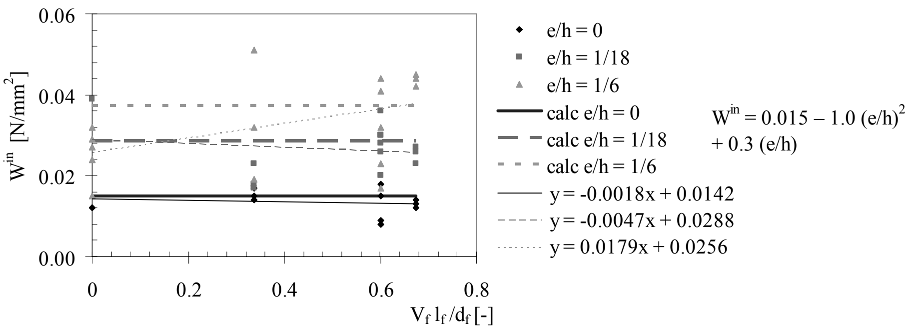

Fig. F.11: Test results, best fits and model approach for the inelastic energy

The Filling Degree α_{fd}

The filling degree α_{fd} is presented and explained in section 3.4.3. Fig. F.12 shows the test results, the best fits and the model approach for the shape factor.

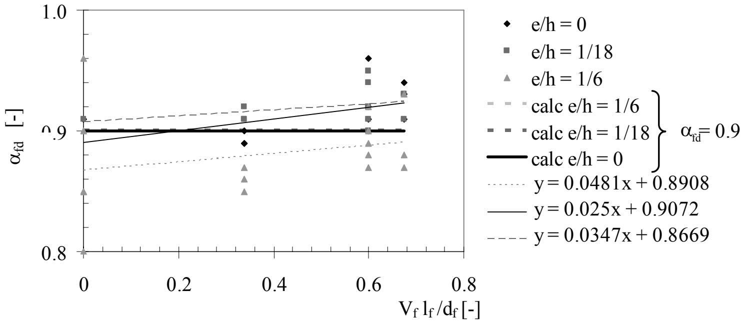

Fig. F.12: Test results, best fits and model approach for the shape factor α_{fd}

Energies in the Post-Peak Range

Section 3.4.3 showed the influence of the fiber addition and the eccentricity of the loading on the damage zone length and on the proportionality factor k. This section presents the energies in the post peak range and the remaining parameters of the compressive damage zone model.

The Damage Zone Length L^d

The damage zone length is presented and discussed in section 3.4.3. Fig. F.13 presents the test results, the best fits and the model approach for the damage zone length divided by the specimen length.

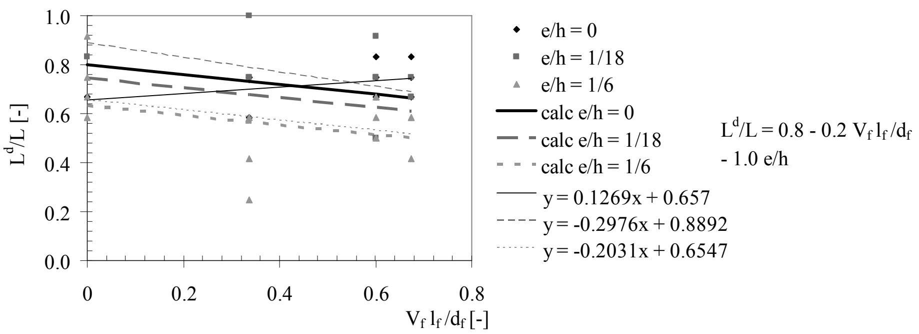

Fig. F.13: Test results, best fits and model approach for the damage zone length

The Energy Dissipated in the Longitudinal Cracks $W^s\, L^d / L$

It was expected that the energy dissipated in the longitudinal cracks would increase with increasing fiber factor. According to the CDZ model, the energy dissipated in the longitudinal cracks $W^s\, L^d / L$ was calculated with equations (3.4) and (3.6), which were reformulated as:

$$W^s\, L^d / L = k\, \alpha_{fd}\, f_c^*\, \varepsilon^{in}\, L^d / L \tag{F.9}$$

The test results and the energy dissipated in the longitudinal cracks obtained with equation (F.9) are shown in Fig. F.14.

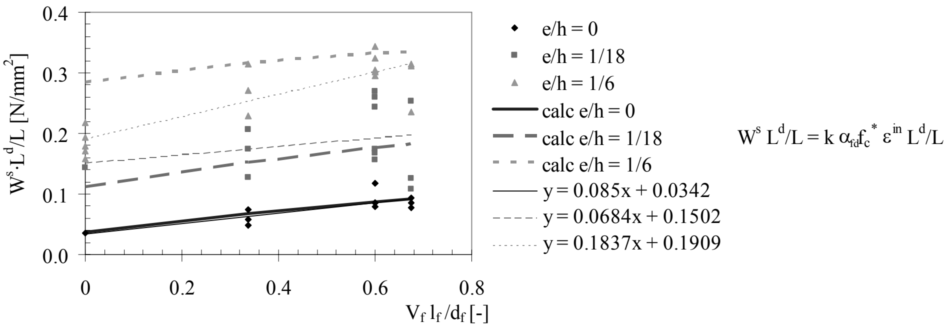

Fig. F.14: Test results and CDZ model approach for the energy dissipated in the longitudinal cracks

In order to illustrate the influence of the fiber addition and the eccentricity of the loading, the energy dissipated in the longitudinal cracks $W^s\, L^d / L$ was alternatively calculated as:

$$W^s\, L^d / L = 0.035 + 0.085\, V_f\, l_f / d_f - 8(e/h)^2 + 2.5(e/h) \tag{F.10}$$

The approximation according to this expression is shown in Fig. F.15.

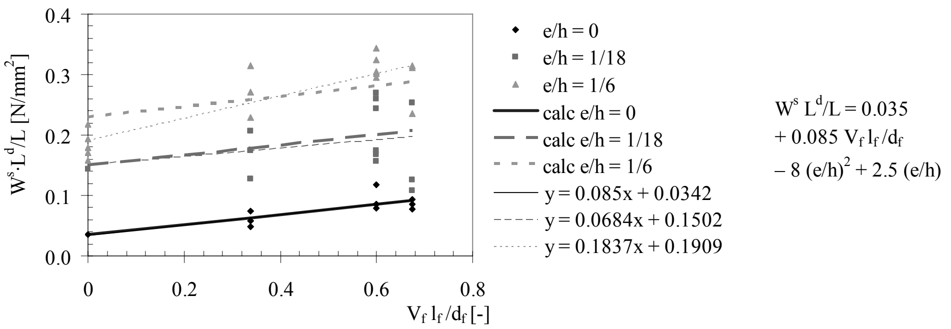

Fig. F.15: Test results, best fits and model approach for the energy dissipated in the longitudinal cracks

As can be seen from the figures, the energy dissipated in the longitudinal cracks increases with increasing fiber factor and increasing eccentricity of the load.

The increase with the fiber factor can be explained by the fact that in the post-peak region, the fibers are activated and contribute to the energy absorption.

The Energy Dissipated in the Shear Band G^l / L

According to the CDZ model, the energy dissipated in the shear band G^l / L was calculated with equation (F.11) as:

$$G^l / L = \beta_{sf}\, w_c\, f_c^* / L \tag{F.11}$$

The test results and the energy dissipated in the shear band obtained with equation (F.11) is shown in Fig. F.16.

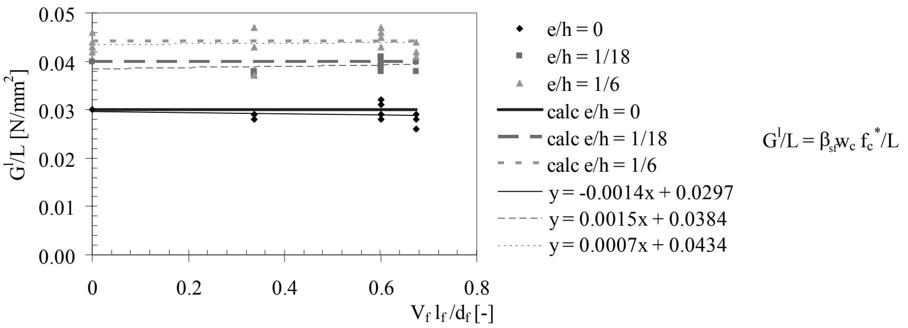

Fig. F.16: Test results and CDZ model approach for the energy dissipated in the shear band

In order to illustrate the influence of the eccentricity of the loading, the energy dissipated in the shear band G^l/L was alternatively calculated as:

$$G^l / L = 0.03 - 1.0(e/h)^2 + 0.25(e/h) \tag{F.12}$$

The approximation according to this expression is shown in Fig. F.17.

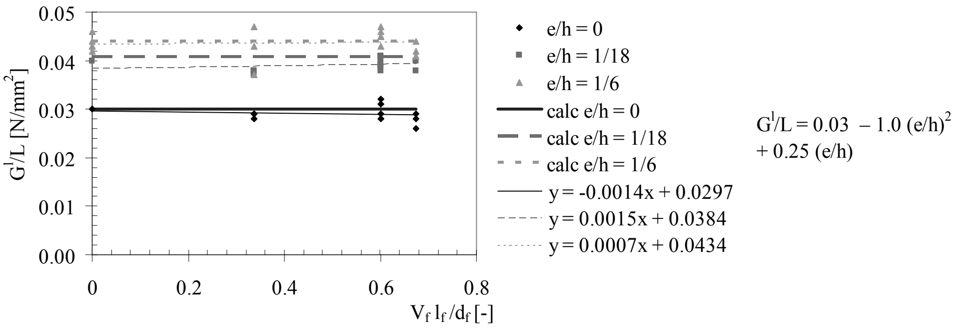

Fig. F.17: Test results, best fits and model approach for the energy dissipated in the shear band

In the calculation procedure, which was applied here, the contribution of the fibers was solely assigned to the opening of the longitudinal cracks. Therefore, the fiber factor did not influence the magnitude of the energy absorbed in the shear band. In reality, the fibers increase both, the energy dissipated in the longitudinal cracks as well as the energy dissipated in the shear band. This would result in a lower increase of the energy dissipated in the longitudinal cracks compared to the proposed model and in an increase in energy dissipated in the shear band. The energy absorbed in the shear band increased with increasing load eccentricity.

The Total Energy Dissipated in the Post-Peak Range $W^s\, L^d / L + G^l / L$

According to the CDZ model, the total energy dissipated in the post-peak range $W^s\, L^d / L + G^l / L$ was calculated with equations (F.10) and (F.11), which were reformulated as:

$$W^s\, L^d / L + G^l / L = k\,\alpha_{fd}\, f_c^{*} \varepsilon^{in}\, L^d / L + \beta_{sf}\, w_c\, f_c^{*} / L \tag{F.13}$$

The results of the model can be seen in the following figure.

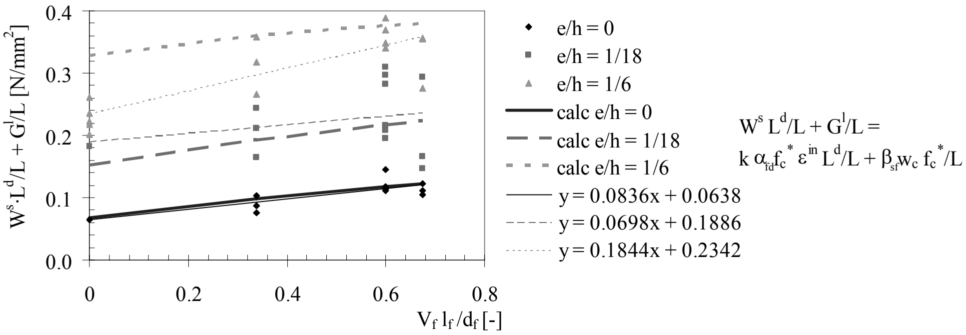

Fig. F.18: Test results and CDZ model approach for the total energy dissipated in the post-peak range

In order to illustrate the influence of the fiber addition and the eccentricity of the loading, the total energy dissipated in the post-peak range can alternatively be calculated as:

$$W^s L^d / L + G^l / L = 0.065 + 0.085\, V_f\, l_f / d_f - 9(e/h)^2 + 2.75(e/h) \qquad \text{(F.14)}$$

The approximation according to this expression is shown in Fig. F.19. Note that this expression will not be used in the calculation procedure for rotation capacity.

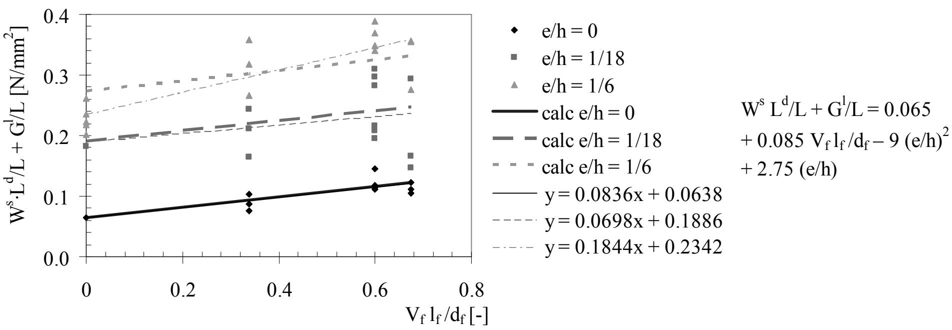

Fig. F.19: Test results, best fits and model approach for the energy dissipated in the post-peak region

As can be seen from the picture, the total energy absorbed in the post-peak region increases with increasing fiber factor and increasing eccentricity. The reasons are the same as explained for the energy absorbed in the longitudinal cracks.

Model Parameters

The Proportionality Factor k

The proportionality factor was presented and explained in section 3.4.3. Fig. F.20 shows the test results, the best fits and the results obtained with equation (3.31).

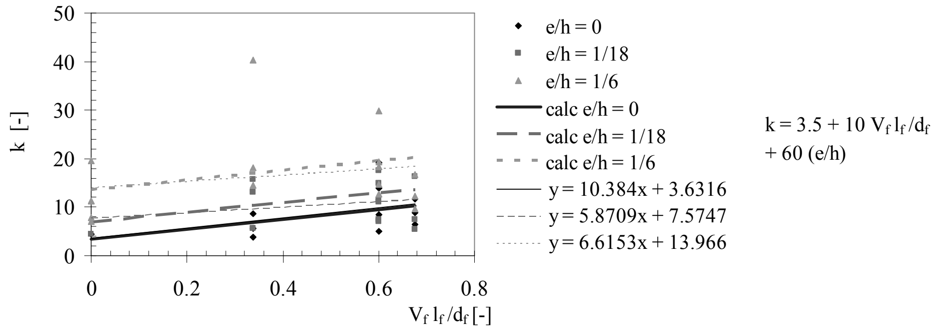

Fig. F.20: Test results, best fits and model approach for the proportionality factor k

The Parameter γ

The parameter γ is a combination parameter in the CDZ model. It can be calculated with:

$$\gamma = \varepsilon^{in} f_c^* / G_F \tag{F.15}$$

The experimental results, the best fits and the calculation results with this formula are shown in the following figure.

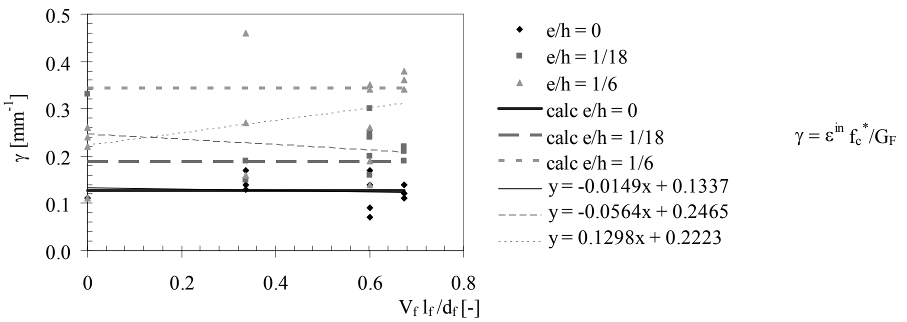

Fig. F.21: Test results, best fits and CDZ model approach for the combination parameter γ

With this approach, the combination parameter γ is independent of the fiber factor and increases with increasing eccentricity of the load.

The Parameter r

It was expected that the parameter r, which is related to the distance of the longitudinal cracks, would decrease with increasing fiber content because the crack distance as well as crack widths tend to decrease with increasing fiber content. The parameter r was calculated with:

$$r = \frac{1}{\alpha_{fd} \cdot \gamma \cdot (1+k)} \tag{F.16}$$

The results of this calculation can be seen in the following figure:

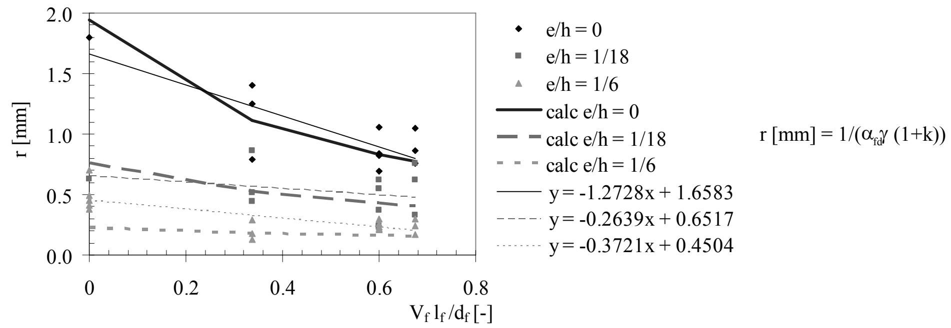

Fig. F.22: Test results and model approach for the parameter r

As can be seen from the figure, the parameter r decreases with increasing fiber factor and increasing eccentricity.

In order to illustrate the influence of the fiber addition and the eccentricity of the loading, the parameter r was alternatively expressed as:

$$r = 1.25 - 0.4\, V_f\, l_f / d_f + 44\,(e/h)^2 - 12\,(e/h) \tag{F.17}$$

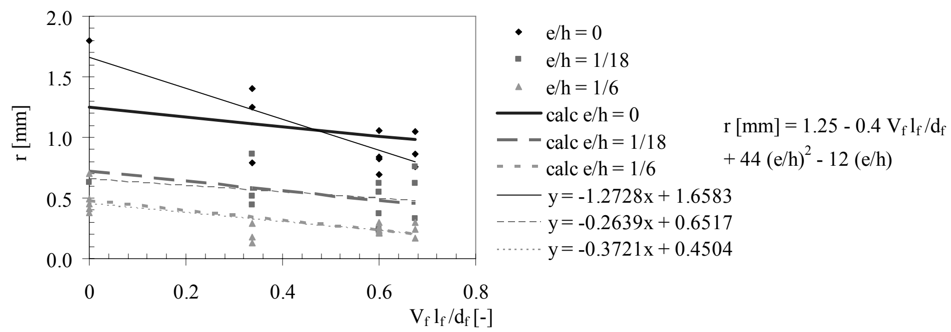

Fig. F.23: Test results, best fits and expression for the parameter r

Summary of the Model Parameters

The following table gives an overview of the model parameters in the original CDZ model proposed by Markeset for plain conventional normal density concrete and in the extended model for SCSFRC. The parameters of the extended model were derived for a concrete strength of 50 N/mm^2 for plain concrete and the expressions are valid for an eccentricity of up to $e/h = 1/6$ and for the fiber factor $V_f\, l_f / d_f$ up to 0.675, which corresponds to the maximum amount of fibers that could be applied in self-compacting concrete at the given mixture compositions.

The alternative equations were derived from the test results to represent the energies absorbed in compressive failure as a function of the fiber factor and the eccentricity of the loading. Note that in the further modeling the extension of the CDZ model as presented in the center column of Table F.1 is used and that the alternative expressions only serve to illustrate the effect of $V_f\, l_f / d_f$ and e/h.

Table F.1: Comparison of the model parameters in the original and extended CDZ model

CDZ model	extension of CDZ to SCSFRC (this thesis)	alternative expressions for the CDZ model parameters and energies (by curve fittings)
f_c	$f_c^* = f_c - 1430(e/h)^2 + 380(e/h)$	$f_c^* = f_c - 1430\ (e/h)^2 + 380\ (e/$
E_c	$E_c = 0.9 \cdot 9500\, f_c^{*(1/3)} = 8550\, f_c^{*(1/3)}$	$E_c = 0.9 \cdot 9500\, f_c^{*(1/3)} - 4000\, V_f\, l_f / d_f$
ε_0	$\varepsilon_0 = 0.7\, f_{cc}^{\ 0.31} \cdot 0.8$ $-7.5(e/h)^2 + 4.7\, e/h$	$\varepsilon_0 = 1.85 + 0.2\, V_f\, l_f / d_f$ $-7.5(e/h)^2 + 4.7\, e/h$
$\varepsilon^{el} = f_c / E_c$	$\varepsilon^{el} = f_c^* / E_c$	$\varepsilon^{el} = 1.55 + 0.25\, V_f\, l_f / d_f$ $-7.5(e/h)^2 + 3.5(e/h)$
$\varepsilon^{in} = \varepsilon_0 - \varepsilon^{el}$	$\varepsilon^{in} = \varepsilon_0 - \varepsilon^{el}$	$\varepsilon^{in} = 0.3 + 1.2(e/h)$
$W^{el} = 0.5\, f_c\, \varepsilon^{el}$	$W^{el} = 0.5\, f_c^*\, \varepsilon^{el}$	$W^{el} = 0.04 - 1.35(e/h)^2 + 0.4(e/h)$
$W^{in} = \alpha\, f_c\, \varepsilon^{in}$	$W^{in} = \alpha\, f_c^*\, \varepsilon^{in}$	$W^{in} = 0.015 - 1.0(e/h)^2 + 0.3(e/h)$
$\beta_{sf} = 0.5$	$\beta_{sf} = 0.5$	$\beta_{sf} = 0.5$
w_c = 0.4 – 0.7 mm	w_c = 0.7 mm for NSSCC, 0.4 for HSSCC	w_c = 0.7 mm for NSSCC, 0.4 for HSSCC
$G^l / L = \beta_{sf} w_c\, f_c / L$	$G^l / L = \beta_{sf} w_c\, f_c^* / L$	$G^l / L = 0.03 - 1.0(e/h)^2$ $+ 0.25(e/h)$

CDZ model	extension of CDZ to SCSFRC (this thesis)	alternative expressions for the CDZ model parameters and energies (by curve fittings)
α_{fd} = 0.8	α_{fd} = 0.9 for NSSCC	α_{fd} = 0.9 for NSSCC, 0.93 for HSSCC
k = 3.0	$k = 3.5 + 10\, V_f\, l_f / d_f + 60\,(e/h)$	$k = 3.5 + 10\, V_f\, l_f / d_f + 60\,(e/h)$
L^d / L	$L^d / L = 0.8 - 0.2\, V_f\, l_f / d_f - e/h$	$L^d / L = 0.8 - 0.2\, V_f\, l_f / d_f - e/h$
$W^s\, L^d / L =$ $k\, \alpha_{fd}\, f_c\, \varepsilon^{in}\, L^d / L$	$W^s\, L^d / L =$ $k\, \alpha_{fd}\, f_c^*\, \varepsilon^{in}\, L^d / L$	$W^s\, L^d / L = 0.035 + 0.085\, V_f\, l_f / d_f$ $-8\,(e/h)^2 + 2.5\,(e/h)$
$W^s\, L^d / L + G^l / L =$ $k\, \alpha_{fd}\, f_c\, \varepsilon^{in}\, L^d / L$ $+ \beta_{sf}\, w_c\, f_c / L$	$W^s\, L^d / L + G^l / L =$ $k\, \alpha_{fd}\, f_c^* \varepsilon^{in}\, L^d / L$ $+ \beta_{sf}\, w_c\, f_c^* / L$	$W^s\, L^d / L + G^l / L = 0.065$ $+ 0.085\, V_f\, l_f / d_f - 9\,(e/h)^2$ $+ 2.75\,(e/h)$
G_F	$G_{F,plain} = 65 \cdot \ln(1 + \frac{f_c^*}{10})$	$G_{F,plain} = 65 \cdot \ln(1 + \frac{f_c^*}{10})$
$\gamma = \varepsilon^{in}\, f_c / G_F$	$\gamma = \varepsilon^{in}\, f_c^* / G_F$	$\gamma = \varepsilon^{in}\, f_c^* / G_F$
r = 1.25 mm	$r = \dfrac{1}{\alpha_{fd}\, \gamma\,(1+k)}$	$r = 1.25 - 0.4\, V_f\, l_f / d_f$ $+ 44\,(e/h)^2 - 12\,(e/h)$

Appendix G: Pull-Out Test Results

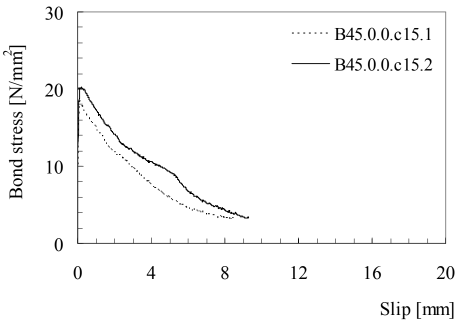

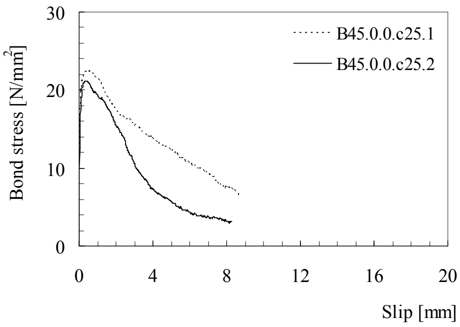

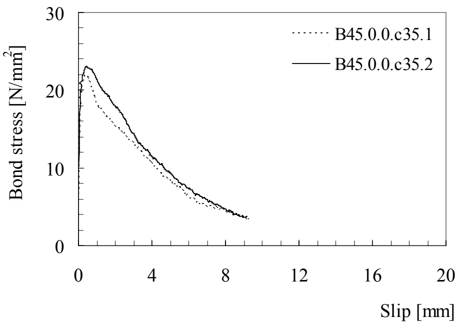

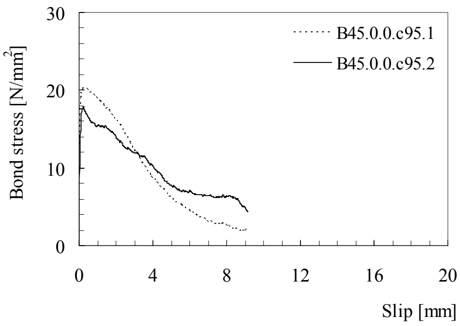

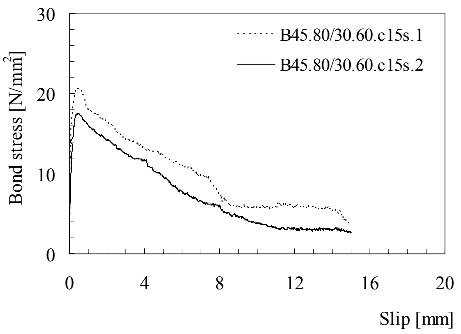

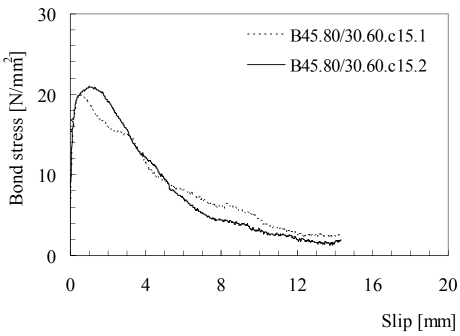

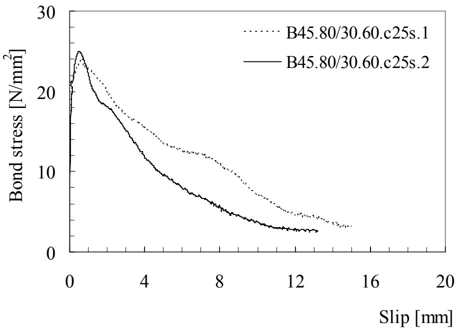
B45.80/30.60.c25s.1
B45.80/30.60.c25s.2
Bond stress [N/mm2]
Slip [mm]

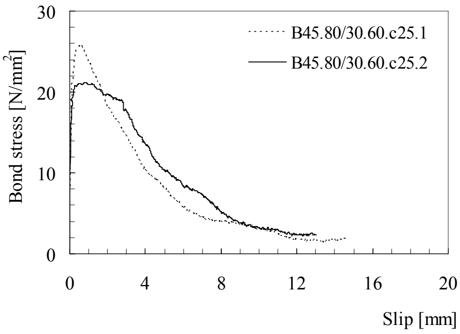
B45.80/30.60.c25.1
B45.80/30.60.c25.2
Bond stress [N/mm2]
Slip [mm]

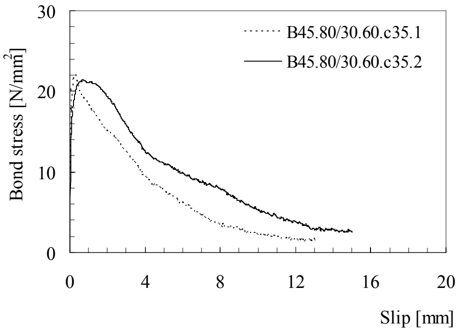
B45.80/30.60.c35.1
B45.80/30.60.c35.2
Bond stress [N/mm2]
Slip [mm]

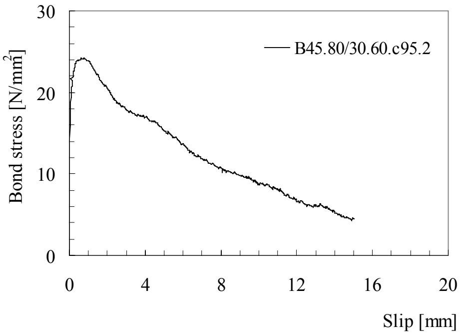
B45.80/30.60.c95.2
Bond stress [N/mm2]
Slip [mm]

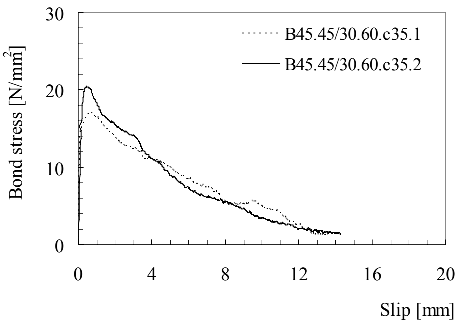
B45.45/30.60.c35.1
B45.45/30.60.c35.2
Bond stress [N/mm2]
Slip [mm]

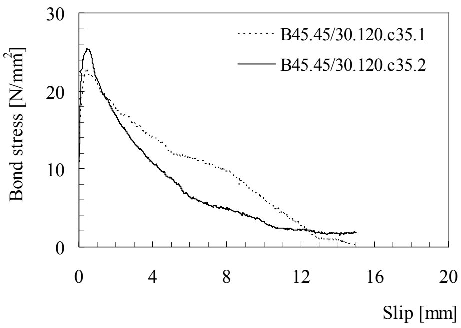
B45.45/30.120.c35.1
B45.45/30.120.c35.2
Bond stress [N/mm2]
Slip [mm]

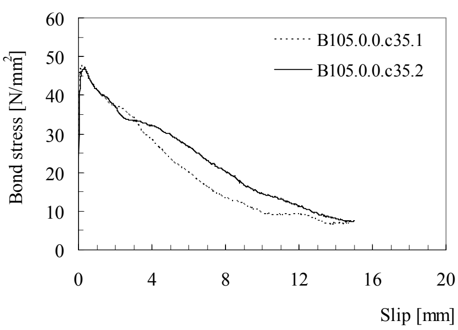
B105.0.0.c35.1
B105.0.0.c35.2
Bond stress [N/mm2]
Slip [mm]

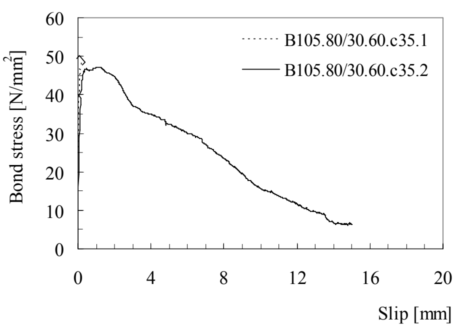
B105.80/30.60.c35.1
B105.80/30.60.c35.2
Bond stress [N/mm2]
Slip [mm]

Appendix H: Range of the LVDTs

The measuring range of the LVDTs shown in Table 6.7 was:

LVDT Number	Range [mm]
09 to 36	2
37 to 57, 59	10
08, 58	20
04, 07	50
05, 06	100

Appendix I: Definition of the Load Steps for the Beam Tests

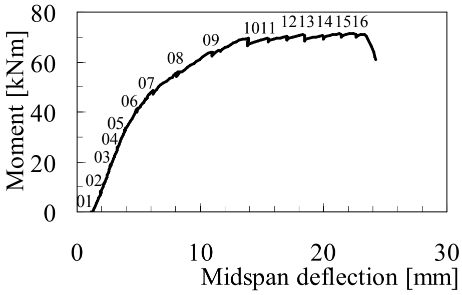

Fig. I.1: B45.0.0.N400

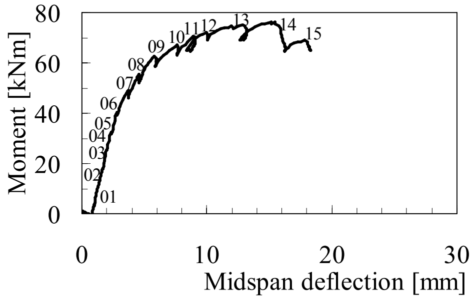

Fig. I.2: B45.80/30.60.N400

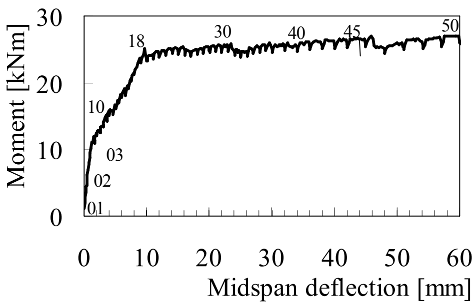

Fig. I.3: B45.0.0.N0

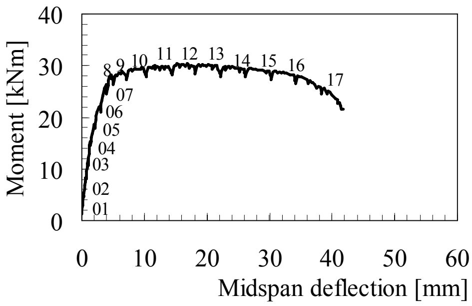

Fig. I.4: B45.80/30.60.N0

Appendix J: Beam Pictures and Crack Widths at Different Load Steps

B45.0.0.N400

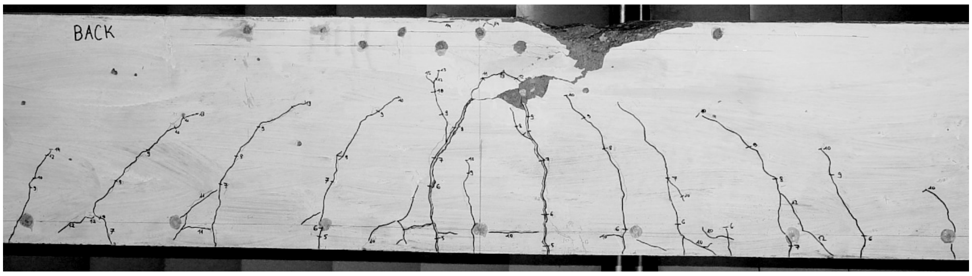

Fig. J.1: B45.0.0.N400 back 1200 mm b

Table J.1: Crack widths [mm] at different load steps (LS) for B45.0.0.N400

LS														
01														
02														
03														
04														
05				<		**<**		**<**						
06			<	<		**<**		**<**	<	<	<		<	
07		<	0.05	0.05		**0.05**		**0.1**	<	0.05	<	<	<	
08		<	0.05	0.1		**0.1**		**0.1**	0.05	0.1	<	0.05	0.05	
09	<	0.1	0.15	0.25		**0.15**	0.1	**0.25**	0.15	0.15	<	0.15	0.1	<
10	0.05	0.2	0.25	0.3	<	**0.4**	0.1	**0.35**	0.15	0.2	<	0.25	0.15	<
11	0.05	0.2	0.3	0.35	<	**0.9**	0.1	**0.35**	0.2	0.2	<	0.25	0.15	<
12	0.05	0.2	0.3	0.35	<	**1**	0.1	**0.8**	0.2	0.2	<	0.3	0.15	<
13	0.05	0.25	0.3	0.35	<	**1.2**	0.1	**1**	0.2	0.25	<	0.3	0.2	<
14	0.05	0.25	0.3	0.35	<	**1.5**	0.1	**1.3**	0.2	0.25	<	0.35	0.2	0.05
15	0.05	0.25	0.35	0.35	<	**1.7**	0.1	**1.6**	0.2	0.3	<	0.35	0.2	0.05
16	0.05	0.25	0.35	0.35	<	**1.8**	0.1	**2**	0.2	0.3	<	0.35	0.2	0.05
17	0.05	0.25	0.35	0.35	<	**2**	0.1	**2.3**	0.35	0.3	<	0.35	0.2	<
Crack length at the last loading step [mm]														
a_i	130	170	180	220		**220**	120	**220**	200	190		170	150	90
Crack opening angle of the cracks wider than 0.05 mm at the last load step [mrad]														
$\Theta_{cr,i}$	0.4	1.5	2.0	1.6		**9.1**	0.8	**10.5**	1.8	1.6		2.1	1.3	

14 cracks 1200 mm
92.3 mm = 1200/13
Sum of the crack opening angles 32.5 mrad
Sum of the crack widths 6.6 mm
Primary cracking at LS 06
8 cracks
s_{cr} primary = 1200/7= 171 mm
Pronounced localization at LS 11

B45.80/30.60.N400

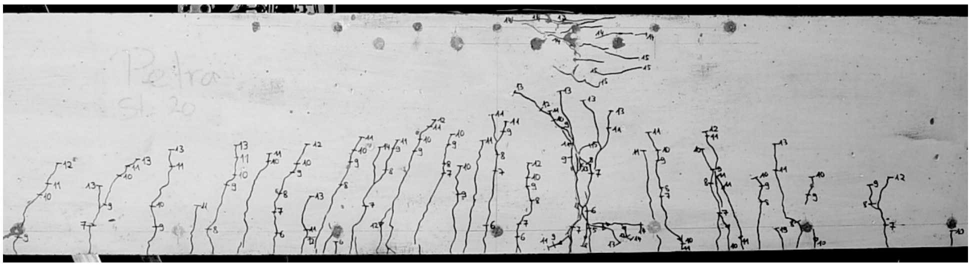

Fig. J.2: B45.80/30.60.N400 back 1200 mm

Table J.2: Crack widths [mm] at different load steps (LS) for B45.80/30.60.N400

LS																																
01																																
02																																
03																																
04																																
05																																
06							<			<		<						<	<		<	<										
07		<					<			<	<	<			<			<	<		<	<		<							<	
08		<			<		<		<	<	<	<			<			<	<	**<**	<	<		<			<		<		<	
09	<	0.05	<		<		<	<	<	<	<	<		<	<	<		<	<	**0.1**	<	0.05		<			<		<		<	
10	<	0.05	<		<	<	<	<	<	<	<	<		<	<	<		<	<	**0.2**	<	0.05		<	<		<		<	<	0.05	<
11	<	0.1	<	<	<	<	<	<	<	<	<	<		<	<	<	<	<	<	**0.35**	<	0.1	<	<	<	<	<		<	<	0.1	<
12	<	0.1	<	<	<	0.05	<	<	<	<	<	<	<	<	<	<	<	<	<	**0.6**	<	0.05	<	<	<	<	<		<	<	0.1	<
13	<	0.1	<	<	<	0.05	<	<	<	<	<	<	<	<	<	<	<	<	<	**1.7**	<	0.05	<	<	<	<	<	<	<	<	0.1	<
14	<	0.1	<	<	<	0.05	<	<	<	<	<	<	<	<	<	0.05	<	<	<	**2.8**	<	<	<	<	<	<	<	<	<	<	0.05	<
15	<	0.1	<	<	<	0.05	<	<	<	<	<	<	<	<	<	0.05	<	<	<	**3.1**	<	<	<	<	<	<	<	<	<	<	0.05	<
Crack length at the last loading step [mm]																																
a_i		120				120										100				**200**		150									100	
Crack opening angle of the cracks wider than 0.05 mm at the last load step [mrad]																																
$\Theta_{cr,i}$		0.8				0.4										0.5				**15.5**											0.5	

32 cracks 1200 mm
38.7 mm
Sum of the crack opening angles 17.8 mrad
Sum of the crack widths 3.35 mm

Primary cracking at LS 06
7 cracks
s_{cr} primary = 1200/6= 200 mm
Primary cracking at LS 07
12 cracks
s_{cr} primary = 1200/11 = 109 mm
Pronounced localization at LS 09

B45.0.0.N0

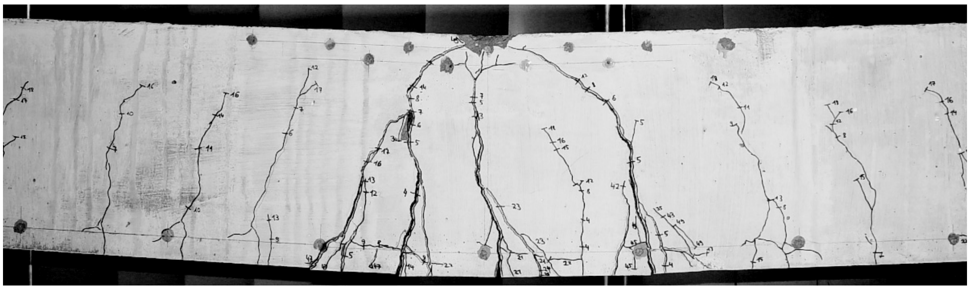

Fig. J.3:B45.0.0.N0 back 1200 mm b

Table J.3: Crack widths [mm] at different load steps (LS) for B45.0.0.N0

LS																		
01																		
02																		
03							**<**		**0.05**									
04							**<**		**0.05**		<							
05						**<**	**0.05**		**0.1**		<		**0.1**	<				
06				0.1		**<**	**0.1**		**0.12**		<		**0.1**	<				
07		<		0.1		**<**	**0.15**		**0.15**		<		**0.1**	<			<	
08		0.05		0.1		**<**	**0.15**		**0.15**		0.05		**0.1**	<		<	0.05	
09		0.05		0.15	<	**<**	**0.2**		**0.2**		0.05		**0.15**	<		0.15	0.1	
10		0.1	<	0.15	<	**<**	**0.2**		**0.2**		0.05		**0.15**	<		0.15	0.1	
11		0.1	0.05	0.15	<	**<**	**0.2**		**0.2**		0.1		**0.15**	<		0.2	0.1	
12	<	0.15	0.1	0.15	<	**0.05**	**0.2**		**0.2**		0.1		**0.15**	<		0.2	0.1	<
13	<	0.15	0.15	0.15	0.05	**0.05**	**0.25**		**0.2**		0.1		**0.15**	0.05		0.2	0.15	0.05
14	0.05	0.15	0.15	0.15	0.05	**0.05**	**0.25**		**0.25**		0.1		**0.15**	0.05		0.2	0.15	0.1
15	0.05	0.2	0.15	0.15	0.05	**0.05**	**0.25**		**0.25**		0.1		**0.15**	0.05		0.2	0.15	0.15
16	0.1	0.2	0.15	0.15	0.05	**0.05**	**0.3**		**0.3**		0.15		**0.2**	0.1		0.25	0.15	0.15
17	0.15	0.2	0.2	0.2	0.05	**0.1**	**0.35**		**0.3**		0.15		**0.2**	0.1		0.3	0.2	0.2
18	0.2	0.25	0.2	0.2	0.05	**0.1**	**0.35**		**0.7**		0.15		**0.2**	0.1	<	0.35	0.2	0.2
19	0.2	0.25	0.2	0.2	0.05	**0.1**	**0.35**		**1**		0.15		**0.25**	0.1	<	0.35	0.2	0.2
20	0.2	0.25	0.2	0.2	0.05	**0.1**	**0.35**		**1.6**		0.15		**0.25**	0.1	<	0.35	0.2	0.2
21	0.2	0.25	0.2	0.2	0.1	**0.1**	**0.35**		**1.8**	<	0.2		**0.25**	0.1	<	0.35	0.2	0.2
22	0.2	0.25	0.2	0.2	0.1	**0.1**	**0.35**		**2**	<	0.2		**0.25**	0.1	<	0.35	0.2	0.2
23	0.2	0.25	0.2	0.2	0.1	**0.1**	**0.4**		**2.2**	<	0.2		**0.25**	0.1	<	0.35	0.2	0.2
24	0.2	0.25	0.2	0.2	0.1	**0.1**	**0.4**		**2.6**	<	0.2		**0.25**	0.1	<	0.35	0.2	0.2
25	0.2	0.25	0.2	0.2	0.1	**0.1**	**1**		**2.8**	<	0.2		**0.25**	0.1	<	0.35	0.2	0.2
26	0.2	0.25	0.2	0.2	0.1	**0.1**	**1.2**		**2.8**	<	0.2		**0.25**	0.1	<	0.35	0.2	0.2
27	0.2	0.25	0.2	0.2	0.1	**0.1**	**1.8**		**2.9**	<	0.2		**0.25**	0.1	<	0.35	0.2	0.2
28	0.2	0.25	0.2	0.2	0.1	**0.1**	**2.2**		**2.9**	<	0.2		**0.25**	0.1	<	0.35	0.2	0.2
29	0.2	0.25	0.2	0.2	0.1	**0.1**	**2.9**		**3**	<	0.2		**0.25**	0.1	<	0.35	0.2	0.2
30	0.2	0.25	0.2	0.2	0.1	**0.1**	**3**		**3**	<	0.2		**0.25**	0.1	<	0.35	0.2	0.2
31	0.2	0.25	0.2	0.2	0.1	**0.1**	**3**		**3.5**	<	0.2		**0.25**	0.1	<	0.35	0.2	0.2
32	0.2	0.25	0.2	0.2	0.1	**0.1**	**3**		**3.5**	<	0.2		**0.7**	0.1	<	0.35	0.2	0.2
33	0.2	0.25	0.2	0.2	0.1	**0.1**	**3.1**		**3.5**	<	0.2		**1.1**	0.1	<	0.35	0.2	0.2
34	0.2	0.25	0.2	0.2	0.1	**0.1**	**3.1**		**3.5**	<	0.2		**1.5**	0.1	<	0.35	0.2	0.2
35	0.2	0.25	0.2	0.2	0.1	**0.1**	**3.1**		**3.8**	<	0.2		**1.6**	0.1	<	0.35	0.2	0.2
36	0.2	0.25	0.2	0.2	0.1	**0.1**	**3.1**		**3.8**	<	0.2		**1.8**	0.4	<	0.35	0.2	0.2
37	0.2	0.25	0.2	0.2	0.1	**0.1**	**3.1**		**3.8**	<	0.2		**2**	0.6	<	0.35	0.2	0.2
38	0.2	0.25	0.2	0.2	0.1	**0.1**	**3.1**		**3.8**	<	0.2		**2.1**	0.7	<	0.35	0.2	0.2
39	0.2	0.25	0.2	0.2	0.1	**0.1**	**3.1**		**4**	<	0.2		**2.1**	0.7	<	0.35	0.2	0.2
40	0.2	0.25	0.2	0.2	0.1	**0.1**	**4.1**		**4**	<	0.2		**2.5**	0.7	<	0.35	0.2	0.2
41	0.2	0.25	0.2	0.2	0.1	**0.1**	**4.1**		**4**	<	0.2	0.35	**3**	0.6	<	0.35	0.2	0.2
42	0.2	0.25	0.2	0.2	0.1	**0.1**	**4.5**		**4**	0.15	0.2	0.6	**3**	0.6	<	0.35	0.2	0.2
43	0.2	0.25	0.2	0.2	0.1	**0.1**	**4.5**		**4**	0.25	0.15	0.6	**3.1**	0.6	<	0.35	0.2	0.2
44	0.2	0.25	0.2	0.2	0.1	**0.1**	**4.9**	0.15	**4**	0.4	0.15	0.7	**3.1**	0.7	<	0.35	0.2	0.2
45	0.2	0.25	0.2	0.2	0.1	**0.1**	**5**	0.15	**4**	0.5	0.15	0.8	**3.1**	0.7	<	0.35	0.2	0.2
46	0.2	0.25	0.2	0.2	0.1	**0.1**	**5**	0.25	**4.5**	0.9	0.15	0.9	**3.9**	0.9	<	0.35	0.2	0.2

47	0.2	0.25	0.2	0.2	0.1	**0.1**	**5**	0.35	**4.5**	1	0.15	0.9	**3.9**	1	<	0.35	0.2	0.2
48	0.2	0.25	0.2	0.2	0.1	**2.5**	**5**	0.45	**4.5**	1	0.15	0.9	**4**	1	<	0.35	0.2	0.2
49	0.2	0.25	0.2	0.2	0.1	**3.5**	**5**	0.45	**4.5**	1	0.15	1	**4**	1	<	0.35	0.2	0.2
50	0.2	0.25	0.2	0.2	0.1	**4**	**5.5**	0.6	**4.5**	1	0.15	1	**4**	1	<	0.35	0.2	0.2
Crack length at the last loading step [mm]																		
a_i	230	230	210	250	60	**280**	**280**	280	**260**	260	180	280	**280**	280		250	200	210
Crack opening angle of the cracks wider than 0.05 mm at the last load step [mrad]																		
$\Theta_{cr,i}$	0.9	1.1	1.0	0.8	1.7	**14.3**	**19.6**	2.1	**17.3**	3.9	0.8	3.6	**14.3**	3.6		1.4	1.0	1.0

18 cracks 1200 mm
70.6 mm
Sum of the crack opening angles 88.2 mrad
Sum of the crack widths 23.45 mm

Primary cracking at LS 10
11 cracks
s_{cr} primary = 1200/10 = 120 mm
Pronounced localization at LS 18, 25, 32, 49

B45.80/30.60.N0

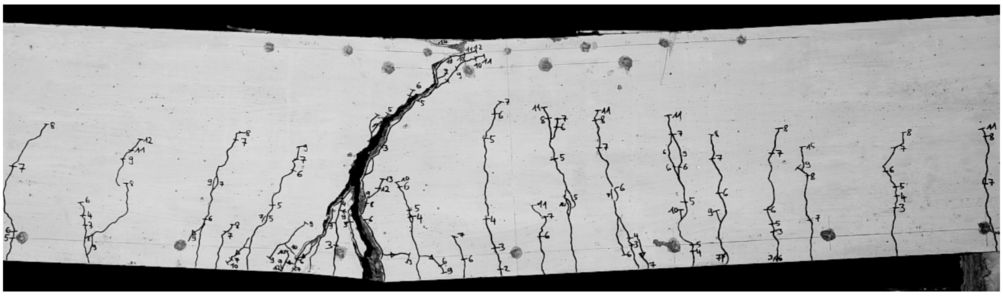

Fig. J.4: B45.80/30.60.N0 back 1200 mm

Table J.4: Crack widths [mm] at different load steps (LS) for B45.80/30.60.N0

LS																					
01																					
02												<									
03		<					<	<				<			<			<		<	
04		<					<	<		<		<			<		<	<		<	
05	<	<			<		<	<	**<**	<		<		<	<		<	<		<	
06	<	<	<		<		<	<	**<**	<	<	<	<	<	<		<	<<		<	
07	<	<	<	<	<	<	<	<	**<**	<	<	<	<	<	<	<	<	<<	<	<	<
08	<	<	<	<	<	<	<	<	**0.5**	<	<	0.05	<	0.05	<	<	<	<<	<	0.05	<
09	<	<	0.05	<	0.05	<	<	<	**1.8**	<	<	0.05	<	0.05	<	<	<	<<	<	0.05	<
10	<	<	0.05	<	0.05	<	<	<	**3.2**	0.05	<	0.1	0.05	0.05	0.05	<	<	<<	<	0.05	<
11	<	<	0.05	<	0.05	<	<	<		0.05	<	0.1	0.05	0.05	0.05	<	<	<<	<	0.05	<
12	<	0.05	0.05	<	0.05	<	<	<	**6.5**	0.05	<	0.1	0.05	0.05	0.05	<	<	<<	<	0.05	<
13	0.05	0.1	0.05	<	0.05	<	<	<	**8**	0.05	<	0.1	0.05	0.05	0.05	0.05	<	<<	<	0.05	0.05
14	0.05	0.1	0.05	<	0.05	<	<	<	**9.3**	0.05	<	0.1	0.05	0.05	0.05	0.05	<	<<	<	0.05	0.05
15	0.05	0.1	0.05	<	0.05	<	<	<	**11**	0.05	<	0.1	0.05	0.05	0.05	0.05	0.05	<<	<	0.1	0.05
16	0.05	0.1	0.05	<	0.05	<	<	<	**12.5**	0.05	<	0.1	0.05	0.05	0.05	0.05	0.05	**<<**	0.05	0.1	0.05
17	0.05	0.1	0.05	<	0.05	<	<	<	**14**	0.05	<	0.1	0.05	0.05	0.05	0.05	0.05	**<<**	0.05	0.1	0.05
Crack length at the last loading step [mm]																					
a_i	170	160	180		160				**280**	130		230	100	210	200	200	200		150	160	160
Crack opening angle of the cracks wider than 0.05 mm at the last load step [mrad]																					
$\Theta_{cr,i}$	0.3	0.6	0.3		0.3				**50**	0.4		0.4	0.5	0.2	0.3	0.3	0.3		0.3	0.6	0.3

23 cracks 1200 mm
54.5 mm
Sum of the crack opening angles 55.1 mrad
Sum of the crack widths 14.85 mm

Primary cracking at LS 04
10 cracks
s_{cr} primary = 1200/9 = 133 mm
Primary cracking at LS 07
22 cracks
s_{cr} primary = 1200/21 = 57 mm
Pronounced localization at LS 08

Appendix K: Parameter Study

Influence of steel fibers on the rotations at different load levels for different normal forces

y onset of steel yielding
max maximum force
u ultimate load step

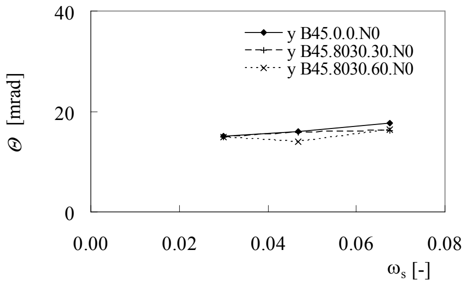

Fig. K.1: Rotation at the onset of steel yielding for N = 0

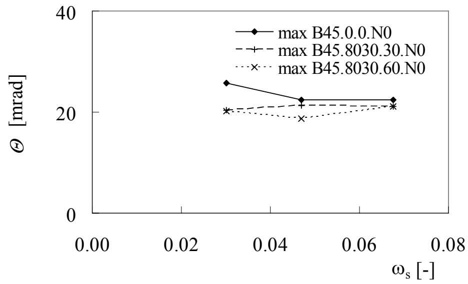

Fig. K.2: Rotation at maximum load for N = 0

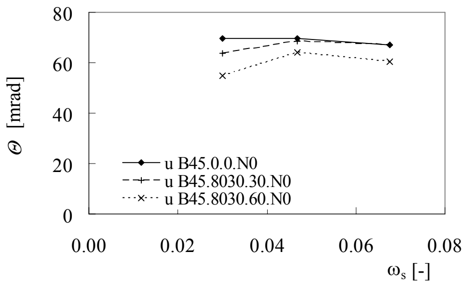

Fig. K.3: Rotation at ultimate load for N = 0

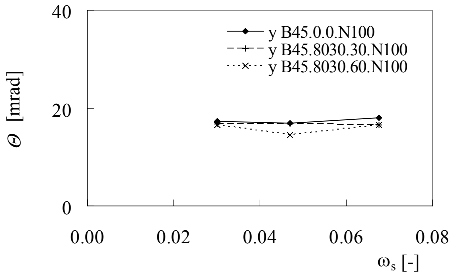

Fig. K.4: Rotation at the onset of steel yielding for N = 100 kN

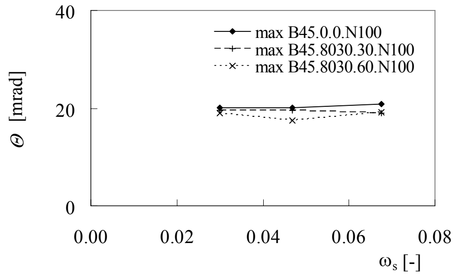

Fig. K.5: Rotation at maximum load for N = 100 kN

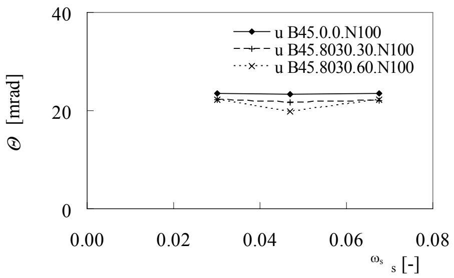

Fig. K.6: Rotation at ultimate load for N = 100 kN

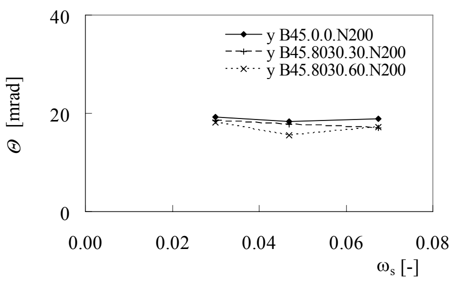

Fig. K.7: Rotation at the onset of steel yielding for N = 200 kN

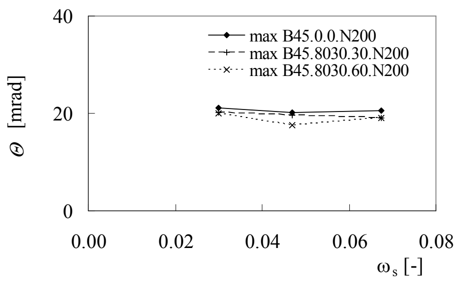

Fig. K.8: Rotation at maximum load for N = 200 kN

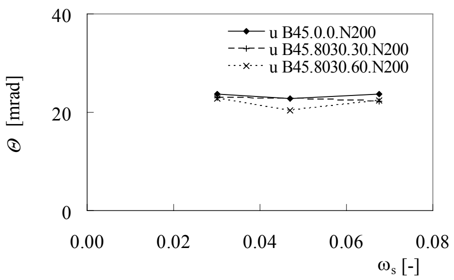

Fig. K.9: Rotation at ultimate load for N = 200 kN

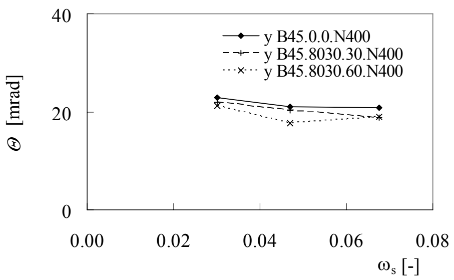

Fig. K10: Rotation at the onset of steel yielding for N = 400 kN

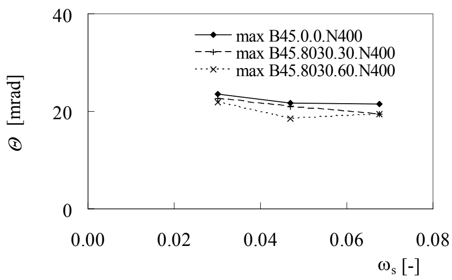

Fig. K.11: Rotation at maximum load for N = 400 kN

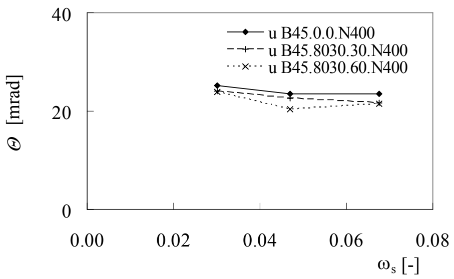

Fig. K.12: Rotation at ultimate load for N = 400 kN

		B45.0.0.N0			B45.80/30.30.N0			B45.80/30.60.N0		
		2 ds 8	2 ds 10	2 ds 12	2 ds 8	2 ds 10	2 ds 12	2 ds 8	2 ds 10	2 ds 12
ω_s	[-]	0.03	0.05	0.07	0.03	0.05	0.07	0.03	0.05	0.07
s_r	[mm]	106	107	109	99	101	103	94	95	98
T_{0y}	[kN]	29	45	65	31	47	67	34	50	70
T_{0u}	[kN]	33	52	75	34	52	75	35	52	75
T_{0u}/T_{0y}	[-]	1.16	1.16	1.16	1.09	1.11	1.12	1.03	1.05	1.08
M_y	[kNm]	15	22	31	18	25	34	20	27	36
θ_y	[mrad]	15	16	18	15	16	16	15	14	16
M_{max}	[kNm]	17	25	34	20	27	36	22	30	39
θ_{max}	[mrad]	26	22	22	20	21	21	20	19	21
$\theta_{max} - \theta_y$	[mrad]	11	6	5	5	5	5	5	5	5
M_u	[kNm]	14	21	29	15	23	31	16	23	33
θ_u	[mrad]	69	70	67	64	69	67	55	64	60
$\theta_u - \theta_y$	[mrad]	54	54	49	49	53	51	40	50	44
x_y/d	[-]	0.18	0.20	0.23	0.19	0.21	0.24	0.20	0.22	0.24
x_{max}/d	[-]	0.08	0.11	0.13	0.09	0.12	0.14	0.10	0.12	0.14
x_u/d	[-]	0.19	0.19	0.20	0.19	0.20	0.20	0.19	0.20	0.20
M_u/M_{max}	[-]	0.79	0.83	0.86	0.76	0.82	0.86	0.74	0.78	0.85

		B45.0.0.N100			B45.80/30.30.N100			B45.80/30.60.N100		
		2 ds 8	2 ds 10	2 ds 12	2 ds 8	2 ds 10	2 ds 12	2 ds 8	2 ds 10	2 ds 12
ω_s	[-]	0.03	0.05	0.07	0.03	0.05	0.07	0.03	0.05	0.07
s_r	[mm]	106	107	109	99	101	103	94	95	98
T_{0y}	[kN]	29	45	65	31	47	67	34	50	70
T_{0u}	[kN]	33	52	75	34	52	75	35	52	75
T_{0u}/T_{0y}	[-]	1.16	1.16	1.16	1.09	1.11	1.12	1.03	1.05	1.08
M_y	[kNm]	28	35	43	30	37	46	32	39	48
θ_y	[mrad]	17	17	18	17	17	16	16	15	17
M_{max}	[kNm]	29	37	45	32	39	48	34	41	50
θ_{max}	[mrad]	20	20	21	19	20	19	19	17	19
$\theta_{max} - \theta_y$	[mrad]	3	3	3	3	3	3	3	3	3
M_u	[kNm]	28	35	44	31	38	46	33	40	48
θ_u	[mrad]	24	23	24	22	22	22	22	20	22
$\theta_u - \theta_y$	[mrad]	6	6	6	5	5	6	6	5	6
x_y/d	[-]	0.25	0.26	0.28	0.26	0.27	0.29	0.26	0.28	0.29
x_{max}/d	[-]	0.13	0.15	0.17	0.14	0.16	0.18	0.15	0.17	0.19
x_u/d	[-]	0.15	0.17	0.18	0.15	0.16	0.19	0.16	0.17	0.20
M_u/M_{max}	[-]	0.96	0.95	0.97	0.97	0.98	0.96	0.95	0.97	0.95

		B45.0.0.N200			B45.80/30.30.N200			B45.80/30.60.N200		
		2 ds 8	2 ds 10	2 ds 12	2 ds 8	2 ds 10	2 ds 12	2 ds 8	2 ds 10	2 ds 12
ω_s	[-]	0.03	0.05	0.07	0.03	0.05	0.07	0.03	0.05	0.07
s_r	[mm]	106	107	109	99	101	103	94	95	98
T_{0y}	[kN]	29	45	65	31	47	67	34	50	70
T_{0u}	[kN]	33	52	75	34	52	75	35	52	75
T_{0u}/T_{0y}	[-]	1.16	1.16	1.16	1.09	1.11	1.12	1.03	1.05	1.08
M_y	[kNm]	39	46	54	42	48	57	44	50	59
θ_y	[mrad]	19	18	19	19	18	17	18	16	17
M_{max}	[kNm]	41	48	56	43	50	59	46	52	61
θ_{max}	[mrad]	21	20	21	20	20	19	20	17	19
$\theta_{max} - \theta_y$	[mrad]	2	2	2	2	2	2	2	2	2
M_u	[kNm]	39	45	52	41	47	54	43	49	56
θ_u	[mrad]	24	23	24	23	23	22	23	20	22
$\theta_u - \theta_y$	[mrad]	5	5	5	4	5	5	5	5	5
x_y/d	[-]	0.30	0.30	0.32	0.30	0.32	0.33	0.31	0.32	0.33
x_{max}/d	[-]	0.20	0.21	0.23	0.21	0.22	0.24	0.21	0.23	0.25
x_u/d	[-]	0.20	0.22	0.25	0.21	0.24	0.26	0.23	0.24	0.26
M_u/M_{max}	[-]	0.95	0.94	0.93	0.94	0.93	0.92	0.93	0.93	0.92

		B45.0.0.N400			B45.80/30.30.N400			B45.80/30.60.N400		
		2 ds 8	2 ds 10	2 ds 12	2 ds 8	2 ds 10	2 ds 12	2 ds 8	2 ds 10	2 ds 12
ω_s	[-]	0.03	0.05	0.07	0.03	0.05	0.07	0.03	0.05	0.07
s_r	[mm]	106	107	109	99	101	103	94	95	98
T_{0y}	[kN]	29	45	65	31	47	67	34	50	70
T_{0u}	[kN]	33	52	75	34	52	75	35	52	75
T_{0u}/T_{0y}	[-]	1.16	1.16	1.16	1.09	1.11	1.12	1.03	1.05	1.08
M_y	[kNm]	61	67	75	63	69	77	64	71	78
θ_y	[mrad]	23	21	21	22	20	19	21	18	19
M_{max}	[kNm]	62	68	76	63	70	77	65	71	79
θ_{max}	[mrad]	24	22	21	23	21	19	22	19	19
$\theta_{max} - \theta_y$	[mrad]	1	1	1	1	1	1	1	1	1
M_u	[kNm]	58	63	69	60	66	70	60	67	74
θ_u	[mrad]	25	23	24	24	23	22	24	20	22
$\theta_u - \theta_y$	[mrad]	2	2	3	2	2	3	3	3	3
x_y/d	[-]	0.38	0.38	0.40	0.38	0.39	0.40	0.39	0.40	0.40
x_{max}/d	[-]	0.35	0.34	0.36	0.34	0.35	0.37	0.35	0.35	0.38
x_u/d	[-]	0.33	0.35	0.36	0.33	0.34	0.37	0.35	0.35	0.36
M_u/M_{max}	[-]	0.94	0.93	0.92	0.94	0.94	0.91	0.91	0.93	0.93

Notations and Abbreviations

Roman Capital Letters

A_c	Concrete cross section	[mm^2]
$A_{c,eff}$	Effective concrete tension area	[mm^2]
A_f	Area of the cross-section of a single fiber	[mm^2]
A_s	Steel cross-section	[mm^2]
E_c	E-modulus of concrete	[N/mm^2]
E_s	E-modulus of steel	[N/mm^2]
F	Force	[kN]
F_{max}	Maximum force	[kN]
F_u	Force at failure	[kN]
F_y	Force at the beginning of steel yielding	[kN]
G_F	Fracture energy of concrete without fibers	[N/mm]
G_f	Fracture energy of concrete with fibers	[N/mm]
G^l	Energy per unit area dissipated in a shear band	[N/mm]
L	Member length	[mm]
L^d	Damage zone length	[mm]
L^l	Compressive test specimen length or distance between successive damage zones	[mm]
L_t	Transmission length	[mm]
L_{tf}	Transmission length of concrete with fibers	[mm]
M	Moment	[kNm]
M_{cr}	Cracking moment	[kNm]
M_{max}	Moment at maximum load	[kNm]
M_{pl}	Plastic moment	[kNm]
M_u	Moment at ultimate load	[kNm]
M_y	Moment at the beginning of steel yielding	[kNm]
N	Normal force	[kN]
N_f	Number of steel fibers per unit area	[1/mm^2]
P	Pull-out force	[N]
R	Radius	[mm]
S	Shear force in an element between two subsequent cracks	[N]
T	Tensile member force or tensile chord force	[N]
T_1	Tensile chord force at crack 1	[N]
T_2	Tensile chord force at crack 2	[N]
T_y	Tensile member force at the beginning of steel yielding	[N]
T_u	Tensile member force at failure	[N]
U_s	Circumference of the steel bar	[mm]
V_f	Fiber content	[m^3/m^3]
W^d	Total energy per unit volume absorbed in the longitudinal cracks	[N/mm^2]
W^{el}	Elastic energy per unit volume	[N/mm^2]
W^{in}	Inelastic energy per unit volume	[N/mm^2]
W^s	Energy per unit volume dissipated in the longitudinal cracks during softening	[N/mm^2]

Roman Lower Case Letters

a	Crack length	[mm]
b	Width of a cross-section	[mm]
c	Clear concrete cover on the bar	[mm]
c_{eff}	Effective concrete cover	[mm]
$c_{eff,max}$	Maximum effective concrete cover	[mm]
c_i	Concrete cover thickness in each of m directions	[mm]
$c_{i,min}$	Smallest concrete cover to be taken into account	[mm]
d	Effective height of a cross-section	[mm]
d_f	Fiber diameter	[mm]
d^l	Depth of the compressive damage zone	[mm]
d_s	Steel bar diameter	[mm]
d_{s1}	Height h minus effective height d	[mm]
e	Eccentricity	[mm]
f_c	Concrete cylinder or prism compressive strength	[N/mm^2]
f_c^*	Concrete compressive strength at the most compressed side	[N/mm^2]
f_{ct}	Concrete tensile strength	[N/mm^2]
$f_{ct,ave}$	Average concrete tensile strength	[N/mm^2]
$f_{ct,lb}$	Lower bound concrete tensile strength	[N/mm^2]
$f_{ctm,ax}$	Average axial concrete tensile strength	[N/mm^2]
$f_{ct,sts}$	Splitting tensile strength of concrete	[N/mm^2]
f_R	Effective rib area	
f_{su}	Ultimate tensile strength of steel	[N/mm^2]
f_{sy}	Yield strength of steel	[N/mm^2]
f_{t2}	Calculation value for trilinear softening relation	[N/mm^2]
h	Height of a cross-section	[mm]
i	Ordinal integer number	[-]
k	Proportionality factor	[-]
k^l	Factor for calculating the damage zone length	[-]
k_{fc}	Factor to account for increased confinement	[-]
l	Span	[mm]
l_f	Fiber length	[mm]
l_0	Total beam length	[mm]
m	Number of directions for calculation of c_{eff}	[-]
n_{rad}	Number of radial cracks	[-]
n_{cr}	Number of cracks	[-]
n_E	Ratio of E-moduli of steel and concrete	[-]
n_l	Number of layers	[-]
r	Material property related to the average distance between successive longitudinal cracks	[mm]
r_h	Hinge radius	[mm]
r_s	Steel bar radius	[mm]
s_{cr}	Crack spacing	[mm]
$s_{cr,ave}$	Crack spacing calculated with average concrete tensile strength	[mm]
$s_{cr,lb}$	Crack spacing calculated with lower boundary concrete tensile strength	[mm]

t_{50}	Time to reach a diameter of 50 cm in the slump test	[s]
u_v	Vertical deflection	[mm]
w	Crack width	[mm]
w_0	Critical crack width	[mm]
w_1	Crack width at the first bending point of the trilinear softening relationship	[mm]
w_2	Crack width at the second bending point of the trilinear softening relationship	[mm]
w_c	Localized deformation	[mm]
w_{ave}	Crack width calculated with average concrete tensile strength	[mm]
w_{int}	Crack width at intersection point; also denotes crack width of the point at which the slope in bilinear softening relationships changes	[mm]
w_{lb}	Crack width calculated with lower boundary concrete tensile strength	[mm]
w_{loc}	Measured crack width at localized crack	[mm]
w_{next}	Measured crack width next to the localized crack	[mm]
x	Compressive zone depth	[mm]
x, y, z	Cartesian coordinate system	[-]

Greek Capital Letters

ΔL	Elongation	[mm]
Δx	Element length	[mm]
$\Delta\varepsilon$	Additional strain	[-]
$\Delta\varepsilon_{peak}$	Additional strain	[-]
$\Delta\sigma$	Change in stress	[N/mm^2]
Θ	Rotation	[mrad]
Θ_A	Rotation at support A	[mrad]
Θ_B	Rotation at support B	[mrad]
Θ_{el}	Elastic rotation	[mrad]
$\Theta_{cr,i}$	Crack opening angle of a crack	[mrad]
Θ_{max}	Rotation at maximum load	[mrad]
Θ_{pl}	Plastic rotation	[mrad]
Θ_{tot}	Total rotation	[mrad]
Θ_u	Rotation at ultimate load	[mrad]
Θ_y	Rotation at the onset of steel yielding	[mrad]

Greek Lower Case Letters

α_{FCM}	Constant (FCM)	[-]
α_{fd}	Filling degree	[-]
α_s	Angle between critical splitting plane and normal to closest surface	[mrad]
β_{FCM}	Constant (FCM)	[-]
$\beta_{FCM,ave}$	Constant (FCM) for average concrete tensile strength	[-]
$\beta_{FCM,crack}$	Constant (FCM) in the crack	[-]
$\beta_{FCM,confinement}$	Constant (FCM) for confinement capacity	[-]
$\beta_{FCM.lb}$	Constant (FCM) for lower bound concrete tensile strength	[-]
β_{sf}	shape factor	[-]
γ	Combination parameter	[mm^{-1}]
δ	Slip	[mm]
ε	Strain	[-]
ε_0	Compressive strain at peak stress	[-]
ε_{1-5}	Input values for concrete strain in compression	[-]
ε_c	Strain in the compressive zone	[-]
ε_{cm}	Strain in the most stressed layer	[-]
ε_d	Strain caused by the opening of the longitudinal cracks	[-]
ε^{el}	Elastic strain	[-]
ε^{in}	Inelastic strain	[-]
ε_m	Average strain	[-]
ε_r	Radial strain	[-]
ε_s	Steel strain	[-]
ε_{su}	Ultimate steel strain	[-]
ε_t	Strain in the tensile zone	[-]
η	Fiber orientation number	[-]
$\eta_{Vol\,SF}$	Volumetric fiber ratio	[m^3/m^3]
η_x	Fiber orientation number in x-direction	[-]
η_y	Fiber orientation number in y-direction	[-]
η_z	Fiber orientation number in z-direction	[-]
η_θ	Fiber orientation number	[-]
$\eta_{\theta 2D}$	2D fiber orientation number	[-]
$\eta_{\theta 3D}$	3D fiber orientation number	[-]
$\eta_\wp$	Fiber orientation number	[-]
θ	Orientation angle; also denotes friction angle	[mrad]
κ	Curvature	[1/km]
κ_{el}	Elastic curvature	[1/km]
κ_{pl}	Plastic curvature	[1/km]
μ	Coefficient of friction	[-]
ν_s	Poisson ratio of the steel	[-]
ρ_s	Geometrical reinforcement ratio	[-]

σ	Stress	[N/mm²]
σ_{1-5}	Input values for concrete stress in compression	[N/mm²]
σ_I	Concrete stress at the first bending point in the trilinear softening relationship	[N/mm²]
σ_{II}	Concrete stress at the second bending point in the trilinear softening relationship	[N/mm²]
σ_c	Concrete compressive stress	[N/mm²]
σ_{cf}	Concrete stress transmitted by the fibers across a crack	[N/mm²]
σ_{ct}	Concrete tensile stress	[N/mm²]
σ_{int}	Stress at the intersection point	[N/mm²]
σ_r	Radial stress	[N/mm²]
σ_s	Steel stress	[N/mm²]
σ_τ	Fiber stress during fiber pull-out	[N/mm²]
τ_b	Bond stress	[N/mm²]
τ_{b1}	Threshold value pull-out or splitting bond failure	[N/mm²]
τ_m	Bond strength	[N/mm²]
φ	Cone angle between cone surface and bar axis	[mrad]
$\chi(c_i)$	Concrete cover dependent indicator function	
ψ	Orientation angle	[mrad]
ψ_{cpo}	Angle indicating concrete cone pull-out	[mrad]
ω_s	Mechanical reinforcement ratio	[-]

Subscripts

ax	Axial
c	Concrete
f	Fiber
i	Numbering variable
m	Average
max	At maximum load
s	Steel
t	Tensile
u	At ultimate load
v	Vertical
x	In the x-direction
y	At the beginning of steel yielding

Abbreviations

1D	1-dimensional
2D	2-dimensional
3D	3-dimensional
3PB	Three-point-bending
4PB	Four-point-bending
CDZ	Compressive Damage Zone
FCM	Fictitious Crack Model
FE	Finite Element
HSC	High strength concrete
LVDT	Linear Variable Displacement Transducer
LWAC	Lightweight aggregate concrete
NSC	Normal strength concrete
RC	Reinforced concrete
RH	Relative humidity
SCC	Self compacting concrete
SCSFRC	Self compacting steel fiber reinforced concrete
SFRC	Steel fiber reinforced concrete
SLS	Serviceability Limit State
TBM	Tunnel boring machine
ULS	Ultimate Limit State
UTT	Uniaxial tension test
WST	Wedge splitting test

Curriculum Vitae

Name	Petra Schumacher
Born	1973 in Darmstadt, Germany

1983 – 1993	High school at Ludwig-Georgs-Gymnasium, Darmstadt, Germany Achieved diploma: Abitur (equivalent to A-levels)
1988 – 1989	High school year at Copper Basin High School, Tennessee, USA
1993 – 1999	Studies of Civil Engineering at Darmstadt University of Technology, Germany Achieved title: Diplom-Ingenieurin Main disciplines: Concrete Structures, Steel Structures, Structural Mechanics
1997 – 1998	Socrates/Erasmus exchange semester at Delft University of Technology, The Netherlands
2000 – 2006	PhD study at the Concrete Structures Group, Faculty of Civil Engineering and Geosciences, Delft University of Technology, The Netherlands
2004 – 2006	Consulting activities at Hotel Reuterhof, Stavenhagen, Germany

Publications Related to this Research

Schumacher, P., Braam, C.R., Walraven, J.C. (2001). *Steel fiber reinforced concrete – Cylinders under uniaxial compressive loading – Preliminary tests*, Stevinreport No. 25.5.01-06, Delft University of Technology, The Netherlands.

Schumacher, P., Braam, C.R., Walraven, J.C. (2002a). Compressive behavior of steel fiber reinforced high strength concrete, *Proc. 6th Int. Symposium on Utilization of High Strength/High Performance Concrete*, Leipzig, Germany, pp. 1377-1390

Schumacher, P., Bigaj-van Vliet, A., Braam, C.R., Uijl, J.A. den, Walraven, J.C. (2002b). "Bond of reinforcing bars in self-compacting steel fiber reinforced concrete" in: *Bond in concrete – from research to standards*, Balázs, G. et al. (ed.), pp. 823-830.

Schumacher, P., Bigaj-van Vliet, A., Braam, C.R., Walraven, J.C. (2002c). "Bond of reinforcing bars in self-compacting steel fiber reinforced concrete", *Beiträge aus der Befestigungstechnik und dem Stahlbetonbau, Festschrift zum 60. Geburtstag von Prof. Dr.-Ing. R. Eligehausen*, (Editors: S. Lettow, J. Hofmann), ibidem Verlag Stuttgart, Stuttgart 2002.

Schumacher, P.; Braam, C.R.; Walraven, J.C. (2002d). Compressive behavior of steel fiber reinforced concrete, *Bauingenieur Sonderpublikation 4th Int. PhD Symposium*, pp. 269-274, München, Germany.

Schumacher, P., Uijl, J.A. den, Braam, C.R., Walraven, J.C. (2003a). *Self-compacting steel fiber reinforced concrete prisms under compressive loading*, Stevinreport 25.5-03-11, Delft University of Technology, The Netherlands.

Schumacher, P.; Uijl, J.A. den; Walraven, J.C. (2003b). *Fracture energy determined from three-point bending tests on self-compacting steel fiber reinforced concrete*, Stevinreport 25.5-03-18, Delft University of Technology, The Netherlands.

Schumacher, P., Uijl, J.A. den, Walraven, J.C., Bigaj-van Vliet, A.J. (2004). Bond of reinforcing bars in steel fiber reinforced concrete, *5th Int. PhD Symposium in Civil Engineering*, pp. 1205-1212, Delft, The Netherlands.

Walraven, J.C., Schumacher, P. (2005a). Anwendungen für Ultra-Hochleistungsbetone, *Tiefbau* April 2005, pp. 230-234, ISSN 0944-8780.

Schumacher, P., Uijl, J.A. den, Walraven, J.C., Bigaj-van Vliet, A.J. (2005b). Bewe(ä)rter Stahlfaserbeton, *Braunschweiger Bauseminar 2005*, Heft 190 Schriftenreihe iBMB, S. 27-36, TU Braunschweig, Germany.

Schumacher, P., Walraven, J.C., Uijl, J.A. den, Bigaj-van Vliet, A.J. (2006). Rotation capacity of steel fiber reinforced concrete beams, *6th Int. PhD Symposium in Civil Engineering*, pp. 136-137 and CD file 257_Schumacher.pdf, Zurich, Switzerland.